Excitation and Saturation of White Dwarf Pulsations

Thesis by

Wu, Yanqin

In Partial Fulfillment of the Requirements

for the Degree of

Doctor of Philosophy

California Institute of Technology

Pasadena, California

1998

(Submitted December 29, 1997)

dedicated to my parents,

Abstract

Variable hydrogen white dwarfs (DAV) pulsate in a number of low-order gravity-modes with periods from 100 s to 1200 s and amplitudes no larger than a few percent. We answer two questions in this thesis: the driving for these pulsations, and the saturation of their amplitudes.

The surface convection zone in these stars, which adjusts its entropy level instantaneously during the pulsation, can drive the observed modes. This mechanism (called 'convective driving') was discovered by Brickhill but has been largely neglected so far. We find that modes with periods shorter than the thermal adjustment time of the convection zone can become overstable, but those with very short periods are hardly visible at the surface. As the star cools and the convection zone deepens, longer period modes can be excited. The driving rates increase sharply with period. We relate these to the time-scale of mode variability. We include complications arising from nonadiabaticity in the radiative interior and turbulent damping at the convective-radiative boundary. The former limits the driving and damping rates for strongly nonadiabatic modes, and relates the phase and amplitude of surface horizontal velocity in a gravity-mode to those of its flux variation. The turbulent damping results from the horizontal velocity shear below the convection zone, inside which there is little velocity shear and negligible damping. This suppresses the amplitudes of long period modes to below detection. The width of the theoretical DAV instability strip is about 1000 K.

The growth of an overstable mode can be saturated by parametric instability, where energy transfers resonantly into two damped modes of roughly half its frequency. This occurs above a critical amplitude which depends on the 3-mode coupling coefficient and the nonadiabatic damping rates. The critical amplitudes all fall below a few percent, with longer period modes having larger surface amplitudes. Combined with the amplitude limits due to turbulent damping, our estimates compare well with observations. Other types of mode couplings are needed to explain the observed 'mode selection'.

Finally, we show that the combination frequencies found in pulsation power spectra are produced by the time-varying convection zone which nonlinearly affects mode visibility.

Acknowledgements

Thanks go to Peter Goldreich, without whose scientific(?) contributions and massive editing, this thesis would have been banal. He has written Chapter 3, and has contributed heavily to the other chapters. I am very grateful for such an 'analytical' advisor, not least for his many useful advices along the way – though I have never been able to 'get up early' except due to jet-lags and during the final panic.

Chris Clemens and Scot Kleinman came to Caltech with rich experiences in variable white dwarfs. Together with Marten van Kerkwijk, they have employed new observing techniques to test theories on white dwarf pulsations – hopefully some of our predictions will make it. The enthusiasm and efforts of these observers have led us to implement our work towards testability. Chapter 8 in this thesis spawned from the dicussions with them, and they have permitted me to use their data pre-publication.

Paul Bradley at Los Alamos has gracefully provided me with white dwarf models on which many calculations in this theis are based. He also illuminated me on various physics concerning these white dwarfs. I also benefited from the equation of state and opacity tables made public by Roger and Iglesias at Lawrance Livermore. Angela Putney of Caltech provided many fun discussions about mysteries in white dwarfs.

Many current and past members of the TAPIR group, Nahum Arav, Lars Bildsten, Roger Blandford, Eugene Chiang, Brad Hansen, Dong Lai, Zhiyun Li, Yoram, Maxim Lyutikov, Andrew Melatos, Sterl Phinney, Nir Shaviv, Glenn Soberman, Greg Willet (what an anarchistic state!) etc., have widened my scope and kept improving my understanding of physical processes. I enjoyed the many lunch dicussions (even when it was about killing the grass) and the interaction room interactions.

The final version of the thesis have benefited from the many comments by Sterl Phinney, James McCarthy, Judy Cohen and Marshall Cohen. And I am once again impressed with their conscientious (??) working attitude and strong curiosity.

Some part of my brain says, 'No, I don't want a sentimental story here'; while the other parts say, 'I want to tell about their love and friendship'. For my family and my friends, 'thanks' is a hypocritical word.

'*mā má mă mà*' are not that hard, right, Marten?

Contents

Chapter 1 Introduction

Asteroseismology provides an excellent window into stellar interiors. While stellar spectra tell us about photospheres, and binaries about global properties such as mass and radius, the optically thick interior is best revealed by periodic pulsations; that is, if the star decides it likes to make music. This branch of astrophysics has already yielded much useful information (see the reviews by Brown & Gilliland 1994; Gautschy & Saio 1996). On-going and future observational efforts of monitoring variable stars over longer time spans, in new wavelength bands, and using larger telescopes promise new knowledge and exciting insights about pulsating stars – if the theory can catch up with the observations. Theoretical studies of stellar pulsations divide into linear and nonlinear categories (Cox & Giuli 1968). In the linear approach the equation of motion is approximated under the assumption of infinitely small pulsation amplitudes. Then adiabatic calculations yield eigenfrequencies and eigenmodes and the nonadiabatic calculations growth or damping rates. The identification of observed frequencies with appropriate eigenmodes yields precious information about pulsating stars. The simplicity of linear theory makes physical understanding of stellar pulsations accessible. Nonlinear theory, on the other hand, suffers from complications associated with the infamous word nonlinear. Although more difficult to apply than its linear counterpart, it can be more fruitful. In particular, it may be used to determine what happens when overstable modes grow to saturation.

My thesis focuses on pulsating white dwarfs with hydrogen envelopes (ZZ Ceti variables). It includes contributions to both linear and nonlinear theory. The first part sets criteria for the linear stability of gravity-modes (g-modes) in white dwarfs with hydrogen envelopes (called DA white dwarfs). In the second part some first steps are made towards deducing saturation amplitudes of overstable modes. Along our successful yet tortuous path, a final physical understanding has always been the goal.

1.1 Overview of Pulsating Stars: Connections

During the evolution of a star, it enters and leaves phases of pulsational instability several times.[1] We look at a typical low mass star like our Sun (a G-type dwarf).

[1] For a slightly more complicated picture than is given here, see Becker 1987.

1.1.1 Main-Sequence Sun

From the star's birth till the end of its main sequence life, it is relatively quiet. We do not have much pulsational information about the earliest stage when it is fully convective. While it is on the main sequence, we detect only random variability associated with rotation and magnetic activity. However, the main-sequence Sun is known to pulsate with minute amplitudes in a multitude of pressure-modes (p-modes). This has spawned a new field of astronomy called 'helioseismology'. Searches are being made for similar pulsations in solar-type stars (Gilliland et al. 1993; Brown et al. 1991; Brown & Gilliland 1990). A report of a successful detection in η-Bootis (Kjeldsen et al. 1995) sets off a flurry of theoretical activities, even before this result was soon refuted by Brown et al. (1997). This illustrates how eager we are to learn from stellar oscillations.

Accurate measurements of solar eigenfrequencies provide detailed information on the sound speed in the solar interior, on the settling of helium relative to hydrogen close to the core, and on the differential rotation inside the Sun. The first two results constrain the 'standard solar model' (Christensen-Dalsgaard 1996), and severely limit possible astrophysical solutions to the solar neutrino problem (Bahcall & Krastev 1996). They also enable us to infer the structure of the convective region in the Sun and thereby calibrate both the efficiency of convective heat transport in the superadiabatic layer near the surface (Monteiro et al. 1996), and the extent of convective overshooting at the base (Christensen-Dalsgaard et al. 1995).

The internal rotation of stars is also an unique product from pulsational study. Rotational splittings of solar p-modes are consistent with uniform rotation in the solar radiative interior. This finding bears on the evolution of angular momentum in solar-like stars. The rigid rotation in the radiative region has led to various theoretical speculations, including a hypothesis of angular momentum transport by gravity waves (Kumar & Quataert 1997). Magnetic fields can also act to transport angular momentum, with perhaps a role by the weak field MHD instability (Balbus & Hawley 1994). Moreover, contrary to theoretical expectation based on ideas of momentum transfer in convective region, the isorotational surfaces inside the solar convection zone are not cylindrical. The absence of significant differential rotation at the convective-radiative boundary also raises questions about the role played by magnetic fields and convective overshooting.

With all these excellent works by the helioseismologists, the large scale internal magnetic fields seem about the only thing left to be measured in the Sun. It is amusing to be able to claim to the geophysicists that we know the interior of the distant Sun better than we know that of the Earth.

Main sequence stars slightly more massive than the Sun (spectral types A to F) may be unstable to pressure-mode or gravity-mode oscillations. These are called δ-Scuti variables, and their pulsations are thought to be excited by the opacity-mechanism (κ-mechanism). δ-Scutis are of particular interest to us as many of them are multi-periodic, just like the pulsating white dwarfs. Only a few of their modes are excited to observable amplitudes, out of a large population of similar modes. So

called 'mode selection', this behaviour may well be explained in the same fashion as we do here for ZZ Cetis, i.e., nonlinear mode coupling including parametric instability and direct resonance (see also Dziembowski & Krolikowska 1985). The amplitudes of individual modes are typically of order 0.02 mag,[2] slightly larger than those in ZZ Cetis, and these amplitudes are observed to vary in time (Korzennik et al. 1995). We may be able to understand the amplitudes of pulsations in δ-Scutis with the same methodology we use for ZZ Cetis. Unlike ZZ Cetis, though, it is possible to observe high spherical degree, non-radial pulsations ($8 \leq \ell \leq 16$), at least in rapidly rotating δ Scutis using rotationally broadened lines (Kennelly et al. 1991). Different parts of the stellar surface are projected to different parts of the line profile, and the high ℓ oscillations can be detected as regular wiggles in the lines. A similar technique has been applied to rapidly rotating B variables. By contrast, even in relatively fast rotating ZZ Cetis, pressure broadening disguises the rotational signal, and only $\ell = 1$ and $\ell = 2$ modes are observable from photometric or spectroscopic variations.

Some F-type stars exhibit weak pulsation in non-radial g-modes with periods ranging from 5 hours to 2 days (see, for example, Krisciunas et al. 1995). The excitation of these modes is not well understood. The problem of mode selection exists here too, since these multiperiodic oscillations exhibit only a few modes out of a whole sea of available modes. Changes in pulsational amplitudes have been reported. This is another example to which we may be able to apply the results described in this thesis.

1.1.2 Life After the Main-Sequence

But let us come back to the evolution of a solar-type star. After a long and quiescent main-sequence phase, it becomes increasingly flamboyant, pulsation-wise.

During the red-giant phase (hydrogen shell burning outside a degenerate helium core), the star may be observed as a slow, irregular (Lb type) or semi-regular variable showing low Q (quality factor) oscillations with periods between 20 and 2000 days. Next comes strong mass-loss followed by an interval spent on the horizontal branch (core helium burning). During part of this time it may become an RR Lyrae variable, showing regular variations with amplitudes of about 1 mag and periods of about a day. RR Lyrae pulsations are excited in hydrogen and helium ionization zones. Besides their astronomical importance as standard candles, RR Lyraes are interesting in the context of this thesis because convective energy transport plays an important role at the red edge of their instability strip, much like the ZZ Cetis. From the earliest reports (Baker 1965) to the latest news (Bono & Stellingwerf 1993), interaction between pulsation and convection and its consequence for the location of the red edge has been a matter of great debate. For the cooler members of the class, convective energy transport is most important and the convective turn-over time is much shorter

[2]Luminosity variations are usually described in the unit of magnitudes. With the logarithmic base, 0.02 mag means that $\delta L/L$ is about 0.02, where δL is the size of variation in stellar luminosity. Later in this thesis, we introduce the unit of mma, 1 mma $= 10^{-3}$ mag $\sim 0.1\%$.

than the pulsation period in their outer layers and much longer deeper down. Analyses which ignore perturbations to the convective flux predict a cooler red edge than observed. Recent models incorporating time-dependent convection appear to remove this discrepancy (Bono et al. 1995). In these models, the radial extent and the efficiency of convection changes significantly during the pulsation cycles. Most of these investigations are numerical, which tends to obscure simple physical understanding. Perhaps when combining the traditional assumption of frozen-in convective flux valid in the limit of extremely long adjustment time, with the assumption of instantaneous adjustment in the other limit (see below), one may be able to find a more transparent way of understanding the location of the red edge of RR Lyraes.

The horizontal branch stage ends when the star's hydrogen-burning shell starts to dominate its luminosity. Shortly thereafter the star metamorphoses into a fluffy asymptotic giant branch (AGB) star. In this phase it becomes a glamorous Mira variable, pulsating radially with long periods and large amplitudes. These pulsations are thought to be driven in hydrogen or helium ionization zones located close to the surface, although the situation is again muddied by the presence of a convective envelope in which the convective flux dominates the energy transport and the convective turn-over time is comparable to the mode period (Gautschy & Saio 1996). Mass loss rates of order 10^{-7} to $10^{-4} M_{\odot} \mathrm{yr}^{-1}$ (Pijpers & Harbing 1989) are observed for these stars. They are thought to be due to a combination of mass ejection produced by shocks and radiation pressure acting on dust grains, the shocks being associated with the pulsations.

1.1.3 Along the White Dwarf Cooling Track

PG1159 Stars: Driving and Rotation

After a few more twists on the H-R diagram, the star finds itself in the domain of this thesis – that of the white dwarfs. It begins its descent along the white dwarf cooling track as a PG1159 type star. While oscillating, it is classified as a PNNV star if surrounded by a planetary nebulae, or as a DOV or GW Vir star once the nebula has dissipated. Observationally, pulsations in low ℓ g-modes occur across a broad range of temperature; the instability strip is not well-defined. Excitation at the extremely high photospheric temperature of $\sim 10^5$ K is thought to be due to cyclic ionization of carbon and oxygen (Starrfield et al. 1984). A paradox that remains to be explained is that some pairs of spectroscopic twins exhibit different pulsational stabilities (Werner 1993). A hint as to the solution may come from the recent discovery that the photospheric nitrogen abundance is correlated with the pulsational behavior (Dreizler 1996).

Compared to the important but monotonous Cepheid or RR Lyrae variables, pulsating white dwarfs play far more interesting music, and their light variations carry more information about their internal structure. For PG1159-035, 115 individual frequencies are found, with periods ranging from

385 s to 1000 s. The Whole Earth Telescope consortium (for an introduction see Winget et al. 1991) targets these stars during long and uninterrupted observing runs, obtaining detailed light curves from which masses, chemical compositions, and possibly even cooling times are deduced (Winget 1991; Kawaler et al. 1995; Bond et al. 1996). The amplitudes of PG1159 stars vary significantly on the time-scale of months (variables with planetary nebulae) to years (those without). It is difficult to pin down their exact period structure even with prolonged observations. Nevertheless, the existence of chemically stratified atmospheres has been inferred for both PG1159-035 and PG2131+066 with a composition discontinuity around $10^{-3}M_{\odot}$ (measured from the surface), presumably where helium separates from the carbon/oxygen core. However, it might be best to be suspicious of this claim at this moment. A conservative estimate for the thermal time at this discontinuity yields at least a year. This is inconsistent with the assumption that mode excitation takes place in the C/O ionization zone.

Rotation in the PG1159 stars poses another intriguing puzzle. Measured rotation periods range between 5.1 hrs (PG2131+066) and 1.6 days (PG0122+200), with a few pulsators closely clustered around 1 day. Almost every star that has been looked at with sufficient frequency resolution shows rotational splittings. These results, taken at face value,[3] have two important implications. First, if DB stars (and possibly DA stars, both of them will be discussed in detail next) are direct descendants of these rapidly rotating PG1159 variables, they should all have rotation rates shorter than a day – assuming angular momentum is conserved during the cooling and shrinking of a pre-white-dwarf. Such a fast rotation rate for a DA or DB star would be resolved with observations over a couple of nights. But rotation rates are observed for only four out of two dozen DA variables (with periods ranging from 8.9 hours for G226-29 to 4.2 days for GD165), and for only 1 out of 8 DB variables (with a period around 1.6 days for GD358). How can this be reconciled with the rotation measurements for the PG1159 stars?

The second implication of the rapid rotation rates is related to the question of angular momentum evolution in low and medium mass stars. In order that a sufficient fraction of the initial angular momentum be preserved in the white dwarf forming core, the rotational disengagement between the stellar core and its envelope must occur at or before the AGB phase. We know that this must have happened for at least some magnetic white dwarfs, another population of white dwarfs for which rotation can be reliably measured. At least some of these stars are rotating fast, much faster than they would be if disengagement never took place. The high proportion of fast rotators in PG1159 stars seems to imply that the decoupling happens more often in nonmagnetic stars. Is this process a sudden one? Are there significant differences between the angular momentum evolution of magnetic white dwarfs (which might have magnetic Ap stars as progenitors) and pulsating white dwarfs (which are ordinary except that they are passing through special temperature ranges)? Alas, even small,

[3]For an example of a rotation rate in doubt, see Bond et al. 1996.

degenerate dwarfs can be enigmatic.

DAs and DBs: Driving the Pulsations

As PG1159 stars cool down and contract, they may become DA or DB stars, with spectra showing partially ionized hydrogen or helium, respectively. Chemical evolution during this stage and beyond is an active field with many unsolved puzzles.

Variable DA white dwarfs, the subject of this thesis, are also called ZZ Cetis after the prototype, or DAVs for short. They are found in a narrow temperature range around 12000 K (the ZZ Ceti instability strip) and show multiple periods ranging from 100 to 1200 s. The amplitudes of individual peaks range from 1 to 100 mma (1 mma $\sim$ 0.1%). Flux variations are produced as pulsations compress and inflate different parts of the star. Only a handful of modes are excited to observable amplitude in any particular star; energy stored in such an excited mode may be as large as 10^{30} erg. Even before the excitation mechanism is well understood, it is possible to extract much of the information about the white dwarf from the observed period structure. For details, I refer readers to the review by Gautschy & Saio (1996), which documents these efforts and their results.

DB variables are physically similar to DAs – substitute a helium layer for the hydrogen layer and raise the temperature such that the outer electron in a helium atom is beginning to be ionized in the atmosphere and you transform a DA variable to a DB variable. A significant observational difference is that power spectra in DBVs tend to show a larger number of peaks than those of DAVs.

For both types (though we will focus on DAVs from now on), the opacity maximum associated with H or He ionization causes convection in the outer envelope, and in this region almost all stellar flux is carried by convection. The depth of the surface convection zone increases sharply with decreasing effective temperature. The overstability of g-modes is sensitive to the manner in which the convective heat transfer responds to pulsations. Perhaps because the ZZ Ceti instability strip is an extension of the Cepheid instability strip (which includes pulsators like Cepheids, δ-Scuti, and oscillating Ap stars) and because hydrogen is partially ionized in the surface layers of these white dwarfs, it is often stated that the κ-mechanism (opacity-mechanism) is responsible for their excitation. But due to the high gravity, the zone of partial ionization is very thin, and its thermal relaxation time is orders of magnitude shorter than the mode periods. Driving in this zone falls far short of overcoming damping from the radiative interior. On the other hand, the thermal time-scale at the bottom of the convection zone is similar to the mode periods. This turns out to be an essential feature of the excitation mechanism we discuss below.

The response of a convection zone to pulsations is an unsolved problem. Most investigations rely on the 'frozen-in' approximation (Baker & Kippenhahn 1965), in which the convective flux is assumed to be unaffected by pulsational perturbations. This assumption is valid in the limit that pulsations periods are much shorter than the typical convective eddy turn-over time. Pesnell (1987)

shows that when this assumption is valid, the bottom of the convection zone contributes to mode excitation; this mechanism is called 'convective blocking'. Application of the 'frozen-in' approximation to white dwarfs has produced overstable modes in the correct temperature range. However, this approximation is inappropriate in this context. Brickhill (1991a and all his other papers cited here) emphasizes that the convective turn-over time in even the coolest DAVs is of order a second, much shorter than the periods of the observed gravity-modes. To understand the convection-pulsation interaction in this limit, we may either rely on numerical hydrodynamic simulations (Gautschy et al. 1996), or look for a valid, simplifying assumption. Brickhill (1983, 1991a, 1991b) assumes that the convection responds *instantaneously* to the pulsational state. When in hydrostatic and thermal equilibrium, an efficient convection zone has an almost flat entropy profile, thanks to the labor of turbulent eddies (Schwarzschild 1966). If the energy flux injected into the bottom of the convection zone varies over a time-scale much longer than the typical eddy turn-over time, the convection zone maintains its *isentropic* profile by changing its entropy uniformly. For this uniform entropy rise (drop), it absorbs (releases) energy from (into) the incoming flux, allowing only part of the flux variation to emerge at the stellar surface. As Brickhill's work demonstrates, and ours confirms, this interaction is responsible for exciting gravity-modes in DAV white dwarfs. The convection zone functions like a heat engine, absorbing heat when compressed and releasing it when expanded. This mechanism of mode excitation is called 'convective driving' (Brickhill 1983).

1.2 Outline of the Thesis

1.2.1 Driving of G-modes

After this lengthy preamble, we proceed to describe the outline of this thesis.

Scaling relations for both the white dwarf models and their gravity modes are presented in Chapter 2. These relations are used throughout the thesis.

In Chapter 3, we derive an analytic criterion for overstability of g-modes based on 'convective driving'. The key approximations are the instantaneous adjustment of the convective flux to the pulsation, and the quasiadiabatic approximation in the radiative interior. We demonstrate that a *necessary* condition for 'convective driving' to produce overstability is for the mode period to be shorter than τ_c, the thermal adjustment time-scale for the whole convection zone. This time-scale is the ratio between the heat absorbed or released by the convection zone during pulsation and the perturbation to the photospheric flux; the latter determines the entropy variation in the whole convection zone under the assumption of instantaneous adjustment. For DA variables, τ_c is about 20 times larger than the conventional thermal time at the base of the convection zone, τ_b; the latter is approximately the ratio of the internal energy above a given depth to the equilibrium luminosity. The factor of 20 originates from the increase in photospheric entropy when flux rises, as well as

from the steepening of the superadiabatic gradient below the photosphere to transport a larger convective flux. A DA white dwarf enters the blue edge of the ZZ Ceti instability strip when its effective temperature drops to a value at which its convection zone satisfies $\omega\tau_c \geq 1$ for the $n = 1$, $\ell = 1$ g-mode (with a period, $p = 2\pi/\omega$, of $\sim 100\,\mathrm{s}$).[4] For modes with $\omega\tau_c \gg 1$, the photospheric flux perturbation is reduced by a factor of $1/(\omega\tau_c) \ll 1$ relative to the flux perturbation entering the bottom of the convection zone. This reduced visibility of overstable modes is partially responsible for the red edge of the DA instability strip, where all overstable modes have periods much shorter than τ_c.

Clemens (1993) summarizes several observational correlations involving ZZ Ceti pulsators. He finds that cooler stars pulsate in modes of longer periods and larger amplitudes than hotter ones. The correlation between effective temperature and mode periods fits nicely into the 'convective driving' picture: cooler variables have larger τ_c, so they can drive modes of longer periods. To understand the correlation between temperature and amplitudes, one would have to investigate the nonlinear saturation of overstable modes. This is discussed later.

Turbulent stress in the convection zone presents a complication which is dealt with in Chapter 4. We show there that turbulent viscosity suppresses the shear in the convection zone to the extent that it gives rise to negligible viscous dissipation. An interesting consequence is the presence of a finite jump in the horizontal velocity across the lower boundary of the convection zone. We investigate the Kelvin-Helmholtz instability triggered by this velocity jump and the subsequent turbulent dissipation. The latter depends on the size of the velocity jump and therefore the pulsation amplitude. The lowest frequency modes are most strongly affected by this dissipation.

The quasiadiabatic calculations in Chapter 3 suffer from a more serious limitation. Modes which are both overstable ($\omega\tau_c \geq 1$) and easily visible have $\omega\tau_b < 1$ at the bottom of the convection zone. Thus their dimensionless entropy perturbation (δs) is of order the Lagrangian pressure perturbation ($\delta p/p$) at the top of the radiative region. This leads us to investigate the fully nonadiabatic perturbations in Chapter 5. We find that radiative diffusion affects the eigenfunctions of overstable modes, and stabilizes some long period modes which are overstable in the quasiadiabatic calculations. But the theoretical prediction for the longest period of overstable modes still lingers around 2000 s, much larger than the 1200 s deduced from observations. When we extend the same nonadiabatic calculations to stable modes, we find their damping rates are limited from above to of order $\omega/(2\pi n)$, where n is the radial order of the mode. In Chapter 5, we provide a physical explanation for this relation. These new damping rates can be orders of magnitudes smaller than those derived from quasiadiabatic calculations, and they are very important for our later results on pulsation amplitudes.

[4] From the observational point of view, it might be best to define a blue edge where the $n = 1$, $\ell = 2$ g-mode starts being overstable, as this is the shortest period mode that can be readily observed. But in this thesis, we largely ignore $\ell = 2$ modes for simplicity.

We rely on models of DA white dwarfs supplied by Bradley to obtain g-mode eigenfrequencies. We also build our own series of model envelopes; these extend from the photosphere down to a depth well below the convection zone and cover a range of effective temperature that includes the observed instability strip. Our models utilize the LLNL hydrogen opacity and equation of state, as well as a simple mixing-length prescription for convection. They are described in Appendix B. Their fine gridding in the superadiabatic layer of the convection zone proves to be essential for assessing the width of the theoretical instability strip. These models are also employed in Chapters 4 and 5 to study the effects of heat leakage and viscosity. Due to the uncertainty in convection prescription, the comparison between the observations and the theoretical predictions obtained using these models needs to be taken with caution.

1.2.2 Amplitudes of Pulsations

Having gained insight into the problem of mode excitation, we turn our attention to the more challenging issues of amplitude limitation and mode selection in white dwarf pulsations. Here, we first review some relevant observational results.

As stated previously, ZZ Ceti stars exhibit photometric variations with amplitudes ranging from 1 mma (the detection limit) to 100 mma. Based on observations of over two dozen DAVs, Clemens (1993) concludes that a star pulsates in longer periods and larger amplitudes as it cools from the blue to the red edge of the instability strip. He finds an approximately quadratic correlation between pulsation amplitude and the energy-weighted mean period.

The above correlation is at best statistical. Mode amplitudes at any given time do not appear to depend on their frequencies or the (n, ℓ, m) quantum numbers in an easily rationalizable way. Winget et al. (1994) showed this for the DBV GD358, and this appears typical for other pulsators as well. The pulsational energy in the whole star can be dominated by a few modes, while their neighboring modes are not detected at all. The process leading to this kind of irregular energy distribution is often called 'mode selection'. Moreover, amplitude ratios within rotationally split multiplets are usually incompatible with the hypothesis of equal excitation modified by the effect of geometrical projection.

Apart from the correlation between mode periods and amplitudes, Clemens (1993) also finds that larger amplitudes are associated with stronger time variability. This is clearly seen in ZZ Psc (G29-38), the pulsational properties of which have been carefully monitored and documented by Kleinman (1995). We compile a shortened form of his data into Table 1.1 to provide a flavor of the amplitude variations. Notice the 614 s mode: it dominates the power spectrum at some epochs, but completely evades detection at others. The same is true for the 860 s mode. Large phase changes in the 614 s mode have been reported (Winget et al. 1990, Kleinman et al. 1994), and mode amplitudes are observed to vary on time-scales of months or even days. There is a correlation between mode

approximate period(s)	Amplitudes (mma) at different epochs				
	Aug85	X2N88	Sep89	X8S92	Sep93
284	3.5	3.5	6.4	6.9	3.6
400	7.0	5.6	9.7	11.2	6.0
614	31.3	58.0	...	10.6	31.6
860	24.6	...	...	...	...

Table 1.1: Amplitudes of various modes in ZZ Psc during different observing campaigns (Kleinman 1995). The dots '...' represent non-detection at that frequency.

period and amplitude variability, with shorter period modes exhibiting stronger stability: the 284 s mode has relatively constant amplitude. Kleiman (1995) reports changes in frequency spacing and relative amplitudes within close triplets that were interpreted as rotational split multiplets.

These observations raise the following questions. What determines the observed amplitudes of pulsations? What causes the fluctuations in mode phases and amplitudes? What sets the time-scales for these fluctuations, or, why are short period modes more stable than long period ones? What is the cause of mode selection? What determines the different amplitudes within a rotationally split multiplet? Why does the frequency spacing between rotationally split multiplets vary among modes in some stars (for example, in GD358)? Are these stars really differentially rotating? How could these multiplet spacings change with time as they appear to do in G29-38?

In the second part of this thesis, we focus on understanding the physical mechanisms in ZZ Ceti variables that limit the amplitudes of overstable modes. Our work provides answers to the first three questions in the above list, and suggest some possible solutions to the fourth question.

Dziembowski (1993) mentions two amplitude limiting mechanisms in pulsating stars, viz., saturation of the driving when mode amplitudes become sufficiently large, and nonlinear transfer of energy from overstable modes to damped ones. The first mechanism applies to RR Lyraes and Cepheids, while the second one operates in ZZ Cetis and other small amplitude pulsators.

In Chapter 6, we summarize useful information for understanding nonlinear mode interaction. For gravity-modes in a stratified medium, the lowest order interaction involves three modes. We derive the expression for the three-mode coupling coefficient based on adiabatic perturbations. This coupling coefficient, κ, measures the efficiency of energy and angular momentum transfer among three standing waves at given amplitudes. Later in Appendix G, we take great care to correctly integrate the above expression for the coupling coefficient; the results are compared with analytical estimates. We come back to Chapter 6. Here, we derive the amplitude equations, a group of complex equations that govern the temporal evolution of mode amplitudes. This is followed by the energy equations (derived in Appendix F), which describe the secular evolution of mode energy due to

the nonlinear interaction. We then investigate two types of three-mode couplings, viz., parametric resonance and direct resonance. In a parametric resonance, a large energy mode (the parent mode) interacts with two lower energy modes of roughly half its frequency (daughter modes). We derive the criterion for parametric instability (see also Landau & Lifshitz 1976), and verify this criterion using numerical simulations. In a direct resonance, at least two strong modes couple with another mode of roughly the sum or difference of their frequencies. We discuss briefly the role of direct resonance in modulating mode amplitudes. Numerical evolution of the amplitude equations in our work is vastly facilitated by the application of an efficient numerical integrator, the 'symplectic integrator' (discussed in Appendix C).

We devote Appendix E to a more detailed study of the nonlinear dynamics in globally or selectively coupled systems. For conservative systems (with no driving or damping), we discuss current understanding on the process of energy equipartition. For dissipative systems (with driven and damped modes), we estimate the equilibrium energy. In both these studies, we support our arguments using numerical simulations. Our conclusions in this appendix help to illuminate the complicated dynamics in a multimode pulsating star.

During our numerical study, we frequently encounter an intrinsic instability in the amplitude equations. This instability occurs when a system with only cubic nonlinearity (three-mode coupling) has too large energy. Documented in Appendix D, this instability puzzled us for a long time until we realize that it cannot happen in physical systems. We provide an analytical explanation to the instability in order that others will be able to avoid being confused by it as we were.

We describe some of the most interesting results from this thesis in Chapter 7. There, we demonstrate that parametric instability can stop the growth of overstable modes at the observed amplitudes. Whenever the amplitude of an overstable parent mode rises above a critical value, the linearly damped daughter modes are parametrically excited and receive energy from the parent mode cataclysmically. If energy in the daughter modes can be quickly dissipated, the parent mode will stop growing at this critical amplitude, also called the 'parametric amplitude'. For a given pair of daughter modes, the parametric amplitude scales roughly linearly with the linear decay rates in the daughter modes, and inversely linearly with the coupling coefficient. In pulsating white dwarfs, each overstable mode interacts with many pairs of daughter modes, and the pair that give rise to the lowest parametric amplitude determine the theoretical upper limit for the pulsation amplitude in the parent mode. We find that the amplitudes of fractional density perturbations in low radial order modes are limited to lower values, with associated flux perturbations of order a few mma, while high order modes have higher amplitudes, corresponding to flux variations up to ~ 100 mma. The sense of the correlation between amplitudes and periods, as well as the numerical values for the amplitudes, correspond quite well with observations. Effects due to the convection zone visibility (discussed in Chapter 3), limb-darkening and viewing geometry all need to be taken into accout for

a more detailed comparison.

Results from the previous chapters are integrated into the prediction for these mode amplitudes. The nonadiabatic calculations discussed in Chapter 5 produce damping rates that can be orders of magnitudes smaller than those from the quasiadiabatic calculations. These new damping rates prove essential for obtaining the correct parametric amplitudes. The discussions and simulations in Chapter 6 provide theoretical basis for estimating the parametric amplitudes, and our confidence in the numerical values of the coupling coefficients originates from the careful study in Appendix G. Also, turbulent damping at the convective-radiative boundary (see Chapter 4) effectively limits the amplitudes of many long period overstable modes to below the detection limit. This process seems to reconcile the theoretical prediction and the observational fact concerning the longest period of overstable modes.

In Chapter 7, we also briefly discuss the mechanism of 'mode selection'. We find that the most important nonlinear couplings for mode selection are parametric resonances in which one or two of the daughter modes are also overstable. These couplings can effectively suppress the amplitudes of low radial order modes. More theoretical efforts are obviously needed before we can understand the complete cause of the irregular energy distributions among overstable modes.

In Appendix H, we expand the concept of parametric instability to include 'coherent parametric instability'. We discover that when there are N_c pairs of daughter modes 'coherently' interacting with the parent mode, the latter transfers energy unstably to the daughters above a critical amplitude that is N_c times lower than it would be if there were only one pair. Coherent parametric instability occurs in white dwarfs when the daughter modes are so strongly damped that they are only running waves inside the star (§7.4).

We can also address the question of mode variability. The equilibrium state of a dynamical system with a large number of driven and damped modes is most likely a statistical one. On average, an overstable mode loses energy through mode couplings at the same rate as its linear growth. The former depends on the energy in this mode, while the latter does not. This determines the equilibrium energy in this mode. Fluctuations in its amplitude and phase are caused by the same nonlinear couplings that limit the linear growth. The time-scale of these fluctuations is necessarily the time-scale of the linear growth. According to results in Chapters 2 and 3, the growth time for a low-order g-mode ($\ell = 1, n = 1$) is of order 10^7 yrs; while it is of order a few days for a higher order mode ($\ell = 1, n = 20$). This is consistent with the shorter period modes having more stable amplitudes than the longer period ones.

In summary, we believe that we have obtained satisfactory answers to two basic questions posed by observations, viz., what determines the amplitudes of the modes, and what determines the time-scales of amplitude fluctuations in different modes. As Dziembowski stresses, nonlinear studies may not offer useful asteroseismological information at the present stage, but developing a theory which

appears capable of rationalizing the observed phenomena is an important step.

1.2.3 Combination Frequencies

This brings us to one practical application of our theory. Cool DAVs share a common characteristic besides long period pulsations, large amplitudes, and strong variability. This is that their power spectra all show prominent peaks at linear combinations of frequencies of the real modes. In fact, this is true not only for cool DAVs; every DA variable which has been observed with sufficiently high signal to noise ratios exhibits linear combination frequencies (Brassard et al. 1995).

Three distinct hypotheses exist for the origin of these combination frequencies. The first, resonant mode coupling, is generally dismissed because it is unable to account for the rich spectrum of the observed combinations. The second, due to Brassard et al. (1995), is that the photospheric temperature perturbation is harmonic and that combination frequencies result from the nonlinear relation between the emergent flux and the photospheric temperature. The third hypothesis is due to Brickhill (1992). He argues that the pressure and horizontal velocity vary harmonically in the radiative zone. In his scheme, the nonlinearity arises when the convection zone responds to variations in the flux entering it from below. Brickhill also provides a quantitative comparison between theory and observations.

We disagree with the basic assumption of Brassard et al. (1995), and favor Brickhill's hypothesis. The flux perturbation at the surface is related to that at the bottom of the convection zone by a complex visibility factor that involves both the mode frequency and the depth of the convection zone. The nonlinearity is due to the modulation of this visibility factor corresponding to the variations in the depth of the convection zone, the latter being affected by the rise and fall of the entropy level in the convection zone. This modulation is evaluated in Chapter 8. Simple analytical relations are derived for the amplitudes of the combination frequencies in terms of the amplitudes of the real modes. These relations account for limb-darkening and disc averaging but neglect the wavelength dependence of the opacity. Expressions for these ratios involve three physical parameters: the depth of the convection zone, the convection reaction time, and the inclination of the quantization axis to the line of sight. We either choose values for the above parameters and compare the predictions with observations, or deduce these parameters from the observed amplitudes of the combination frequency peaks. Results are presented for two large amplitude pulsators, GD358, a DBV, and ZZ Psc, a DAV, both mentioned above. Comparison with observations is satisfactory.

It is noteworthy that while combination frequencies are a prominent feature of DA and DB power spectra, they are absent in power spectra of PG1159 stars. Perhaps this is evidence that the presence of a convection zone is essential to the production of these nonlinear features.

It has been a pleasure working with the white dwarfs.

Bibliography

Bahcall, J. N., & Krastev, P. I. 1996, Phys. Rev. D., 53, 4211

Baker, N. 1965, in IAU Colloquium: The Position of Variable Stars in the Hertzsprung-Russell Diagram, Bamberg, 122

Baker, N., & Kippenhahn, R. 1965, ApJ, 142, 869

Balbus, S. A., & Hawley, J. F. 1994, MNRAS, 266, 769

Becker, S. A. 1987, in Stellar Pulsation, Lecture Notes in Physics, ed. Araki, H., Ehlers, J., Hepp, K., Kippenhahn, R., Weidenmuller, H. A., Wess, J. & Zittartz, J., (Springer-Verlag), 16

Bond, H. E., Kawaler, S. D., Ciardullo, R., Stover, R., Kuroda, T., et al. 1996, AJ, 112, 2699

Bono, G., Caputo, F., Castellani, V., Marconi, M., Staiano, L., & Stellingwerf, R. F. 1995, ApJ, 442, L59

Bono, G., & Stellingwerf, R. F. 1993, ApJS, 93, 233

Brassard, P., Fontaine, G., & Wesemael, F. 1995, ApJS, 96, 546

Brickhill, A. J. 1983, MNRAS, 204,537

Brickhill, A. J. 1990, MNRAS, 246, 510

Brickhill, A. J. 1991a, MNRAS, 251, 673

Brickhill, A. J. 1991b, MNRAS, 252, 334

Brickhill, A. J. 1992, MNRAS, 259, 519

Brown, T. M., & Gilliland, R. L. 1990, ApJ, 350, 839

Brown, T. M., Gilliland, R. L., Noyes, R. W., & Ramsey, L. W. 1991, ApJ, 368, 599

Brown, T. M., & Gilliland, R. L. 1994,ARA&A, 32, 37

Brown, T. M., Kennelly, E. J., Korzennik, S. G., Nisenson, P., Noyes, R. W., & Horner, S. D. 1997, ApJ, 475, 322

Christensen-Dalsgaard, J. 1996, Science, 272, 1286

Christensen-Dalsgaard, J., Monteiro, M. J. P. F. G., & Thompson, M. J. 1995, MNRAS, 276, 283

Clemens, J. C. 1993, Baltic Astronomy, 2, 407

Clemens, J. C. 1994, Ph.D. thesis, University of Texas at Austin

Cox, J. P., & Giuli, R. T. 1968, Principles of Stellar Structure, V. II, Application to Stars, (Gordon & Breach)

Dreizler, S. 1996, in White Dwarfs, ed. Isern, J., Hernanz, M., & Garcia-Berro, E., (Kluwer), 207

Dziembowski, W., & Krolikowska, M. 1990, Acta Astron. 40, 19

Dziembowski, W. 1993, in IAU Colloquium 137: Inside the Stars, ed. Weiss, W. W., & Baglin, A., ASP conference series, vol 40

Gautschy, A., Ludwig, H. G., & Freytag, B. 1996, A&A, 311, 493

Gautschy, A., & Saio, H. 1996, ARA&A34, 551

Gilliland, R. L., Brown, T. M., Kjeldsen, H., MaCarthy, J. K., & Peri, M. L. 1993, AJ, 106, 2441

Kawaler, S. D., O'Brian, M. S., Clemens, J. C., Nather, R. E., Winget, D. E., et al. 1995, ApJ, 450, 350

Kennelly, E. J., Walker, G. A. H., Yang, S., & Hubeny, I. 1991, PASP, 103, 1250

Kjeldsen, H., Bedding, T. R., Viskum, M., & Frandsen, S. 1995, AJ, 109, 1313

Kleinman, S. J., 1995, Ph.D. thesis, University of Texas at Austin

Kleinman, S. J., et al. 1994, ApJ, 436, 875

Korzennik, S. G., Noyes, R. W., Brown, T., Nisenson, P., & Horner, S. 1995, ApJ, 443, L25

Krisciunas, K., Griffin, R. F., Guinan, E. F., Luedeke, K. D., & McCook, G. P. 1995, MNRAS, 273, 662

Kumar, P., & Quataert, E. J. 1997, ApJ, 475, L143

Landau, L. D., & Lifshitz, E. M. 1976, Mechanics, Third Edition, (Pergamon Press), 80

Monteiro, M. J. P. F. G., Christensen-Dalsgaard, J., & Thompson, M. J. 1996, A&A, 307, 624

Pesnell, W. D. 1987, ApJ, 314, 598

Pijpers, F. P., & Harbing, H. J. 1989, A&A, 215, 334

Schwarzschild, M. 1958, Structure & Evolution of the Stars, (Princeton University Press)

Starrfield, S., Cox, A. N., Kidman, R. B., & Pesnell, W. D. 1984, ApJ, 281, 800

Thompson, M. J., Toomre, J., Anderson, E. R., Antia, H. M., Berthomieu, G., Burtonclay, D., Chitre, S. M., Christensen-Dalsgaard, J., Corbard, T. et al. 1996, Science, 272, 1300

Werner, K. 1993, in White Dwarfs: Advances in Observation & Theory, ed. Barstow, M. A., NATO ASI Ser. C, vol 403, (Dordrecht: Kluwer)

Winget, D. E., et al. 1990, ApJ, 357, 630

Winget, D. E., Nather, R. E., Clemens, J. C., et al. 1991, ApJ378, 326

Winget, D. E. 1991, in White Dwarfs, ed. Vauclair, G., & Sion, E., (Kluwer Academic Publishers)

Winget, D. E., Nather, R. E., Clemens, J. C., et al. 1994, ApJ, 430, 839

Chapter 2 Gravity Modes in White Dwarfs

2.1 Introduction

DAV (stands for DA variable) white dwarfs have shallow surface convection zones overlying stably stratified interiors. Different elements are well separated by gravity; with increasing depth the composition changes from hydrogen to helium, and then in most cases to a mixture of carbon and oxygen. From center to surface the luminosity is carried first by electron conduction, then by radiative diffusion, and finally by convection.

Photometric variations observed in these stars are associated with non-radial gravity-modes (g-modes); for the first conclusive proof, see Robinson et al. (1983). A g-mode is a standing gravity wave trapped within a cavity inside the star. The restoring force is gravity which opposes departures of surfaces of constant density from those of constant gravitational potential. The cavity is the region where the mode frequency, ω, is smaller than both the acoustic frequency (the Lamb frequency, L_ℓ), and the buoyancy frequency (the Brunt-Väisälä frequency, N). Every g-mode of a spherical star is characterized by a triplet of eigenvalues, (n, ℓ, m). Here n is the number of radial nodes in the radial component of the displacement vector, ℓ is the angular degree, and m the azimuthal separation parameter (as in $Y_{\ell m}$). Except for the case of fast rotators (stars that rotate close to break-up and are not spherical any more), m does not affect the radial structure of the mode, and introduces only a small additive term to the eigenfrequency. G-modes detected in DAV stars have modest radial orders, $1 \leq n \leq 25$, and low angular degrees, $1 \leq \ell \leq 2$.[1]. Their periods fall in the range from 100 s to 1200 s.[2]

For the convenience of exposition in subsequent chapters, we summarize here scaling relations appropriate to g-modes. These include the dispersion relation, the WKB eigenfunction, the amplitude normalization, and estimates for driving and damping rates.

Most of the modes we are interested in, i.e., those that are overstable, do not propagate right below the convection zone. The top of their propagating cavity lies well below the bottom of the convection zone. We first look at these modes. However, the amplitudes of overstable modes saturate due to their nonlinear couplings to damped modes. Many of these damped modes propagate right below the convection zone. So we derive scaling relations for them as well. The velocity shear in the convection zone is estimated in §2.10.

[1] The latter is an observational selection effect.

[2] Mode periods increase with n and decrease with ℓ.

2.2 White Dwarf Interiors

Electron degeneracy causes the Brunt-Väisälä frequency to be very small in the interior of a white dwarf. As a consequence, g-modes are confined to the outer few percent of the stellar radius. This makes it convenient to apply a plane-parallel approximation in which the coordinate z measures depth below the layer of zero pressure, and the gravitational acceleration, g, is considered constant.

We adopt standard notation for the pressure, p, density, ρ, temperature, T, and specific entropy, s. Our s is dimensionless; we measure it in units of k_B/m_p, where k_B is the Boltzmann constant and m_p the proton mass. The equation of hydrostatic equilibrium reads

$$\frac{dp}{dz} = g\rho, \tag{2.1}$$

from which we define the pressure scale-height,

$$H_p \equiv \frac{p}{g\rho}. \tag{2.2}$$

We also define the adiabatic sound speed, c_s, by

$$c_s^2 \equiv \left.\frac{\partial p}{\partial \rho}\right|_s, \tag{2.3}$$

the radian acoustic (Lamb) frequency, L_ℓ, by

$$L_\ell^2 = \ell(\ell+1)\left(\frac{c_s}{r}\right)^2, \tag{2.4}$$

and the radian buoyancy frequency, N, by

$$N^2 \equiv g\left.\frac{\partial \ln \rho}{\partial s}\right|_p \frac{ds}{dz}. \tag{2.5}$$

As discussed above, N^2 is negative in the unstably stratified, convective envelope, positive in the stably stratified, radiative interior, and approaches zero in the degenerate core. This is shown in Figure 2.1.

A few order of magnitude relations to keep in mind are: $p \sim g\rho z$, $c_s^2 \sim gz$, $d\ln p/dz = 1/H_p \sim 1/z$, $d\ln\rho/dz \sim 1/z$. In the upper radiative interior, $N^2 \sim g/z \sim (c_s/z)^2$. Figure 2.1 shows the deviation from this scaling due to degeneracy in the deep interior. In the convection zone, $N^2 \sim -(v_{\rm cv}/c_s)^2 g/z \sim -(v_{\rm cv}/z)^2$, where $v_{\rm cv}$ is the convective velocity. We will make repeated use of these in what follows.

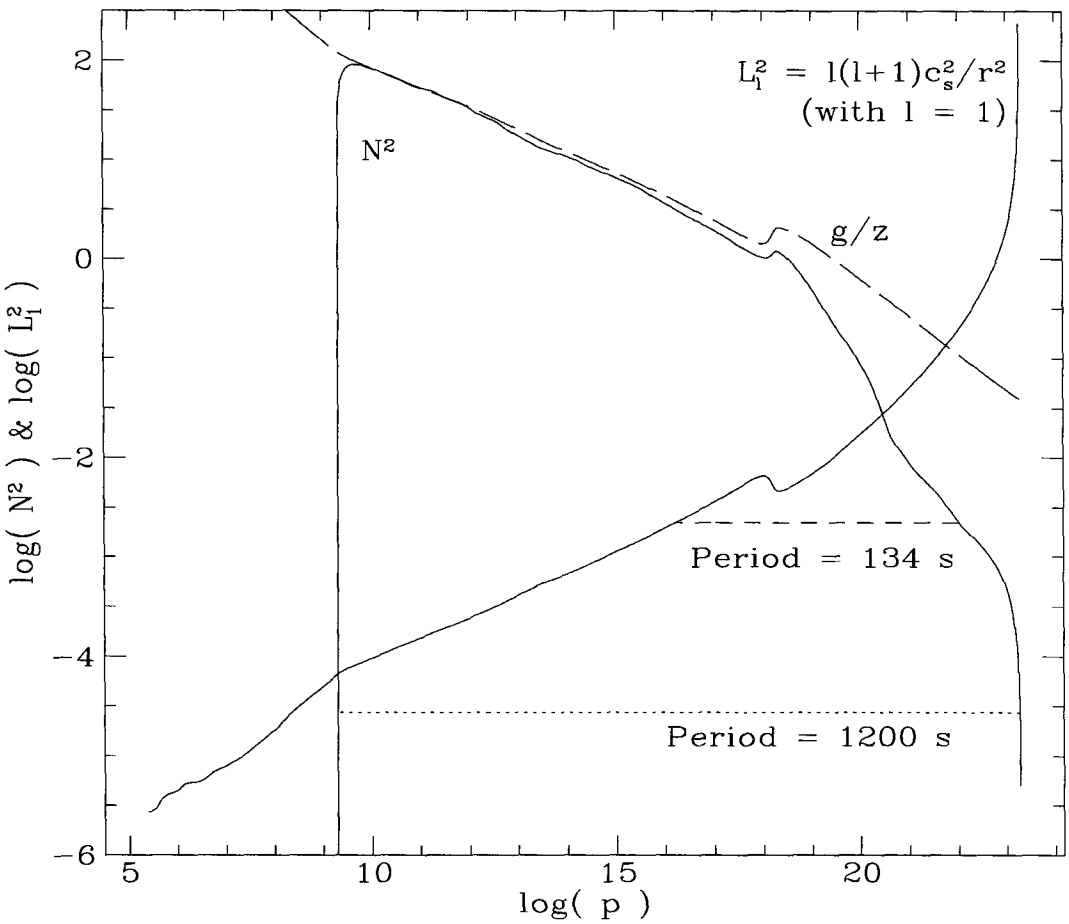

Figure 2.1: The squares of the Brunt-Väisälä frequency, N^2, and the Lamb frequency, L_ℓ^2, as functions of pressure inside a white dwarf. We use the DA models provided to us by P. Bradley; this particular one has an effective temperature of 12,000 K ($\tau_b = 300$ s). N^2 is negative in the surface convection zone ($\log p \leq 9.3$), and approaches zero in the degenerate interior ($\log p \geq 24.0$). Here, we show only positive N^2. The little bump in N^2 occurring around $\log(p) \sim 19$ is due to the thin transition layer where the composition changes from hydrogen to helium. The long dashed line is our analytical approximation, $N^2 \sim (g/z)$. Notice the deviation as degeneracy becomes important. G-modes with frequency ω can only propagate in regions where both $\omega < N$ and $\omega < L_\ell$ are satisfied, they are depicted by horizontal dashed lines for both the 134 s mode and the 1200 s mode (both have $\ell = 1$). The latter propagates immediately below the convection zone.

The horizontal component of the propagation vector, k_h, is related to the angular degree ℓ by

$$k_h^2 = \frac{\ell(\ell+1)}{R^2}, \tag{2.6}$$

where R is the stellar radius. Degeneracy implies that $N^2 \ll g/R$ in the deep interior. This ensures that for each angular degree the frequency of the lowest order g-mode satisfies

$$\frac{\omega^2}{gk_h} \ll 1. \tag{2.7}$$

2.3 Deriving the Wave Equations

We begin with the linearized equations of mass and momentum conservation augmented by the linearized, adiabatic equation of state. Readers are referred to Unno et al. (1989) for detailed derivations of these equations. Adopting the Cowling approximation, i.e., ignoring perturbation to the gravitational potential, these equations read:

$$\frac{\delta\rho}{\rho} = -ik_h\xi_h - \frac{d\xi_z}{dz}, \tag{2.8}$$

$$\omega^2\xi_h = ik_h\left[\frac{p}{\rho}\left(\frac{\delta p}{p}\right) - g\xi_z\right], \tag{2.9}$$

$$\omega^2\xi_z = \frac{p}{\rho}\frac{d}{dz}\left(\frac{\delta p}{p}\right) + g\left(\frac{\delta p}{p} - \frac{\delta\rho}{\rho} - \frac{d\xi_z}{dz}\right), \tag{2.10}$$

$$\delta p = c_s^2\delta\rho, \tag{2.11}$$

where we have assumed a time and horizontal space dependence of the form $\exp i(k_h x - \omega t)$. Lagrangian perturbations are denoted by δ. The symbols ξ_h and ξ_z represent the horizontal and vertical components of the displacement vector. The Eulerian pressure perturbation $p' = \delta p - \xi_z dp/dz = \delta p - g\rho\xi_z$.

After some manipulation, equations (2.9) and (2.10) yield

$$\xi_h = \frac{ig^2k_h}{(gk_h)^2 - \omega^4}\left[\frac{p}{g\rho}\frac{d}{dz}\left(\frac{\delta p}{p}\right) + \left(1 - \frac{\omega^2 p}{g^2\rho}\right)\left(\frac{\delta p}{p}\right)\right], \tag{2.12}$$

and

$$\xi_z = \frac{-g\omega^2}{(gk_h)^2 - \omega^4}\left[\frac{p}{g\rho}\frac{d}{dz}\left(\frac{\delta p}{p}\right) + \left(1 - \frac{k_h^2 p}{\omega^2\rho}\right)\left(\frac{\delta p}{p}\right)\right]. \tag{2.13}$$

Notice that these two equations are independent of the assumption of adiabaticity (see eq. [2.11]). As mentioned previously, $gk_h \gg \omega^2$ for g-modes.

The linear, adiabatic wave equation for the fractional, Lagrangian pressure perturbation, $\delta p/p$,

follows from combining equations (2.8), (2.12), and (2.13),

$$\frac{d^2}{dz^2}\left(\frac{\delta p}{p}\right) + \frac{d}{dz}\left(\ln\frac{p^2}{\rho}\right)\frac{d}{dz}\left(\frac{\delta p}{p}\right) + \left[k_h^2\left(\frac{N^2}{\omega^2}-1\right) + \left(\frac{\omega}{c_s}\right)^2\right]\left(\frac{\delta p}{p}\right) = 0. \tag{2.14}$$

The advantages of choosing $\delta p/p$ as the dependent variable will become apparent as we proceed. An equivalent, Eulerian form of the wave equation is

$$\begin{aligned} \frac{d\xi_z}{dz} + \frac{g}{c_s^2}\xi_z + \left(1 - \frac{L_\ell^2}{\omega^2}\right)\frac{p'}{\rho c_s^2} &= 0, \\ \frac{1}{\rho}\frac{dp'}{dz} - \frac{g}{\rho c_s^2}p' + (N^2-\omega^2)\xi_z &= 0, \end{aligned} \tag{2.15}$$

where $ik_h p' = \omega^2\rho\xi_h$. These equations are used in actual numerical integrations.

2.4 Gravity Wave Cavity

A g-mode is a gravity wave trapped inside a resonant cavity. The wave propagates within the cavity and is evanescent both above and below. Inside the cavity, $k_z H_p > 1$, viz., the environment changes gradually on the scale of the wavelength of the mode.[3] When $k_z H_p \gg 1$, we can substitute the WKB ansatz

$$\frac{\delta p}{p} = \mathcal{A}\exp\left(i\int^z dz\, k_z\right), \tag{2.16}$$

into equation (2.14), and obtain the local dispersion relation[4]

$$k_z^2 \approx \left(\frac{N^2}{\omega^2} - 1\right)k_h^2, \tag{2.17}$$

and amplitude relation inside the propagating cavity ($\omega \ll N$),

$$\mathcal{A}^2 \propto \frac{\rho}{k_z p^2} \propto \frac{\rho}{Np^2}. \tag{2.18}$$

Note that both k_z and $\mathcal{A}$ vary on scale H_p.

The cavity is bounded from below at $z = z_l$ where $N = \omega$.

At the top of the cavity ($z = z_1$), either $\omega \approx N$ or $\omega \approx L_\ell$. The former pertains if the mode propagates up to the bottom of the convection zone, where the gravity-waves become evanescent; otherwise the latter applies. In this case, taking $c_s \sim (gz)^{1/2}$ and $r \approx R$, we arrive at

$$z_1 \sim z_\omega \equiv \frac{\omega^2}{gk_h^2}. \tag{2.19}$$

[3]This condition is violated at compositional discontinuities which are better viewed as separating linked cavities.

[4]In g-mode's propagating cavity, $\omega \leq L_l$. The $(\omega/c_s)^2$ term is negligible for g-modes, although dominant for p-modes.

In subsequent calculations we often set $z_1 \approx z_\omega$. Substituting $N^2 \sim g/z$ into the dispersion relation (2.17) then yields $k_z z_1 \sim 1$; z_1 is identified with the first radial node point of $\delta p/p$. Unless stated otherwise, we assume $z_1 \geq z_b$ in what follows.

2.4.1 Dispersion Relations

The global dispersion relation is obtained from

$$n\pi \approx \int_{z_1}^{z_l} dz\, k_z. \tag{2.20}$$

Carrying out the integration using $N^2 \sim g/z$, $z_1 \sim z_\omega$, and equation (2.17), we obtain $\omega^2 \approx g k_h/n$. This relation is a good approximation to the g-mode dispersion relation for a polytropic atmosphere. The proportionality

$$\omega^2 \propto \frac{k_h}{n} \tag{2.21}$$

provides a satisfactory fit to the high frequency modes in DAV white dwarfs. However, low frequency modes penetrate deeply into the interior where the approximation $N \sim (g/z)^{1/2}$ fails because of electron degeneracy (cf. Fig. 2.1). As a result of the steep drop in N, z_l is nearly independent of ω for $\omega \leq \Omega \approx 10^{-2}\,\mathrm{s}^{-1}$. This flattens the dependence of ω on n such that

$$\omega \propto \frac{k_h}{n}. \tag{2.22}$$

Numerical results for the dispersion relations are shown in Figure 2.2.

2.4.2 WKB Envelope

Equation (2.18) describes the z-dependence of the WKB amplitude for $\delta p/p$ within the g-mode cavity. It has a simple, physical interpretation in terms of the conservation of the vertical energy flux carried by gravity waves. This flux may be written as[5]

$$\mathcal{F} \approx \rho v_{gz} \omega^2 \left(\xi_h^2 + \xi_z^2\right), \tag{2.23}$$

where the vertical group velocity

$$v_{gz} \equiv \frac{\partial \omega}{\partial k_z} \approx \frac{\omega}{k_z} \approx \frac{\omega^2}{N k_h}. \tag{2.24}$$

Expressions for ξ_h and ξ_z in terms of $\delta p/p$ and $d/dz(\delta p/p)$ are given by equations (2.12) and

[5]Here ξ_h and ξ_z are to be interpreted as envelope amplitudes.

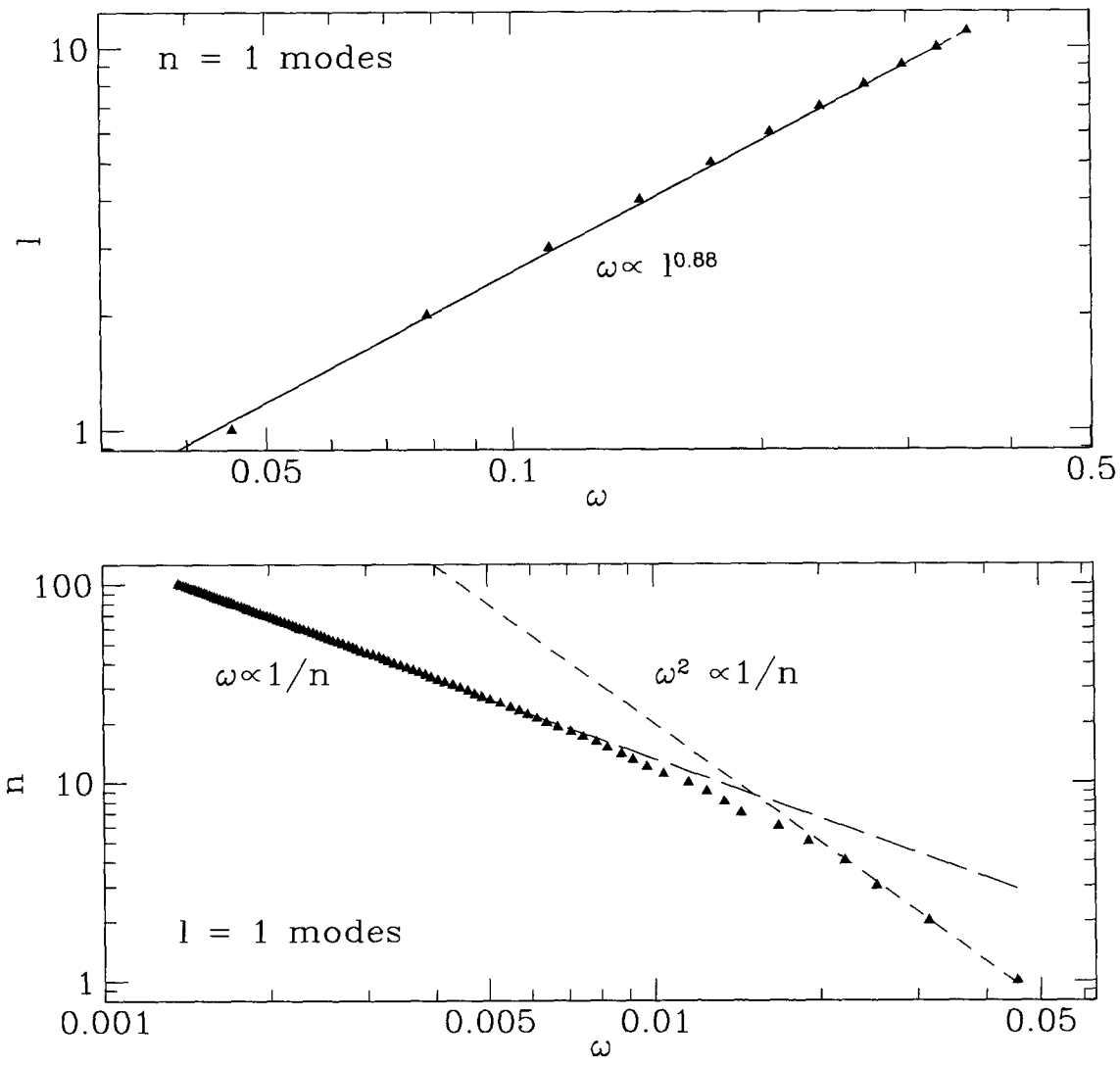

Figure 2.2: Frequencies of gravity-modes as functions of radial order n and spherical degree ℓ. The eigenvalues are from Bradley's white dwarf model ($T_{\rm eff} = 12,000\,{\rm K}$, $\tau_b = 300\,{\rm s}$). The upper panel is for $n = 1$ modes with various ℓ values, while the lower panel is for $\ell = 1$ and different n numbers. The dispersion relation (eq. [2.21]) fits well for low-order (small n) modes; at larger n, a different scaling applies (eq. [2.22]). We adopt these empirical laws in our analytical studies.

(2.13). To leading order in $(k_z z)$ these read

$$\xi_h \approx \frac{k_z}{k_h}\frac{p}{g\rho}\left(\frac{\delta p}{p}\right), \tag{2.25}$$

and

$$\xi_z \approx -\frac{p}{g\rho}\left(\frac{\delta p}{p}\right). \tag{2.26}$$

Combining the above relations yields

$$\mathcal{F} \approx \frac{\omega^2}{g^2 k_h}\frac{Np^2}{\rho}\left(\frac{\delta p}{p}\right)^2. \tag{2.27}$$

Substitution of $\mathcal{A}^2$ for $(\delta p/p)^2$ confirms the constancy of $\mathcal{F}$. We note that $\mathcal{F}$ decreases with distance below z_l and above z_1.

G-modes are relatively incompressible; equations (2.25) and (2.26) imply that $ik_h\xi_h + d\xi_z/dz = 0$ to lowest order in z_1/z. Expressed more precisely, we find

$$\frac{\delta\rho}{\rho} = \frac{p}{c_s^2\rho}\frac{\delta p}{p} \sim \frac{g}{c_s^2}\frac{\omega}{N}\xi_h \sim \left(\frac{z_\omega}{z}\right)^{1/2} k_h\xi_h. \tag{2.28}$$

The amplitude of $\delta\rho/\rho$, which is of order ξ_z or $k_h\xi_h$ at z_1 drops much faster with depth than that of either ξ_z or ξ_h; the incompressible approximation works well in the WKB region.

2.5 Upper Evanescent Layer

For the purpose of this discussion, we pretend that both $\rho \to 0$ and $p \to 0$ as $z \to 0$. Then $z = 0$ is a singular point of the wave equation (2.14). Since the physical solution is regular at $z = 0$,

$$\frac{d}{dz}\left[\ln\left(\frac{\delta p}{p}\right)\right] \sim -\left(\frac{N}{\omega}\right)^2 k_h^2 z. \tag{2.29}$$

This reduces to

$$\frac{d}{dz}\left[\ln\left(\frac{\delta p}{p}\right)\right] \sim \left(\frac{v_{\rm cv}}{c_s}\right)^2 \frac{1}{z_\omega}, \tag{2.30}$$

in the convection zone where $N^2 \approx -(v_{\rm cv}/z)^2$, and

$$\frac{d}{dz}\left[\ln\left(\frac{\delta p}{p}\right)\right] \sim -\frac{1}{z_\omega}, \tag{2.31}$$

in the top of the radiative interior where $N^2 \sim (c_s/z)^2$.

We see that $\delta p/p$ is nearly constant for $z \ll z_\omega$ in the upper evanescent layer.[6] It then follows

[6]That is why we chose to use it as the dependent variable in the wave equation.

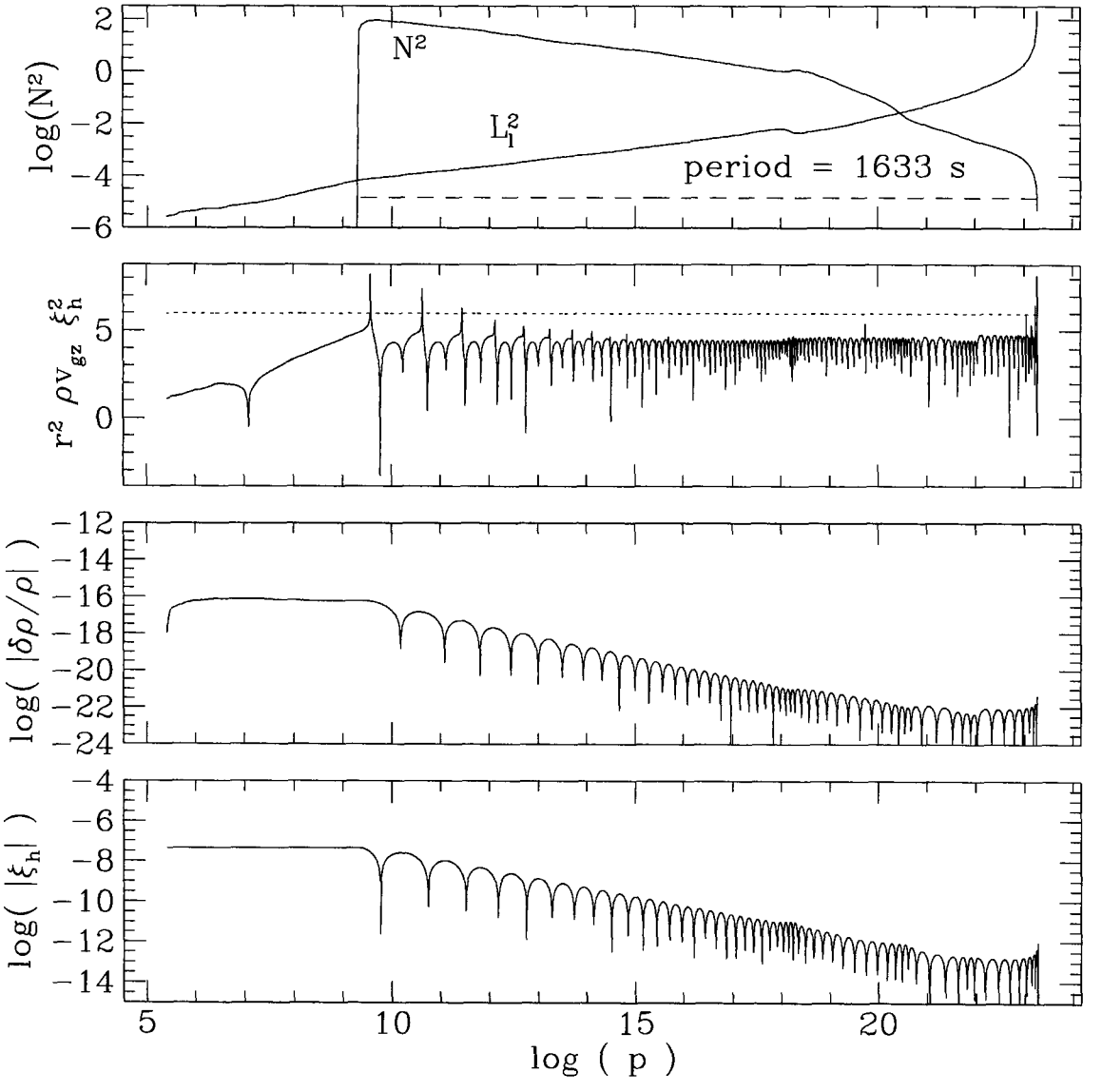

Figure 2.3: Radial eigenstructure of a mode with $n = 54, \ell = 1$, and a period of 1633 s. The top panel, which is similar to Figure 2.1, illustrates how the mode cavity (depicted by the dashed line) is formed. Note that for this mode $z_1 \sim z_b$. The WKB energy flux is plotted in the second panel. The energy flux is constant inside the cavity and decays outside it; this flux can be higher in part of the propagating cavity if the mode is trapped inside it. The lower two panels display the depth dependences of ξ_h and $\delta\rho/\rho$.

from equations (2.12) and (2.13) that, to leading order in z/z_ω,

$$\xi_h \approx \frac{i}{k_h}\left(\frac{\delta p}{p}\right), \tag{2.32}$$

and

$$\xi_z \approx \frac{-\omega^2}{g k_h^2}\left(\frac{\delta p}{p}\right). \tag{2.33}$$

Thus the displacement vector is also nearly constant for $z \ll z_\omega$. The situation for $\delta\rho/\rho$ is more subtle since it could vary on scale z should $p/(c_s^2\rho)$ do so. However, in practice, this quantity is not only of order unity but also exhibits only mild depth variations. Thus, equation (2.32) implies that

$$\frac{\delta\rho}{\rho} \sim -ik_h\xi_h, \tag{2.34}$$

in the upper evanescent layer. Equation (2.34) should be compared to equation (2.28). It shows that the relative incompressibility that characterizes propagating g-modes does not extend to their evanescent tails.

2.6 Combined Expressions for Depth Dependences

Here we combine the depth dependences into unified expressions for eigenfunctions in the the stably stratified portion of the upper evanescent region and in the cavity. For convenience, let $\hat{z} = \mathrm{Max}(z, z_\omega)$, $\hat{\rho} = \mathrm{Max}(\rho, \rho_\omega)$, where ρ_ω is the density of the star at z_ω. Following equation (2.31), when $z_b \leq z < z_\omega$, , the vertical gradient of the eigenfunctions, $d/dz \sim 1/z_\omega$. In the cavity, $d/dz \sim k_z \sim 1/(zz_\omega)^{1/2}$, as a result of the local dispersion relation, equation (2.17). We combine the two as $d/dz = 1/(\hat{z}z_\omega)^{1/2}$.

The near incompressibility of g-modes relates ξ_z to ξ_h as

$$\frac{\partial\xi_z}{\partial z} \sim \frac{\xi_z}{(\hat{z}z_\omega)^{1/2}} \sim k_h\xi_h. \tag{2.35}$$

G-modes are characterized by nearly horizontal, sloshing motions.

The dominance of ξ_h over ξ_z, together with the constancy of the WKB energy flux, lead to the following scaling for ξ_h within the cavity:

$$\xi_h \sim \left(\frac{z_\omega}{\hat{z}}\right)^{\frac{1}{4}}\left(\frac{\rho_\omega}{\hat{\rho}}\right)^{\frac{1}{2}}\xi_h(0), \tag{2.36}$$

where $\xi_h(0)$ is the value of ξ_h at $z = 0$. This expression applies to the region $0 < z < z_l$, where z_l is the lower boundary of g-mode's cavity; for $0 < z < z_\omega$, $\xi_h \approx \xi_h(0)$.

Equation (2.35) which relates ξ_z to ξ_h then implies

$$\xi_z \sim \left(\frac{\hat{z}}{z_\omega}\right)^{\frac{1}{4}} \left(\frac{\rho_\omega}{\hat{\rho}}\right)^{\frac{1}{2}} \xi_z(0), \tag{2.37}$$

for $0 < z < z_l$. The meaning of $\xi_z(0)$ is similar to that of $\xi_h(0)$.

Approximating equation (2.12) as

$$ik_h\xi_h \sim \frac{1}{g\rho}\frac{d\delta p}{dz} \sim \left(\frac{\hat{z}}{z_\omega}\right)^{\frac{1}{2}} \frac{\delta\rho}{\rho}, \tag{2.38}$$

gives

$$\frac{\delta\rho}{\rho} \sim \left(\frac{z_\omega}{\hat{z}}\right)^{\frac{1}{2}} k_h\xi_h \sim \left(\frac{z_\omega}{\hat{z}}\right)^{\frac{3}{4}} \left(\frac{\rho_\omega}{\hat{\rho}}\right)^{\frac{1}{2}} \frac{\delta\rho}{\rho}(0), \tag{2.39}$$

$\delta\rho/\rho$ is approximately constant for $0 < z < z_\omega$.

2.7 Normalization of Eigenfunctions

We conform to standard practice and set

$$\frac{\omega^2}{2}\int_0^R r^2 dr\rho\left(\xi_h^2 + \xi_z^2\right) = 1. \tag{2.40}$$

To achieve a simple analytic result, we take advantage of the following: $|\xi_h| \gg |\xi_z|$, ξ_h nearly constant for $z \ll z_\omega$, and the envelope of $\rho v_{gz}\xi_h^2$ nearly constant for $z \gg z_\omega$ (cf. §2.4.2). This enables us to write

$$\frac{\omega^2}{2}R^2\xi_h^2(0)\left(\rho v_{gz}\right)_{z_\omega}\int\frac{dz}{v_{gz}} \approx 1. \tag{2.41}$$

Using

$$\int_0^R \frac{dz}{v_{gz}} \approx \frac{\pi n}{\omega}, \tag{2.42}$$

we arrive at

$$\left(\rho v_{gz}\right)_{z_\omega} = \left(\frac{\omega^2\rho}{k_h N}\right)\Bigg|_{z_\omega} \sim \left(\frac{\omega^2 pz}{k_h c_s^3}\right)\Bigg|_{z_\omega} \sim \frac{k_h^2 F\tau_\omega}{\omega}, \tag{2.43}$$

where F is the radiative flux, and

$$\tau_\omega \approx \frac{pz}{F}\Bigg|_{z_\omega} \tag{2.44}$$

is the thermal time scale at z_ω. Putting these relations together, we obtain

$$k_h^2\xi_h^2(0) \sim \frac{1}{n\tau_\omega L}, \tag{2.45}$$

where $L = 4\pi R^2$ is the stellar luminosity. Moreover, equation (2.32) then implies

$$\left(\frac{\delta\rho}{\rho}\right)^2\Bigg|_{z_\omega} \sim \frac{1}{n\tau_\omega L}. \tag{2.46}$$

This is the normalization formula we are after. In §2.9, we derive similar estimates for modes which propagate immediately below the convection zone. This scaling for the normalization is compared with numerically calculated values in Figure 2.4.

2.8 Quasiadiabatic Driving/Damping Rates

We can estimate order of magnitude driving and damping rates without detailed knowledge of what causes the driving and damping. When the perturbed quantities are normalized according to equation (2.40), the exponential growth or damping rate of the mode energy is given by the work integral:

$$\gamma = \frac{\omega}{2\pi}R^2 \oint dt \int_0^R dz\, \rho \frac{k_B}{m_p}\delta T \frac{d\delta s}{dt} = \frac{\omega}{8\pi^2}L \oint dt \int_0^R dz \frac{\delta T}{T}\frac{d}{dz}\left(\frac{\delta F}{F}\right). \tag{2.47}$$

If we can also calculate the imaginary part of the eigenfrequency, ω_i, we will find that $\omega_i = \gamma/2$.

We assume that the quasiadiabatic approximation holds in the radiative interior. Perturbing the equation of radiative diffusion, we obtain the following expression for the perturbed radiative flux:

$$\frac{\delta F}{F} = -(1+\kappa_\rho)\frac{\delta\rho}{\rho} + (4-\kappa_T)\frac{\delta T}{T} - \frac{d\xi_z}{dz} + \left(\frac{d\ln T}{dz}\right)^{-1}\frac{d}{dz}\left(\frac{\delta T}{T}\right). \tag{2.48}$$

Here $\kappa_\rho \equiv \partial \ln\kappa/\partial\ln\rho|_T$ with κ being the radiative opacity; similarly, $\kappa_T \equiv \partial\ln\kappa/\partial\ln T|_\rho$. Moreover, for adiabatic perturbations,

$$\frac{\delta T}{T} = \frac{\partial \ln T}{\partial \ln \rho}\Bigg|_s \frac{\delta\rho}{\rho}. \tag{2.49}$$

According to §2.6, the terms on the right-hand side of equation (2.48) are of order

$$\begin{aligned} \frac{d\xi_z}{dz} &\sim \left(\frac{\hat{z}}{z_\omega}\right)^{\frac{1}{2}}\frac{\delta\rho}{\rho}, \\ \left(\frac{d\ln T}{dz}\right)^{-1}\frac{d}{dz}\left(\frac{\delta T}{T}\right) &\sim k_z H_p \frac{\delta\rho}{\rho} \sim \frac{z}{(\hat{z}z_\omega)^{1/2}}\frac{\delta\rho}{\rho}. \end{aligned} \tag{2.50}$$

Retaining the largest terms in each of the evanescent and the propagating regions, and setting all logarithmic derivatives to unity, we find

$$\frac{\delta F}{F} \sim \left(\frac{\hat{z}}{z_\omega}\right)^{\frac{1}{2}}\frac{\delta\rho}{\rho}. \tag{2.51}$$

To evaluate the work integral, we substitute equations (2.49) and (2.51) into equation (2.47),

and adopt the depth dependence and normalization for $\delta\rho/\rho$ given by equations (2.39) and (2.46). These steps yield[7]

$$\gamma \sim L \int \frac{dz}{z_\omega} \left(\frac{\delta T}{T}\right)^2 \sim L \left(\frac{\delta\rho}{\rho}\right)^2 (0) \sim \frac{1}{n\tau_\omega}. \tag{2.52}$$

This estimate formally applies to the radiative region (eq. [2.48]), and is the rate of radiative damping. But the magnitude of γ applies more generally. This scaling relation is compared with numerically calculated values of γ in Figure 2.4.

2.9 Modes Propagating Immediately Below the Convection Zone

Modes with $z_\omega < z_b$ have cavities that are bounded above by z_b ($z_1 \sim z_b$). Previously derived scaling laws must be modified for these modes. Throughout the radiative region, $\hat{z}$ in §2.4.2 takes the value of z and $d/dz \sim k_z \sim 1/(zz_\omega)^{1/2}$. Within a scale-height below the convection zone, $H_p k_z \sim (z_b/z_\omega)^{1/2} \geq 1$.

The constancy of the WKB energy flux below the convection zone leads to the scaling

$$\xi_h \sim \left(\frac{z_b}{z}\right)^{\frac{1}{4}} \left(\frac{\rho_b}{\rho}\right)^{\frac{1}{2}} \xi_h(0), \tag{2.53}$$

for $z \geq z_b$. The normalization equation (2.40) now yields

$$(k_h \xi_h(0))^2 \sim \left(\frac{z_b}{z_\omega}\right)^{3/2} \frac{1}{nL\tau_b}. \tag{2.54}$$

As usual, ξ_h is approximately independent of z for $z \leq z_b$. Equation (2.38) remains valid so

$$\frac{\delta\rho}{\rho} \sim i \left(\frac{z_\omega}{z}\right)^{1/2} k_h \xi_h \sim i \frac{z_\omega^{1/2} z_b^{1/4}}{z^{3/4}} \left(\frac{\rho_b}{\rho}\right)^{1/2} k_h \xi_h(0). \tag{2.55}$$

Using equation (2.40), the normalized value for $\delta\rho/\rho$ at the surface is

$$\left(\frac{\delta\rho}{\rho}\right)^2 (0) \sim \frac{1}{n\tau_b L} \left(\frac{z_b}{z_\omega}\right)^{\frac{1}{2}}. \tag{2.56}$$

For $z_\omega < z_b$, this estimate is smaller than that given by equation (2.46). For fixed ω, the mode mass increases when the convection zone deepens past z_ω.

From equation (2.50), the dominant terms in $\delta F/F$ are of order $(z/z_\omega)^{1/2}\delta\rho/\rho$. This, combined

[7]The contribution to the work integral drops off sharply below $z \sim z_\omega$.

with equation (2.55), yields a radiative damping rate

$$\gamma \sim \frac{1}{n\tau_b}\left(\frac{z_b}{z_\omega}\right)^{\frac{3n}{2}}, \tag{2.57}$$

with most of the contribution coming from the scale-height below z_b. This equation predicts that γ decreases sharply in magnitude when cooling causes z_b to increase beyond z_ω.

Scaling relations from equations (2.56) and (2.57) are compared with numerical results in Figure 2.4.

The estimates given by equations (2.52) and (2.57) require severe modification for modes that are strongly nonadiabatic in the main driving/damping region. The condition for strong nonadiabaticity is discussed in §5.3. Nonadiabatic driving and damping rates are also calculated in Chapter 5.

2.10 Velocity Shear in the Convection Zone

Brickhill (1990) argues that turbulent viscosity should enforce a depth independent horizontal velocity in DAV convection zones. Simulations by Gautschy et al. (1996) show that unless ξ_h is nearly constant, $\gamma < 0$ for all g-modes.

Efficient convection zones are only slightly superadiabatic. Here we show that the shear associated with g-modes is extremely small provided that a layer is isentropic in both its undisturbed state and in perturbation. We proceed by writing the curl of the linearized equation of motion in the form

$$\omega^2 \nabla \times \vec{\xi} = -\nabla \times \left[\frac{1}{\rho}\nabla p'\right] + \nabla \times \left[\frac{\rho'}{\rho}\nabla\Phi\right]. \tag{2.58}$$

For an isentropic configuration $\nabla p/p = \Gamma_1 \nabla\rho/\rho$, and for an adiabatic perturbation $\delta p/p = \Gamma_1 \delta\rho/\rho$. Thus

$$\nabla \times \vec{\xi} = 0. \tag{2.59}$$

Written in terms of components, this yields

$$\frac{d\xi_h}{dz} = ik_h\xi_z \sim \left(\frac{z_\omega}{R}\right)\frac{\ell\xi_h}{R}. \tag{2.60}$$

We consider effects of the mean entropy gradient and nonadiabatic perturbations in §4.2. Both of these increase the velocity shear in the convection zone. However, even with this enhanced shear, viscous damping in the convection zone is unimportant (see Chap. 4).

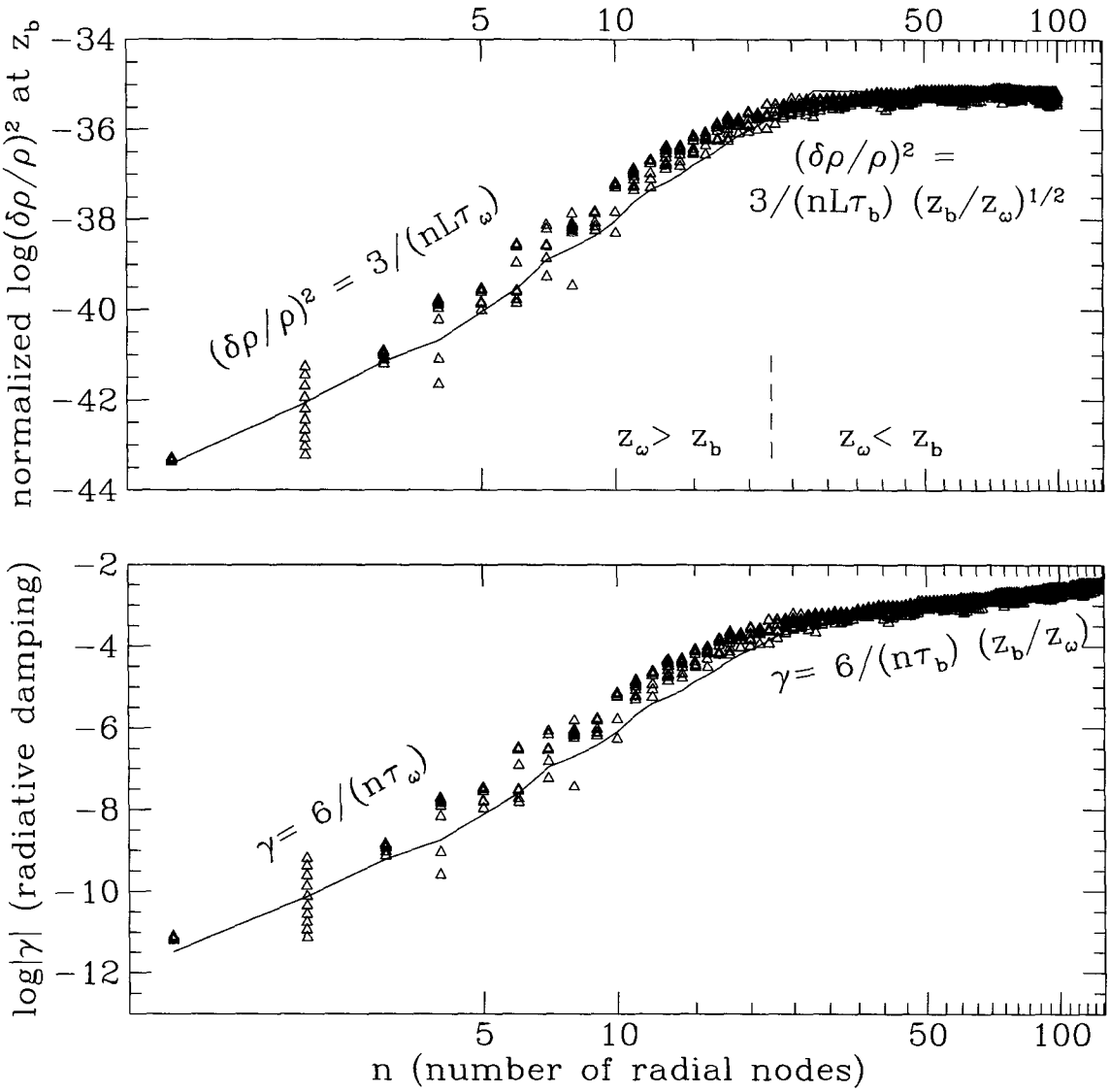

Figure 2.4: Mode normalization and driving/damping rates. We compare numerical values obtained from Bradley's model of $T_{\rm eff} = 12,000\,{\rm K}$ ($\tau_b = 300\,{\rm s}$) with estimates derived in §2.7-§2.9. The eigenfunctions are normalized according to equation (2.40). The upper panel shows the normalized values of $(\delta\rho/\rho)^2$ at $z = z_b$ for modes with $n = 1 - 100$, $\ell = 1 - 10$. We choose the horizontal axis to be n, since these properties depend on n much more strongly than on ℓ. The solid line represents the analytical estimates, using equation (2.46) for $z_\omega > z_b$ and equation (2.56) for $z_\omega \leq z_b$. Here, z_ω is chosen to be $(3\pi\omega^2)/(2gk_h^2)$. In the upper panel, numerical radiative damping rates are shown in triangles, with the analytical estimates in solid lines. For $z_\omega < z_b$ cases, we choose a slightly flatter dependence than that in equation (2.57). The assumption about the dominant term in equation (2.48) is valid only for even higher order modes.

2.11 Summary

We derive a number of scaling relations for g-modes in DAV white dwarfs. There are heavily relied upon in subsequent studies in this thesis.

A g-mode's cavity coincides with the radial interval within which ω is smaller than both N and L_ℓ. Inside this cavity the mode's velocity field is relatively incompressible. The modal period is equal to twice the time it takes for a gravity wave to travel the distance between consecutive radial nodes. The precipitous decline of N in the stellar core caused by electron degeneracy affects global dispersion relation which relates ω to n and ℓ.

The Lagrangian pressure perturbation is an appropriate dependent variable. It is almost constant in the convection zone and varies slowly in the rest of the upper evanescent region. Its envelope scales with depth in the cavity so as to maintain a constant vertical energy flux. An equal amount of energy is stored between every consecutive pair of radial nodes. For modes having $z_\omega > z_b$, the value of the normalized eigenfunction at the top of the cavity is approximately given by $1/(n\tau_\omega L)^{1/2}$, and driving and decay rates are of order $1/(n\tau_\omega)$. Modes of sufficiently low frequency have cavities which are truncated from above by the bottom of the convection zone. As a white dwarf cools, more modes enter this category. Their normalized surface amplitude and driving/damping rates decrease as the convection zone deepens. Numerical quasiadiabatic results are compared with the analytical estimates in Figure 2.4. These estimates are inadequate for modes that are nonadiabatic in the driving/damping region, as is shown in Chapter 5.

Adiabatic perturbations in an isentropic region are irrotational. This implies a very small velocity shear which is an important factor in limiting damping due to turbulent viscosity in the convection zone. However, a more complete analysis is needed to assess the effects on the velocity shear of both the nonadiabatic perturbations and the superadiabaticity of the mean entropy profile in the convection zone.

Bibliography

Brickhill, A. J. 1990, MNRAS, 246, 510

Gautschy, A., Ludwig, H. G., & Freytag, B. 1996, A&A, 311,493

Robinson, E. L., Kepler, S. O., Nather, R. E. 1982, ApJ,259, 319

Unno, W., Osaki, Y., & Ando, H. 1989, Nonradial Oscillations of Stars, (University of Tokyo Press), 241

Chapter 3 G-Mode Stability: Quasiadiabatic Approximation

3.1 Introduction

Our aim is to describe the mechanism responsible for the overstability of g-modes in ZZ-Ceti stars. The basic properties of g-modes are outlined in Chapter 2. We calculate the perturbations associated with these modes in §3.2. Then in §3.3, we apply these perturbations to evaluate work integrals and thereby estimate rates of driving and damping.

Our presentation is largely analytical, although we appeal to numerical stellar models and numerically computed eigenfunctions for guidance. Since theoretical details are of limited interest, we summarize selected results at the end of each section. As an aid to the readers, symbols used in the paper are defined in Appendix A.

This topic has received attention in the past. Initial calculations of overstable modes are published in (Dziembowski & Koester 1981; Dolez & Vauclair 1981; Winget et al. 1982). These are based on the assumption that the convective flux does not respond to pulsation; this is often referred to as the frozen convection hypothesis. Because hydrogen is partially ionized in the surface layers of ZZ-Ceti stars, these workers attribute mode excitation to the κ-mechanism. In so doing, they ignore the fact that the thermal time-scale in the layers of partial ionization is many orders of magnitude smaller than the periods of the overstable modes. Pesnell (1987) points out that in calculations such as those just referred to, mode excitation results from the outward decay of the perturbed radiative flux at the bottom of the convective envelope. He coins the term 'convective blocking' for this mechanism.[1] While convective blocking is responsible for mode excitation in the above cited references, it does not occur in the convective envelopes of ZZ-Ceti stars. The dynamic time-scale for convective readjustment in these stars is much shorter than the mode periods. Noting this, Brickhill (1983,1991a,1991b) assumes an instantaneous response of the convection to the state of pulsation. He presents the first physically consistent calculations of mode overstability, mode visibility, and instability strip width. Our investigation supports most of his conclusions. As a result, we hope that his papers will finally receive the recognition they deserve.

[1]This mechanism is described in a general way by Cox & Guili (1968), and explained in detail by Goldreich & Keeley (1977).

3.2 Perturbations Associated with Pulsations

Here we derive relations that will be used in §3.3 to evaluate the driving and damping of g-modes in various parts of the star. We start with the radiative interior and proceed outward through the convection zone to the photosphere. A new symbol, Δ, is introduced to denote variations associated with a g-mode at a particular level, such as the photosphere, or within a particular layer, such as the convection zone. These variations are not to be confused with Lagrangian variations denoted by δ.

This section is replete with thermodynamic derivatives. We take ρ and T as our independent variables. Unless specified otherwise, it is implicitly assumed that partial derivatives with respect to one are taken with the other held constant. We adopt the shorthand notation: $p_\rho \equiv \partial \ln p/\partial \ln \rho$, $p_T \equiv \partial \ln p/\partial \ln T$, $s_\rho \equiv \partial s/\partial \ln \rho$, $s_T \equiv \partial s/\partial \ln T$, $\kappa_\rho \equiv \partial \ln \kappa/\partial \ln \rho$, $\kappa_T \equiv \partial \ln \kappa/\partial \ln T$.

We only consider modes that do not propagate immediately below the convection zone, $z_1 \sim z_\omega > z_b$.

3.2.1 Radiative Interior

In an optically thick region, the radiative flux can be expressed as

$$F = \frac{4\sigma}{3\kappa\rho}\frac{dT^4}{dz}. \tag{3.1}$$

Its Lagrangian perturbation takes the form

$$\frac{\delta F}{F} = -(1+\kappa_\rho)\frac{\delta\rho}{\rho} + (4-\kappa_T)\frac{\delta T}{T} - \frac{d\xi_z}{dz} + \left(\frac{d\ln T}{dz}\right)^{-1}\frac{d}{dz}\left(\frac{\delta T}{T}\right). \tag{3.2}$$

Next we express $\delta F/F$ in terms of $\delta p/p$. This is best done separately for the upper evanescent layer and the gravity-wave cavity. Within the quasiadiabatic approximation,

$$\frac{\delta\rho}{\rho} = \frac{p}{c_s^2\rho}\frac{\delta p}{p}, \tag{3.3}$$

and

$$\frac{\delta T}{T} = -\frac{s_\rho}{s_T}\frac{p}{c_s^2\rho}\frac{\delta p}{p}. \tag{3.4}$$

1) *Upper Evanescent Layer*

For $z \le z_\omega$, equation (2.9) implies

$$\frac{d\xi_z}{dz} \approx \frac{\delta p}{p} - \frac{\delta\rho}{\rho}. \tag{3.5}$$

Moreover,

$$\left(\frac{d\ln T}{dz}\right)^{-1}\frac{d}{dz}\left(\frac{\delta T}{T}\right)\approx-\left(\frac{d\ln T}{dz}\right)^{-1}\frac{d}{dz}\left(\frac{s_\rho}{s_T}\frac{p}{c_s^2\rho}\right)\frac{\delta p}{p}. \tag{3.6}$$

Because the material in the upper part of the radiative interior is well approximated as a completely ionized hydrogen plasma, we set $p_\rho\approx 1$, $p_T\approx 1$, $s_\rho\approx -2$, $s_T\approx 3$, and $c_s^2\rho/p\approx 5/3$. This enables us to discard the term given by equation (3.6), although it is of the same order in z/z_ω as the other terms we retain in $\delta F/F$. With these caveats,

$$\frac{\delta F}{F}\approx\frac{(3-3\kappa_\rho-2\kappa_T)}{5}\frac{\delta p}{p}. \tag{3.7}$$

2) *G-Mode Cavity*

For $z\geq z_\omega$, the dominant contributions to $\delta F/F$ come from the last two terms in equation (3.2). The first transforms to

$$\frac{d\xi_z}{dz}\approx -ik_z\frac{\delta p}{g\rho}, \tag{3.8}$$

as most easily seen from equation (2.10). It then follows that

$$\frac{\delta F}{F}\approx\frac{ik_z p}{g\rho}\frac{d\ln p}{d\ln T}\left(\left.\frac{\partial\ln T}{\partial\ln p}\right|_s-\frac{d\ln T}{d\ln p}\right)\frac{\delta p}{p}\approx\frac{ik_z N^2}{g}\left(\frac{p}{g\rho}\right)^2\frac{d\ln p}{d\ln T}\frac{\delta p}{p}, \tag{3.9}$$

where we have again set $p_\rho\approx 1$ and $p_T\approx 1$.

3.2.2 Convective Envelope

The Lagrangian temperature variation can be separated into an adiabatic and a nonadiabatic component. Thus

$$\frac{\delta T}{T}=-\frac{s_\rho}{s_T}\frac{p}{c_s^2\rho}\frac{\delta p}{p}+\frac{p_\rho}{p_\rho s_T-p_T s_\rho}\delta s. \tag{3.10}$$

The nonadiabatic part is associated with net absorption of heat by the convective envelope in the amount

$$\Delta Q=\int_{\rm cvz}dz\,\rho\frac{k_B}{m_p}T\,\delta s\approx\Delta s_b\int_{\rm cvz}dz\,\rho\frac{k_B}{m_p}T, \tag{3.11}$$

where s_b is the specific entropy evaluated at the bottom of the convection zone. The latter expression pertains because the convection is efficient, except just below the photosphere, and its response time is much shorter than the g-mode period.

We treat convection by means of a crude mixing-length model. The convective flux is set equal to[2]

$$F\sim\rho v_{\rm cv}H\frac{k_B}{m_p}T\frac{ds}{dz}, \tag{3.12}$$

[2]Where the convection is efficient, F is comparable to the total flux.

with the convective velocity given by

$$v_{\rm cv}^2 \sim -gH^2 \frac{\partial \ln \rho}{\partial s}\bigg|_p \frac{ds}{dz} = -N^2 H^2. \tag{3.13}$$

Eliminating $v_{\rm cv}$ and solving for ds/dz, we find

$$s_b - s_{\rm ph} \equiv \int_{\rm cvz} dz \frac{ds}{dz} \approx f \left(\frac{p_\rho s_T - p_T s_\rho}{p_T} \right)^{1/3} \left(\frac{1}{\rho p} \right)^{1/3} \left(\frac{m_p F}{k_B T} \right)^{2/3}, \tag{3.14}$$

where we have made use of

$$\frac{\partial s}{\partial \ln \rho}\bigg|_p = -\frac{p_\rho s_T - p_T s_\rho}{p_T} < 0. \tag{3.15}$$

Though the entropy jump in equation (3.14) requires integration over the whole convection zone, most of the contribution comes from right below the photosphere. The right-hand side of equation (3.14) is to be evaluated at the photosphere. The dimensionless factor f is of order unity. It is proportional to $\alpha^{-4/3}$, where α is the ratio of the mixing-length to the pressure scale-height. In applications, f is determined by comparison with numerical stellar models.

Mode driven variations in $s_b - s_{\rm ph}$ are given by

$$\begin{aligned} \frac{\Delta(s_b - s_{\rm ph})}{(s_b - s_{\rm ph})} = \frac{1}{12} \Bigg\{ & 6 + \frac{p_T(1-\kappa_\rho) + \kappa_T(1+p_\rho)}{p_\rho + \kappa_\rho} + \frac{1}{p_T(p_\rho s_T - p_T s_\rho)} \\ & \Big[p_T(p_{\rho T} s_T + p_\rho s_{\rm TT} - p_T s_{\rho T}) - p_T^2 s_{\rho T} - p_{\rm TT} p_\rho s_T \\ & + \left(\frac{p_T + \kappa_T}{p_\rho + \kappa_\rho} \right) \left(p_T^2 s_{\rho\rho} - p_T(p_{\rho\rho} s_T + p_\rho s_{\rho T}) + p_\rho p_{\rho T} s_T \right) \Big] \Bigg\} \frac{\Delta F}{F}, \end{aligned} \tag{3.16}$$

where ΔF is the perturbation to the convective flux. In practice, only a few terms in this complicated expression make significant contributions.

3.2.3 Photosphere

The photospheric temperature, pressure, and temperature gradient are determined by

$$T \approx \left(\frac{F}{\sigma} \right)^{1/4}, \tag{3.17}$$

$$p = \frac{2}{3} \frac{g}{\kappa}, \tag{3.18}$$

and the equation of radiative diffusion,

$$\frac{dT}{dz} = \frac{3\kappa\rho}{16\sigma T^3} F, \tag{3.19}$$

provided most of the flux in the photosphere is carried by radiation. Combining the above equations with the hydrostatic equilibrium equation (2.1) yields

$$\frac{d\ln T}{d\ln p} = \frac{1}{8}, \tag{3.20}$$

which is to be compared to the adiabatic gradient,

$$\left.\frac{\partial \ln T}{\partial \ln p}\right|_s = \frac{s_\rho}{p_T s_\rho - p_\rho s_T}. \tag{3.21}$$

We find that the convection zone extends up to the photosphere for DA white dwarfs which lie inside the instability strip. This is confirmed by comparison with Bradley's models.

Next we relate changes in the thermodynamic variables at the photosphere to changes in the emergent flux. Thus

$$\frac{\Delta T}{T} = \frac{1}{4}\frac{\Delta F}{F} \tag{3.22}$$

is an immediate consequence of equation (3.17). Expressions for $\Delta\rho/\rho$ and $\Delta p/p$ follow in a straightforward manner from the thermodynamic identity

$$\frac{\Delta p}{p} = p_\rho \frac{\Delta \rho}{\rho} + p_T \frac{\Delta T}{T}, \tag{3.23}$$

and the perturbed form of equation (3.18)

$$\frac{\Delta p}{p} = -\kappa_\rho \frac{\Delta \rho}{\rho} - \kappa_T \frac{\Delta T}{T}. \tag{3.24}$$

Together, these yield

$$\frac{\Delta \rho}{\rho} = -\frac{1}{4}\left(\frac{p_T + \kappa_T}{p_\rho + \kappa_\rho}\right)\frac{\Delta F}{F}, \tag{3.25}$$

and

$$\frac{\Delta p}{p} = \frac{1}{4}\left(\frac{p_T \kappa_\rho - p_\rho \kappa_T}{p_\rho + \kappa_\rho}\right)\frac{\Delta F}{F}. \tag{3.26}$$

It is then a simple step to show that

$$\Delta s = \frac{1}{4}\left[s_T - \left(\frac{p_T + \kappa_T}{p_\rho + \kappa_\rho}\right) s_\rho\right]\frac{\Delta F}{F}. \tag{3.27}$$

3.2.4 Putting It All Together

We begin by collecting a few key equations obtained in previous subsections. Then these are combined to determine how the entropy and flux variations in the convection zone and photosphere depend upon the pressure perturbation associated with the g-mode.

1) *Key Equations*

The quasiadiabatic flux perturbation entering the bottom of the convective envelope from the radiative interior is obtained from equation (3.7).

$$\frac{\Delta F_b}{F} = A\left(\frac{\delta p}{p}\right)_b, \tag{3.28}$$

where

$$A \equiv \frac{(3 - 3\kappa_\rho - 2\kappa_T)}{5} \tag{3.29}$$

is also evaluated at z_b.

We obtain the photospheric entropy variation as a function of $\Delta F_{\rm ph}$ from equation (3.27),

$$\Delta s_{\rm ph} = B\frac{\Delta F_{\rm ph}}{F}, \tag{3.30}$$

where

$$B \equiv \frac{1}{4}\left[s_T - \left(\frac{p_T + \kappa_T}{p_\rho + \kappa_\rho}\right) s_\rho\right]. \tag{3.31}$$

Equation (3.16) gives the variation of the jump in specific entropy across the convection envelope;[3]

$$\Delta(s_b - s_{\rm ph}) = C\frac{\Delta F_{\rm ph}}{F}, \tag{3.32}$$

with

$$\begin{aligned} C \equiv\ & \frac{1}{12}(s_b - s_{\rm ph})\Bigg\{6 + \frac{p_T(1-\kappa_\rho) + \kappa_T(1+p_\rho)}{p_\rho + \kappa_\rho} + \frac{1}{p_T(p_\rho s_T - p_T s_\rho)} \\ & \Big[p_T(p_{\rho T}s_T + p_\rho s_{\rm TT} - p_T s_{\rho T}) - p_T^2 s_{\rho T} - p_{\rm TT}p_\rho s_T \\ & + \left(\frac{p_T + \kappa_T}{p_\rho + \kappa_\rho}\right)\left(p_T^2 s_{\rho\rho} - p_T(p_{\rho\rho}s_T + p_\rho s_{\rho T}) + p_\rho p_{\rho T} s_T\right)\Big]\Bigg\}. \end{aligned} \tag{3.33}$$

The net heat variation, ΔQ, and specific entropy variation, Δs_b, of the convective envelope are related by equation (3.11). Thus

$$\Delta Q \approx F\tau_b \Delta s_b, \tag{3.34}$$

with

$$\tau_b \equiv \frac{1}{F}\int_{\rm cvz} dz\, \rho \frac{k_B}{m_p} T. \tag{3.35}$$

The time constant τ_b is closely related to the thermal relaxation time at the bottom of the

[3]The convective envelope extends all the way up to the photosphere in white dwarf models of relevance to this study.

convective envelope. The standard definition of the thermal time-scale at depth z reads

$$\tau_{\rm th} \equiv \frac{1}{F}\int_0^z dz\,\rho\, c_p \frac{k_B}{m_p} T, \tag{3.36}$$

where

$$c_p = T\frac{\partial s}{\partial T}\bigg|_p = \frac{p_T s_T - p_\rho s_\rho}{p_T}. \tag{3.37}$$

The differential equation

$$\frac{d\Delta Q}{dt} = \Delta F_b - \Delta F_{\rm ph} \tag{3.38}$$

completes our set of key equations. Here, we ignore horizontal heat transport for good reason. Transport by radiation is completely negligible because $k_h z_b \ll 1$. Turbulent diffusion acts to diminish Δs_b, but only at the tiny rate $k_h^2\, z_b\, (v_{\rm cv})_b \ll \omega$.

Approximating the bottom part of the convective envelope as an isentropic, completely ionized, hydrogen plasma, we arrive at:

$$\begin{aligned} z_b &\approx \frac{5p_b}{2g\rho_b}, \\ \tau_b &\approx \frac{p_b z_b}{7F}, \\ \tau_{\rm th} &\approx \frac{5p_b z_b}{14F}. \end{aligned} \tag{3.39}$$

Before leaving this subsection, we point out that A, B, and C are each dimensionless, and in practical applications, positive. A is evaluated at the boundary between the radiative interior and the bottom of the convective envelope as is τ_b, whereas B and C are computed at the photosphere.

2) *Implications Of Key Equations*

Taken together, the five homogeneous equations (3.28), (3.30), (3.32), (3.34), and (3.38) enable us to solve for the five quantities Δs_b, $\Delta s_{\rm ph}$, $\Delta F_b/F$, $\Delta F_{\rm ph}/F$, and ΔQ in terms of $(\Delta p/p)_b$.[4] For compactness of notation, we define a new thermal time constant, τ_c, closely related to τ_b, by

$$\tau_{\rm c} \equiv (B + C)\tau_b. \tag{3.40}$$

Our principal results, derived for an assumed time dependence $\propto \exp(-i\omega t)$, are listed below:

$$\Delta s_b = \frac{A(B+C)}{1 - i\omega\tau_c}\frac{\delta p_b}{p_b}, \tag{3.41}$$

$$\Delta s_{\rm ph} = \frac{AB}{1 - i\omega\tau_c}\frac{\delta p_b}{p_b}, \tag{3.42}$$

[4] We include $\Delta F_b/F$ in this list for completeness although it is already expressed in terms of $\delta p_b/p_b$ by equation (3.28).

$$\frac{\Delta F_b}{F} = A\frac{\delta p_b}{p_b}, \tag{3.43}$$

$$\frac{\Delta F_{\rm ph}}{F} = \frac{A}{1 - i\omega\tau_c}\frac{\delta p_b}{p_b}, \tag{3.44}$$

$$\Delta Q = F\tau_b \Delta s_b. \tag{3.45}$$

3.3 Driving and Damping

The time average rate of change of the mode's energy is obtained from the work integral,

$$\gamma \equiv \frac{\omega}{2\pi}\oint dt\frac{dE}{dt}. \tag{3.46}$$

When the eigenfunction is normalized so that $E = 1$ as in equation (2.40), $\gamma = 2\omega_i$, where ω_i is the imaginary part of the eigenfrequency. Useful forms for γ are reproduced below.

$$\gamma = 2\omega R^2 \oint dt \int_0^R dz\, \rho \frac{k_B}{m_p}\delta T \frac{d\delta s}{dt} = \frac{\omega}{2\pi} L \oint dt \int_0^R dz \frac{\delta T}{T}\frac{d}{dz}\left(\frac{\delta F}{F}\right). \tag{3.47}$$

Regions of driving and damping are associated with positive and negative values of the integrand.

There are a few cases to consider. These are conveniently classified by the values of the dimensionless parameters $\omega\tau_c$ and z_b/z_ω. The most important cases correspond to $z_b/z_\omega \leq 1$. Fortunately, these are also the simplest, and we consider them here. The origin of this simplicity is the near constancy of $\delta p/p$ for $z \leq z_\omega$.

3.3.1 Convective Driving

We substitute equations (3.10) and (3.41) into the first form for γ given by equation (3.47). It is apparent that the net contribution comes entirely from the adiabatic part of $\delta T/T$. Since the integrand is strongly weighted toward the bottom of the convective envelope, we evaluate all quantities there and arrive at

$$\gamma_{\rm cvz} \approx \frac{(\omega\tau_c)^2}{1 + (\omega\tau_c)^2}\left(\frac{AL}{5}\right)\left(\frac{\delta p_b}{p_b}\right)^2. \tag{3.48}$$

Since A is positive, so is $\gamma_{\rm cvz}$. The convective envelope is the seat of mode driving.

3.3.2 Radiative Damping

Here it proves more convenient to use the second form for γ given by equation (3.47).

The contribution from $z_b \leq z \leq z_\omega$, obtained with the aid of equations (3.4) and (3.43), reads

$$\gamma_{r_u} \approx -\left(\frac{AL}{10}\right)\left(\frac{\delta p}{p}\right)_b^2 + \frac{L}{10}\int_{z_b}^{z_\omega} dz \left(\frac{\delta p}{p}\right)^2 \frac{dA}{dz}. \tag{3.49}$$

The first term on the right-hand side of equation (3.49) is to be evaluated at z_b. It generally dominates over the second as A does not vary significantly over this region.

At $z \geq z_\omega$, we substitute equation (3.9) for $\Delta F/F$ which yields

$$\gamma_{r_l} \approx \frac{-9k_h^2 L}{125 g^3 \omega^2} \int_{z_\omega}^{\infty} dz N^4 c^4 \frac{d\ln p}{d\ln T} \left(\frac{\delta p}{p}\right)^2 . \tag{3.50}$$

Appeal to equation (2.27) giving the WKB envelope relation for $\delta p/p$ establishes that the integrand peaks close to z_ω. Thus,

$$\gamma_{r_l} \sim -L \left(\frac{cN}{g}\right)^4 \left(\frac{\delta p}{p}\right)^2 \sim -L \left(\frac{\delta p}{p}\right)^2 , \tag{3.51}$$

where in this context $\delta p/p$ represents the WKB envelope evaluated at z_ω. The magnitude of this envelope at z_ω is significantly smaller than the value of $\delta p/p$ at z_b. Thus this contribution to the radiative damping is negligible provided $z_\omega \geq z_b$.

To a fair approximation $\gamma_{\rm rad} \equiv \gamma_{r_u} + \gamma_{r_l}$ may be set equal to the first term on the right-hand side of equation (3.49). Thus

$$\gamma_{\rm rad} \approx -\left(\frac{A\,L}{10}\right) \left(\frac{\delta p_b}{p_b}\right)^2 . \tag{3.52}$$

Comparison with equation (3.48) reveals that

$$\gamma_{\rm rad} \approx -\frac{1+(\omega\tau_c)^2}{2(\omega\tau_c)^2} \gamma_{\rm cvz} . \tag{3.53}$$

3.3.3 Turbulent Damping

Damping due to turbulent viscosity acting on the velocity shear in the convection zone is estimated from equation (3.46) with

$$\frac{dE_{\rm visc}}{dt} \approx 4\pi R^2 \omega^2 \int_0^{z_b} dz\, \rho\, \nu\, |\xi_{ij}|^2 , \tag{3.54}$$

where $\nu \approx H_p v_{\rm cv}$ is the turbulent viscosity and $-i\omega\xi_{ij}$ is the velocity shear tensor.

Estimating turbulent damping is a subtle business. This is delayed until Chapter 4 where we show that it is negligible in comparison to radiative damping. However, this is not immediately obvious. For example, taking $d\xi_h/dz \sim -\xi_h/z_\omega$, as pertains in the radiative portion of upper evanescent layer, leads to $\gamma_{\rm visc} \sim -L(z_b/z_\omega)(c_s/v_{\rm cv})^2(\delta p/p)^2$, which is much larger than $\gamma_{\rm rad}$.

3.3.4 Net Driving

The net driving follows from equations (3.48) and (3.53);

$$\gamma_{\rm net} \approx \frac{(\omega\tau_c)^2 - 1}{(\omega\tau_c)^2 + 1} \left(\frac{A\,L}{10}\right) \left(\frac{\delta p}{p}\right)_b^2 . \tag{3.55}$$

With the aid of equation (2.46), we reduce equation (3.55) to a cruder, but more revealing form,

$$\gamma_{\rm net} \sim \frac{(\omega\tau_c)^2 - 1}{(\omega\tau_c)^2 + 1}\left(\frac{1}{n\tau_\omega}\right). \tag{3.56}$$

3.3.5 Simplified Derivations

Both the origin of the overstability and the linear growth rate admit simple derivations in the limit $\omega\tau_c \gg 1$. We consider each in turn below.

1) *Origin of Overstability*

The perturbed flux in the radiative interior varies in phase with the pressure perturbation because adiabatic compression causes the opacity to decrease. The fractional perturbations $\delta T/T$ and $\delta F/F$ are proportional to $\delta p/p$. All three decline with increasing depth for $z \leq z_\omega$. For $z \geq z_\omega$ they oscillate about zero with rapidly decreasing amplitude. To the extent that the coefficients of proportionality connecting $\delta T/T$ and $\delta F/F$ are depth independent, we find

$$\gamma_{\rm rad} \approx \frac{L}{2}\int_{z_b}^{z_\omega} dz \frac{\delta T}{T}\frac{d}{dz}\left(\frac{\delta F}{F}\right) \approx -\frac{L}{4}\left(\frac{\delta T}{T}\right)_b \frac{\Delta F_b}{F}. \tag{3.57}$$

The fractional temperature perturbation in the convective envelope is approximately adiabatic, in phase with the pressure perturbation, and independent of z. The first and second properties are a consequence of $\omega\tau_c \geq 1$, while the third follows from the near constancy of $\delta p/p$ in the convection zone. The perturbed flux which enters the bottom of the convective zone produces a z-independent entropy perturbation that lags the pressure perturbation by a quarter cycle. This behavior is a consequence of the rapid response of the convection to perturbation and its high efficiency. From these properties, we deduce that for $0 \leq z \leq z_b$,

$$\frac{d\Delta s_b}{dt}\int_0^{z_b} dz\, \rho \frac{k_B}{m_p} T \approx \Delta F_b. \tag{3.58}$$

Thus

$$\gamma_{\rm cvz} = 2\pi R^2 \int_0^{z_b} dz\, \rho \frac{k_B}{m_p}\delta T \frac{d\delta s}{dt} \approx \frac{L}{2}\frac{k_B}{m_p}\left(\frac{\delta T}{T}\right)_b \frac{\Delta F_b}{F}. \tag{3.59}$$

Together, equations (3.57) and (3.59) imply

$$\gamma_{\rm net} \approx \frac{L}{4}\left(\frac{\delta T}{T}\right)_b \frac{\Delta F_b}{F}. \tag{3.60}$$

2) *Growth Rate*

Next we estimate the terms in equation (3.60). These are evaluated at $z = z_b \leq z_\omega$, that is, in the upper evanescent layer. As a start we replace $\delta T/T$ and $\delta F/F$ by $\delta p/p$. Thus

$$\gamma_{\rm net} \sim L \left(\frac{\delta p}{p}\right)_b^2. \tag{3.61}$$

To estimate $(\delta p/p)_b$ we make note of the following. Compression accounts for a significant fraction of a g-mode's energy density inside the upper evanescent layer.[5] The g-mode eigenfunction is normalized by setting the energy equal to unity. Equal fractions of the energy are stored between each of the n nodes, and a comparable fraction resides in the upper evanescent layer. From these facts, we deduce that

$$\Delta E \sim 4\pi R^2 z_\omega p_\omega \left(\frac{\delta p}{p}\right)_b^2 \sim \frac{1}{n}, \tag{3.62}$$

so

$$\left(\frac{\delta p}{p}\right)_b^2 \sim \frac{1}{n\tau_\omega}. \tag{3.63}$$

Combining equations (3.61) and (3.63), we arrive at

$$\gamma_{\rm net} \sim \frac{1}{n\tau_\omega}. \tag{3.64}$$

This is identical to equation (2.52).

3.4 Short Summary

We analyze the stability of g-modes in ZZ-Ceti stars under the quasiadiabatic approximation. Our investigation confirms many results first obtained by Brickhill in his underappreciated series of papers. All the relevant physical processes take place in the outer layer of hydrogen rich material. This consists of two parts, a convective envelope overlying a radiative interior. The dynamic time-scale for convective readjustment is much shorter than the shortest mode period. Moreover, the convection is efficient; the convective envelope is nearly an isentrope except just below the photosphere. The flux in the radiative interior increases with compression. As a result, the radiative interior contributes to mode damping. The convective envelope is the seat of mode excitation because it bottles up the perturbed flux which enters it from below. Dissipation associated with turbulent viscosity in the convective envelope is another source of damping. However, careful assessment shows it to be negligible. Driving exceeds damping by as much as a factor of two provided $\omega\tau_c \geq 1$, where ω is the radian frequency of the mode and τ_c is closely related to but somewhat larger than the thermal time

[5] Within the g-mode cavity the energy density stored in compression is much smaller than that stored in vertical displacement.

at the base of the convective envelope. Overstable modes have growth rates of order $\gamma \sim 1/(n\tau_\omega)$, where n is the mode's radial order and τ_ω is the thermal time-scale evaluated at the top of the mode's cavity. The growth time $(1/\gamma)$ ranges from a few hours for the longest period modes ($P \approx 10$ minutes) to several thousand years for those of shortest period ($P \approx 2$ minutes).

Chapter 4 explores the dynamical interaction between the viscous convection zone and pulsation, and Chapter 5 completes the overstability study by including nonadiabatic effects. A complete summary of overstability results is presented at the end of Chapter 5.

Bibliography

Brickhill, A. J. 1983, MNRAS, 204, 537

Brickhill, A. J. 1991a, MNRAS, 251, 673

Brickhill, A. J. 1991b, MNRAS, 252, 334

Cox, J. P., & Giuli, R. T. 1968, Principles of Stellar Structure, (Gordon and Breach), 1096

Dolez, N., & Vauclair, G. 1981, A&A, 102, 375

Dziembowski, W., & Koester, D. 1981, A&A, 97, 16

Goldreich, P., & Keeley, D. A. 1977, ApJ, 211, 934

Pesnell, W. D. 1987, ApJ, 314, 598

Winget, D. E., Van Horn, H. M., Tassoul, M., Hansen, C. J., Fontaine, G., & Carroll, B. W. 1982, ApJ, 252, L65

Chapter 4 Turbulent Damping on Gravity-Modes in White Dwarfs

4.1 Introduction

In this and the chapter which follows, we discuss two dissipative processes which must be incorporated into realistic overstability calculations. Here we treat the dynamical interaction between g-modes and convective eddies. Radiative diffusion is investigated in Chapter 5. Both effects modify the structure of g-modes and impact their stability.

The large-scale motion associated with a g-mode advects and shears small scale convective eddies. Our present understanding of these interactions is rudimentary. In the absence of a quantitative theory, we model them as giving rise to a turbulent viscous stress which acts to reduce the mode's velocity gradient. Then we incorporate the resulting turbulent damping into our calculations of mode overstability.

Gravity modes cause mostly horizontal sloshing of the fluid. We concentrate on the largest component of velocity gradient, dv_h/dz, the vertical gradient of the horizontal velocity. In the dual limit of an isentropic convection zone and vanishing entropy perturbation, we prove in §2.10 that $dv_h/dz \sim v_h/R$, where R is the stellar radius. When the entropy perturbation is included, dv_h/dz can be as large as v_h/z_ω (eq. [4.13]), where z_ω is the depth at the top of the g-mode's propagating cavity. The inclusion of the viscous stress reduces this gradient by a factor of $\omega t_{\rm cv}$, where $t_{\rm cv}$ is the eddy turn-over time (§4.2). This factor is typically so small that viscous damping is *insignificant* (§4.3).

The story does not end here. The discontinuity in viscosity across the convective-radiative boundary results in a discontinuity of horizontal velocity. The latter is Kelvin-Helmholtz unstable and produces a turbulent layer at the top of the radiative interior where the fluid is only weakly stratified. Damping due to turbulent viscosity in this layer is a source of nonlinearity which limits the mode amplitude. This is discussed in §4.4.

4.2 Velocity Gradient in the Convection Zone

We are concerned with the manner in which the viscous stress limits the value of dv_h/dz, where $v_h = -i\omega\xi_h$. This prepares us for estimating the magnitude of turbulent damping in §4.3.

An adiabatic disturbance in an isentropic region is irrotational. According to §2.10, the corre-

sponding $d\xi_h/dz \sim \xi_h/R$, where R is the stellar radius. Both the static entropy gradient and the Lagrangian entropy change associated with a nonadiabatic pulsation increase this estimate, whereas the viscous stress decreases it. These effects are evaluated below.

We write the viscous stress tensor as

$$\sigma_{ij} = 2\rho\nu S_{ij}, \tag{4.1}$$

where the shear tensor

$$\mathcal{S}_{ij} = -i\omega\left[\frac{1}{2}\left(\frac{\partial\xi_i}{\partial x_j} + \frac{\partial\xi_j}{\partial x_i}\right) - \frac{\delta^i_j}{3}\frac{\partial\xi_k}{\partial x_k}\right]. \tag{4.2}$$

The turbulent kinematic viscosity ν is of order $v_{\rm cv}l_{\rm cv}$, where $v_{\rm cv}$ and $l_{\rm cv}$ are characteristic turbulent velocity and length scales; $l_{\rm cv} \sim H_p \sim z$. We define the convective turn-over time as

$$t_{\rm cv} \sim \frac{l_{\rm cv}}{v_{\rm cv}}. \tag{4.3}$$

The viscous force is the divergence of the viscous stress. Its horizontal and vertical components take the form[1]

$$\alpha_h = \frac{d}{dz}\left(2\rho\nu\mathcal{S}_{hz}\right) + 2ik_h\rho\nu\mathcal{S}_{hh} \approx -i\omega\frac{d}{dz}\left(\rho\nu\frac{d\xi_h}{dz}\right); \tag{4.4}$$

$$\alpha_z = \frac{d}{dz}\left(2\rho\nu\mathcal{S}_{zz}\right) + 2ik_h\rho\nu\mathcal{S}_{hz} \approx -i\omega\left[\frac{4}{3}\frac{d}{dz}\left(\rho\nu\frac{d\xi_z}{dz}\right) + ik_h\rho\nu\frac{d\xi_h}{dz}\right]. \tag{4.5}$$

Augmenting the equation of motion by the viscous force (Landau & Lifshitz 1976), we arrive at

$$\omega^2\xi_h = ik_h\left(\frac{p}{\rho}\frac{\delta p}{p} - g\xi_z\right) + \frac{1}{\rho}\alpha_h, \tag{4.6}$$

$$\omega^2\xi_z = \frac{p}{\rho}\frac{d}{dz}\left(\frac{\delta p}{p}\right) + g\left(\frac{\delta p}{p} + ik_h\xi_h\right) + \frac{1}{\rho}\alpha_z. \tag{4.7}$$

To order of magnitude

$$\frac{1}{\rho}\alpha_h \sim \frac{\omega z}{t_{\rm cv}}\frac{d\xi_h}{dz}. \tag{4.8}$$

To a good approximation the vertical component of the equation of motion reduces to hydrostatic equilibrium. Both the inertial and viscous terms are negligible.[2] For modes with $z_\omega \geq z_b$, it follows that

$$\frac{\delta p}{p} \approx -ik_h\xi_h. \tag{4.9}$$

[1] We neglect bulk viscosity.

[2] The viscous term is of order $\omega v_{\rm cv}/g \sim (\omega t_{\rm cv})z(ds/dz) \ll 1$ with respect to each term in the round brackets.

We proceed to estimate $d\xi_h/dz$. Differentiating equation (4.6), we obtain,

$$\left(\omega^2 + \frac{i\omega}{t_{\rm cv}}\right)\frac{d\xi_h}{dz} \approx ik_h\left[\frac{d}{dz}\left(\frac{p}{\rho}\frac{\delta p}{p}\right) + g\left(\frac{\delta\rho}{\rho} + ik_h\xi_h\right)\right]. \tag{4.10}$$

In arriving at this expression we make the approximation

$$\frac{d}{dz}\left(\frac{\alpha_h}{\rho}\right) \sim \frac{\omega}{t_{\rm cv}}\frac{d\xi_h}{dz}. \tag{4.11}$$

The Lagrangian density variation, decomposed into an adiabatic and a nonadiabatic part, takes the form

$$\frac{\delta\rho}{\rho} = \frac{p}{c^2\rho}\frac{\delta p}{p} + \rho_s\delta s, \tag{4.12}$$

where $\rho_s \equiv \partial \ln\rho/\partial s|_p$. Substituting equations (4.7) and (4.12) into (4.10), we obtain[3]

$$\frac{d\xi_h}{dz} \approx \frac{-\omega t_{\rm cv}}{1-i\omega t_{\rm cv}}\frac{gk_h\rho_s}{\omega^2}\left[\frac{p}{g\rho}\frac{ds}{dz}\left(\frac{\delta p}{p}\right) - \delta s\right]. \tag{4.13}$$

As equation (4.10) makes apparent, the viscous stress significantly reduces $d\xi_h/dz$ provided $\omega t_{\rm cv} \ll 1$. In fact, in this limit, α_h as given by equation (4.8) is independent of $t_{\rm cv}$.

We can think of $\delta p/p$ and δs as providing the adiabatic and nonadiabatic forcing of $d\xi_h/dz$. Their relative sizes, as estimated at $z = z_b$, are given by

$$\left(\frac{p}{g\rho}\frac{ds}{dz}\right)_b\left|\frac{\delta p}{p}\right|_b\frac{1}{|\delta s|_b} \sim \left(\frac{p}{g\rho}\frac{ds}{dz}\right)_b\frac{[1+(\omega\tau_c)^2]^{1/2}}{A(B+C)} \sim \left[\left(\frac{v_{\rm cv}}{c_s}\right)^4 + (\omega t_{\rm cv})^2\right]_b^{1/2} \ll 1, \tag{4.14}$$

where we make use of equation (3.41), and the relations $gds/dz \sim (v_{\rm cv}/c_s)^2$ and $t_{\rm cv}/\tau_{\rm th} \sim (v_{\rm cv}/c_s)^2$. This establishes nonadiabatic forcing as the principal driver of velocity shear in the convection zone. The horizontal displacement would have a curvature of order z_ω were it not for the viscosity, which forces it to be very flat inside the convection zone. A similar conclusion is arrived at by Brickhill (1990).

4.3 Estimating Viscous Damping

The damping rate due to viscous dissipation is given by equation (3.46),

$$\gamma_{\rm vis} \approx -\pi R^2\omega^2\int_0^{z_b} dz\,\rho\nu\left(\frac{d\xi_h}{dz}\right)^2, \tag{4.15}$$

where only the dominant component of the shear is retained. Since we use normalized eigenfunctions, $\gamma = 2\omega_i$.

[3]We discard the inertial and viscous terms in equation (4.7).

To evaluate $\gamma_{\rm vis}$ given by equation (4.15), we retain only the nonadiabatic term on the right-hand side of equation (4.13). It then follows that

$$\gamma_{\rm vis} \sim \frac{-(\omega\tau_c)^2}{1+(\omega\tau_c)^2} L \left(\frac{z_b}{z_\omega}\right) \left(\frac{v_{\rm cv}}{c_s}\right)_b^2 \left(\frac{\delta p}{p}\right)_b^2 . \tag{4.16}$$

Comparison with equation (3.52) shows that viscous damping is always negligible with respect to radiative damping.

It is clear from equations (4.13) and (4.15) that for a given mode viscous damping is maximal for a viscosity such that $\omega t_{\rm cv} \sim 1$. For smaller ν, $\gamma_{\rm vis} \propto \nu$, and for larger ν, $\gamma_{\rm vis} \propto \nu^{-1}$. Since $\omega t_{\rm cv} \ll 1$ for overstable modes of DAVs, the appropriate limit is that of large viscosity.

4.4 Convective-Radiative Boundary Conditions

Inclusion of the viscous stress in the convection zone requires new boundary conditions to be applied across its interface with the radiative interior. Although δp, δs, and ξ_h remain continuous, ξ_h does not. This discontinuity has important implications for mode damping which we explore in §4.5.

Our investigation of the jump in $d\xi_h/dz$ begins with a slightly modified version of equation (4.6), namely

$$\omega^2 \xi_h = ik_h \left(\frac{p}{\rho}\frac{\delta p}{p} - g\xi_z\right) - i\frac{\omega g^2}{4}\frac{d}{dp}\left(\rho^2 \nu \frac{d\xi_h}{dp}\right). \tag{4.17}$$

Integrating this equation from the photosphere ($p = 0$) to the bottom of the convection zone ($p = p_b$), we arrive at

$$\omega^2 \int_0^{p_b} dp\, \xi_h = ik_h \int_0^{p_b} dp \left[\frac{p}{\rho}\left(\frac{\delta p}{p}\right) - g\xi_z\right], \tag{4.18}$$

where the viscous term vanishes because the viscous stress vanishes at both boundaries.[4]

We transform equation (4.18) in two steps, the first using an identity and the second equation (4.7).

$$\begin{aligned} \omega^2 \int_0^{p_b} dp\, \xi_h &= ik_h p_b \left[\frac{p}{\rho}\left(\frac{\delta p}{p}\right) - g\xi_z\right]_b - ik_h \int_0^{p_b} dp\, p \frac{d}{dp}\left[\frac{p}{\rho}\left(\frac{\delta p}{p}\right) - g\xi_z\right] \\ &= \omega^2 p_b\, \xi_h(z_b^+) + ik_h \int_0^{p_b} \frac{dp\, p}{\rho}\left[p\rho_s \frac{ds}{dp}\left(\frac{\delta p}{p}\right) - \rho_s \delta s - \frac{\omega^2 \xi_z}{g} + \frac{\alpha_z}{g\rho}\right]. \end{aligned} \tag{4.19}$$

Here $z_b^{\pm}$ denotes the limit taken as z_b is approached from below (the radiative side) or above (the convective side). We discard the terms containing ξ_z and α_z; it is not difficult to confirm that they are negligible compared to those we retain. Next we approximate the left-hand side of equation

[4]The viscous stress vanishes in the radiative region, and is continuous across the radiative-convective boundary to avoid large accleration.

(4.19) by

$$\omega^2 \int_0^{p_b} dp\, \xi_h \approx \omega^2 p_b \xi_h(z_b^-), \tag{4.20}$$

since for $\omega t_{\rm cv} \ll 1$, ξ_h is nearly constant within the convection zone. Thus we arrive at an expression for the discontinuity of ξ_h across the convective-radiative boundary.

$$\xi_h \Big|_{z_b^-}^{z_b^+} \approx \frac{-ik_h}{\omega^2 p_b} \int_0^{p_b} dp\, \frac{p\rho_s}{\rho} \left[\frac{p}{g\rho} \frac{ds}{dz} \left(\frac{\delta p}{p} \right) - \delta s \right]. \tag{4.21}$$

Equation (4.21) merits a few comments. It may be simplified by taking advantage of near constancy of $\delta p/p$ and δs within the convection zone. The former is constant due to rapid momentum transfer, and the latter due to a rapid entropy transfer. Both transfers proceed on the time scale $t_{\rm cv}$. Comparison with equation (4.13) reveals that the discontinuity in ξ_h is closely related to the total variation that ξ_h would experience within the convection zone in the absence of viscosity. The fractional change in ξ_h across z_b is estimated to be of order z_b/z_ω for marginally overstable modes.

The discontinuity of $d/dz(\delta p/p)$ is related to that of ξ_h by equation (4.7).[5]

$$\frac{p}{g\rho} \frac{d}{dz} \left(\frac{\delta p}{p} \right) \Big|_{z_b^-}^{z_b^+} \approx -ik_h \xi_h \Big|_{z_b^-}^{z_b^+} \approx \frac{-k_h^2}{\omega^2 p_b} \int_0^{p_b} dp\, \frac{p\rho_s}{\rho} \left[\frac{p}{g\rho} \frac{ds}{dz} \left(\frac{\delta p}{p} \right) - \delta s \right], \tag{4.22}$$

while inside a strongly viscous convection zone,

$$\frac{d}{dz} \left(\frac{\delta p}{p} \right) \ll \frac{1}{z_\omega} \left(\frac{\delta p}{p} \right). \tag{4.23}$$

In the nonadiabatic calculations discussed in Chapter 5, we simply require that $\delta p/p$ be constant inside the convection zone, and that its gradient experience a jump at the convective-radiative boundary as described by equation (4.22). The relative size of the jump increases with mode periods in the same star.

4.5 Dissipation Arising from the Velocity Jump

Our deduction that the horizontal velocity associated with a g-mode is discontinuous across the boundary between the convective envelope and radiative interior is an idealization. In reality this transition takes place across a layer of finite thickness, inside of which the originally weakly stratified fluid is strongly sheared and becomes turbulent. The structure and the extent of this layer is difficult to assess not least because it is disturbed by convective overshoot. Fortunately, these details are of secondary importance to our investigation. Our primary concern is the rate of energy dissipation in

[5] Note that δp and ξ_z are continuous, and the term involving α_z is negligible.

this layer, since that will limit the amplitude which an overstable mode can achieve.[6]

It is customary (see, e.g., Landau & Lifshitz 1976, Tritton 1977) to parameterize the shear stress associated with a velocity jump Δv across a layer of fluid having density ρ in terms of a drag coefficient C_D by

$$\sigma = \frac{C_D}{2}\rho\left(\Delta v\right)^2 . \tag{4.24}$$

The magnitude of C_D is typically much less than unity. This reflects the anticorrelation between the magnitudes of the shear and the turbulent viscosity.[7] As one might expect, C_D is larger for turbulent shear flows between rough plates than between smooth ones. It seems likely that the bottom of the convection zone acts more like a rough plate than a smooth one. In what follows, we treat C_D as a free parameter to be assigned a value based on fitting the observed mode amplitudes.[8]

The rate of energy dissipation per unit area is

$$\frac{1}{A}\frac{dE}{dt} = \sigma\Delta v = \frac{C_D}{2}\rho\left(\Delta v\right)^3 . \tag{4.25}$$

From equation (4.21), we approximate

$$\Delta v \approx \frac{gk_h z_b}{\omega}|\delta s| \approx \frac{z_b}{z_\omega}\frac{\omega R}{\ell}\delta s. \tag{4.26}$$

For overstable modes δs is related to $\delta p/p$ by

$$\delta s \sim \frac{-i}{\omega\tau_b}\frac{\delta p}{p}, \tag{4.27}$$

which enables us to write

$$\Delta v \sim \frac{z_b}{z_\omega}\frac{R}{\ell\tau_b}\frac{\delta p}{p}. \tag{4.28}$$

Balancing the rate of energy dissipation in the shear layer,

$$\frac{dE}{dt} \sim 2\pi R^2 C_D \rho_b \left(\Delta v\right)^3 , \tag{4.29}$$

by the rate of energy gain due to convective driving,

$$\frac{dE}{dt} \sim L\left(\frac{\delta p}{p}\right)^2 , \tag{4.30}$$

[6]This is not the only nonlinear process that limits mode amplitudes.

[7]Most of the velocity gradient is distributed in the small scales. When estimating the viscous stress using the global velocity jump, C_D is necessarily much smaller than unity.

[8]Since the shear flows associated with g-modes are periodic in both space and time, the value of C_D we adopt represents an average value.

yields the nonlinear amplitude relation,

$$\frac{\delta p}{p} \sim \frac{\omega^6 \tau_b^2 R^3}{C_D g^2 \ell^3 z_b}. \tag{4.31}$$

This expression makes two significant predictions for the amplitudes of overstable modes: 1) $\delta p/p$ for different modes in the same star will exhibit a sharp decrease with increasing mode period; 2) $\delta p/p$ for the same mode in different stars will show a steep rise with decreasing effective temperature. However, these predictions should not be confronted by observation until other nonlinear effects that limit mode amplitudes are assessed.

4.6 Summary

Nonadiabatic effects due to turbulent viscosity modify the structure of gravity-modes. Inside the convection zone, the viscous stress associated with convective turbulence suppresses the velocity shear to such an extent that its contribution to mode damping is negligible. However, this suppression is responsible for the formation of a turbulent shear layer at the top of the radiative interior. Turbulent dissipation in this layer limits the amplitudes of overstable g-modes. The limiting amplitude declines with increasing mode period. It is larger in cooler stars which have deeper convective envelopes. This is estimated quantitatively in §5.6.

Bibliography

Brickhill, A. J. 1990, MNRAS, 246, 510

Landau, L. D., & Lifshitz, E. M. 1959, Fluid Mechanics, (Pergamon Press), 166

Tritton, D. J. 1977, Physical Fluid Dynamics, (New York: van Nostrand Reinhold), 28

Chapter 5 Effects Of Radiative Diffusion On Gravity-Modes In White Dwarfs

5.1 Introduction

The driving/damping rates calculated in Chapter 3 are based on a quasiadiabatic approximation. These rates are accurate provided radiative diffusion may be neglected. Fractional corrections to an eigenmode due to radiative diffusion are measured by the dimensionless parameters $1/(\omega\tau_{\rm th})$ where the mode is evanescent, and by $(k_z z)^2/(\omega\tau_{\rm th})$ where it propagates. Here $\tau_{\rm th}$ is the local thermal time-scale as defined by equation (3.36) in Chapter 3, and k_z is the vertical component of the propagation vector.

For simplicity, consider a hot DA white dwarf whose radiative interior extends all the way up to its photosphere. The flux perturbation associated with a g-mode is almost independent of depth above the critical level where the effects of radiative diffusion as defined above become of order unity. This is a consequence of the limited heat capacity of the material above that depth. When situated above the mode's cavity, the critical layer generally dominates mode damping and driving because the matter higher up cannot trap or release much energy, and the entropy perturbation declines steeply with depth below this layer.

The story is more complicated in a cooler DA white dwarf whose radiative interior is overlaid by a surface convection zone. The convective region behaves in a qualitatively different manner from a radiative region of similar thermal content. Moreover, its behavior depends upon an additional parameter, $\omega t_{\rm cv}$, where $t_{\rm cv}$ is the dynamical response time of the convective eddies, often referred to as the eddy turn-over time. We are mainly concerned with the value of $t_{\rm cv}$ at the bottom of the convection zone (at $z = z_b$).

For g-modes in ZZ Cetis, the convective response is rapid; $\omega t_{\rm cv} \ll 1$ throughout the convection zone. Thus in Chapter 3 we assume that the convection zone reacts instantaneously to the pulsation. Moreover, we neglect the entropy gradient except in a thin superadiabatic layer just below the photosphere. This implies that the main body of the perturbed convection zone is an isentrope. The globally uniform entropy perturbation, δs, determines the perturbation to the local convective flux.[1] As a consequence of its rapid convective response, the entire convection zone is characterized by a single thermal adjustment time, τ_c. For ZZ Cetis, τ_c is typically about 20 times longer than the conventional thermal time-scale $\tau_b = \tau_{\rm th}(z_b)$. This large factor reflects the increased impedance

[1] We ignore both the unperturbed and perturbed radiative flux.

provided by the superadiabatic layer and the photosphere to a flux increase. The drop in entropy between the main body of the convection zone and the photosphere grows with increasing flux because a larger superadiabatic gradient is needed to carry a larger flux, while photospheric entropy rises at the same time with the increasing effective temperature and radiative opacity. Chapter 3 establishes $\omega\tau_c \geq 1$ as a necessary condition for a g-mode to be overstable. Since the flux perturbation is reduced by a factor $(\omega\tau_c)^{-1}$ between the radiative interior and the photosphere, modes detected photometrically are likely to have $\omega\tau_b < 1$.[2] These modes would be nonadiabatic immediately below the convection zone.

Except for the papers by Brickhill (1990, 1991a), previous investigations of g-mode overstability in ZZ Cetis proceed by setting $\delta F_c = 0$; that is they neglect the Lagrangian perturbation of the convective flux. This is tantamount to assuming that $\omega t_{\rm cv} \gg 1$. Within this framework the perturbed flux is purely radiative, $\delta F = \delta F_r$, and $|\delta F_r|$ decreases sharply above the bottom of the convection zone. This reflects the steep decline of F_r in the same region since the ratio $\delta F_r/F_r$ varies smoothly across it. Because the opacity decreases with compression in the radiative interior, δF_r varies in phase with δp there. Thus the decline of $|\delta F_r|$ above the bottom of the convection zone makes this a mode driving region. Convective blocking is the name conventionally attached to this type of mode excitation. Its fundamental difference from convective driving should be apparent.

5.2 Equations and Boundary Conditions

5.2.1 Equations in the Radiative Region

The linear equations describing nonadiabatic pulsations read

$$\begin{aligned}
\frac{\omega^2}{g}\xi_z &= \frac{d}{d\ln p}\left(\frac{\delta p}{p}\right) - \frac{\rho g}{p}\frac{d\xi_z}{d\ln p} + \frac{\delta p}{p} - \frac{\delta\rho}{\rho}, \\
\frac{\omega^2}{g}\xi_h &= ik_h\left(\frac{p}{g\rho}\frac{\delta p}{p} - \xi_z\right), \\
\frac{\delta\rho}{\rho} &= -ik_h\xi_h - \frac{\rho g}{p}\frac{d\xi_z}{d\ln p}, \\
\frac{\delta F}{F} &= (4-\kappa_T)\frac{\delta T}{T} - (1+\kappa_\rho)\frac{\delta\rho}{\rho} - \frac{\rho g}{p}\frac{d\xi_z}{d\ln p} + \frac{d\ln p}{d\ln T}\frac{d}{d\ln p}\left(\frac{\delta T}{T}\right), \\
-i\omega T\delta s &= \frac{gF}{p}\frac{m_p}{k_B}\frac{d}{d\ln p}\left(\frac{\delta F}{F}\right), \\
\frac{\delta\rho}{\rho} &= \frac{1}{\Gamma_1}\frac{\delta p}{p} + \rho_s\delta s, \\
\frac{\delta T}{T} &= \nabla_{ad}\frac{\delta p}{p} + T_s\delta s,
\end{aligned} \tag{5.1}$$

[2] Until recently, modes in ZZ Cetis had only been observed photometrically.

where we assume an $\exp(-i\omega t)$ temporal dependence for all the perturbed quantities. New symbols which appear here are $\rho_s \equiv \partial \ln \rho / \partial s|_p = 1/s_\rho$, and $c_p \equiv \partial s / \partial \ln T|_p = 1/T_s = s_T$. All others are used in Chapter 3 and are listed with their definitions in Appendix A. These linearized equations express in turn, the vertical and horizontal components of momentum conservation, mass conservation, radiative diffusion in the optically thick limit, energy conservation, and thermodynamic transformations relating density and temperature to pressure and entropy.

We adopt $\ln p$ as our independent variable, and investigate the radial structure of the four quantities, $(\delta p/p)$, $d(\delta p/p)/d\ln p$, $(\delta F/F)$, and δs. Equations (5.1) can be recast as

$$\frac{d}{d\ln p}\left(\frac{\delta p}{p}\right) - X = 0, \tag{5.2}$$

$$\frac{dX}{d\ln p} + X + \left(\frac{p}{g\rho}\right)^2 \left[k_h^2\left(\frac{N^2}{\omega^2} - 1\right) + \left(\frac{\omega}{c_s}\right)^2\right]\left(\frac{\delta p}{p}\right) - \frac{p}{g\rho}\frac{(gk_h)^2 - \omega^4}{g\omega^2}\rho_s \delta s = 0, \tag{5.3}$$

$$\frac{d}{d\ln p}\left(\frac{\delta F}{F}\right) + i\omega \frac{pT}{gF}\frac{k_B}{m_p}\delta s = 0, \tag{5.4}$$

$$\begin{aligned} &\frac{1}{c_p \nabla}\frac{d\delta s}{d\ln p} + \left[\frac{(4-\kappa_T)}{c_p} + \kappa_\rho \rho_s + \nabla \frac{d}{d\ln p}\left(\frac{1}{c_p}\right)\right]\delta s \\ &+ \left[(4-\kappa_T)\nabla_{ad} - \frac{\kappa_\rho}{\Gamma_1} - \left(1 - \frac{k_h^2 p}{\rho\omega^2}\right)\frac{\omega^4}{(gk_h)^2 - \omega^4} - 1 + \nabla\frac{d\nabla_{ad}}{d\ln p}\right]\left(\frac{\delta p}{p}\right) \\ &+ \left[\frac{\nabla_{ad}}{\nabla} - \frac{g^2 k_h^2}{(gk_h)^2 - \omega^4}\right] X - \left(\frac{\delta F}{F}\right) = 0, \end{aligned} \tag{5.5}$$

where $\nabla \equiv d\ln T/d\ln p$. Notice that since equation (5.4) includes a factor i, all four variables are *complex*. Moreover, the eigenfrequency ω is also complex; its imaginary part, ω_i, gives the rate of growth or decay of the pulsation amplitude. We write each complex variable in the form

$$Q = (Q_r + iQ_i)\exp^{-i\omega t}. \tag{5.6}$$

The real part of Q, which represents the physical perturbation, is $e^{\omega_i t}(Q_r \cos\omega_r t + Q_i \sin\omega_r t)$. Setting $\delta s = 0$ reduces the nonadiabatic pulsation equations to the adiabatic ones.

5.2.2 Equations in the Convection Zone

The small value of $\omega t_{\rm cv}$ constrains g-mode perturbations within the convection zone. Rapid momentum diffusion enforces $d\xi_h/dz \approx 0$ which in turn implies (see Chap. 4)

$$\frac{d}{d\ln p}\left(\frac{\delta p}{p}\right) \approx 0. \tag{5.7}$$

Similarly, rapid energy transport ensures that

$$\frac{d\delta s}{d\ln p} \approx 0 \tag{5.8}$$

except in the thin superadiabatic layer. The total flux perturbation, convective plus radiative, then follows from equations (5.4) and (5.8).[3] Equation (5.5) determines the radiative flux perturbation in terms of δp and δs.

Equation (5.8) does not apply in the superadiabatic layer. The entropy gradient there increases with increasing convective flux. But as this region is thin and of low density, it is sufficient to incorporate its effect into the boundary conditions.

5.2.3 Boundary Conditions

Before we can solve the four linear, homogeneous, first-order, differential equations (5.2)-(5.5) to obtain eigenvalues and eigenfunctions, we require a total of five boundary conditions. One of these is trivial and merely sets the magnitude scale for the eigenfunction. The remaining four express physical constraints imposed upon the g-mode by the physical environment outside the domain in which the differential equations are to be solved.

In principle our boundary conditions should be set at the stellar photosphere and at the center of the star. However, the simple approximations described in §5.2.2 enable us to lower the upper boundary to the top of the radiative interior at z_b. Furthermore, we raise the bottom boundary condition up to depth $z = z_{\rm deep}$ at which $p = 10^{16}\,{\rm dyne\,cm^{-2}}$.[4] Since $\tau_{\rm th} \approx 10^{10}\,{\rm s}$ at $z_{\rm deep}$, the quasiadiabatic approximation is valid there for all g-modes of interest to our investigation.

The three boundary conditions applied at the top of the radiative interior read:

$$\left(\frac{\delta p}{p}\right) = \text{constant}, \tag{5.9}$$

$$\frac{d}{d\ln p}\left(\frac{\delta p}{p}\right) = \frac{-k_h^2}{\omega^2 p_b}\int_0^{p_b} dp\,\frac{p\rho_s}{\rho}\left[\frac{p}{g\rho}\frac{ds}{dz}\left(\frac{\delta p}{p}\right) - \delta s\right], \tag{5.10}$$

$$\delta s = \frac{(B+C)}{1-i\omega\tau_c}\left(\frac{\delta F}{F}\right). \tag{5.11}$$

Equation (5.9) is the trivial boundary condition referred to earlier which sets the overall scale of the eigenfunction. Equation (5.10) is the combined result of equations (5.7) and (4.22); the latter gives the discontinuity of $d\delta p/dz$ across the radiative-convective boundary. Equation (5.11) follows from equations (3.41) and (3.43).

[3] Equation (5.8) is equivalent to enforcing a simple mixing-length prescription for the convective flux at any moment during the pulsation.

[4] This step alters the spectrum of the eigenvalues ω so that they differ from those of a complete star. However, a simple correction allows us to recover appropriate values for ω_i.

Two additional boundary conditions are applied at $z = z_{\rm deep}$. They read

$$\frac{d}{d\ln p}\left(\frac{\delta p}{p}\right) + \left(1 - \frac{k_h^2 p}{\omega^2 \rho}\right)\frac{\delta p}{p} = 0, \tag{5.12}$$

$$\left(\frac{\delta F}{F}\right) + M_1\left(\frac{\delta p}{p}\right) + M_2 \frac{d}{d\ln p}\left(\frac{\delta p}{p}\right) = 0. \tag{5.13}$$

Equation (5.12) is a mechanical boundary condition. It states that $\xi_z = 0$ at $z = z_{\rm deep}$. Thus we imagine that our model is bounded from below by a rigid wall. Equation (5.13) is our thermal boundary condition. It is the quasiadiabatic limit of the radiative diffusion equation (5.5) which defines the coefficients M_1 and M_2.[5]

5.3 Where Is δs Important?

Here we estimate the relative importance of nonadiabaticity in the radiative region. Nonadiabaticity is represented by the Lagrangian entropy perturbation, δs. We evaluate how δs affects both $\delta p/p$ and $\delta F/F$. The former effect measures how energy diffusion reduces the effective local buoyancy, whereas the latter measures the loss in the matter's ability to store thermal energy. Then we relate δs to $\delta p/p$. This step determines how nonadiabaticity depends upon the parameter $\omega\tau_{\rm th}$.

5.3.1 Nonadiabatic Effects in the Evanescent Region

The effect of δs on $\delta p/p$ is contained in equation (5.3). Scaling the adiabatic terms in this equation in a manner appropriate to the evanescent region $z < z_\omega$ yields

$$\begin{aligned}
\frac{d}{d\ln p}\left(\frac{\delta p}{p}\right) &\sim \frac{z}{z_\omega}\left(\frac{\delta p}{p}\right), \\
\frac{d^2}{d\ln p^2}\left(\frac{\delta p}{p}\right) &\sim z\frac{d}{dz}\left(\frac{z}{z_\omega}\frac{\delta p}{p}\right) \sim \frac{z}{z_\omega}\left(\frac{\delta p}{p}\right), \\
\left(\frac{p}{\rho g}\right)^2\left[k_h^2\left(\frac{N^2}{\omega^2} - 1\right) + \left(\frac{\omega}{c^2}\right)^2\right]\left(\frac{\delta p}{p}\right) &\sim \frac{k_h^2 z^2 N^2}{\omega^2}\left(\frac{\delta p}{p}\right) \sim \frac{z}{z_\omega}\left(\frac{\delta p}{p}\right),
\end{aligned} \tag{5.14}$$

where we make use of $z \sim H_p$ and $N^2 \sim g/z$. The nonadiabatic term is of order,

$$\frac{p}{\rho g}\frac{(gk_h)^2 - \omega^4}{g\omega^2}\rho_s \delta s \sim \frac{z}{z_\omega}\delta s. \tag{5.15}$$

Equations (5.14) and (5.15) establish that the nonadiabatic corrections to $\delta p/p$ are of order δs.

[5] We can also use $\delta s = 0$ or $d\delta s/d\ln p = 0$ at $z_{\rm deep}$ instead of equation (5.13). But our choice is more accurate since δs decays inward.

To relate δs to $\delta p/p$, we turn to equations (5.4) and (5.5). With appropriate scalings they yield[6]

$$\begin{aligned} \delta s &\sim \frac{1}{\omega\tau_{\rm th}}\frac{d}{d\ln p}\left(\frac{\delta F}{F}\right) \sim \frac{1}{\omega\tau_{\rm th}}\frac{\delta F}{F}, \\ \frac{\delta F}{F} &\sim \frac{\delta p}{p} + \delta s. \end{aligned} \tag{5.16}$$

Together, equations (5.15)-(5.16) imply that the ratio of the nonadiabatic to adiabatic contributions to both $\delta p/p$ and $\delta F/F$ is of order $1/\omega\tau_{\rm th}$.

5.3.2 Nonadiabatic Effects in the G-Mode Cavity

We follow a procedure similar to that in §5.3.1 with one notable exception. All perturbation quantities are taken to vary on a vertical scale k_z^{-1} where $k_z z \geq 1$.

Scaling the adiabatic terms in equation (5.3) now yields

$$\begin{aligned} \frac{d}{d\ln p}\left(\frac{\delta p}{p}\right) &\sim (k_z z)\left(\frac{\delta p}{p}\right), \\ \frac{d^2}{d\ln p^2}\left(\frac{\delta p}{p}\right) &\sim (k_z z)^2\left(\frac{\delta p}{p}\right), \\ \left(\frac{p}{\rho g}\right)^2\left[k_h^2\left(\frac{N^2}{\omega^2}-1\right)+\left(\frac{\omega}{c^2}\right)^2\right]\left(\frac{\delta p}{p}\right) &\sim \frac{z}{z_\omega}\left(\frac{\delta p}{p}\right) \sim (k_z z)^2\left(\frac{\delta p}{p}\right), \end{aligned} \tag{5.17}$$

where we have made use of the relation $k_z \sim (z z_\omega)^{-1/2}$. The nonadiabatic term becomes

$$\frac{p}{\rho g}\frac{(g k_h)^2-\omega^4}{g\omega^2}\rho_s \delta s \sim \frac{z}{z_\omega}\delta s \sim (k_z z)^2 \delta s. \tag{5.18}$$

From equations (5.4) and (5.5), we obtain

$$\begin{aligned} \delta s &\sim \frac{1}{\omega\tau_{\rm th}}(k_z z)\left(\frac{\delta F}{F}\right), \\ \left(\frac{\delta F}{F}\right) &\sim \frac{d}{d\ln p}\left[\left(\frac{\delta p}{p}\right)+\delta s\right] \sim (k_z z)\left[\left(\frac{\delta p}{p}\right)+\delta s\right]. \end{aligned} \tag{5.19}$$

Combining equations (5.17)-(5.19), we determine that the ratio of the nonadiabatic to adiabatic contributions to both $\delta p/p$ and $\delta F/F$ is of order $(k_z z)^2/\omega\tau_{\rm th}$. This measure has a simple physical interpretation. Since $\tau_{\rm th}$ is the time-scale for thermal diffusion across distance z, the time-scale for thermal diffusion across distance k_z^{-1} must be $\tau_{\rm th}/(k_z z)^2$. Nonadiabaticity is measured by the ratio of the mode period to this time-scale.

[6]The coefficient connecting $\delta p/p$ to $\delta F/F$ in equation (5.5) varies on scale of z.

5.4 Numerical Realizations

The equations and boundary conditions for nonadiabatic oscillations are set out in §5.2. Here we describe the numerical procedure we employ to obtain the complex eigenfrequencies and eigenfunctions.

In place of a complete stellar model, we work with plane-parallel hydrogen envelopes designed to resemble the outer layers of DA white dwarfs. Details of the construction of these envelopes is documented in Appendix B.

5.4.1 Nonadiabatic Code

We follow a two step procedure to solve the linear pulsation equations (5.2)-(5.5) for the four dependent variables subject to the five boundary conditions given by equations (5.9)-(5.13). The initial step consists of guessing a value for the complex eigenfrequency and then using a relaxation method to solve the differential equations subject to four out of the five boundary conditions. The remaining boundary condition, which can be anyone except equation (5.9), is then used to determine the eigenvalue. Both minimization and root finding techniques work well in this step. Normally, we reserve equation (5.12) for our final boundary condition, but the results do not change when others are used instead. We devote the following two paragraphs to descriptions of the relaxation procedure and the root finding technique.

In the relaxation procedure (Press et al. 1992), the N first order differential equations are transformed to finite difference equations on a mesh of M points. This yields a matrix equation involving an $[(NM) \times (MN)]$ block diagonal matrix.[7] The boundary conditions are incorporated into the matrix. An initial guess is provided for each of the $N \times M$ variables, and the matrix equation is solved by iteration. Compared to the shooting method, the relaxation method has the advantage of faster convergence. Moreover, it is superior in dealing with a set of 'stiff' differential equations, as it is equivalent to the shooting method with M meeting points. For convergence, we require the dependent variables to satisfy both the pulsation equations and the boundary conditions to 10^{-7} of a scaling factor provided by the corresponding adiabatic eigenfunction at individual points. This precision is routinely achieved using double precision programs.

Thereafter, eigenvalues are obtained either by minimization or by root finding applied to equation (5.12). Both procedures start from an initial guess for the complex ω. The minimization procedure is the downhill simplex method described in Press et al. (1992). It is aimed at minimizing the absolute value of the left-hand side of equation (5.12). Reliable results are obtained provided the initial simplex (a triangle) encompasses an eigenvalue. Otherwise, it is vulnerable to getting hung up at local minima. We need to check for global convergence by starting from different initial simplexes.

[7] The matrix is block diagonal because the finite differences only involve neighboring points.

We find a globally convergent Newton's method (root finding) to be a better approach. A handful of line searches and backtrackings suffice to locate a precise root of equation (5.12).

5.4.2 Eigenvalues for Stellar G-Modes

Our numerical integrations yield eigenvalues for a plane-parallel hydrogen envelope bounded from below by a rigid wall. We attach primes to these to denote that they apply to plane-parallel envelope and not to a complete stellar model. To derive values of ω_i appropriate to g-modes of a DA white dwarf, we associate each nonadiabatic mode of the plane-parallel layer with an adiabatic mode of a complete stellar model by their frequencies. From the latter we determine the ratio between the number of radial nodes above $z_{\rm deep}$ (n') and the total number of radial nodes in the entire star (n).[8] Since the region between each radial node makes an equal contribution to the mode mass,[9] and the energy gain/loss at the upper atmosphere is shared by all nodes, we have

$$\omega_i \approx \frac{n'}{n}\omega_i'. \tag{5.20}$$

We verify this relation by varying $z_{\rm deep}$ and evaluating ω_i with different n'.

Our procedure for converting ω_i' to ω_i requires that nonadiabatic effects be small well above $z_{\rm deep}$, as is the case for all modes of interest to our investigation. Moreover, it only applies to modes that have at least one node above $z_{\rm deep}$. Thus it cannot handle the highest frequency g-modes. We compute values of ω_i for these using the work integral.

5.4.3 The Work Integral

The work integral provides an alternate method for evaluating the driving or damping of a mode. It is most commonly used in cases where the quasiadiabatic approximation applies. In such cases, accurate driving or damping rates may be obtained from adiabatic eigenfunctions. The work integral is less useful when nonadiabatic eigenvalues and eigenfunctions are computed, since the driving or damping rate is given directly by ω_i.[10] However, the work integral still provides physical insight because its integrand reveals the spatial distribution of the regions of driving and damping.

The work integral may be expressed in a variety of forms. One version, given by Unno et al. (1989), and equation (3.47), is displayed below.

$$\gamma \;=\; \frac{\omega}{2\pi}R^2 \oint dt \int_0^R dz\, \rho T \frac{k_B}{m_p}\frac{\delta T}{T}\frac{d\delta s}{dt}$$

[8] In general, neither n' nor n is an integer. In practice, we determine n' and n by interpolation using adiabatic eigenfunctions whose frequencies bracket ω_r'.

[9] Strictly speaking, this statement applies only to nodes within the adiabatic region.

[10] The work integral computes $\gamma = 2\omega_i$.

$$= \frac{\omega R^2}{2} \int_0^R dz \, \nabla_{ad} \, \rho \, \frac{k_B}{m_p} T \left[\left(\frac{\delta p}{p} \right)_r \delta s_i - \left(\frac{\delta p}{p} \right)_i \delta s_r \right]. \tag{5.21}$$

This expression applies to periodic pulsations. Because the overstable g-modes in ZZ Cetis have high Qs (the quality factors), their linear pulsations are nearly periodic. We substitute precisely periodic solutions for $\delta p/p$ and δs into equation (5.21) to obtain γ. These are computed by using our relaxation code to solve the nonadiabatic equations with fixed ω_r and $\omega_i = 0$.

5.5 Results and Discussions

5.5.1 Nonadiabatic Effects: Qualitative Analysis

The quasiadiabatic results of Chapter 3 imply that overstable g-modes require $\omega\tau_c > 1$. But the large disparity between τ_b and τ_c cautions us that the quasiadiabatic approximation is not to be trusted for those modes for which $\omega\tau_c$ is just slightly larger than unity. Since these are the modes whose photometric variations are most easily detectable, this is a significant concern. Indeed, it is the main motivation for the nonadiabatic calculations reported in this chapter.

Consider a periodic pulsation of a fully radiative star. Flux perturbations are able to stream out freely above a depth where $\omega\tau_{\rm th} < 1$. Thus this strongly nonadiabatic region provides little driving or damping. The presence of a surface convection zone introduces additional complications. Some of these are discussed in §5.1. In particular, the convective flux responds almost instantaneously to the pulsation of an overstable g-mode in a ZZ-Ceti star. This implies that the entire convective envelope complies with a single thermal time constant, τ_c. Moreover, τ_c exceeds the radiative thermal time constant at the top of the radiative interior, τ_b, by at least an order of magnitude.

The thermal effects of the convection zone are nicely illustrated by comparing integrands of the work integral computed with nonadiabatic and adiabatic eigenfunctions. We present three examples corresponding to g-modes with periods of 136 s, 1,200 s, and 2,400 s for a stellar model with effective temperature of 12,000 K.[11] We normalize the phase of the pressure perturbation ($\delta p/p$) to be real in the adiabatic interior. Thus the imaginary component of the flux perturbation arises from nonadiabatic effects.

Nonadiabaticity increases with mode period. As shown in Figure 5.1, the 136 s mode, for which $\omega\tau_b = 1.9$, is quite adiabatic in the radiative interior. The imaginary part of its flux perturbation is negligible except near the photosphere. The photospheric flux perturbation is greatly reduced in magnitude and delayed in phase from that at the bottom of the convection zone. As discussed in Chapter 3, this results from the finite heat capacity of the convective envelope. Nonadiabatic effects are more pronounced for the 1,200 s mode which has $\omega\tau_b = 0.2$. As is seen in Figure 5.2, radiative

[11] quasiadiabatic predict overstability for each of these modes.

diffusion below z_b reduces both the convective driving and the radiative damping. It also results in a small region of radiative driving at the top of the radiative interior. The 2,400 s mode with $\omega\tau_b = 0.1$ is nonadiabatic all the way down to the top of its cavity. As a result, the phase shift between $\delta F/F$ and $\delta p/p$ at the bottom of the convection zone is so large that the convective driving predicted by the adiabatic code turns into convective damping. This mode is now stable.

In general, radiative diffusion reduces the growth rates and limits the longest periods of overstable modes. However, the latter effect is not large. In particular, it cannot account for the observed period cut-off at around 1,200 s for g-modes in ZZ Ceti stars.

Both radiative diffusion and convection introduce phase shifts between photospheric flux and velocity perturbations. Now that the velocity perturbations are detectable (see Chap. 8), the information contained in these phase shifts, as well as the amplitude ratios between light and velocity variations, may yield insights about the nature of both the star and its modes. Our nonadiabatic calculations provide a theoretical basis for interpreting the phase shifts and amplitude ratios, an example of which is depicted in Figure 5.4 for a $P = 800$ s mode in a star with $T_{\rm eff} = 12,300$ K.

5.5.2 Nonadiabatic Effects On Driving/Damping Rates

In this section we report on the results of nonadiabatic calculations of driving and damping rates of g-modes. This material is presented graphically. Our nonadiabatic calculations predict that as the star cools inside the instability strip, more and longer period modes become overstable. This is consistent with observations.

Direct calculations of ω_i and those based on the work integral yield consistent results. This provides a measure of confidence in both. Modest discrepancies are found for some marginally overstable modes. We believe the eigenvalue calculations to be more reliable. Work integrals for marginally overstable modes suffer from cancellation between comparable contributions of driving and damping.

The value of ω_i for an individual g-mode undergoes an interesting evolution with decreasing $T_{\rm eff}$. Although this behavior may be gleaned from the numerical data presented in Figures 5.5-5.9, we summarize it here as well. We consider in turn three $\ell = 1$ g-modes with periods of approximately 135 s, 1,000 s, and 2,000 s.

The 135 s mode has a single radial node. It is overstable below $T_{\rm eff} \approx 12,800$ K. The upper lid of its cavity lies far beneath the bottom of the convection zone for all stars in the instability strip. Thus it is largely immune to both nonadiabatic effects and the deepening of the convection zone with decreasing $T_{\rm eff}$. Consequently, the driving/damping rate for this mode is of order $10^{-12}\,{\rm s}^{-1}$, independent of $T_{\rm eff}$. This value is consistent with the estimate $1/n\tau_\omega$, where τ_ω is the thermal time-scale at the top of the cavity.

The 1,000 s mode has approximately 21 radial nodes. It becomes overstable at $T_{\rm eff} \approx 12,000$ K.

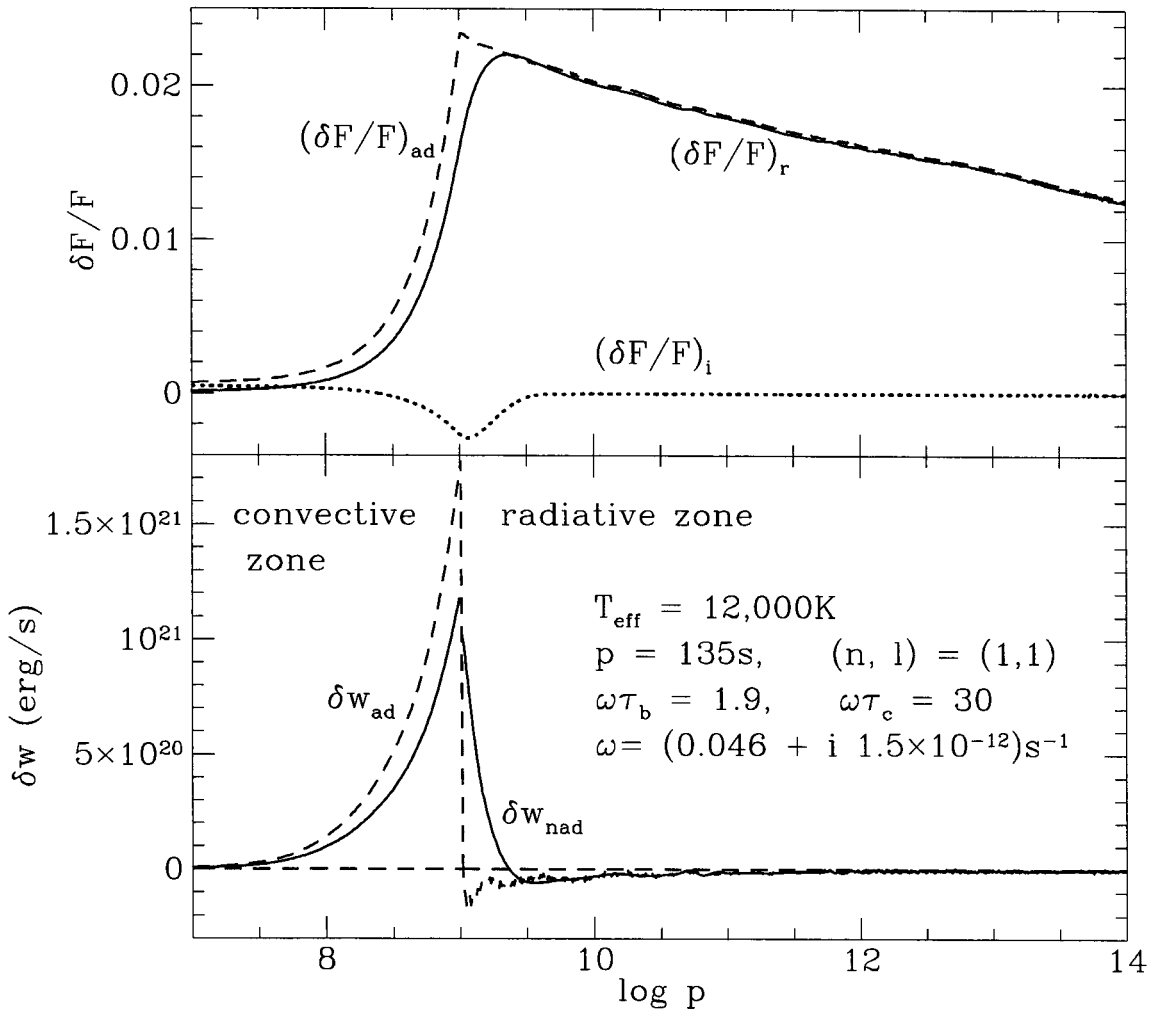

Figure 5.1: Comparison between adiabatic and nonadiabatic g-mode eigenfunctions, as well their respective work integrals. The upper panel displays the $\delta F/F$ as a function of $\log p$ for both the adiabatic case (dashed line) and the nonadiabatic case (real part solid line and imaginary part dotted line). Inside the convection zone, both $\delta F/F$ are dictated by the isentropic entropy perturbation. The lower panel shows the differential work, δW, defined by $W = \int \delta W d\log p$ plotted against $\log p$ for both the adiabatic (dashed line) and nonadiabatic (solid line) cases.

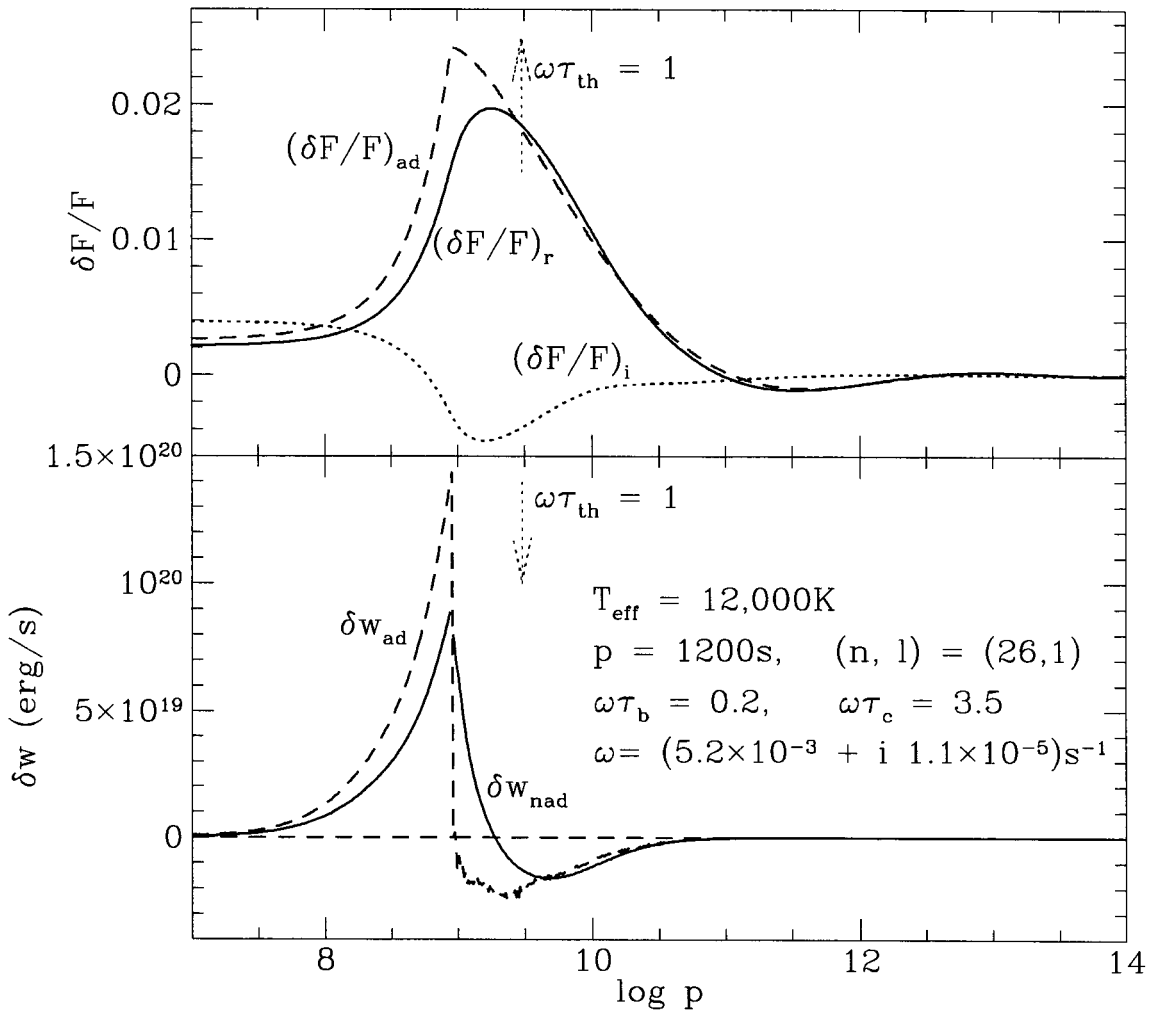

Figure 5.2: Similar to Figure 5.1, but for a mode which is moderately nonadiabatic immediately below the convective envelope. The division between strongly nonadiabatic and adiabatic regions is marked by the dashed arrow where $\omega\tau_{th} = 1$. Both convective driving and radiative damping are reduced by radiative diffusion. However, the mode remains overstable.

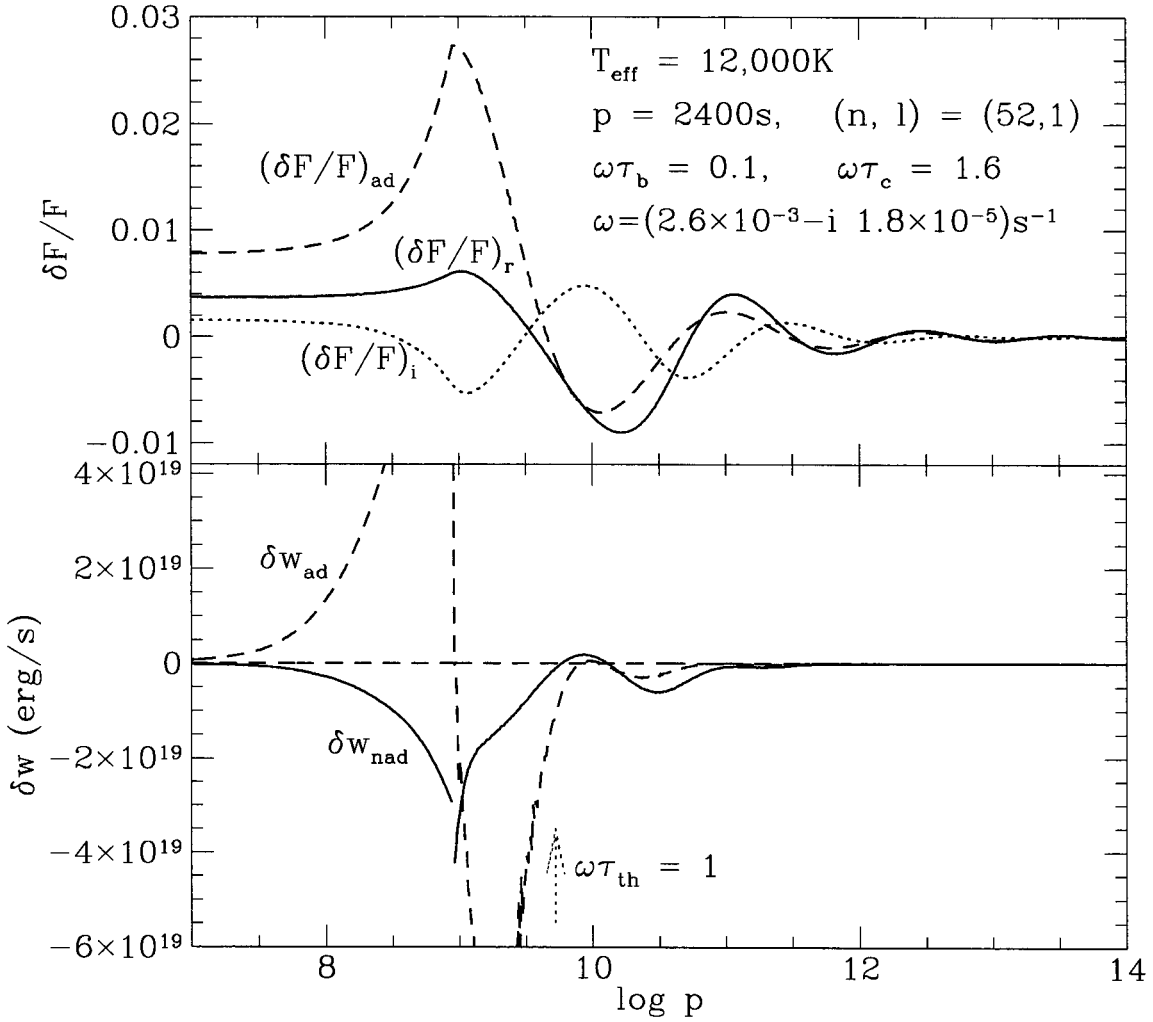

Figure 5.3: Similar to Figure 5.1, but for a mode which is significantly nonadiabatic throughout its upper evanescent region. The phase difference between $\delta F/F$ and $\delta p/p$ at the bottom of the convection zone results in convective damping. This mode is damped, although a quasiadiabatic calculation predicts it to be overstable. Notice the reduced photospheric $|\delta F/F|$ for the nonadiabatic eigenfunction.

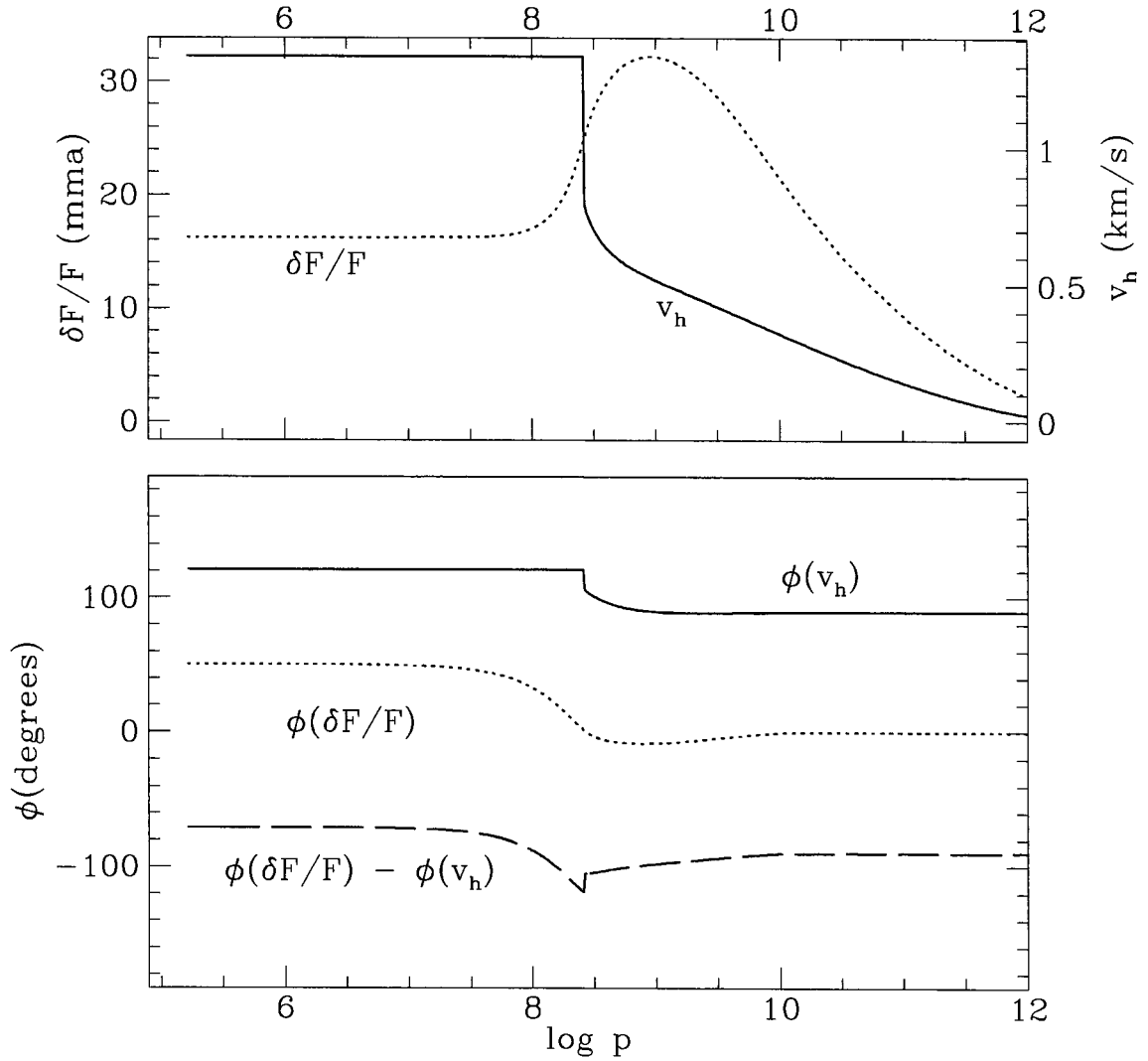

Figure 5.4: The amplitudes and phases of flux perturbation ($\delta F/F$) and horizontal pulsational velocity (v_h) as a function of $\log p$ for an 800 s mode in a star of $T_{\rm eff} = 12,300$ K ($\omega\tau_c = 1.14$, $\omega\tau_b = 0.07$). A photospheric amplitude for $\delta F/F$ of 16 mma[13] corresponds to a surface velocity $v_h = 1.3$ km/s. This scaling ignores the effects of limb-darkening, disc averaging, and inclination angle. The phase ϕ is defined by $X = X_0 \cos(\omega t - \phi)$, where X is the time dependent perturbation, and X_0 the absolute amplitude of this perturbation. In the adiabatic interior, velocity maximum lags the light maximum by 90 deg. Nonadiabaticity reduces this relative phase difference to about ~ 70 deg at the photosphere.

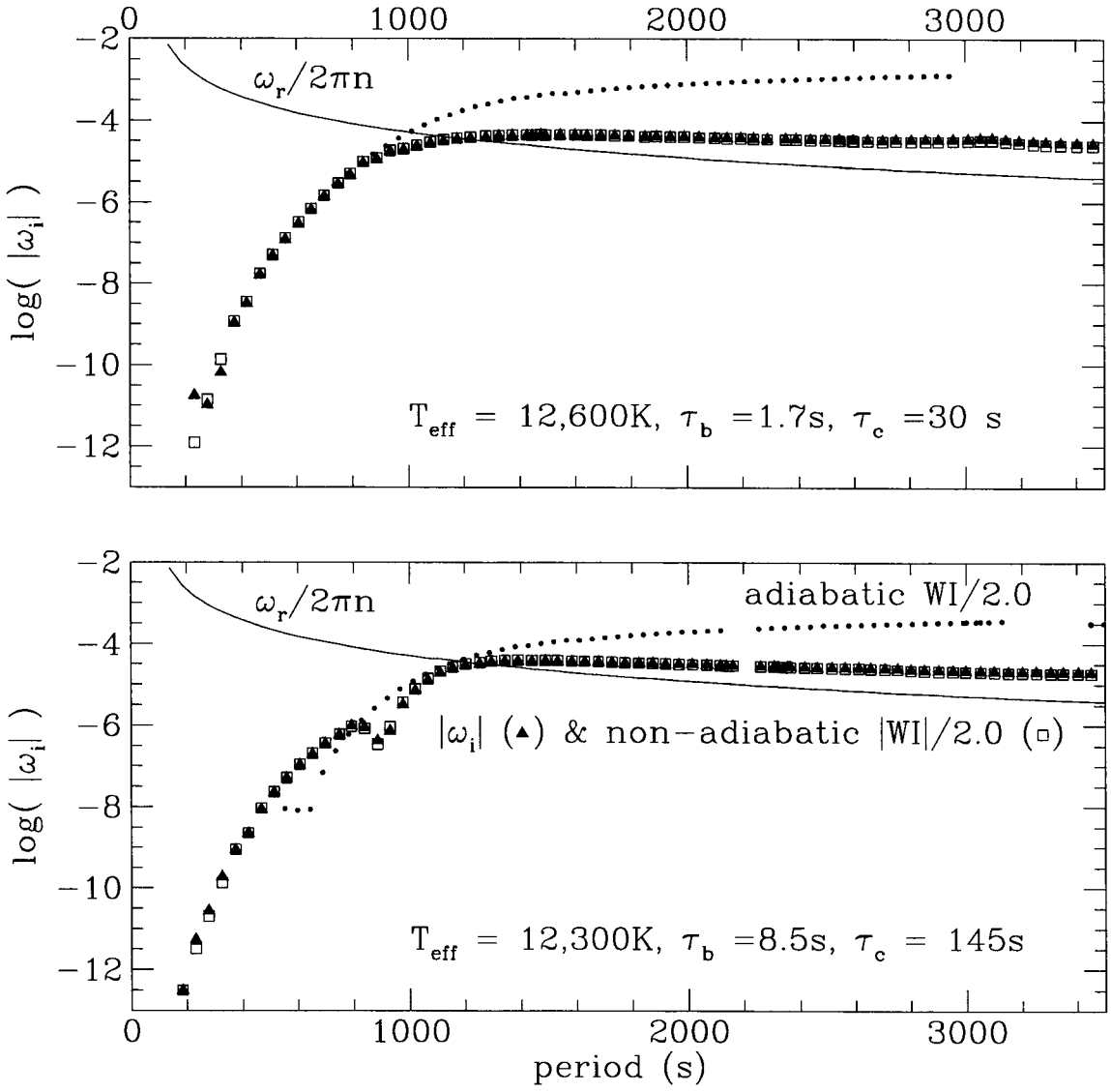

Figure 5.5: Driving/damping rates for $\ell = 1$ modes in stars of $T_{\rm eff} = 12,600\,{\rm K}$ and $12,300\,{\rm K}$ are plotted against mode period. Solid triangles show values of $|\omega_i|$ obtained as eigenvalues, and open squares and dots those calculated from nonadiabatic and quasiadiabatic work integrals. Rates for the short period modes ($P < 500\,{\rm s}$) are only calculated from the work integral, as they do not have a node within $z_{\rm deep}$. The transition between overstable and damped modes occurs around $P = 200\,{\rm s}$ for the warmer model and at $P \approx 900\,{\rm s}$ for the cooler model, both marked by dips in the values of $|\omega_i|$. For long period modes, the nonadiabatic values of $|\omega_i|$ are suppressed relative to the adiabatic ones. Moreover, the former are approximately equal to $\omega_r/2\pi n$, where n is the number of radial nodes.

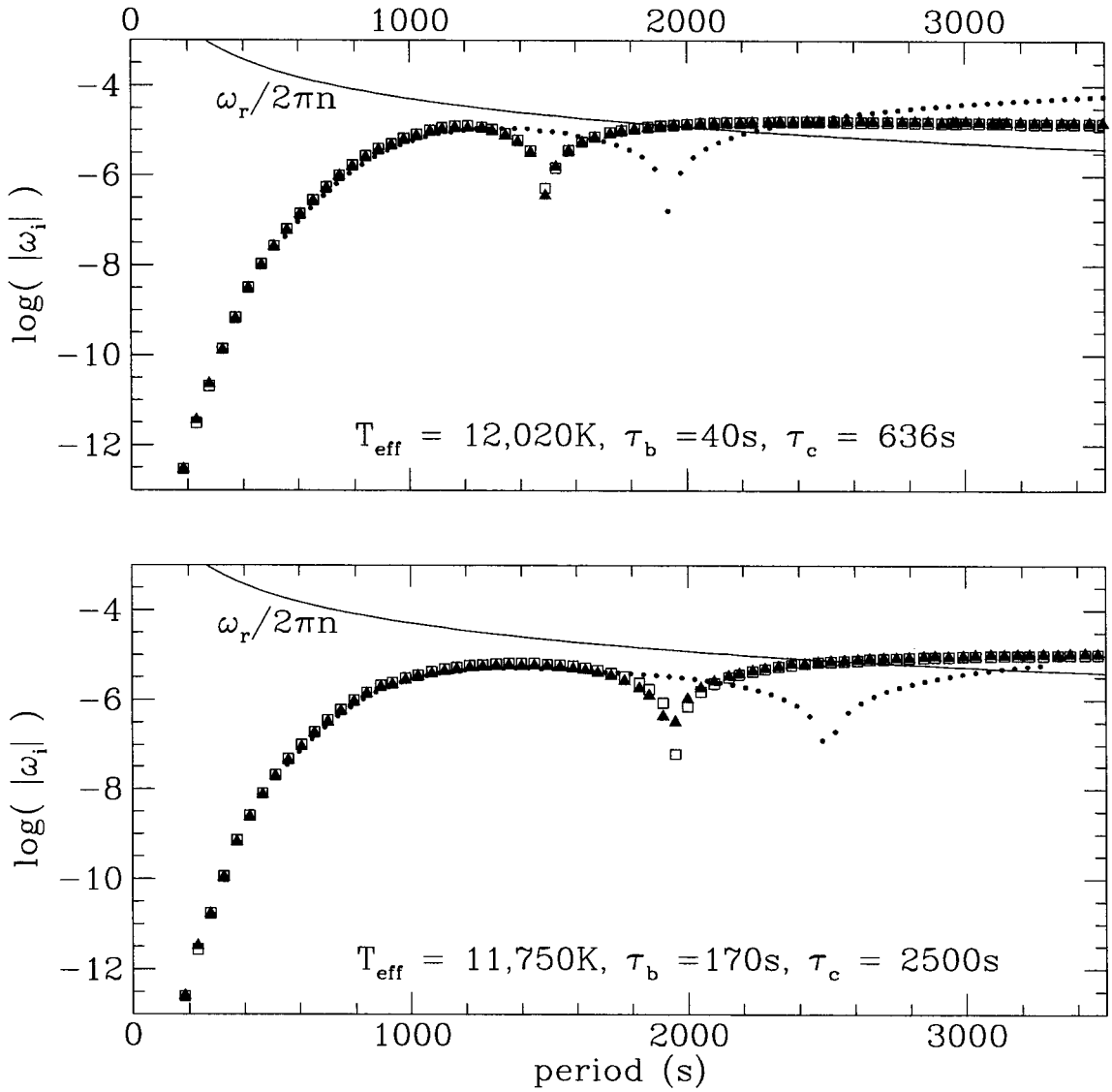

Figure 5.6: Similar to Figure 5.5, but for stars of $T_{\rm eff} = 12,000\,{\rm K}$ and $11,750\,{\rm K}$.

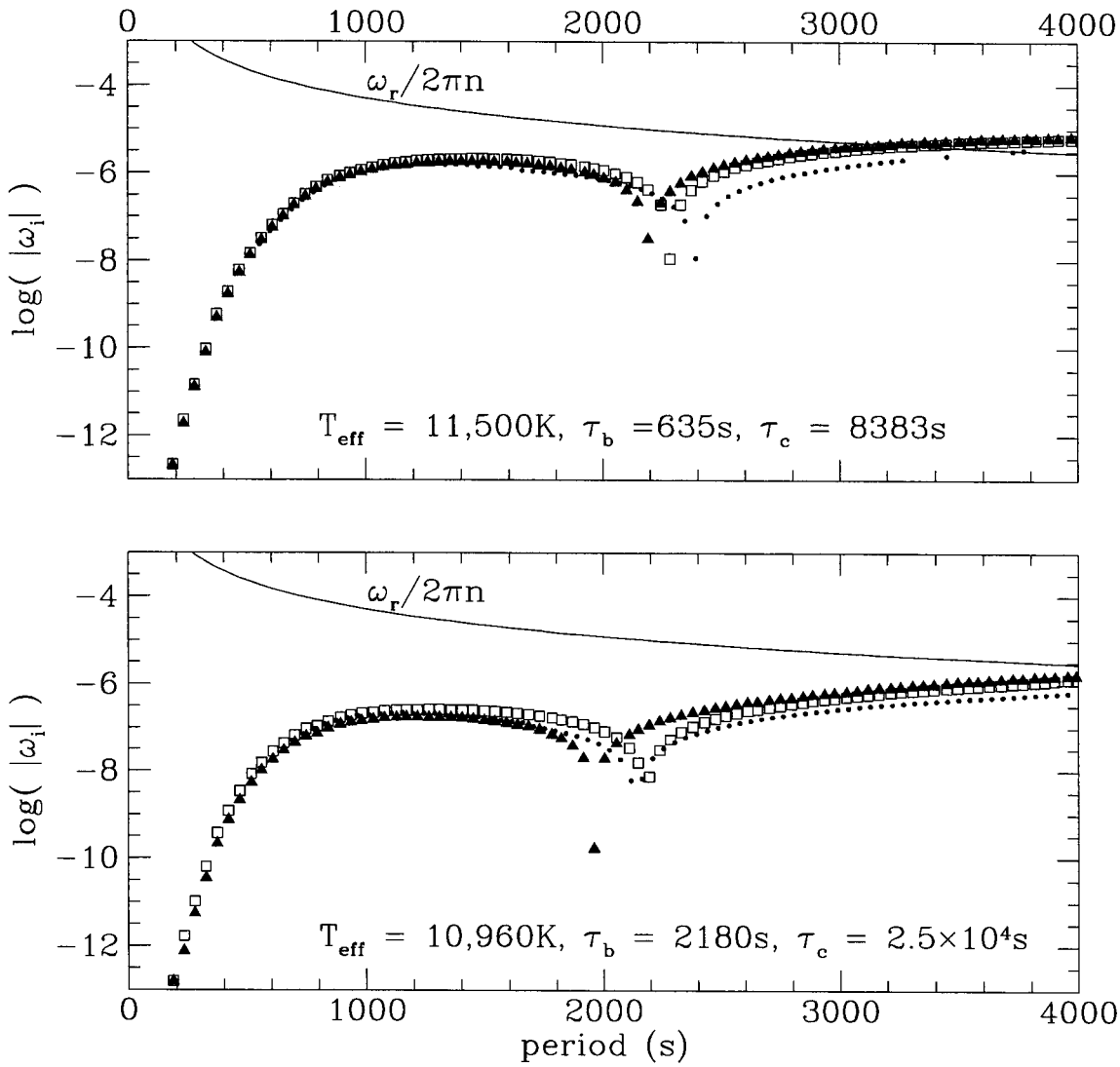

Figure 5.7: Similar to Figure 5.5, but for stars of $T_{\rm eff} = 11,500\,{\rm K}$ and $11,220\,{\rm K}$.

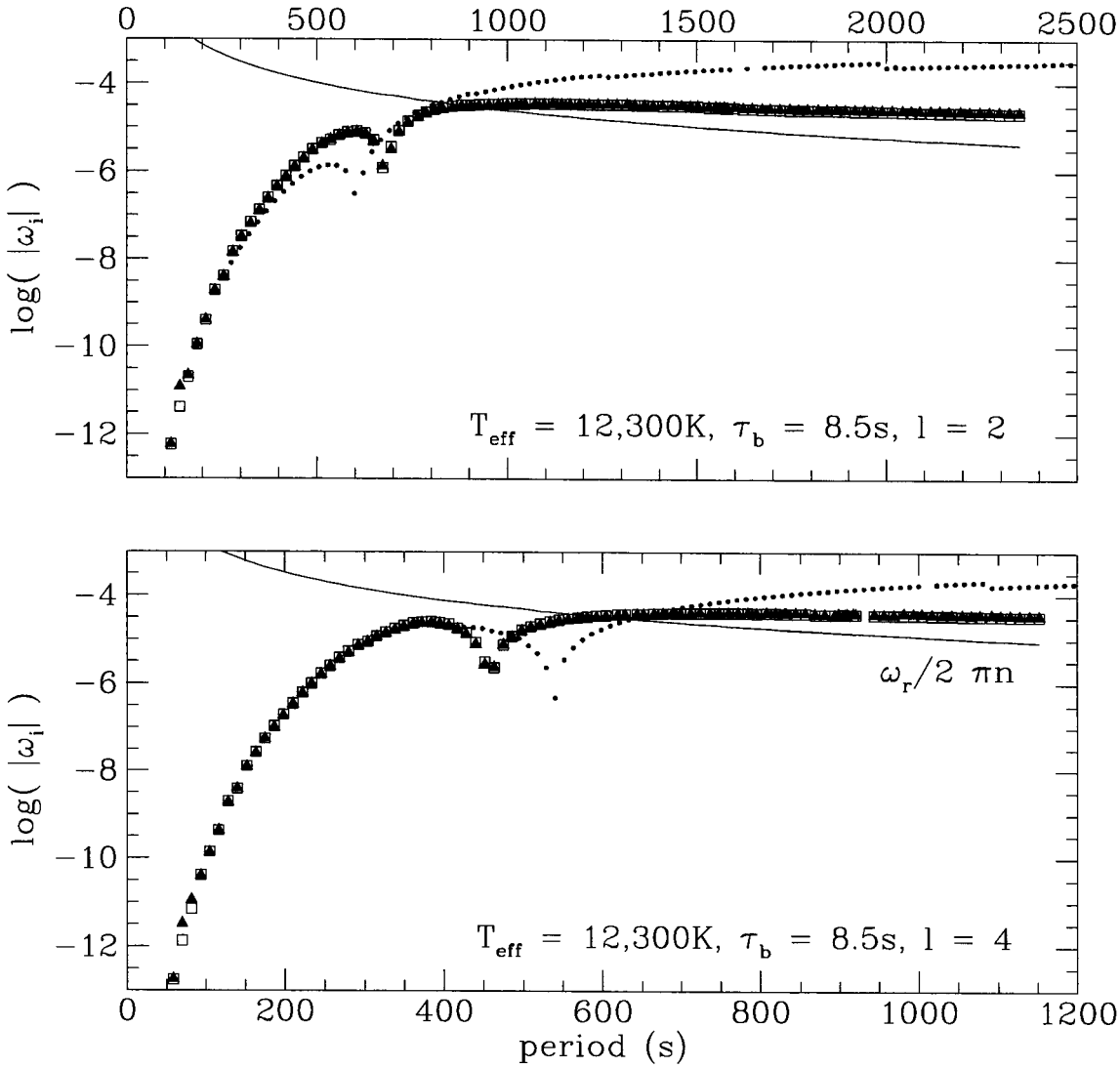

Figure 5.8: Similar to Figure 5.5, but for $\ell = 2$ and $\ell = 4$ modes in a star of $T_{\rm eff} = 12,300\,{\rm K}$ ($\tau_b = 8.5\,{\rm s}$, $\tau_c = 145\,{\rm s}$).

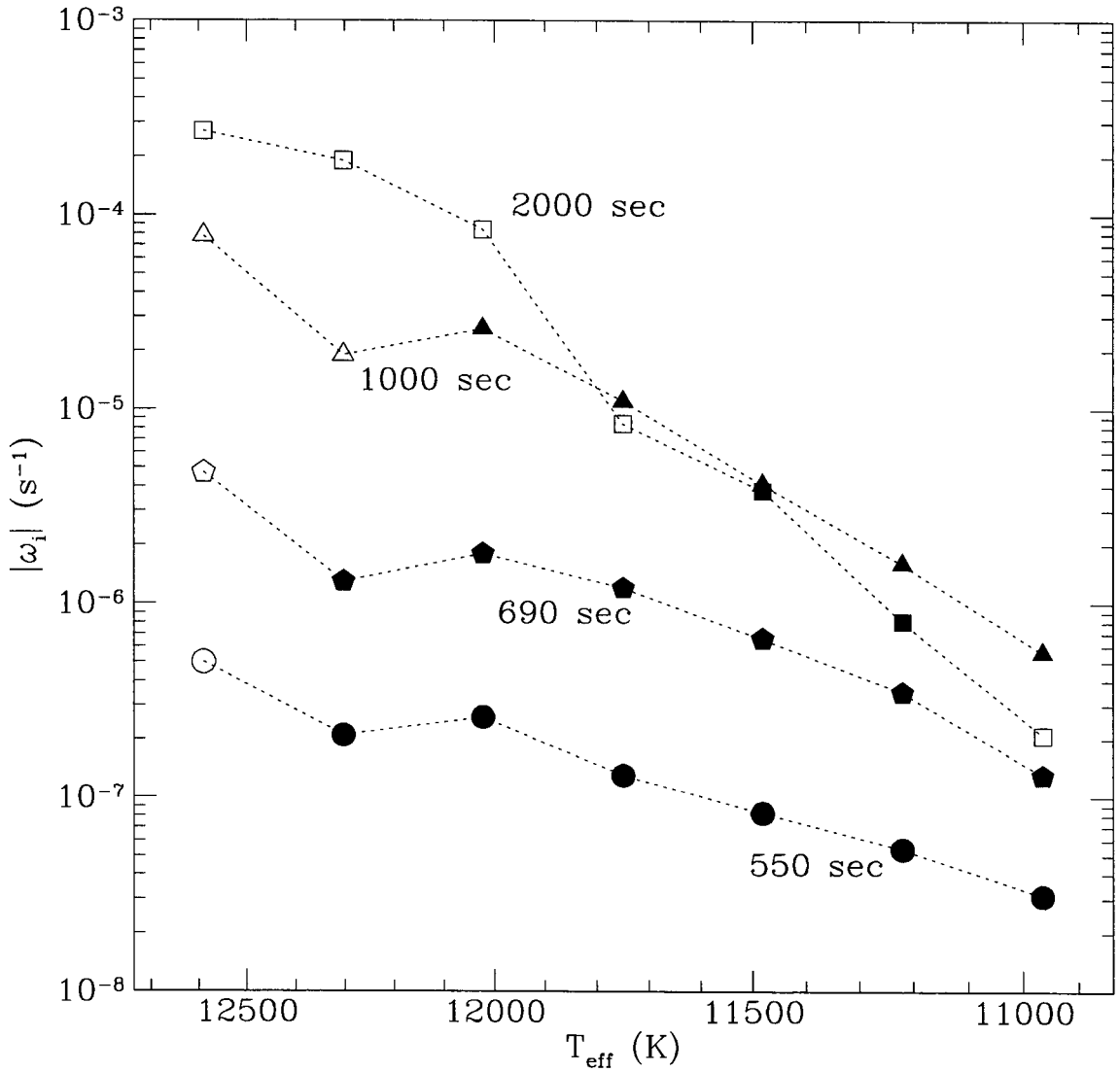

Figure 5.9: Temperature dependence of the driving/damping rates for four $\ell = 1$ modes with periods of 550 s (circles), 690 s (stars), 1000 s (triangles) and 2000 s (squares), respectively. Filled symbols denote overstable modes. The magnitude of ω_i decreases as the convection zone deepens, more markedly for high order than for low order modes. This decrease is explained in equation (2.57).

The value of its $|\omega_i|$ exhibits a steady decline with decreasing $T_{\rm eff}$. This occurs because $\delta p/p$ is constant in the convection zone. Hence as the depth of the convection zone increases, so does the depth of the upper lid of the mode's cavity. Since $|\omega_i| \sim 1/n\tau_{\rm th}$, where $\tau_{\rm th}$ is evaluated at the top of the cavity, it follows that $|\omega_i|$ must decline with decreasing $T_{\rm eff}$.

The 2,000 s mode is weakly overstable in a narrow temperature range from 11,500 K to 11,200 K. For hot stars its $|\omega_i|$ is much smaller than the adiabatic value and saturates around $\omega_r/(2\pi n)$. This is a consequence of the nonadiabatic effect of radiative diffusion which persists all the way down to the top of the mode's cavity. As a result, the reflection coefficient of upward traveling gravity waves is reduced to near zero. These features, which are common to all long period modes, are discussed in more detail below.

A Toy Model For Nonadiabatic Modes

We describe a simple toy model for nonadiabatic modes. It is particularly useful for interpreting damping rates in the limit of strong dissipation.

Consider waves which satisfy the one-dimensional, homogeneous, acoustic wave equation

$$\frac{\partial^2 \xi}{\partial t^2} = c_s^2 \frac{\partial^2 \xi}{\partial z^2}, \tag{5.22}$$

in the interval $0 \leq z \leq L$. Here ξ is the displacement and c_s is the constant sound speed. The dispersion relation connecting frequency, ω, and wave vector, k, reads $\omega^2 = k^2 c_s^2$. The lower boundary is a rigid wall, so

$$\xi(L) = 0. \tag{5.23}$$

Dissipation is introduced by means of a partially reflective upper boundary, where R denotes the ratio of the amplitudes of the incident to reflected waves. This is expressed through the boundary condition at $z = 0$:

$$\left(\frac{\partial}{\partial t} - c_s \frac{\partial}{\partial z}\right) \xi = R \left(\frac{\partial}{\partial t} + c_s \frac{\partial}{\partial z}\right) \xi. \tag{5.24}$$

We write the general solution of equation (5.22) in the form of oppositely traveling waves;

$$\xi = A e^{-i\omega t - ikz} + B e^{-i\omega t + ikz}. \tag{5.25}$$

Application of the boundary conditions given by equations (5.23) and (5.24) yields

$$k_r = \frac{n\pi}{L}, \tag{5.26}$$

where n is the number of half wavelengths between the walls, and

$$\omega_i = \frac{k_i}{k_r}\omega_r = -\frac{\omega_r}{2\pi n}\ln\left(\frac{1}{R}\right), \tag{5.27}$$

where n is an integer.

Equation (5.27) is the key result from our toy model. It demonstrates that ω_i grows logarithmically with R in the limit of strong dissipation ($R \to 0$). Moreover, it clarifies the ω_r/n dependence of ω_i when $R \ll 1$. During each period, the mode loses all the energy stored in the top wavelength of the upward propagating wave.

Equation (5.27) provides a good estimate for the damping rate of strongly nonadiabatic modes in a pulsating star. Radiative diffusion limits the effective reflection coefficients of these modes to small values. This occurs when $\omega\tau_\omega \leq 1$. In hot stars this applies to modes with periods in excess of $1,200\,\mathrm{s}$ (cf. Fig. 5.5).

5.6 Amplitude Saturation By Turbulent Dissipation

A finite amplitude mode generates a turbulent shear layer below the radiative-convective boundary. Energy dissipation in this layer is proportional to the 3/2 power of the mode's energy. Thus it acts to nonlinearly limit the mode's amplitude (cf.§4.5).

We estimate an upper limit to the amplitude of each overstable mode by balancing its linear, nonadiabatic growth rate with its nonlinear turbulent damping rate.[14] This procedure requires assigning a value to the drag coefficient C_D. Terrestrial experiments indicate that C_D depends logarithmically on the ratio of wall roughness to boundary layer width, with values as small as 10^{-3} being characteristic of flows over smooth walls. We might imagine that penetrative convection makes the upper boundary of the shear layer behave like a rough wall, but that is only speculation. Since we have no physical basis for assigning a reliable value to C_D, we treat it as a free parameter subject to the constraint $10^{-3} \leq C_D \leq 10^{-1}$. For example, the choice $C_D = 0.02$ implies an upper limit of $\delta F/F \approx 10\,\mathrm{mma}$ for a $500\,\mathrm{s}$ mode on a $12,300\,\mathrm{K}$ star. As this limit is in accord with observations, we stick with the choice $C_D = 0.02$ in arriving at the estimates presented below.

Upper limits for the photometric amplitudes of overstable g-modes in stars of different temperatures are displayed in Figure 5.10 for $\ell = 1$ modes, and in Figure 5.11 for $\ell = 2$ and $\ell = 4$ modes.[15] The general trends are in accord with the analytic scaling presented in equation (4.31). Namely, $\delta F/F$ declines with increasing P at fixed $T_{\rm eff}$, and rises with decreasing $T_{\rm eff}$ at fixed P.

[14] Realistic limits must await consideration of additional nonlinear, amplitude limiting processes.

[15] These amplitudes do not take into account the effects of limb darkening, inclination, and disc averaging.

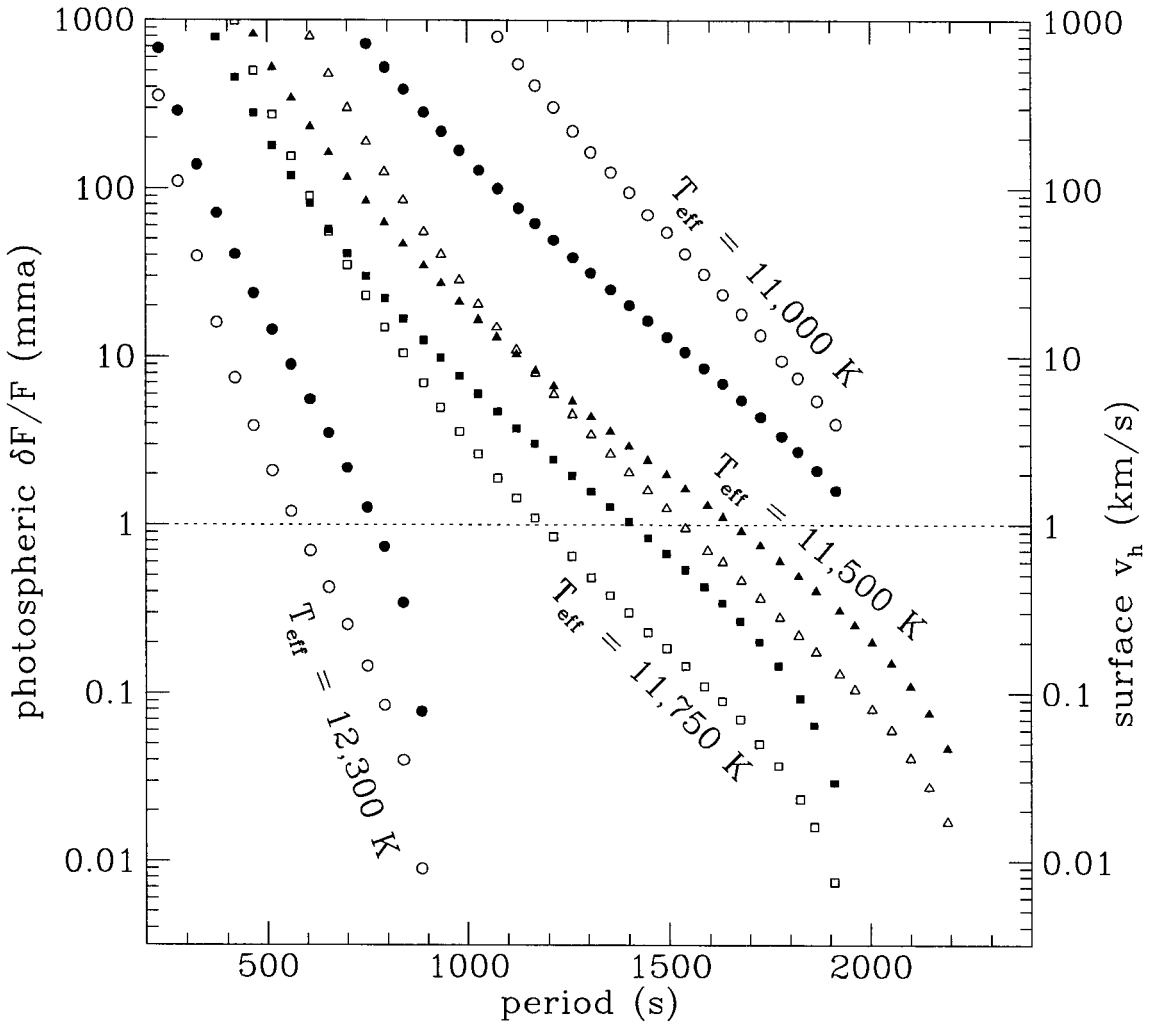

Figure 5.10: Upper limits in pulsation amplitudes due to the turbulent damping below the convection zone. Photospheric flux variations are plotted as solid symbols and horizontal velocities are shown by open symbols. Rough observational limits are set at $\delta F/F > 1$ mma and $v_h > 1\,\mathrm{km\,s^{-1}}$. Note that photometric variations are relatively more observable than velocity variations in the hotter stars, while velocity variations are more observable in the cooler stars. This is due to the deepening of the convection zone and its increasing thermal capacity.

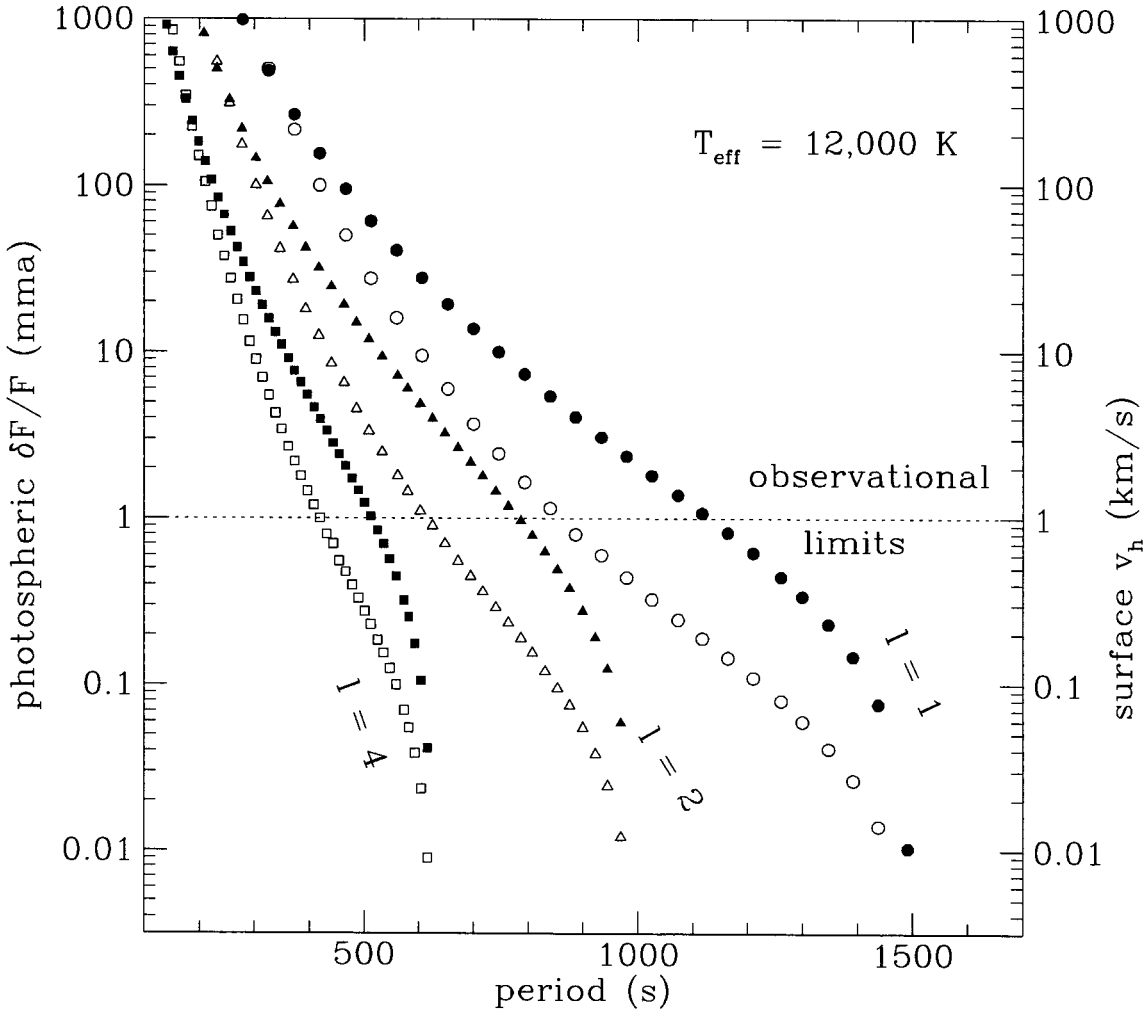

Figure 5.11: Similar to Figure 5.10, but including a comparison between $\ell = 1$, $\ell = 2$ and $\ell = 4$ modes. Amplitude limits decrease with increasing ℓ at fixed period.

5.7 Summary

At this point in my thesis, it is informative to summarize the stage we have reached in our theoretical understanding of ZZ Ceti pulsations.

There seems little doubt that 'convective driving', as originally proposed by Brickhill (1991a), is the correct linear overstability mechanism. Not only is it physically self-consistent, it also offers convincing explanations for observational facts. It accounts in a general way for the location of the instability strip, although a precise specification depends upon the prescription for modeling the convection (e.g., the mixing-length parameter). It shows that as a star cools, the maximum period of its overstable modes increases. Moreover, it makes the testable prediction that velocity variations become relatively more observable than photometric variations towards the red edge of the instability strip.

We confirm, in agreement with Brickhill, that $\omega\tau_c \geq 1$ is a necessary condition for mode overstability. However, we find that it is not a sufficient condition for modes with periods in excess of $1,000\,\mathrm{s}$. This conclusion applies even in the quasiadiabatic limit, and it is strengthened when nonadiabatic effects are fully accounted for. Since $\tau_b \approx 0.05\tau_c$, modes with $\omega\tau_c \approx 1$ are rather nonadiabatic for some distance below the top of the radiative interior. The nonadiabatic region can extend all the way down to the top of the mode's cavity for long period modes.

We also agree with Brickhill's conclusion (1990) that turbulent convection forces the horizontal velocity to be nearly independent of depth within the convective envelope. Consequently, mode damping due to turbulent dissipation within the convection zone is reduced to a negligible level. However, suppression of the horizontal shear in the convective envelope induces a turbulent shear layer at the top of the radiative interior, and dissipation in this layer works towards limiting the mode amplitude.

Our predictions for mode overstability are shown in Figures 5.12. A comparison with observations is given in Figure 5.13

Our nonadiabatic calculations yield a maximum period of about $2,200\,\mathrm{s}$ for overstable modes. This clashes with the maximum period of $1,200\,\mathrm{s}$ for observationally detected modes. It may turn out that this discrepancy is erased by the amplitude limit set by turbulent dissipation on long period modes. Figure 5.13 suggests that this might push the longest period of an observable, overstable mode as far down as $1,000\,\mathrm{s}$. Support for this view comes from a careful look at the figures in Clemens (1993) which show that the photometric amplitudes of modes with periods above $1,000\,\mathrm{s}$ are much smaller than those of modes with periods shorter than $1,000\,\mathrm{s}$. However, at this point it is premature to draw any conclusions. We plan to return to this issue after we have completed our investigation of other amplitude limiting mechanisms.

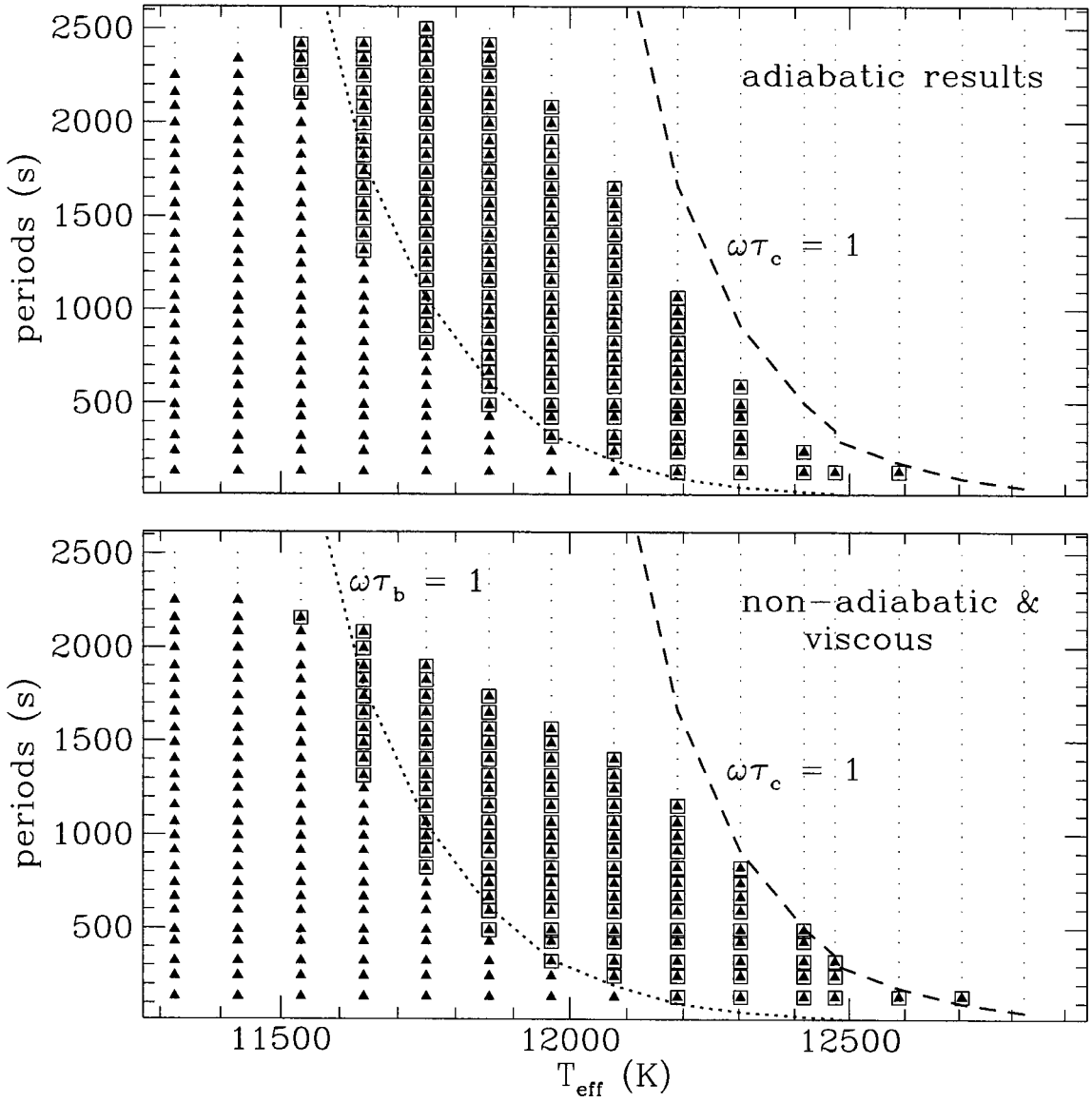

Figure 5.12: Results on mode overstability from quasiadiabatic (upper panel) and fully nonadiabatic (lower panel) calculations. The dots represent fiducial modes from our truncated stellar models which have periods similar to stellar g-modes. Overstable modes are denoted by filled triangles. These are surrounded by open squares if they correspond to modes for which $\omega\tau_c \leq 20$. Recall that the photospheric flux variation is reduced relative to that at the bottom of the convection zone by a factor $[1 + (\omega\tau_c)^2]^{-1/2}$. The long-dashed line corresponds to $\omega\tau_c = 1$, while the short-dashed one to $\omega\tau_b = 1$. Most of the visible overstable modes are nonadiabatic below the convection zone. The nonadiabatic treatment predicts fewer overstable modes than the quasiadiabatic one, but the difference is not large. Nonadiabatic effects are more pronounced in reducing mode growth and decay rates, as shown by §5.5.2.

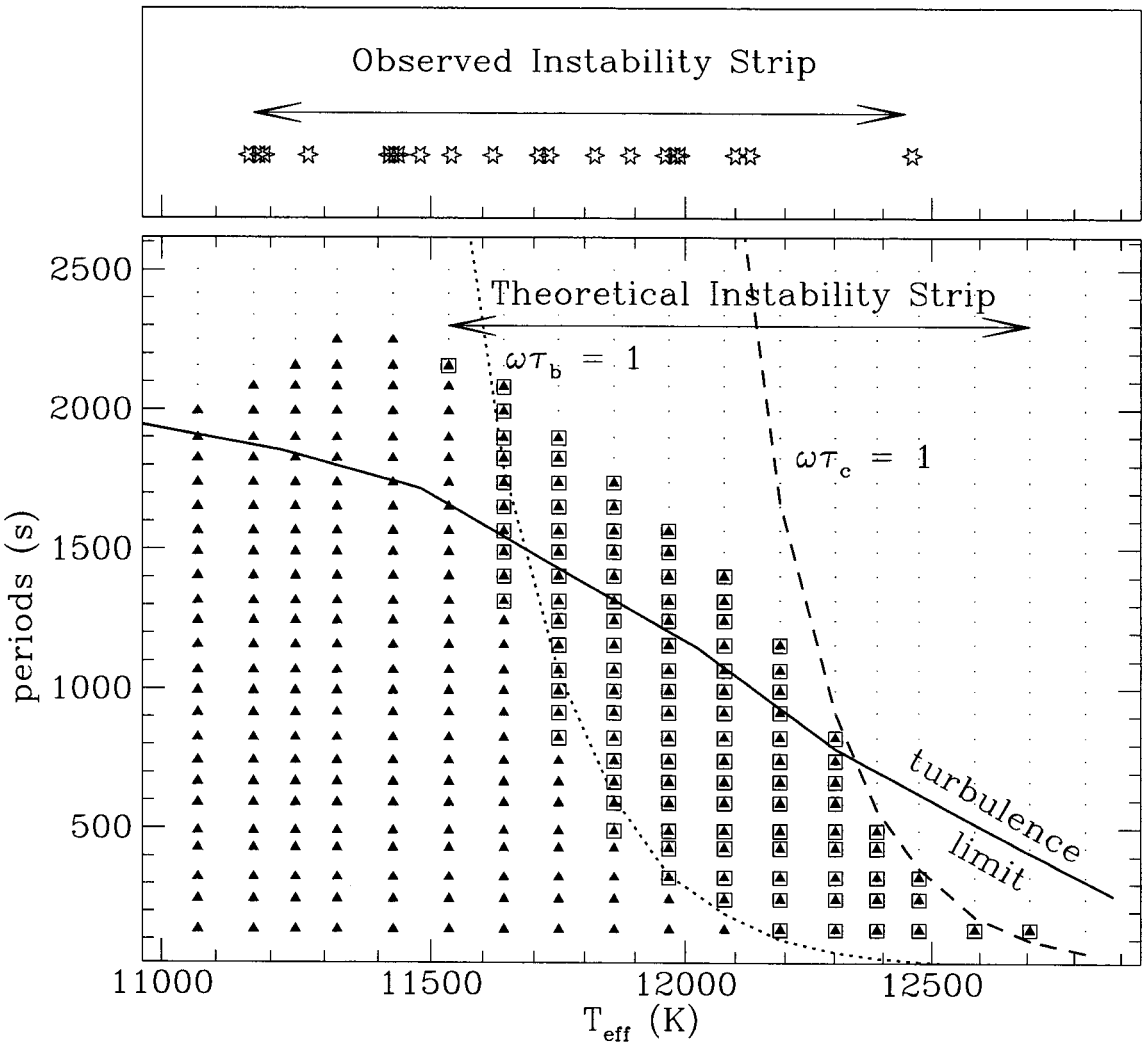

Figure 5.13: Observed and theoretical instability strips for DA white dwarfs. Inferred effective temperatures for all known pulsators are marked in the upper panel (Bergeron et al. 1995). The lower panel repeats the material shown in the lower panel of Figure 5.12. To this we add a solid line denoting the locus of modes for which turbulent dissipation (with $C_D = 0.02$) yields a photospheric flux variation $\delta F/F \approx 10^{-3}$. The blue edge of the theoretical instability strip coincides with the condition that $\omega\tau_c = 1$ for the $(n = 1, \ell = 1)$ mode. At this stage, the location of the red edge (at $\sim 11,600\,\mathrm{K}$) is determined by the visibility and the limited amplitudes of the overstable modes. However, we cannot pin it down until we have a more complete understanding of the nonlinear processes that limit the mode amplitudes. When comparing the locations of observed and theoretical instability strips, one should bear in mind that both depend upon the assumed mixing-lengths.

Bibliography

Bergeron, P., Wesemael, F., Lamontagne, R., Fontaine, G., Saffer, R. A., & Allard, N. F. 1995, ApJ, 449, 258

Brickhill, A. J. 1990, MNRAS, 246, 510

Brickhill, A. J. 1991, MNRAS, 251, 673

Clemens, J. C. 1993, Baltic Astronomy, 2, 407

Press, W. H., Teukolsky, S. A., Vetterling, W. T., & Flannery, B. P. 1992, Numerical Recipes in Fortran, (Cambridge University Press), 403, 753,

Unno, W.,Osaki, Y., & Ando, H. 1989, Nonradial Oscillations of Stars, (University of Tokyo Press), 238

Chapter 6 Nonlinear Mode Coupling: Basics

6.1 Introduction

One of the most interesting results in this thesis is that nonlinear mode coupling can limit the amplitudes of overstable modes in white dwarfs to observed values. This is demonstrated in Chapter 7. Here we present information on nonlinear mode interactions that is needed by nonspecialists to understand the results in Chapter 7.

The hydrodynamical equations are nonlinear in nature. Resonant nonlinear interactions promote exchanges of energy and angular momentum among eigenmodes[1] gravity-modes in a stratified medium is three-mode coupling.[2] In our study, we assume the nonlinearity is weak and restrict ourselves to this lowest order interaction.

In §6.2, the perturbative scheme is realized by transforming the equations of fluid motion into equations describing the amplitude evolution for individual modes. These 'amplitude equations' describe temporal variationd of the complex amplitudes under periodic phase evolution, linear driving/damping and nonlinear mode interactions. The latter involve 'coupling coefficients' which measure the efficiency with which modes interchange energy and angular momentum at given amplitudes. The coupling coefficients are derived from an action principle. The amplitude equations are time-averaged to capture long term variations in mode energy. We call the resulting expressions the 'energy equations'. The amplitude equations and the energy equations are the basic tools we use to study nonlinear mode interactions.

An efficient numerical tool is another important ingredient. We introduce the 'symplectic integrator' (Appendix C) into our study of nonlinear systems. Based on the 'symplectic' (phase-space conserving) nature of a Hamiltonian, an implicit numerical integrator can be constructed to advance the system forward in time. This integrator accurately preserves a time independent Hamiltonian down to the round-off error, and only allows coordinate errors to grow linearly with time. In both attributes, it is superior to conventional integrators. The efficiency of the 'symplectic integrator' is related to its accuracy. The nonlinear systems we are interested in have both a fast and a slow time scale, and all important dynamics takes place on the long time scale. With a 'symplectic integrator', even a low-order one, we can numerically advance the system with a time-step of order the fast time scale (usually the mode periods) while preserving accuracy. This is possible with other integrators only when the order is high. In Appendix C, we also list the extension of 'symplectic integrator' to

[1] The eigenmode analysis is useful when these interactions may be regarded as perturbations.
[2] It is possible for two out of these three modes to be identical modes.

dissipative systems.

Our aim is to understand the statistical energy equilibrium that is reached due to energy transfer from excited modes to damped modes through three-mode couplings. The couplings of interest to us can be classified into two types. One type involves the cataclysmical transfer of energy from a high frequency overstable mode to two lower frequency damped modes; this proceeds due to parametric instability. The other type involves more than one excited mode. Following Dziembowski (1982), we call the latter type 'direct resonance'. In §6.3, we apply the energy equations to derive the energy threshold for parametric instability. Also using the energy equations, we describe the equilibrium state of modes that engage in direct resonance. In a pulsating white dwarf, these two kinds of resonance operate simultaneously. We show in Chapter 7 that parametric instability limits mode amplitudes to the observed range. We suggest that direct resonance is instrumental in modulating these amplitudes into the observed irregular distribution (the behaviour of 'mode selection').

Appendix E is devoted to understanding the intricate dynamics in multi-mode systems ($N > 3$). There, we deal with 'globally' coupled systems, conservative and dissipative. We sought to capture some universality buried inside the complicated dynamics. In particular, we discuss in detail the processes of 'energy equipartition' and 'mode slaving'. The energy equations discussed in this chapter are extensively used there to predict the equilibrium state of these multi-mode systems. In the end of that appendix, we briefly investigate systems that are not globally interacting and are therefore more similar to pulsating white dwarfs.

One important aspect of a system with only cubic nonlinearity is the existence of 'amplitude instability'. This is discussed in detail in Appendix D. Whenever the total energy of a system is larger than some critical value, there *can* be unstable nonlinear growth of mode amplitudes. The kinetic and interaction energies run away towards positive and negative infinity, respectively, with the total energy remains constant. We show that the critical energy is related to the number of modes that are globally interacting.[3] The larger the number of modes, the more stringent in energy this stability criterion becomes. Geometrically, the instability results from the shape of the potential ($\mathcal{H}_3$, the interactive part of the Hamiltonian) for three-mode couplings. This potential is asymmetric in configuration space, with one side sloping down infinitely. The system is hindered from spilling over to infinity only by a small hill, the height of which decreases with the number of modes. This instability has been encountered by others during their investigations of three-mode couplings. But it has never been fully understood and documented. The 'amplitude instability' is not important for pulsating white dwarfs. Whenever a realistic system has energy that exceeds the threshold, it is strongly nonlinear and higher order couplings become as important as three-mode couplings. Also, global coupling as defined above is not realistic for most physical systems since different couplings generally have very different coupling coefficients. Overstable modes in a large system are often

[3]Each mode couples equally strongly to any pair of modes.

separeted into domains within which interactions are strong, with only weak connections between different domains.

6.2 Formulation of Nonlinear Mode Coupling

There are at least two ways to construct equations to describe mode coupling, and to calculate the strength of such an interaction. One method spawns from the equation of motion (as in Dziembowski 1982), the other relies on the systems action. Both methods should give identical results. We adopt the second approach here.

6.2.1 Coupling Coefficients

The Hamiltonian of a system is directly related to its Lagrangian. We derive Lagrangian densities for an adiabatic, inviscid, ideal gas under perturbations. The derivations in this section and §6.2.1 are mostly taken from Kumar & Goldreich (1989). They are included in this thesis for completeness.

An ideal gas with adiabatic index Γ_1, velocity v and potential ψ, has a Lagrangian (Newcomb 1962)

$$L = \int d\vec{x}_0 \rho_0(\vec{x}_0) \left[\frac{v^2}{2} - \frac{p(\vec{x})}{(\Gamma_1 - 1)\rho(\vec{x})} - \psi(\vec{x}) \right], \tag{6.1}$$

where $\vec{x}_0$ and $\vec{x}$ represent the unperturbed and perturbed coordinates respectively. They are related by the Lagrangian displacement vector, $\vec{x} = \vec{x}_0 + \vec{\xi}$. In our application, we neglect perturbations to the gravitational potential ψ, because gravity-modes are strongly concentrated towards the stellar surface and cause mostly horizontal motions.

Mass conservation implies

$$\rho d\vec{x} = \rho_0 d\vec{x}_0, \tag{6.2}$$

and adiabatic perturbations satisfy

$$p\rho^{-\Gamma_1} = p_0 \rho_0^{-\Gamma_1}. \tag{6.3}$$

The Jacobian of the coordinate transform is

$$\mathcal{J} = \det\left(\frac{\partial \vec{x}}{\partial \vec{x}_0}\right) = \det\left(1 + \frac{\partial \vec{\xi}}{\partial \vec{x}_0}\right). \tag{6.4}$$

If the gradients of the displacement are small, we can expand the Jacobian to the third order as

$$\mathcal{J} = 1 + (\nabla \cdot \vec{\xi}) - \frac{1}{2}(\nabla \cdot \vec{\xi})^2 + \frac{1}{3}\xi^{i,j}\xi^{j,k}\xi^{k,i} - \frac{(\nabla \cdot \vec{\xi})}{2}\xi^{i,j}\xi^{j,i} + \frac{1}{6}(\nabla \cdot \vec{\xi})^3. \tag{6.5}$$

When non-Cartesian coordinates (e.g., spherical coordinates) are used, as is often the case, the above derivatives should be thought of as covariant derivatives (i.e., ',' changed to ';').

The expansion of $\mathcal{J}$ yields the second and third orders of the Lagrangian densities:

$$\begin{aligned}
\mathcal{L}_2 &= \frac{\rho_0}{2}\left|\frac{\partial\vec{\xi}}{\partial t}\right|^2 - \frac{p_0}{2}\left[(\Gamma_1-1)(\nabla\cdot\vec{\xi})^2 + \xi^{i,j}\xi^{j,i}\right]; \\
\mathcal{L}_3 &= p_0\left[\frac{(\Gamma_1-1)^2}{6}(\nabla\cdot\vec{\xi})^3 + \frac{(\Gamma_1-1)}{2}(\nabla\cdot\vec{\xi})\xi^{i,j}\xi^{j,i} + \frac{1}{3}\xi^{i,j}\xi^{j,k}\xi^{k,i}\right].
\end{aligned} \tag{6.6}$$

The Hamiltonian density is related to the Lagrangian density by

$$\mathcal{H} = \frac{\delta\mathcal{L}}{\delta\partial_t\xi_i}\partial_t\xi_i - \mathcal{L}, \tag{6.7}$$

which leads to

$$\begin{aligned}
\mathcal{H}_2 &= \frac{\rho_0}{2}\left|\frac{\partial\vec{\xi}}{\partial t}\right|^2 + \frac{p_0}{2}\left[(\Gamma_1-1)(\nabla\cdot\vec{\xi})^2 + \xi^{i,j}\xi^{j,i}\right]; \\
\mathcal{H}_3 &= \mathcal{L}_3.
\end{aligned} \tag{6.8}$$

The second order Hamiltonian density ($\mathcal{H}_2$) represents the sum of the kinetic and potential energy of a harmonic oscillator. For a strictly periodic oscillation, these two parts contribute equally. The third order Hamiltonian ($\mathcal{H}_3$) is the energy in the lowest order interaction.

Any arbitrary perturbation in $\vec{\xi}$ can be projected into linear combinations of eigenmodes,

$$\vec{\xi} = \sum_\alpha (A_\alpha\vec{\xi}_\alpha + A_\alpha^*\vec{\xi}_\alpha^*). \tag{6.9}$$

$\vec{\xi}_\alpha$ and $\vec{\xi}_\alpha^*$ represent the spatial dependence of mode α. Normalized values of these quantities are related to unity mode energy. The complex variable $A_\alpha \propto e^{-i\omega_\alpha t}$, A_α^* is its complex conjugate. A_α has the unit of squared root of energy. Let us denote $\mathcal{R}(A_\alpha) \equiv \frac{1}{2}(A_\alpha + A_\alpha^*)$.

Integrating equation (6.8) over the whole volume gives

$$\begin{aligned}
H_2 &= \int d^3x\mathcal{H}_2 = \sum_\alpha (\mathcal{R}(A_\alpha))^2 = \sum_\alpha E_\alpha; \\
H_3 &= \sum_{\alpha\beta\gamma}\kappa_{\alpha\beta\gamma}\mathcal{R}(A_\alpha)\mathcal{R}(A_\beta)\mathcal{R}(A_\gamma).
\end{aligned} \tag{6.10}$$

Here, the coupling coefficient, κ, has the inverse unit of A_α. And for any triplet combination, κ reads

$$\begin{aligned}
\kappa_{\alpha\beta\gamma} \equiv -\int d^3x\frac{p_0}{6}\Big\{&(\Gamma_1-1)^2(\nabla\cdot\vec{\xi}_\alpha)(\nabla\cdot\vec{\xi}_\beta)(\nabla\cdot\vec{\xi}_\gamma) + \xi_\alpha^{i,j}\xi_\beta^{j,k}\xi_\gamma^{k,i} + \xi_\alpha^{i,j}\xi_\gamma^{j,k}\xi_\beta^{k,i} \\
&+(\Gamma_1-1)\left[(\nabla\cdot\vec{\xi}_\alpha)\xi_\beta^{i,j}\xi_\gamma^{j,i} + (\nabla\cdot\vec{\xi}_\beta)\xi_\gamma^{i,j}\xi_\alpha^{j,i} + (\nabla\cdot\vec{\xi}_\gamma)\xi_\alpha^{i,j}\xi_\beta^{j,i}\right]\Big\}.
\end{aligned} \tag{6.11}$$

The conservation of angular momentum is implicit in the integration over solid angles. The above expression for κ is symmetric under index exchanges, and it includes all non-degenerate terms with proper weights.

6.2.2 Amplitude Equations

The amplitude equations are a set of equations describing the temporal variations of mode energies and phases. These equations can be derived using the action-angle variables (J_1 and ϕ_1), as in Kumar & Goldreich (1989). They are[4]

$$\begin{aligned} \frac{d\phi_1}{dt} &= \omega_1 + \frac{3\omega_1\kappa_{123}}{\sqrt{8}}\sqrt{\frac{E_2E_3}{E_1}}\cos\Phi; \\ \frac{dJ_1}{dt} &= \frac{12s_1\kappa_{123}}{\sqrt{8}}\sqrt{E_2E_3E_1}\sin\Phi, \end{aligned} \tag{6.12}$$

where

$$\begin{aligned} \Phi &\equiv s_1\phi_1 + s_2\phi_2 + s_3\phi_3, \\ E_1 &= \frac{\omega_1 J_1}{2}, \end{aligned} \tag{6.13}$$

and s_1, s_2, s_3 can be $+1$ or -1. The complex amplitude, A_i, is related to the above variables by

$$A_i = \sqrt{E_i}e^{i\phi_i}. \tag{6.14}$$

Here i can be 1, 2, or 3. Summing s_2 and s_3 over $+1$ and -1 (all possible frequency combinations for the same three modes), we obtain the following evolution equation for the amplitudes,

$$\frac{dA_1}{dt} = i\omega_1 A_1 + i\frac{3}{\sqrt{8}}\omega_1\kappa_{123}A^2, \tag{6.15}$$

where $A \equiv \sum_i (A_i + A_i^*)$.

When modes have non-zero driving/damping rates ($\gamma \neq 0$), the system is no longer Hamiltonian. But in the case of weak nonadiabaticity, i.e., $|\gamma| \ll \omega$, we can approximate the amplitude evolution by

$$\frac{dA_1}{dt} = \gamma_1 A_1 + i\omega_1 A_1 + i\frac{3}{\sqrt{8}}\omega_1\kappa_{123}A^2. \tag{6.16}$$

The above equation is our starting point for studying the nonlinear behaviour of multi-mode systems.

[4]Here κ is integrated over volume, instead of radius as is the case in their paper.

6.2.3 Energy Equations

When each mode is oscillating close to its natural frequency (no 'slaving'), we can average out the terms with fast oscillations in equation (6.16), and retain only those terms that vary slowly (the 'resonant terms'). For example, a triplet with frequency closure $s_1\omega_1 + s_2\omega_2 + s_3\omega_3 = \delta\omega \approx 0$ (where s_1, s_2 and s_3 are either $+1$ or -1 depending on the situation) has energy equations of the form,

$$\begin{aligned}
\frac{dE_1}{dt} &= 2\gamma_1 E_1 + \frac{9}{8} s_1\omega_1\kappa^2 \frac{\Gamma}{\Gamma^2 + (\delta\omega)^2} \left(s_3\omega_3 E_1E_2 + s_2\omega_2 E_1E_3 + s_1\omega_1 E_2E_3\right); \\
\frac{dE_2}{dt} &= 2\gamma_2 E_2 + \frac{9}{8} s_2\omega_2\kappa^2 \frac{\Gamma}{\Gamma^2 + (\delta\omega)^2} \left(s_3\omega_3 E_1E_2 + s_2\omega_2 E_1E_3 + s_1\omega_1 E_2E_3\right); \\
\frac{dE_3}{dt} &= 2\gamma_3 E_3 + \frac{9}{8} s_3\omega_3\kappa^2 \frac{\Gamma}{\Gamma^2 + (\delta\omega)^2} \left(s_3\omega_3 E_1E_2 + s_2\omega_2 E_1E_3 + s_1\omega_1 E_2E_3\right). \qquad (6.17)
\end{aligned}$$

Here, $\Gamma = s_1\gamma_1 + s_2\gamma_2 + s_3\gamma_3$, and $|\Gamma| \sim \mathrm{Max}(|\gamma_1|, |\gamma_2|, |\gamma_3|)$; κ is the coupling coefficient for this triplet. The factor $\Gamma/[\Gamma^2 + (\delta\omega)^2]$ represents the reduction in coupling strength when the interaction occurs in the Lorentzian wing. A detailed derivation of the energy equations can be found in Appendix F.

Expectation values for mode energies are estimated by setting the left-hand sides of the above equations to zero, and solving for E_1, E_2 and E_3 simultaneously. For conservative systems ($\gamma_i = 0$), the equilibrium state of a resonant system is obviously $E_1 = E_2 = E_3$. This is energy equipartition, about which we will discuss in more detail in §E.2.

6.3 Two Types of Three-mode Couplings

In this section, we discuss the dynamics and equilibrium states of three-mode couplings.

6.3.1 Parametric Instability

Parametric instability involves one excited mode (mode 1) and a pair of modes (modes 2 and 3) with negligible energy, where the frequency condition is $\omega_1 - \omega_2 - \omega_3 = \delta\omega \approx 0$. We call ω_1 the parent mode, while the other two its 'daughter modes'. For simplicity, we assume the daughter modes are damped with rates $\gamma_2 \sim \gamma_3 < 0$, while mode 1 is either (i) excited, but $\gamma_1 \ll |\gamma_2|$; or (ii) neutral ($\gamma_1 = 0$), but with much larger initial energy than its daughter modes. The line-width of this coupling $\Gamma \sim 2|\gamma_2|$. In both cases, we have $E_1 \gg E_2 \sim E_3$, and the term E_2E_3 in the right-hand side of equation (6.17) can be neglected.

If the parent mode's energy exceeds a threshold, E_{para}, the energy of the daughter modes grows exponentially. This is parametric instability. Here we derive E_{para} in the simplest case of identical daughter modes: $\omega_2 = \omega_3 \approx \omega_1/2$, $\gamma_2 = \gamma_3$. Since the instability develops on a time scale much

longer than the mode periods, we consider the energy equations (6.17). For the daughter mode,

$$\begin{aligned}\frac{dE_2}{dt} &= 2\gamma_2 E_2 + \frac{9}{8} s_2\omega_2\kappa^2 \frac{\Gamma}{\Gamma^2+(\delta\omega)^2}\left(s_3\omega_3 E_1E_2 + s_2\omega_2 E_1E_3 + s_1\omega_1 E_2E_3\right) \\ &\approx 2\gamma_2 E_2 + \frac{9}{16}\omega_1^2\kappa^2 \frac{(-2\gamma_2)}{(2\gamma_2)^2+(\delta\omega)^2} E_1E_2. \end{aligned} \tag{6.18}$$

Mode 2 can be excited whenever

$$E_1 \geq \frac{16}{9\kappa^2}\left[\left(\frac{2\gamma_2}{\omega_1}\right)^2 + \left(\frac{\delta\omega}{\omega_1}\right)^2\right]. \tag{6.19}$$

Except for notation, this result is identical to equation (27.12) in Laudau & Lifshitz (1976). The existence of an energy threshold for exciting modes 2 and 3 justifies the word 'instability'.

In a general three mode system where parametric instability is the only interaction, equation (6.17) can be solved to yield the equilibrium energy for all three modes. We obtain a similar relation for near-identical daughter modes as in equation (6.19). Mode 1 excites its daughter modes whenever its energy exceeds a critical value, and this critical value is also the mean energy for mode 1, independent of whether this mode is neutral or overstable.

The relevant amplitude equations are numerically integrated to confirm the above results. We obtain satisfactory comparison, as is shown by Figure 6.1 for both $\gamma_1 > 0$ and $\gamma_1 = 0$.

Analytical calculation shows that the equilibrium system is unstable to small perturbations when $|\gamma_2| \geq \gamma_1/2$. This is confounded by the fact that we cannot find a physical solution for mode energy using equation (6.17) when $|\gamma_2| < \gamma_1/2$.

Moreover, in numerical simulations, we observe that when $|\gamma_2|/\gamma_1 < a_{\min}$, where $a_{\min}$ is of order 4 to 10, the system never reaches stable energy equilibrium as the kind predicted in equation (6.19). This is because that under these circumstances, the assumption of $E_2 \sim E_3 \ll E_1$ is broken down.

We also investigate the time-dependent behaviour of these systems. We find that neutral and overstable parent modes result in different dynamics (Fig. 6.2), even though equation (6.19) predicts a similar equilibrium state. In the case of $\gamma_1 = 0$, energy transfer stops after mode 1 decays to the level described by equation (6.19). This is characteristic of an instability, where there is energy transfer only when some stability criterion is violated. In the case of $\gamma_1 > 0$, energy of the parent mode grows linearly until it reaches the same limit, then it parametrically loses energy to the two daugther modes. The system descends into a limit-cycle. Then equation (6.19) is better regarded as giving the time-averaged energy in the parent mode.

The conclusion from these numerical experiments is that equation (6.19) describes the instability threshold as well as the average energy of a parametric system. In a dissipative system, the dynamics is that of a limit-cycle type.

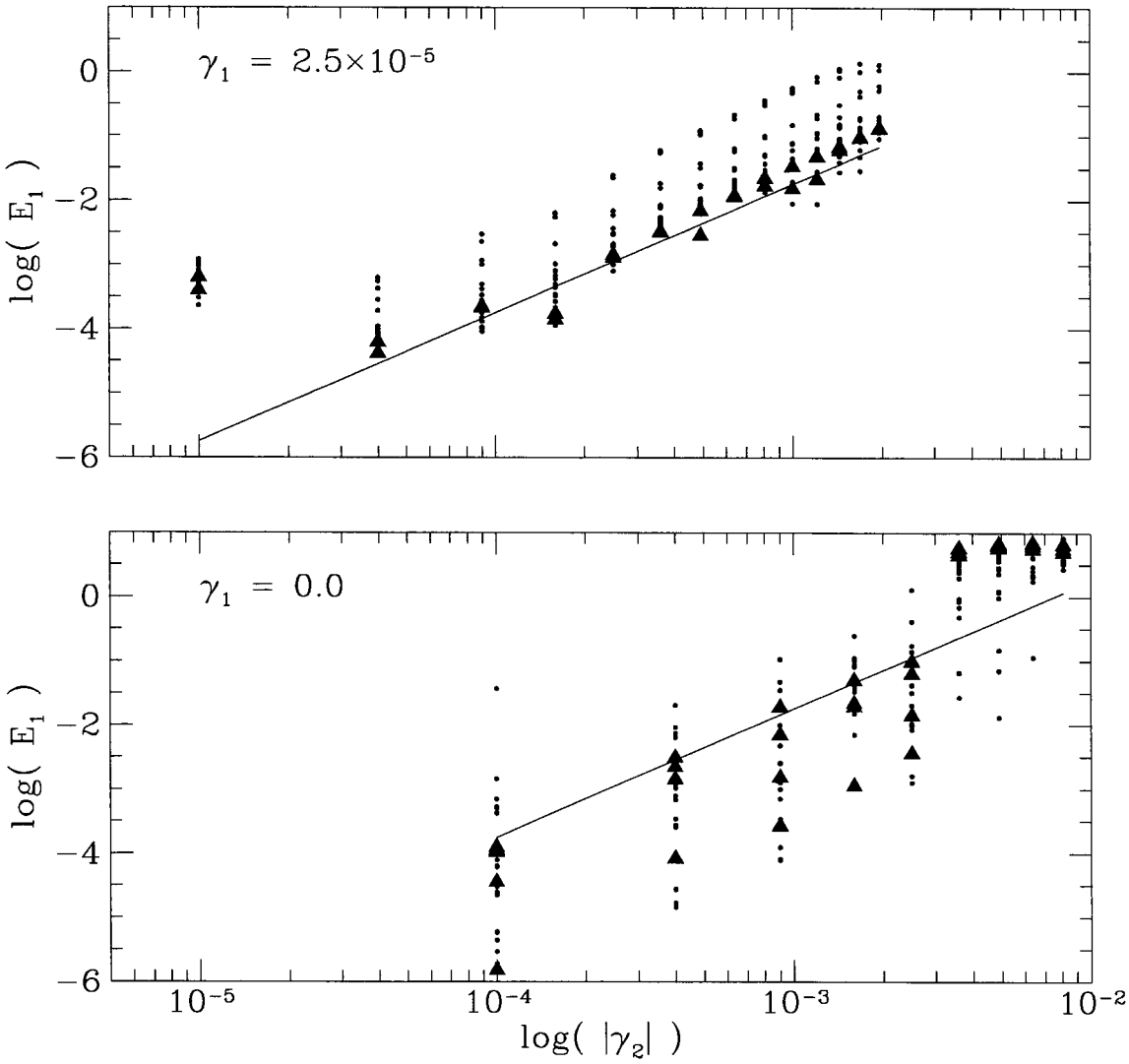

Figure 6.1: Equilibrium energy in mode 1 obtained from numerical integration of the amplitude equations (in triangles and dots) is compared here with that predicted by equation (6.19) (straight lines) in systems vulnerable to parametric instability. The daughter modes are randomly selected, with $|\omega_2 + \omega_3 - \omega_1| \leq \Gamma$. The triangles represent pairs satisfying $|\omega_2 - \omega_3| < 0.05$, and dots are other pairs. In the upper panel, these near-identical daughter pairs give rise to the lowest equilibrium energy, which are well fitted by the straight line. The systems cannot reach reach energy equilibrium through parametric instability when $|\gamma_2| \leq \gamma_1/2$, and the growth in mode 1 is undeterred. In the lower panel, mode 1 is not excited. Its energy starts from a high value and is later limited to a value below the straight line when the daughter modes are identical, and slightly higher when they are not. The approximation of weak dissipation breaks down when $|\gamma_2| \geq 3 \times 10^{-3}$, therefore the deviation. Here, we show the time average of $\log E_i(t)$ instead of $E_i(t)$, and we set $\kappa = 1$.

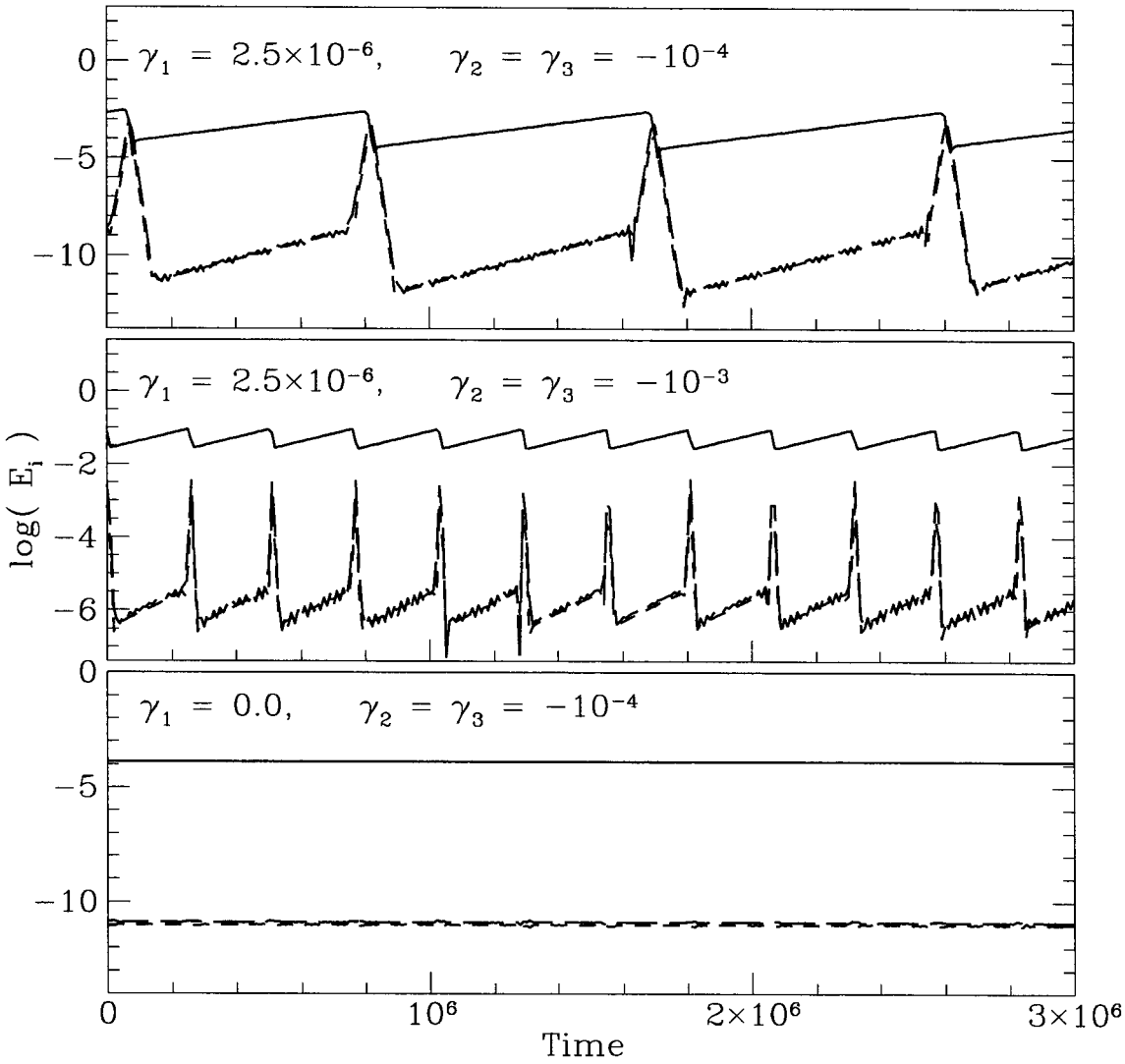

Figure 6.2: Different time-dependent behaviour of parametric instability in various systems. The solid line shows the energy of mode 1, the dashed lines that of the daughter modes. All three cases have $\omega_1 = 0.5, \omega_2 = 0.102, \omega_3 = 0.398$, so $\delta\omega = \omega_1 - \omega_2 - \omega_3 \ll |\gamma_2|$. The upper and the middle panels illustrate a limit-cycle behaviour that occurs when $\gamma_1 > 0$. The two relevant time-scales here are the growth time for the parent mode and the damping time for its daughters. The lower panel shows that for $\gamma_1 = 0$, mode 1 settles into a constant equilibrium state after it reaches the threshold value (eq. [(6.19)]). Here, $\kappa = 1$.

6.3.2 Direct Resonance

In the above parametric resonance ($\omega_1 - \omega_2 - \omega_3 \sim 0$), when one of the daughter modes is also overstable and has appreciable energy (let this be mode 2), the interaction is called 'parametric down-conversion', and it is one of the three types of direct resonance that we are interested in. Assume mode 2 is limited in energy by parametric instability with another pair of daughters. The energy equations for these modes are,

$$\begin{aligned}
\frac{dE_1}{dt} &\approx 2\gamma_1 E_1 - \frac{9}{8}\omega_1\omega_3\kappa_1^2\frac{\Gamma_1}{\Gamma_1^2+(\delta\omega)_1^2}, \\
\frac{dE_2}{dt} &\approx 2\gamma_2 E_2 + \frac{9}{8}\omega_2\omega_3\kappa_1^2\frac{\Gamma_1}{\Gamma_1^2+(\delta\omega)_1^2} - \text{damping from its daughters}, \\
\frac{dE_3}{dt} &\approx 2\gamma_3 E_3 + \frac{9}{8}\omega_3^2\kappa_1^2\frac{\Gamma_1}{\Gamma_1^2+(\delta\omega)_1^2},
\end{aligned} \tag{6.20}$$

where $\Gamma_1 = \gamma_1 - \gamma_2 - \gamma_3$, $(\delta\omega)_1 = \omega_1 - \omega_2 - \omega_3$. The energy of mode 3 is obviously restricted around an equilibrium value that depends on $E_2 E_3$. This coupling effectively increases the driving rate for mode 2, while it effectively reduces the rate for mode 1. Moreover, when mode 2 has energy large enough to excite its daughters (see eq. [6.19]),

$$E_2 \geq \frac{16}{9\kappa_2^2}\left[\left(\frac{\Gamma_2}{\omega_2}\right)^2 + \left(\frac{\delta\omega_2}{\omega_2}\right)^2\right], \tag{6.21}$$

we have

$$\begin{aligned}
\frac{dE_1}{dt} &\approx \left[2\gamma_1 - 4\Gamma_1\frac{\kappa_1^2}{{\kappa_2}^2}\frac{\Gamma_2^2+(\delta\omega)_2^2}{\Gamma_1^2+(\delta\omega)_1^2}\right]E_1, \\
&\approx \left[2\gamma_1 - 4\Gamma_1\frac{\gamma_1}{\gamma_2}\frac{n_2^2}{n_1^2}\frac{\Gamma_2^2+(\delta\omega)_2^2}{\Gamma_1^2+(\delta\omega)_1^2}\right]E_1,
\end{aligned} \tag{6.22}$$

where we have used the scaling law $\kappa^2 \sim 1/(n^3 L\tau_\omega) \sim \gamma/n^2$ for modes 1 and 2. Equation (6.22) in many cases predicts that mode 1 is nonlinearly damped. Or, parametric down-conversion preferentially suppresses high frequency modes.

The second type of direct resonance happens when all three modes are overstable, $\omega_1 \pm \omega_2 \pm \omega_3 \sim 0$. We can assume all three modes have amplitude upper-limits determined by some other mechanism, e.g., parametric instability, and study the effect of such interaction. We see colourful outcomes and lively dynamics. The direction of the energy flow at any moment is approximately towards energy equipartition.

The third type of direct resonance happens for $\delta\omega = \omega_1 + \omega_2 - \omega_3 \sim 0$, where mode 3 is damped, and modes 1 and 2 are overstable. The latter two lose energy to mode 3 at a rate of $\sim \omega^2\kappa^2\Gamma/[\Gamma^2 + (\delta\omega)^2]E_1E_2$. This is simulated and discussed in §E.3.1. The dispersion relation of gravity-modes implies that this type of interaction is likely to be rare as it is difficult to find good

frequency resonance.

We believe the first two types of interaction are largely responsible for producing the observed irregular energy distribution among white dwarf eigenmodes. They also introduce chaotic time dependences. It is likely that the variability time-scale is of order the mode's growth time, which ranges from 10^6 years for the lowest order ($n = 1$, period $\sim 130\,\mathrm{s}$) mode to of order a day for the highest order ($n \sim 25$, period $\sim 1500\,\mathrm{s}$) overstable modes.

Bibliography

Dziembowski, W. 1982, Acta Astronomica, 32, 147

Kumar, P., & Goldreich, P. 1989, ApJ, 342, 558

Landau, L. D., & Lifshitz, E. M. 1976, Mechanics, Third Edition, (Pergamon Press), 80

Newcomb, W. A. 1962, Nuclear Fusion: Supplement Part 2, (Vienna: International Atmoic Energy Agency), 451

Chapter 7 Amplitudes of White Dwarf Pulsations

7.1 Introduction

Multi-mode pulsators (including variable white dwarfs, δ Scuti stars, β Cepheids, variable Ap stars) are observed to have pulsation amplitudes that are much lower than those of the classical variables, such as Cepheids, RR Lyraes, etc. There are two main differences between these two groups of pulsators besides their amplitudes. Members of the second group usually pulsate in their fundamental or low overtone radial modes, and the density of modes in this frequency range is small; in contrast, the first group pulsates with radial and/or non-radial modes, and the density of available modes is usually higher. The small amplitude pulsators also tend to show fluctuations in amplitudes and phases, while the larger ones appear to change their pulsational behaviour only on the time scale of stellar evolution.[1] These characteristics point to different amplitude-limiting mechanisms in the two groups.

For Cepheids and RR Lyraes, the amplitude of excited modes is likely to be limited by their distortion of the driving environment. Stellar luminosity is converted into mode energy in the driving region until the gas property in this region has been significantly disturbed and the region becomes neutral to pulsation. Amplitudes in this case are invariably large, with fractional light variations of order 10% or higher.

For low amplitude pulsators, the relatively high density of modes suggests that nonlinear mode coupling may be responsible for amplitude saturation. Overstable modes gain energy from the driving region, lose it to other modes via mode interaction, and maintain an approximate equilibrium at the observed amplitudes. The lowest order couplings,[2] three-mode couplings, are most effective in transporting energy across the modes. Properties of three-mode coupling are explored in Chapter 6 and extensively studied in Appendix E.

In this chapter, we focus on parametric instability. In the present context, it refers to a three-mode coupling that involves *one* overstable parent mode and two daughter modes each having

[1] There are, however, reports of mode-switching in these pulsators, which may be a counter-example to this statement.

[2] Under the constraints of energy and angular momentum conservation, gravity-waves propagating in a stratified medium can have three-mode and higher order couplings. In the case of gravity-waves on the surface of homogeneous fluid (e.g., water waves), the lowest order coupling involves four modes, described by $\omega_1 + \omega_2 \rightarrow \omega_3 \pm \omega_4$, similar to the process of phonon-phonon scattering in thermal conduction. Three-mode coupling, on the other hand, is analogous to the process of photon emission or absorption.

roughly half the parent mode's frequency. We stick to the word 'instability', as it describes accurately the nature of this interaction, specifically, the existence of a threshold criterion. We show here that parametric instability can limit the amplitudes of gravity-modes to the observed values. We adopt the observational unit of mma (milli-modulation-amplitude: fractional variation in light of 0.1%) for mode amplitudes.

We briefly discuss another type of three-mode coupling, direct resonance, where at least two out of the three modes are overstable. This process is far less accommodating to analytical study than parametric instability. In a pulsating white dwarf, the number of overstable modes is large, and every overstable mode can be involved in many such direct resonances, all of them combining to affect the amplitudes, leading to the observed 'mode selection'. Even if we can single out the most important resonance, it is still hard to estimate mode amplitudes in such a resonance, as is demonstrated by experiments in §E.3. Here, we will argue that direct resonance is capable of modulating mode amplitudes and causing irregularities in the amplitude distribution.

With every overstable mode involved in many resonant interactions, phase coherence inside each triplet is randomized, leading to stochastic variations of mode amplitudes. We argue in Chapter 6 that the time scales of these variations are likely to be related to the linear growth time for these modes, consistent with reports of longer period modes having more rapid fluctuations.

Here, we need to mention the pioneering work by Dziembowski & Krolikowska (1985) in δ Scuti stars. Based on parametric interaction between pressure-modes and gravity-modes, they produced amplitude estimates that are consistent with the observed values. Our work demonstrates that nonlinear interactions can also be responsible for limiting mode amplitudes to a few percent or lower in pulsating white dwarfs. As most low amplitude pulsators have similar amplitudes, it is not unreasonable to suspect that parametric instability is important in many of them.

Nonlinear mode coupling may not be the only mechanism in limiting mode growth. Chapter 4 demonstrates that the turbulent layer at the convective-radiative boundary, produced by the horizontal velocity shear, may also provide interesting limits to pulsation amplitudes for long period modes.

7.2 Coupling Coefficients for Parametric Instability

Let mode 1 be the parent mode, while 2 and 3 be the daughter modes. The strength of the interaction between parent and daughter modes depends upon the magnitude of the relevant coupling coefficient, the degree to which frequency resonance, $\omega_2 + \omega_3 \approx \omega_1$, is satisfied, and the decay rates of the daughter modes. We consider parent modes of low spherical degree, $\ell = 1$ or 2, since these are the ones that are accessible to photometric observations.

Several methods for numerically calculating the coupling coefficients are described in detail in

Appendix G. Results from the integration-by-parts method (Appendix G.2.3), which we consider the most reliable, are summarized below. These are based on adiabatic eigenfunctions obtained for white dwarf models provided by P. Bradley. The essential characteristics of these models are $M_* = 0.6 M_\odot$, $\log g \approx 8.0$, hydrogen layer mass $M_H \sim 10^{-4} M_\odot$, and helium layer mass $M_{He} \sim 10^{-3} M_\odot$. Most of the numerical results presented in this section apply to a model with $T_{\rm eff} = 12,800\,{\rm K}$ for which $\tau_b = 1\,{\rm s}$. This white dwarf lies close to the blue edge of the ZZ Ceti instability strip.

First, we show that for the same parent mode, the magnitude of the coupling coefficient κ depends upon the similarity between the radial structure of the two daughter modes (Fig. 7.1). The dominant interaction region between parent and daughter modes is the broad region above the top of the parent mode's cavity, $z < z_{\omega 1}$. The radial integrand of κ ($d\kappa$, where $\kappa = \int d\kappa$) peaks just above $z_{\omega 1}$ and declines steeply below it. Contributions from different nodes of the daughter modes add coherently provided

$$\frac{\omega_2^2}{\ell_2(\ell_2+1)} \approx \frac{\omega_3^2}{\ell_3(\ell_3+1)}. \tag{7.1}$$

This condition ensures that $z_{\omega 2} \approx z_{\omega 3}$, and $k_{z2} \approx k_{z3}$ for $z < z_{\omega 1}$. From the dispersion relation for white dwarf g-modes (see §2.4.1), it follows that equation (7.1) corresponds to $n_2 \approx n_3$; so $|n_2 - n_3|$ measures the radial similarity of the pair of daughter modes. The number of radial nodes above $z_{\omega 1}$ in modes 2 and 3 are roughly $n_2' \sim n_2/n_1$ and $n_3' \sim n_3/n_1$. There is insignificant cancellation from different nodes when

$$|n_2 - n_3| \leq n_1. \tag{7.2}$$

Within this tolerance, the magnitude of the coupling coefficient remains close to its peak value as indicated by Figure 7.1. The asymmetry of κ about $|n_2 - n_3| = 0$ is an unexplained feature of this figure. The sign of κ is analgous to the direction of the force. This direction varies among different triplets and eliminates the possibility for amplitude instability (see Appendix D) in a pulsating star.

Second, we demonstrate that the peak value of κ for a given parent mode does not depend on the spherical degrees of its daughter pairs. Here, the angular momentum selection rule, $\ell_3 \in [|\ell_1 - \ell_2|, \ell_1 + \ell_2]$ and ${\rm Mod}[(\ell_3 - \ell_2 - \ell_1), 2] = 0$, has to be satisfied (see Appendix G). The numerical results showing the independence are plotted in Figure 7.2, while §G.3 demonstrates the independence analytically for incompressible fluid. Physically, the lack of dependence of the peak value of κ on ℓ_2 and ℓ_3 follows because the only property of radially similar daughter modes that affects κ is the fraction of their mass that lies above $z_{\omega 1}$. And this fraction, $n_2'/n_2 \approx n_3'/n_3 \approx 1/n_1$, is independent of ℓ_2 and ℓ_3. Because the decay rates of damped modes increase with increasing ℓ at fixed ω, this result implies that the daughter pairs which limit the amplitudes of low ℓ parent modes have modest values of ℓ.

Third, we compare maximum coupling coefficients for different parent modes. These are plotted in Figure 7.3. With increasing n_1, $|\kappa|$ rises steeply as a consequence of the rapid decrease in parent

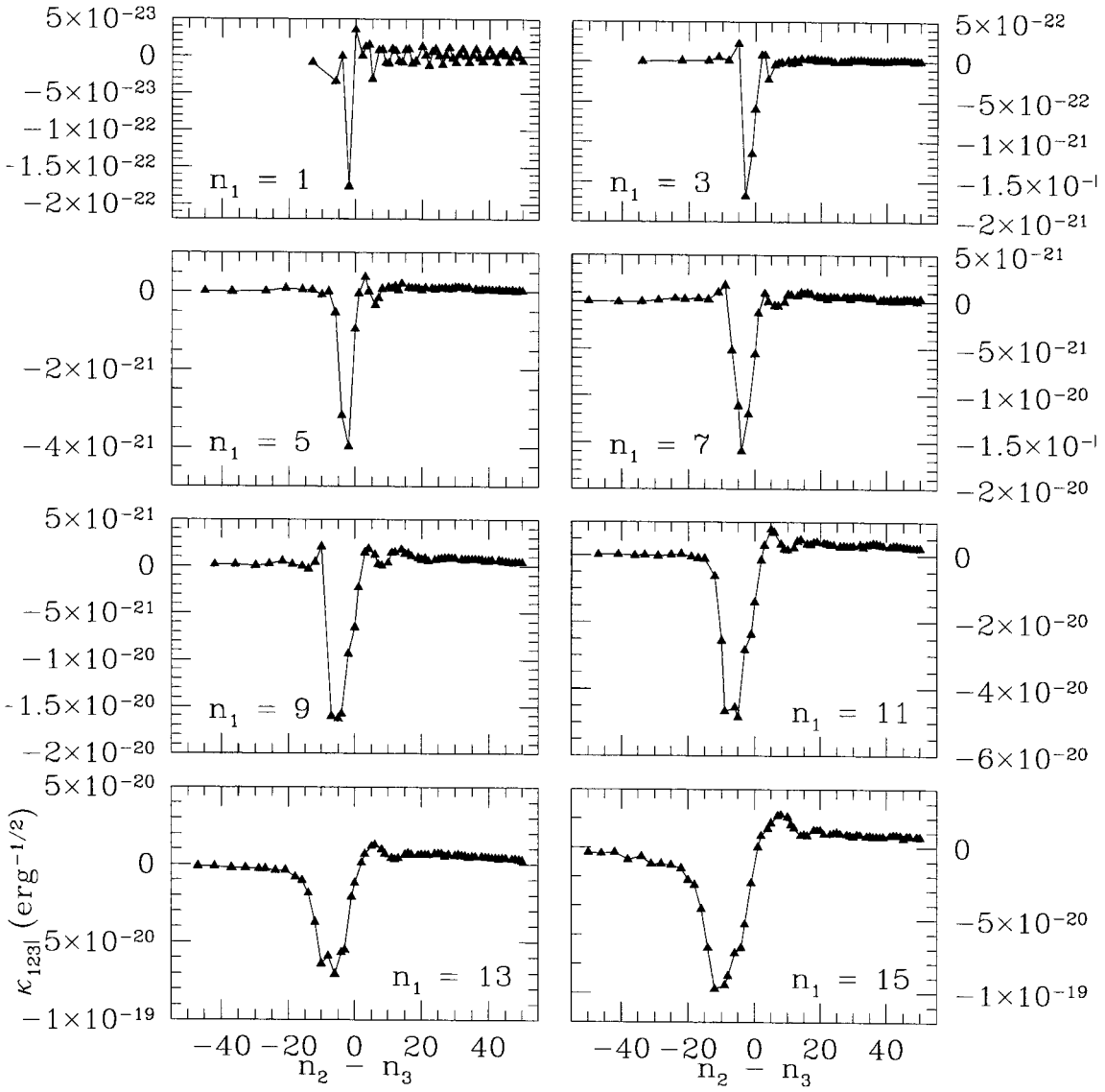

Figure 7.1: Values of coupling coefficients κ are plotted as functions of $|n_2 - n_3|$, a measure of the radial similarity between the daughter modes. We take $\ell_1 = 1$, $\ell_2 = 1$, $\ell_3 = 2$. However, this choice is not restrictive; κ exhibits similar behaviour for other choices of ℓ_2 and ℓ_3. For each daughter mode $(n_2, \ell_2 = 1)$, the second daughter mode $(n_3, \ell_3 = 2)$ is chosen to best satisfy the frequency resonance condition, $\omega_3 \approx \omega_1 - \omega_2$. The width of the peak in κ increases with increasing n_1 as predicted by equation (7.2). These calculations are based on a DA model with $T_{\rm eff} = 12,800\,{\rm K}$. The dimension of κ is $\mathrm{erg}^{-1/2}$.

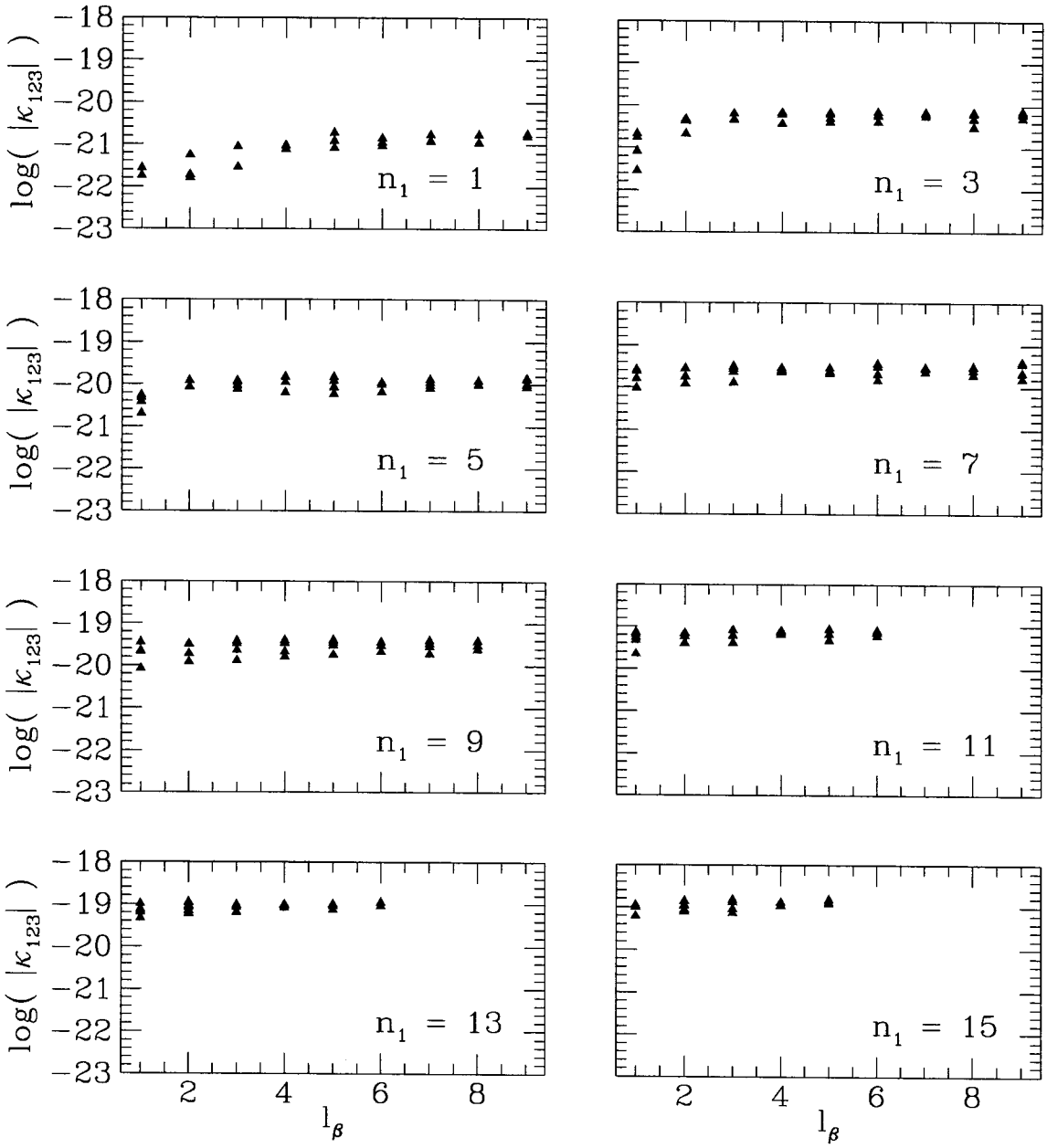

Figure 7.2: The lack of dependence of coupling coefficient κ on the spherical degree ℓ_2 of daughter mode 2. Here $\ell_1 = 1$, and $\ell_3 = \ell_1 + \ell_2$. For each ℓ_2, we choose the pair of resonant daughter modes that couples most strongly to its parent mode. These calculations are based on a DA model with $T_{\rm eff} = 12,800\,{\rm K}$.

mode mass. More specifically, the maximum coupling coefficients scale according to the analytic estimate arrived at by equation (G.29) in Appendix G.

The principal conclusions from this section are: κ peaks for $|n_2 - n_3| \leq n_1$; its peak values are independent of daughter modes' ℓ values, and it scales with n_1 as predicted by equation (G.29). Each of these three results will have bearing on the theoretical predictions for mode amplitudes.

7.3 Amplitudes Limited by Parametric Instability

Here we estimate amplitudes for overstable modes by assuming that they are limited by parametric instability. The daughter modes are assumed to be weakly damped, that is to have decay rates $\gamma \ll \omega/2\pi n$. This is equivalent to assuming high reflectivity at the upper lid of the daughter mode cavity. The opposite case of low reflectivity is treated in the following section.

Each overstable mode can be involved in couplings to many pairs of daughter modes. The parametric amplitude of a parent mode is defined as that at which parametric instability arises within one pair of daughter modes. We suggest that upper limits to the observed amplitudes are associated with the parametric amplitudes arising from the most efficient daughter pairs.[3]

Following equation (6.19), the parametric amplitude satisfies

$$A \sim \frac{1}{|\kappa|}\sqrt{\left(\frac{\delta\omega}{\omega}\right)^2 + \left(\frac{\Gamma}{\omega}\right)^2}, \tag{7.3}$$

where κ, $\delta\omega = |\omega_1 - \omega_2 - \omega_3|$, and Γ are the coupling coefficient, frequency detuning, and effective line-width between the parent mode and the crucial pair of daughter modes.

Consider an $\ell = 1$ parent mode. For each choice of ℓ_2, there are of order n_1 pairs of daughter modes for which κ is close to its peak value, and Γ is near its minimum at that value of ℓ_2. The maximum frequency detuning $\delta\omega$ among these triplets is of order half the period spacing among the daughter modes,

$$\delta\omega \sim \frac{\omega_2}{2n_2} \sim \frac{\omega_1}{4\ell_2 n_1}. \tag{7.4}$$

This estimate indeed falls above all actual values of $\delta\omega$, as is shown in Figures 7.4 and 7.5. Statistically, the minimum value of $\delta\omega$ among the n_1 triplets is expected to be of order

$$\delta\omega_{\min} \sim \frac{\delta\omega}{n_1} \sim \frac{\omega_1}{4\ell_2 n_1^2}, \tag{7.5}$$

though the actual values depend sensitively on the stellar model.

The line-width $\Gamma \equiv \gamma_1 - \gamma_2 - \gamma_3 \sim |\gamma_2 + \gamma_3|$ (see Appendix F). The damping rates for the daughter modes are estimated from a quasiadiabatic calculation in Chapter 2, and computed with

[3]It is crucial that the daughter modes be able to dispose of the energy fed into them by their parent mode.

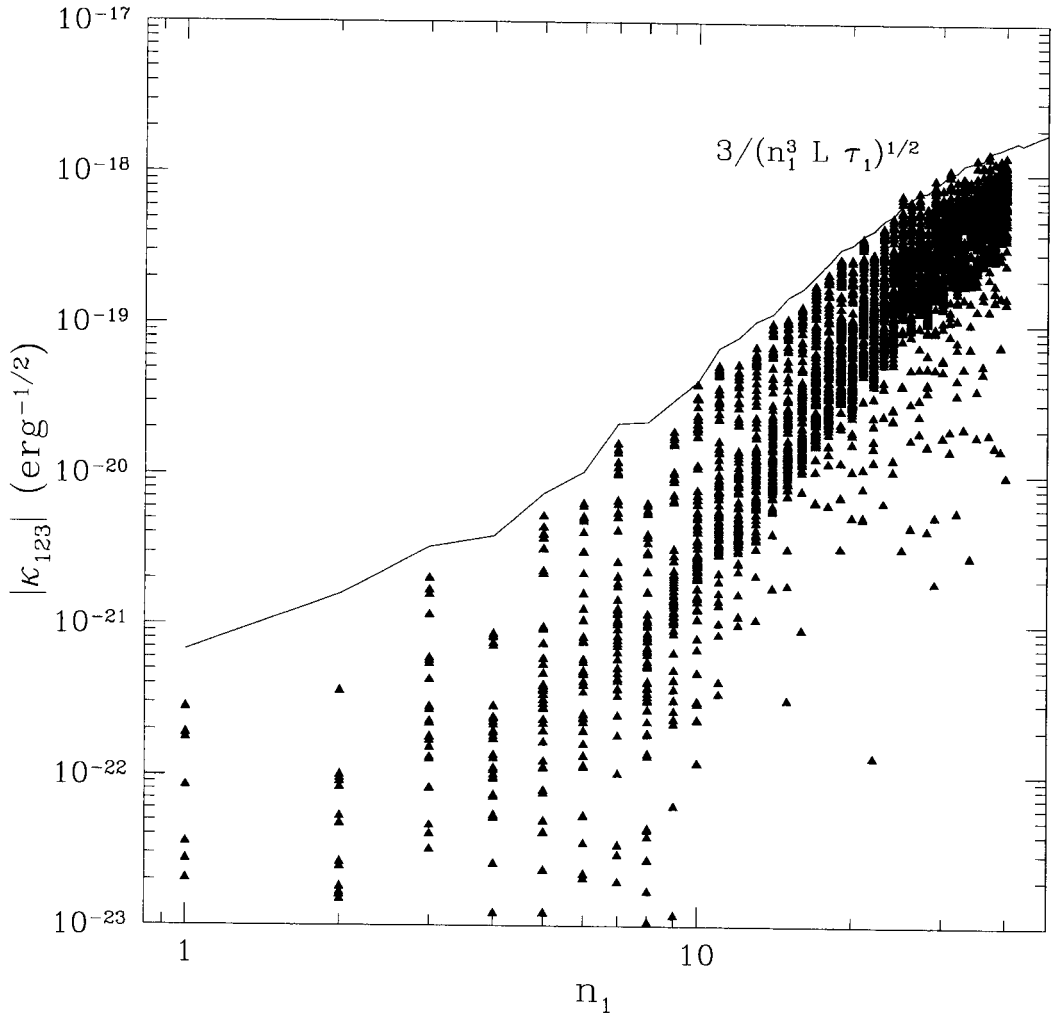

Figure 7.3: The coupling coefficient as a function of the parent mode's radial order. For each ℓ_2, the daughter pairs are chosen to satisfy the frequency closure best among those that are radially similar ($|n_2 - n_3| \leq 2n_1$). ℓ_2 ranges from 1 to 9, and $\ell_3 = \ell_1 + \ell_2 = 1 + \ell_2$. The analytical estimate is taken from equation (G.29) in Appendix G: L is the stellar luminosity, τ_1 the thermal time at $z_{\omega 1}$ (the top of the propagating cavity for the parent mode). These calculations are based on a DA model with $T_{\rm eff} = 12,800\,{\rm K}$.

a fully nonadiabatic code in Chapter 5. For long period modes, the latter method yields values saturating slightly above the values of $\omega/2\pi n$. This is the limit of low reflectivity which is dealt with in the next section. Before saturation, the mode damping rate increases steeply with n. Minimal Γ is achieved for pairs of daughter modes with similar values of n.

For most parametric couplings of interest, $\delta\omega_{\rm min} \leq \Gamma_{\rm min}$ even at $\ell_2 = 1$.[4] In these circumstances, the amplitude limiting daughter modes have $n_2 \approx n_3$, $\ell_2 = 1$, $\ell_3 = 2$, and couple to their parent mode with near-maximal κ. The low spherical degree daughter pairs are preferred as damping rates increase with ℓ when ω is constant.

The fractional density perturbation at the photosphere is related to the mode amplitude A by a normalization constant. Taking the analytic estimate for this constant given by equation (2.46), we find

$$\frac{\delta\rho}{\rho} = \frac{A}{(nL\tau_\omega)^{1/2}}. \tag{7.6}$$

We adopt the analytic estimate for the maximal value of κ given by equation (G.29),

$$\kappa^2 \sim \frac{1}{n^3 L\tau_\omega}, \tag{7.7}$$

where n and τ_ω pertain to the parent mode. Combining equations (7.3), (7.6), and (G.29), we arrive at an analytic estimate for $\delta\rho/\rho$,

$$\frac{\delta\rho}{\rho} \sim n_1\sqrt{\left(\frac{\delta\omega}{\omega}\right)^2 + \left(\frac{\Gamma}{\omega}\right)^2} \sim 2|\gamma_2|\frac{n_1}{\omega_1}. \tag{7.8}$$

The fractional density variation at the surface is of order $\delta F/F$ there, where $\delta F/F$ is the fractional flux variation.

For low n parent modes coupled to low ℓ daughters, $\delta\omega_{\rm min}$ exceeds $\Gamma_{\rm min}$. In this case, the amplitude limiting pair of daughter modes tends to be determined more by a fortuitously good frequency resonance than by a large coupling constant or small value of Γ. Thus the parametric amplitudes of low n overstable modes are expected to show large variations from star to star. The left panels of Figure 7.4 nicely illustrate these features. They show a close resonance involving one pair of daughter modes that holds the parametric amplitude of the parent mode to 3×10^{-4}, more than one order of magnitude below the value held by the other pairs.

Clemens (1995), in his Figure 4, displays the collection of mode periods found in hot DA variables with well-sampled light curves. Based on the similarity between the power spectra of different stars, he argues that periods close to 120 s belong to the $n = 1, \ell = 1$ mode. That only about one half of these hot DAVs show evidence for this mode is consistent with the expected statistical variations of the frequency detuning in its best parametric resonance.

[4]The exceptions involve parent modes of low radial order ($n_1 < 4$).

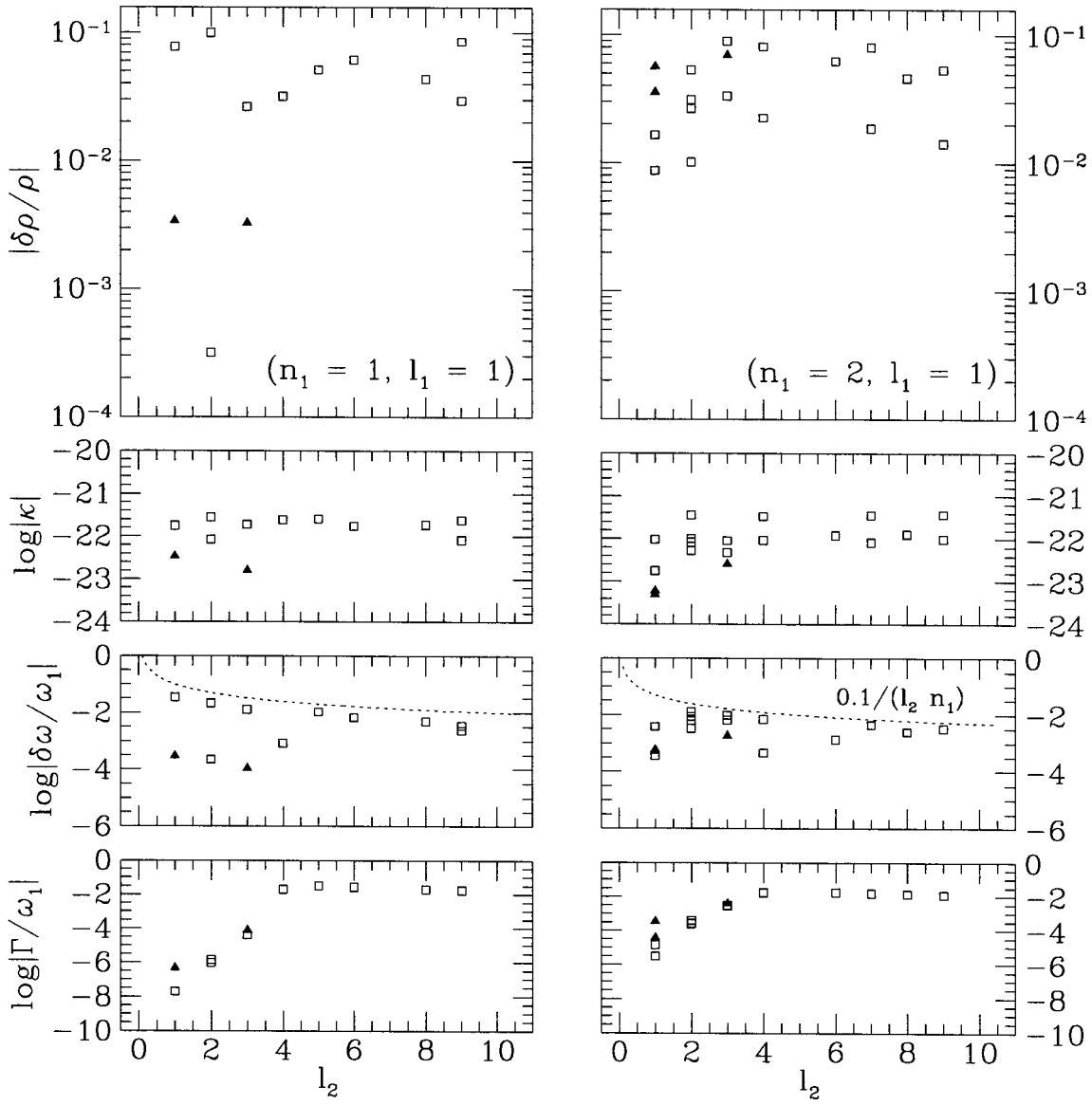

Figure 7.4: Pulsation amplitudes limited by parametric instability of daughter modes with different spherical degrees, for two low radial order parent modes, $(n_1, \ell_1) = (1, 1)$ (left panels) and $(n_1, \ell_1) = (4, 1)$ (right panels). We include couplings that limit amplitudes to $(\delta\rho_1/\rho) \leq 0.1$: open squares represent those that have near maximal κ ($|n_2 - n_3| \leq 2n_1$) and good frequency closure ($\omega_1 \approx \omega_2 + \omega_3$), whereas solid triangles represent those that have not too small a coupling strength ($|n_2 - n_3| \leq 10n_1$) and almost exact frequency closure ($\delta\omega \leq \Gamma$). Obviously, the relative importance of the second group decreases as the mean frequency spacing among the daughter modes decreases with increasing ℓ_2 or increasing n_1. Here, daughter modes with low spherical degrees have high reflectivity at the top of its cavity (standing waves), while ones with high ℓ do not (traveling waves).

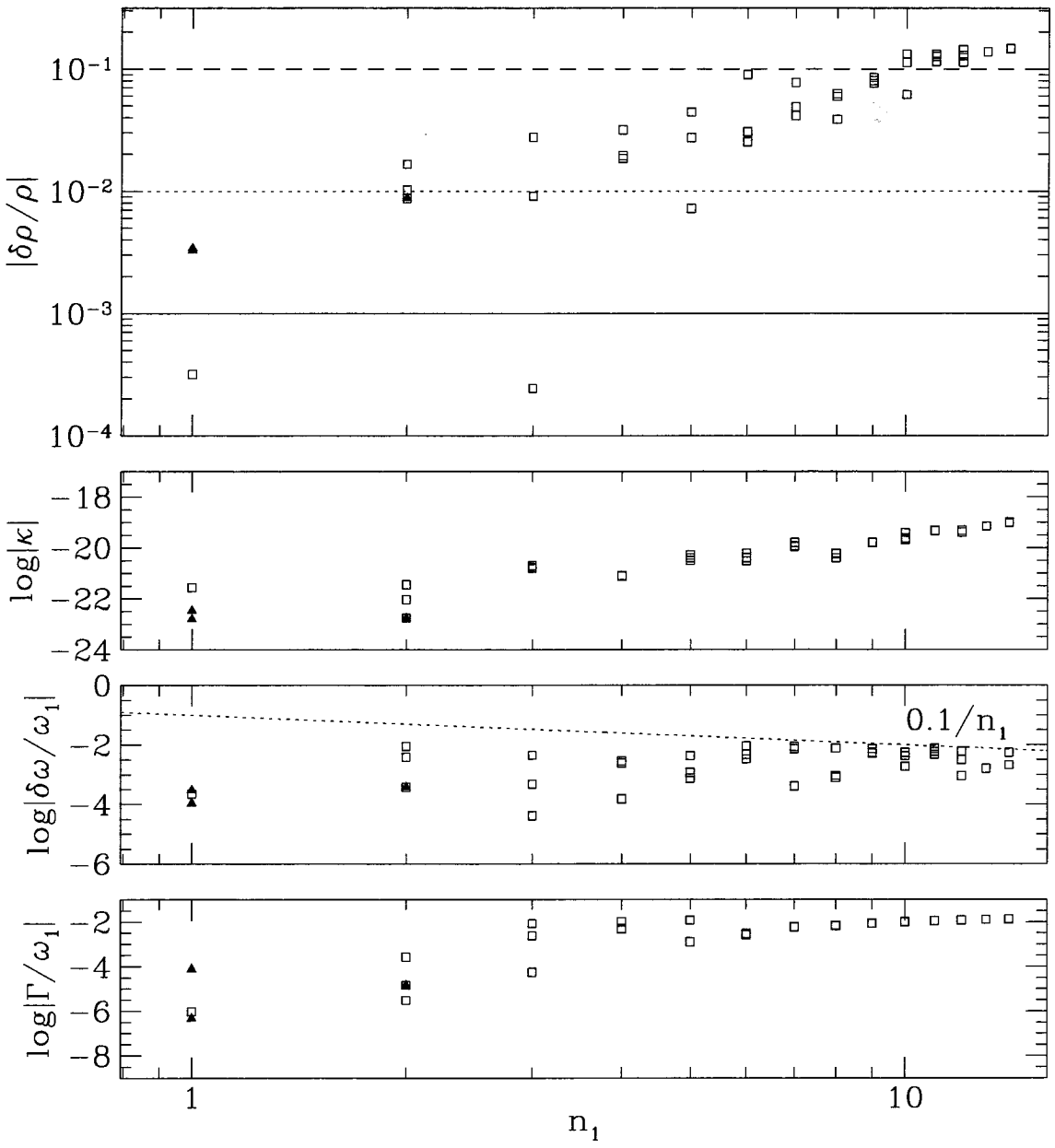

Figure 7.5: Minimum parametric amplitudes as a function of n_1 for $\ell_1 = 1$ modes in a star with $T_{\rm eff} = 12,800\,{\rm K}$ ($\tau_b = 1\,{\rm s}$). The selection of daughter modes is the same as in Figure 7.4, and we include both low Q traveling waves and high Q standing waves. The relative effectiveness of radially similar daughter pairs in limiting the parent mode amplitude increases with increasing n_1 as they minimize Γ and maximize κ. Low spherical degree daughter pairs are most important, except for the $n_1 = 1$ mode. With increasing n_1, the minimum value of $\delta\rho/\rho$ rises, but the mode energy it corresponds to ($E = A^2$) declines. For this star, only the two lowest radial order modes are overstable.

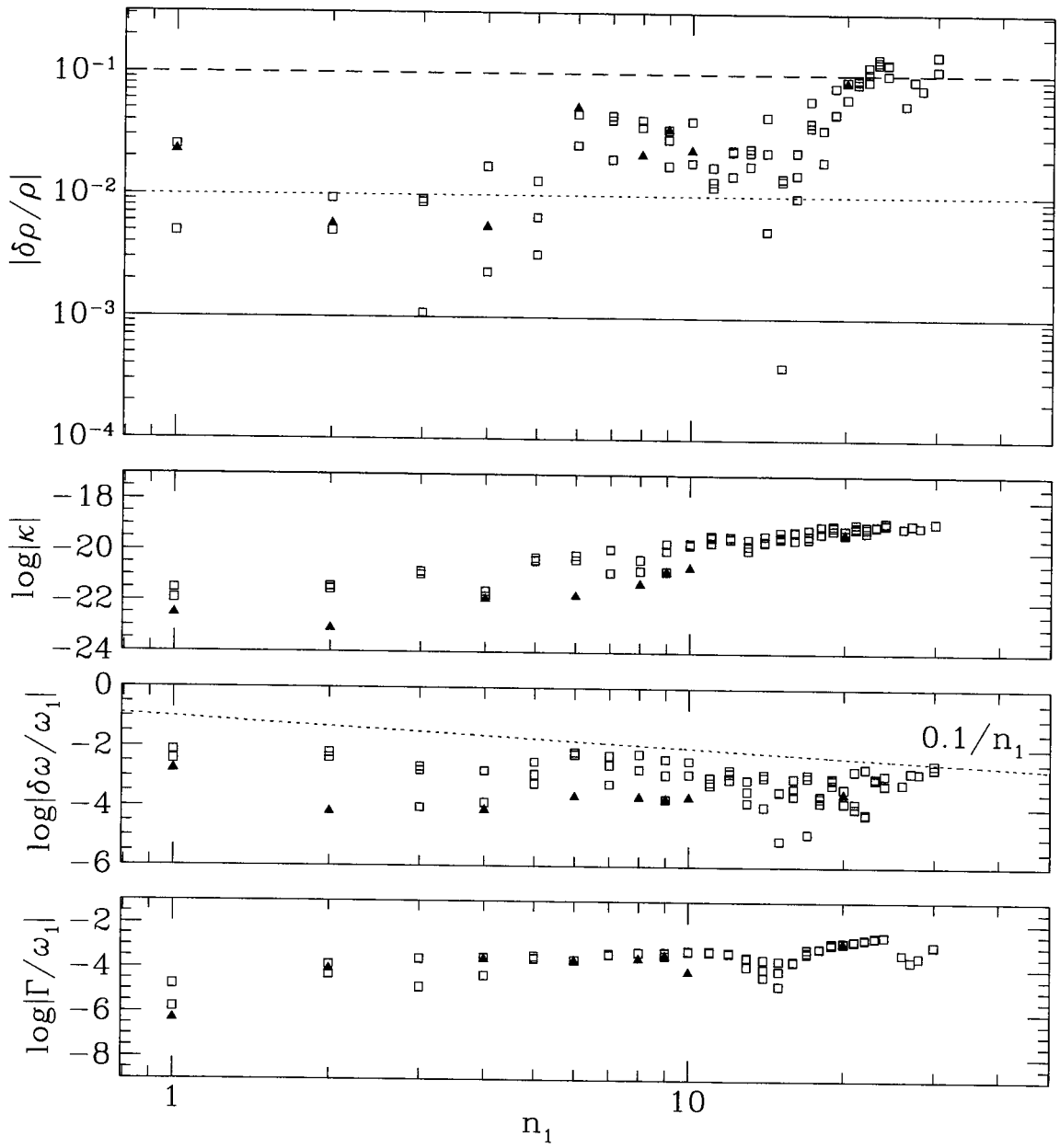

Figure 7.6: Similar to Figure 7.5, but for a much cooler star with $T_{\rm eff} \sim 11,600\,{\rm K}$ ($\tau_b = 300\,{\rm s}$). This star is likely to fall below the observed red edge. The minimum parametric amplitude of the $n = 1$ mode is much higher here than that in Figure 7.5, where it was suppressed as a result of a fortuitously good frequency resonance. On the other hand, the amplitudes of the higher order modes are systematically smaller than in the hotter star. This is a consequence of the decline in mode damping rate with decreasing effective temperature (compare the rates in Fig. 5.5 and those in Fig. 5.7). The $\ell_2 \geq 2$ daughter pairs are only relevant for the lowest few parent modes. All parent modes shown here are overstable. Note that amplitude predictions for short period modes ($n_1 \leq 15$) need to be modified since their daughter modes are also overstable and have non-negligible energy.

The smallest parametric amplitude of a given mode declines with decreasing $T_{\rm eff}$, as is shown in Figure 7.6 for a star of $T_{\rm eff} = 11,600\,{\rm K}$.[5] This trend may be traced to the increase in the depth of the convection zone as the star cools. By pushing down the upper lid of each daughter mode's cavity, the deepening convection zone decreases the mode's damping rate. This effect is discussed in §5.5.2. Note that the temperature dependence of the minimal parametric amplitude is less pronounced at small n_1 where $\delta\omega$ is more important than Γ.

7.4 Parametric Instability for Traveling Waves

Nonlinear interactions between parent and daughter modes are localized within an interaction region above $z_{\omega 1}$, the first node of the parent mode. Therefore, we can carry out a local analysis of the parametric interaction. This is especially relevant when the daughter waves are only weakly reflected at the upper boundary of the propagating cavity ($|\gamma| \geq \omega/(2\pi n)$). Without external forcing, these waves can travel radially only one round-trip before being dissipated.

7.4.1 Local Analysis

We focus on pairs of daughter waves that propagate downward, that are radially similar ($n_2 \sim n_3$), and that satisfy angular selection rules.

These waves travel inside the interaction region for a time

$$\Delta T = \int_0^{z_{\omega 1}} \frac{1}{v_{gz}} dz \sim \frac{n_2' \pi}{\omega_2} \sim \frac{n_2 \pi}{n_1 \omega_2}, \tag{7.9}$$

where n_2' is the number of daughter nodes above $z_{\omega 1}$ (see eq. [G.26]).

The finite interaction time allows all daughter waves within a frequency band of width $1/\Delta T$ to interact coherently with the parent mode.[6] The frequency spacing between neighbouring daughter waves is of order $\omega_2/n_2\pi$, which is the inverse of their radial propagation time over their entire cavity. So each daughter wave packet consists of n_1 waves. Each pair of daughter waves has comparable coupling coefficient (see §7.2).

Consider the amount of energy transferred to each daughter wave during the finite interaction time ΔT. Accounting for the presence of n_1 coherent parametric partners, and the fact that only $1/n_1$ of the parent mode's energy is localised, the energy equation for individual daughter waves becomes

$$\left(\frac{1}{\varepsilon}\frac{d\varepsilon}{dt}\right)_{\rm para} \sim \frac{n_1^2 \omega_2^2}{\Gamma} \kappa^2 E_1, \tag{7.10}$$

[5] According to Bradley, who provided this model, $T_{\rm eff} = 12,000\,{\rm K}$. But as we argue in Appendix B, the convection zone in his model is deeper than expected, as the superadiabatic gradient is not accurately taken care of. We reassign a temperature to this model based on the thermal time at the base of its convection zone.

[6] The concept of 'coherent parametric instability' is explained in Appendix H.

where the line-width Γ should be determined by the finite interaction time, as opposed to the decay rates from the daughters. This leads to

$$\left(\frac{1}{\varepsilon}\frac{d\varepsilon}{dt}\right)_{\rm para} \sim \frac{\omega_1}{4\pi}\left(\frac{n_2}{n_1}\right)\left(\frac{\delta\rho}{\rho}\right)_1^2 \sim \frac{\omega_1}{4\pi}\left(\frac{\ell_2}{\ell_1}\right)\left(\frac{\delta\rho}{\rho}\right)_1^2, \tag{7.11}$$

Here, $(\delta\rho/\rho)_1$ is the fractional density perturbation at the surface due to mode 1. The above expression describes the energy growth rate due to parametric instability for running waves inside the interaction region. Net local growth of wave energy requires that this rate overcome the damping rate due to local radiative diffusion. The radiative damping rate is given by

$$\left(\frac{1}{\varepsilon}\frac{d\varepsilon}{dt}\right)_{\rm dissi} \sim -\frac{(k_{z2}z)^2}{\tau_{\rm th}} \sim -\left(\frac{\ell_2}{\ell_1}\right)^2 \frac{z}{z_{\omega 1}}\frac{1}{\tau_{\rm th}}, \tag{7.12}$$

where k_{z2} is the radial wave vector for wave 2. This rate has a lopsided shape favoring smaller depth. Let $\delta n_2 \leq n_2'$ be the number of daughter nodes above $z_{\omega 1}$ in the region where the parametric growth rate exceeds the local diffusion rate; $\delta n_2 \sim n_2'$ provided that parametric driving exceeds radiative damping by a large margin at $z_{\omega 1}$. This condition takes the form

$$\mathcal{F} \sim \frac{\ell_1}{\ell_2}\omega_1\tau_{\omega 1}\left(\frac{\delta\rho}{\rho}\right)_1^2 \gg 1. \tag{7.13}$$

In our discussion, we assume $\delta n_2 = n_2' \sim n_2/n_1$ if $\mathcal{F} \gg 1$.

We define a gain factor $\mathcal{G}$ to describe the growth of energy in daughter waves during one traverse of the interaction region,

$$\varepsilon(t = \Delta T) \sim \varepsilon(t = 0)e^{\mathcal{G}}. \tag{7.14}$$

The initial energy in these waves comes from small random fluctuations, mostly likely due to forcing by turbulence in the overlying convection zone. A large gain factor is a necessary condition for parametric instability to produce significant energy transfer between the parent mode and the daughter waves;

$$\mathcal{G} \sim \frac{\ell_2\delta n_2}{\ell_1}\left(\frac{\delta\rho}{\rho}\right)_1^2 \sim \left(\frac{\ell_2}{\ell_1}\right)^2\left(\frac{\delta\rho}{\rho}\right)_1^2 \gg 1. \tag{7.15}$$

In this case, the amplitude of the parent mode is effectively limited to

$$\left(\frac{\delta\rho}{\rho}\right)_1^2 \leq \left(\frac{\ell_1}{\ell_2}\right)^2\mathcal{G}. \tag{7.16}$$

The relevant value of $\mathcal{G}$ scales inversely with $\ln\varepsilon(t = 0)$.

For fixed values of $\mathcal{G}$ and $\mathcal{F}$, $(\delta\rho/\rho)_1$ is most effectively limited by daughter waves whose angular

degree satisfies

$$\left(\frac{\ell_2}{\ell_1}\right)^3 \sim \frac{\mathcal{G}}{\mathcal{F}}\omega_1\tau_{\omega 1}. \tag{7.17}$$

The above value of ℓ_2 decreases with increasing n_1. The parent mode's amplitude is limited by traveling waves to a minimum value of

$$\left(\frac{\delta\rho}{\rho}\right)_1^2 \sim \frac{\mathcal{G}^{\frac{1}{3}}\mathcal{F}^{\frac{2}{3}}}{(\omega\tau_{\omega 1})^{\frac{2}{3}}}. \tag{7.18}$$

The amplitude rises sharply with n_1. When we take $\mathcal{G} = \mathcal{F} = 10$, we obtain an amplitude of 10^{-3} for the $n_1 = 1$ mode. The most important traveling waves in this case are those with $\ell_2 \sim 10^3$. In general, equation (7.18) is an underestimate since $\delta n_2 < n_2'$.

7.4.2 Relation to Standing Waves

If after one round-trip inside its cavity, a daughter wave loses the same amount of energy through radiative dissipation as it gains through parametric instability, it forms a standing wave pattern. In this case, the parametric amplitude is predicted by equation (7.8). What is the relation between this equation and equation (7.18), whose derivation is based on local analysis of traveling waves?

A standing pattern is formed when

$$\mathcal{G} \approx \frac{\pi n_2}{\omega_2}|\gamma_2|, \tag{7.19}$$

where γ_2 is the energy damping rate, and $\pi n_2/\omega_2$ is the propagation time across the cavity. Substituting this expression into equation (7.8), taking $\Gamma \sim 2|\gamma_2|$, and ignoring frequency detuning, we obtain

$$\left(\frac{\delta\rho}{\rho}\right)_1^2 \sim \frac{\mathcal{G}^2}{4}\left(\frac{n_1}{n_2}\right)^2 \sim \frac{\mathcal{G}^2}{4}\left(\frac{\ell_1}{\ell_2}\right)^2. \tag{7.20}$$

When plugging in the appropriate ℓ_2/ℓ_1 from equation (7.17), we recover equation (7.18). This demonstrates the equivalence of the traveling wave and the standing wave treatments, when the amplitude of the reflected wave exceeds the amplitude of the noise forced by turbulent convection in the daughter wave's frequency band.

7.5 Mode Selection – Direct Resonance

From observations of white dwarf pulsations, it is clear that some kind of 'mode selection' mechanism is at work. Where one mode may dominate the pulsation energy in the star, its neighbouring modes may be completely invisible. Longer period modes tend to have larger surface amplitudes, but the energy distribution from mode to mode is highly irregular. Parametric instability as discussed in

§7.3 can only provide upper limits for mode amplitudes.

We briefly consider here the process of 'direct resonance', where there are at least two overstable modes in a triplet. When we limit ourselves to the case of two overstable modes, modes 1 and 2, we find three couplings between these two modes that are efficient in transferring energy: (i) $\omega_1 + \omega_2 \approx \omega_3$; (ii) $\omega_1 - \omega_2 \approx \omega_3$ and mode 2 radially similar to mode 1; (iii) $\omega_1 - \omega_2 \approx \omega_3$ and mode 2 radially similar to mode 3.

In the first case, both modes 1 and 2 lose energy to mode 3. But as is discussed in §6.3.2, it is difficult to find a good frequency resonance because the frequency spacing of g-modes increases with increasing frequency. This coupling is important only when there is a fortuitously good frequency resonance.

In the second case, mode 1 loses energy to both modes 2 and 3. The frequency resonance is improved in this case. But its importance is undermined by the smallness of the coupling coefficient, particularly because mode 3 has short radial wavelength.

The third case is similar to the second case except for a much larger coupling coefficient. In general, parametric instability is suppressed here since mode 2 has non-negligible amount of energy. As discussed in detailed in §6.3.2, when mode 2 is parametrically limited by its daughter modes, this coupling is capable of effectively damping out mode 1, the higher frequency mode. This effect may modify our conclusions on parametric amplitudes in cooler stars (e.g., Fig. 7.6) where the very short period overstable modes have overstable daughter modes. Mode 3 is similar to mode 2 and is likely to be overstable when mode 2 is.

At this stage, we can only make very limited statements about the energy distribution among excited modes. Direct resonance, where all three modes are overstable, should also be taken into account in the future. Numerical simulations are needed to determine the energy distributions. One may hope that in the end, comparison with observations will yield information about modes that are invisible to us, and therefore lead to a better understanding of stellar structure.

7.6 Discussion and Summary

We have shown that parametric instability is capable of limiting amplitudes of overstable modes to the observed values, which range from $\sim$ 1mma (the typical detection limit) to $\sim$ 100mma. Observationally, it becomes clear that cooler stars pulsate in longer period modes and with larger amplitudes than hotter ones. Our work in Chapter 3 shows that as a star cools, it excites modes with longer and longer periods. This explains the first part of the correlation. Our work here successfully reproduces the second part of the correlation. Despite stronger coupling to their daughter modes, longer period modes have higher parametric amplitudes because their mode mass is smaller and because their daughter modes have larger damping rates.

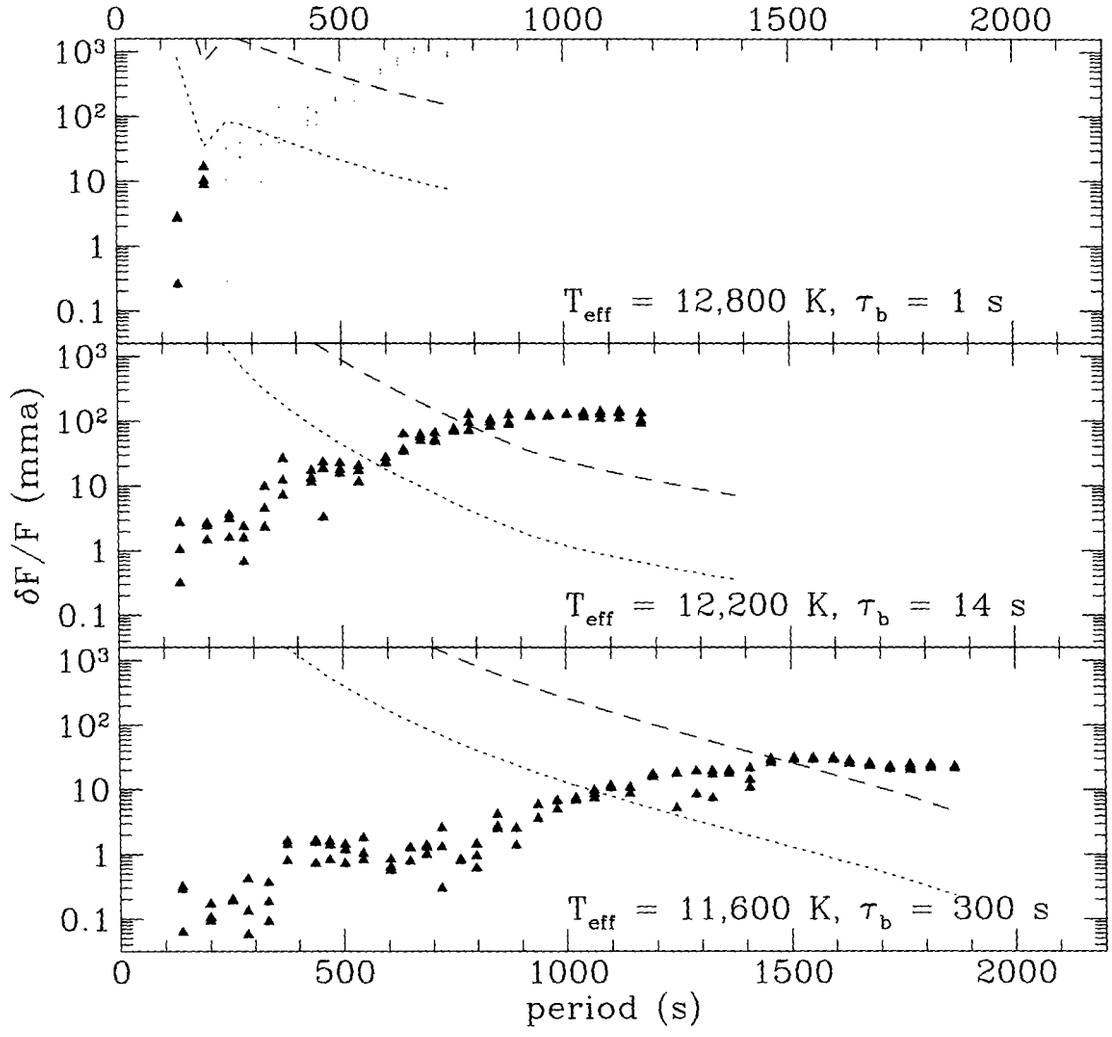

Figure 7.7: Mode ($\ell = 1$) amplitudes limited by parametric instability with damped daughter modes, as well as by turbulent damping below the convection zone. Amplitudes for the former case are indicated by triangles if the parent mode is overstable, and dots if it is not. The lowest parametric amplitudes are mostly due to low spherical degree daughter modes ($\ell_2 = 1$ or 2). Turbulent damping limits amplitudes of long period modes to below the short-dashed (with drag coefficient $C_D = 0.02$) or the long-dashed (with $C_D = 0.001$) curves (see §5.6). Here, we have also taken into account the visibility factor (see §3.2.4) when converting mode amplitudes from $\delta\rho/\rho$ to $\delta F/F$ at the surface. This factor reduces the photospheric flux variations for short period modes in cool stars. The observational detection limit lies around 1 mma.

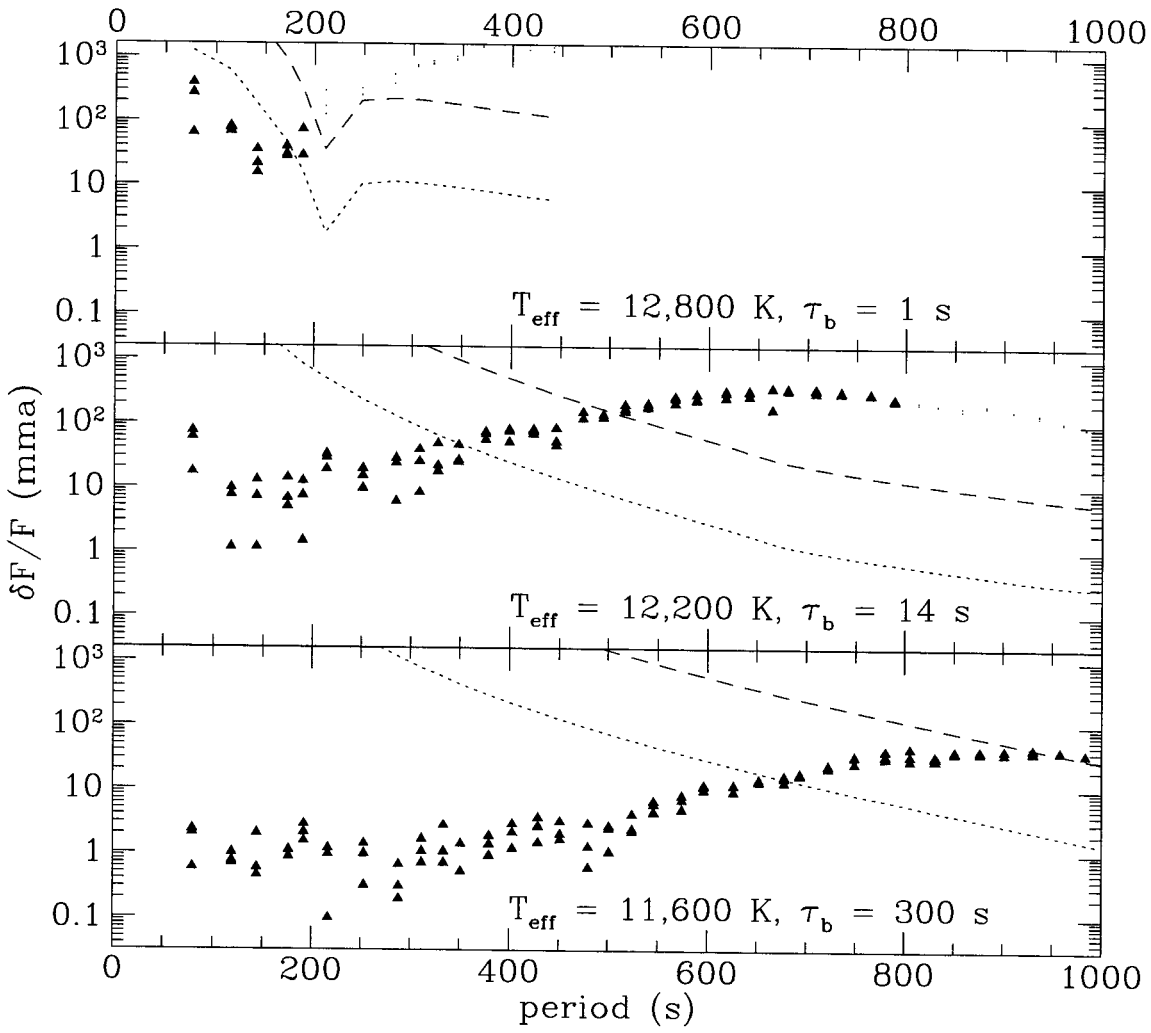

Figure 7.8: Similar to Figure 7.7, but for $\ell = 2$ overstable modes. The observed luminosity variations for these modes ($\delta L/L$) can be an order of magnitude smaller than variations in the flux.

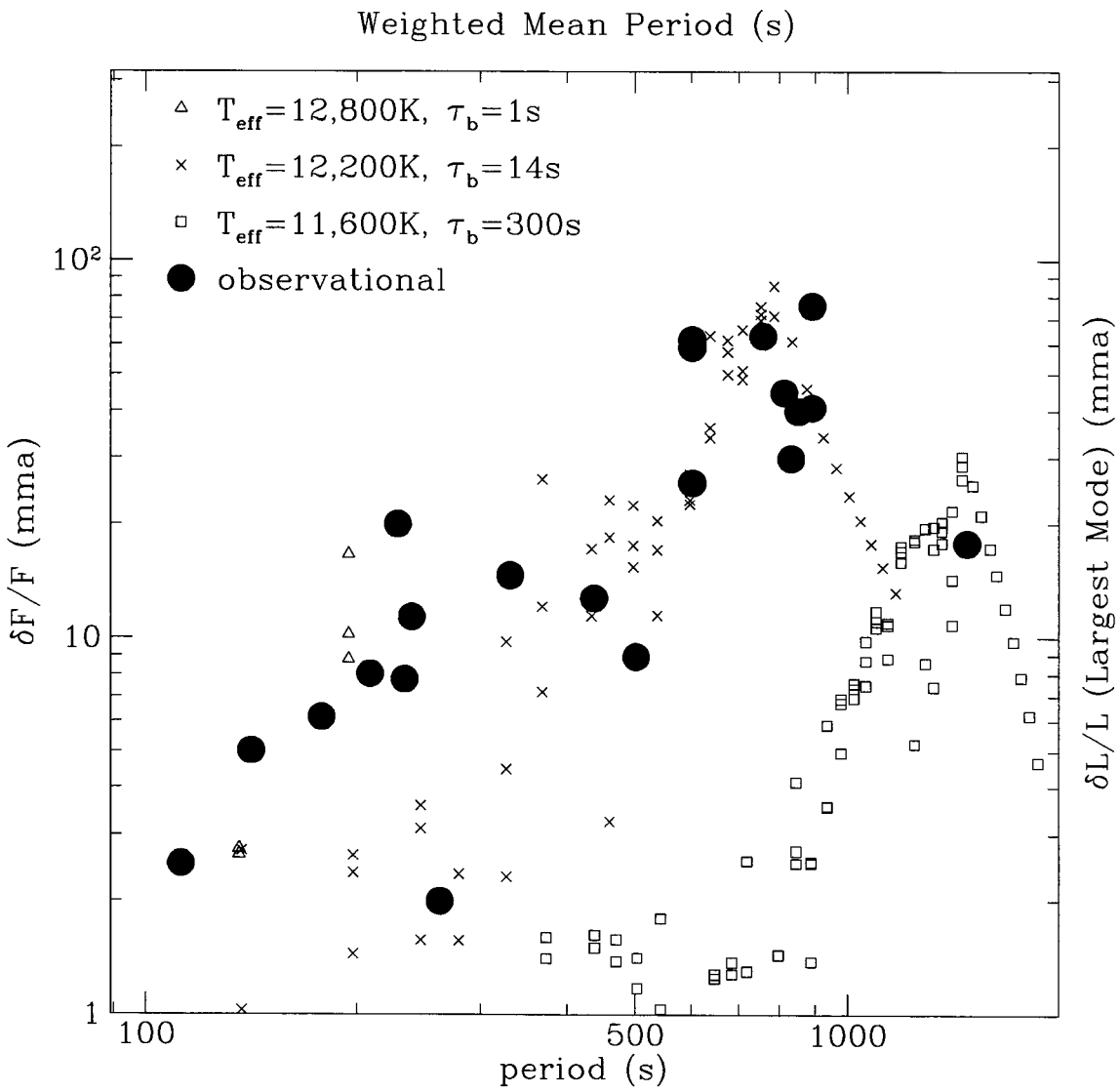

Figure 7.9: Comparison between theoretical mode amplitudes and those summarized by Clemens (1993) from observations of many DA variables. The data (filled circles) are plotted as amplitudes of fractional light variations in the largest modes versus energy weighted mean periods in individual stars. They show a clear correlation that is well reproduced by our theoretical calculations. We include results on $\ell_1 = 1$ overstable modes using three stars (see Fig. 7.7), taking a drag coefficient of $C_D = 0.001$. The theoretical results do not include effects like disc-averaging and limb-darkening. Also, our results are drawn from three stars while the observational data are taken from about two dozen stars.

In §7.4, we explored the scenario where the daughters decay so fast that they cannot form a standing pattern inside the star without external forcing. This arises when the daughters are strongly damped in the nonadiabatic region. We showed that when these waves are parametrically unstable such that there is equal or more energy transferred to them from the parent mode than is lost due to radiative dissipation. These low Q waves can therefore form standing pattern and limit the amplitudes of their parent modes in the same way as the high Q daughter modes (eq. [6.19]).

When a variable white dwarf cools, the amplitude limit due to parametric instability is tightened for most overstable modes due to the decreasing damping rates of their daughter modes. However, this is irrelevant for the few very low-order modes ($n \leq 4$) whose amplitudes depend sensitively on the best frequency resonance available. Of course, in all cases, the fractional flux variations at the photosphere decrease with the visibility factor $1/\sqrt{1+(\omega\tau_c)^2}$ (see Chap. 3).

Turbulent damping arising from the convective-radiative boundary (see §4.4) acts to limit the amplitudes of long period modes. This may resolve the contradiction between theory and observation concerning the longest periods for overstable modes (see §5.7). Unfortunately, estimates of turbulent daming involve a free parameter, i.e., the drag coefficient C_D. We show the scenario for both $C_D = 0.02$ and $C_D = 0.001$ in Figure 7.7.

As a passing note, we mention that strong nonadiabaticity in the gravity-modes is expected to reduce the coupling coefficient, as the local buoyancy force is reduced and the upper lid of the propagating cavity is pushed deeper down. However, we believe that our conclusions here are not significantly affected by this complication.

It is clear from the observations that other physical processes (e.g., direct resonance) are needed to explain the irregular energy distribution among modes (the phenomenon of 'mode selection'). The importance of various types of direct resonance is discussed in §7.5. Parametric resonance where at least one daughter mode is also overstable is capable of suppressing high frequency parent modes.

Another step necessary for a direct comparison between theory and observation is described below. White dwarf pulsations are observed as luminosity variations, the pulsation amplitude is measured in $\delta L/L$, where L is the stellar luminosity averaged over (optical) wavelength and the visible hemisphere, and δL is the size of its variation. The theoretical amplitude, $\delta\rho/\rho$, is related to $\delta L/L$ through the following steps:

1. $(\delta F/F)_b$, the amplitude of the flux perturbation at the bottom of the convection zone, is related to $\delta\rho/\rho$ through the equation of radiative transfer and the equation of state; nonadiabaticity needs to be taken into account;

2. flux perturbations at the photosphere, $(\delta F/F)_{\rm ph}$, are diminished and delayed compared to $(\delta F/F)_b$, as described by equation (3.38);

3. $\delta L/L$, the observed luminosity variation, is obtained by averaging $(\delta F/F)_{\rm ph}$ over the wave-

lengths of interest and the visible hemisphere; both the effects of angular dependence of the pulsation and the limb-darkening have to be taken into account.

In the end, $\delta\rho/\rho$ is related to $\delta L/L$ through a factor that depends on mode period, mode spherical degree (ℓ), the thickness of the convection zone, the reaction of the photosphere to pulsation, and the inclination angle between the line of sight and the pulsational axis. In Figure 7.7, we accomplished the first two steps using results from our nonadiabatic calculations (see Chap. 5). With time-resolved spectroscopy, it is possible to determine the ℓ values of the modes, as well as the inclination angle of the star (see Chap. 8). These two values are essential in the third step.

Various theoretical aspects need to be explored further before a complete picture can emerge. What is the effect of direct resonance on individual modes? What happens to the $\ell = 1$ overstable modes if there are simultaneously many higher ℓ modes excited? When stellar rotation splits modes into closely spaced multiplets, what determines the amplitudes within each multiplet? Is three-mode coupling the only order of coupling that is of interest in pulsating white dwarfs?

Bibliography

Clemens, J. C. 1993, Baltic Astronomy, 2, 407

Clemens, J. C. 1995, Baltic Astronomy, 4, 142

Dziembowski, W., & Krolikowska, M. 1990, Acta Astron. 40, 19

Landau, L. D., & Lifshitz, E. M. 1976, Mechanics, Third Edition, (Pergamon Press), 80

Chapter 8 Combination Frequencies in the Pulsation Power Spectra

8.1 Introduction

In the spectacular Whole Earth Telescope (WET) observations of the helium variable GD358 (Winget et al. 1994), long sequences of uninterrupted monitoring of the stellar light disclosed not only the presence of a large number of pulsational modes in the power spectra, but also the existence of many harmonics and cross terms (for the power spectrum of GD358, see Fig. 7 in their paper; Table 8.2 here lists the values). We call the latter 'combination frequencies', while the physical modes are called 'principal modes' or 'parent modes', not to be confused with the 'parent modes' in parametric instabilities.

The combination frequencies are also seen in many other pulsating white dwarfs, for instance, G29-38 (variable name ZZ Psc, McGraw 1978), GD154 (Robinson et al. 1978), BPM31594 (McGraw 1976; O'Donoghue et al. 1992[1]), G117-B15A (Kepler et al. 1982[2]) and GD165 (Bergeron et al. 1993). In fact, every ZZ Ceti looked at with sufficiently high signal to noise ratios has been shown to possess harmonics or cross terms of the principal modes (Brassard et al. 1995, Fontaine et al. 1991). Figure 8.1 shows the power spectrum of ZZ Psc from a recent Keck observation (van Kerkwijk et al. 1998).

Observations have established the correlation between the strength of the combination frequencies and the amplitudes variations of the pulsational modes (for an early review, see McGraw 1978). Also, the combination frequencies tend to have more complicated fine structure which can be explained by the linear superposition of rotationally split multiplets from the principal modes.

Therefore, these combination frequencies are believed to reflect not the eigenmodes of the star, but rather the perturbation of a nonlinear medium by sinusoidal waves (the principal modes). In this chapter, we are aimed at answering the following questions: which part of the star is the nonlinearity produced? How is the nonlinearity produced? What more can we know about the star using these combination frequencies?

Brassard et al. (1995) proposed one solution for the nonlinearity. They assume that the stellar eigenmodes are temperature waves, and they cause linear[3] temperature perturbations on the surface.

[1] In this paper, the authors believe that direct resonance between modes is responsible for producing the regular pattern in the period structure. The idea of direct resonance (Dziembowski 1982), in which the combinations are real modes, is unlikely mostly because of the lack of eigenmodes in the frequency range concerned.

[2] It is interesting to see that in this paper the intriguing numerology in mode frequencies causes the author to suggest the modes are r-modes.

[3] In this chapter, the terms 'linear' and 'nonlinear' are different from those used in Chapter 7, with 'linear' referring

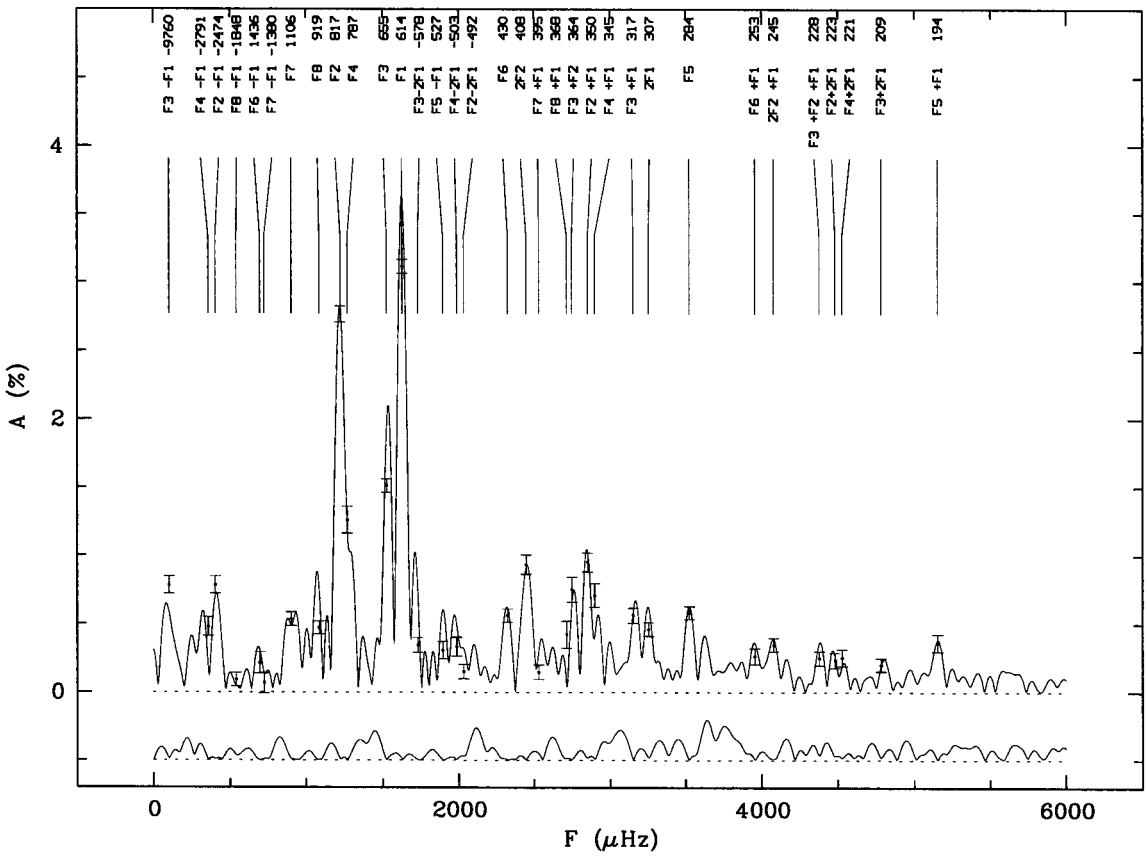

Figure 8.1: Fourier power spectrum using a 5-hour Keck light curve of ZZ Psc (G29-38). The frequency ν is in unit of μHz, $\nu = \omega/2\pi$, where $\omega = 2\pi/\text{period}$. The vertical axis is flux variations in units of 1% ($\sim$ 10 mma, where mma is milli-modulated amplitude, and is $\sim$ 0.1%). Notice the multitude of combination frequencies and the relative simplicity in constructing them by combining the real modes. The light curve was fit with a combination of sine waves; the resulting amplitudes and their uncertainties are indicated with the crosses and error bars. The lower panel shows the power left after taking away the sinusoidal signals identified in the upper panel.

The photospheric flux reacts nonlinearly according to $F = \sigma T^4$ (or more detailed atmospheric modeling), giving rise to the observed combination frequencies. We argue here that their assumption of sinusoidal temperature variations is not physical. The magnitude of the flux coming out of the convection zone determines the location of the photosphere (and $T_{\rm eff}$), but not the reverse. Also, the thin photosphere is energetically incapable of perturbing the stellar flux.

A competing idea is proposed by Brickhill (1992). He suggests that when the depth of the convection zone is fixed during pulsation, the photospheric flux will be reduced in amplitude and lag in phase compared to the flux perturbation entering the convection zone, the magnitudes of both effects are a function of the convection zone depth. So when the perturbation to the depth of the convection zone is also taken into account, a linear signal at the bottom will lead to a jigsaw shaped light curve at the surface, which would introduce harmonics and cross frequencies in the Fourier transform. Brickhill shows that for a pressure perturbation of $\delta p/p \sim 0.1$ at the bottom of the convection zone, the corresponding combinations have power comparable to the observed ones, if the principal modes have spherical degrees $\ell = 1$.[4] Here, the convection zone transforms part of the energy associated with the principal modes into the combination frequencies.

Physically, our approach resembles that of Brickhill's. Based on our results in Chapter 3, we present an analytical method to calculate the power in the combination frequencies. The relevant parameters are the depth of the convection zone, the photospheric properties of the star, and the inclination angle of the spin axis. We compare our estimates with data from GD358 and G29-38, and infer the above parameters for these two stars. We can reproduce the observed values to the orders of magnitude.

The discussions here are largely based on Chapter 3. The readers are referred to that chapter for various symbols.

8.2 Combination Frequencies: Theoretical Backgrounds

8.2.1 Origins

The convection zone produces the observed nonlinearities.

The perturbations within the mode's propagating cavity are likely to be linear. When these perturbations are communicated upward through the convection zone, the time-varying impedence of the convection zone introduces nonlinearity.

We simplify the overall reactions of the convection zone into changes in its depth. We further limit ourselves to the depth changes due to entropy perturbations. As the eddy turn-over time ($t_{\rm cv}$) is much shorter than the pulsation period, we assume that the convection zone is at both

to 'sinusoidal'.

[4] However, Winget et al. (1994) claimed that Brickhill's predictions about the power of combination frequencies for DA variables do not fit the data for the DB variable GD358.

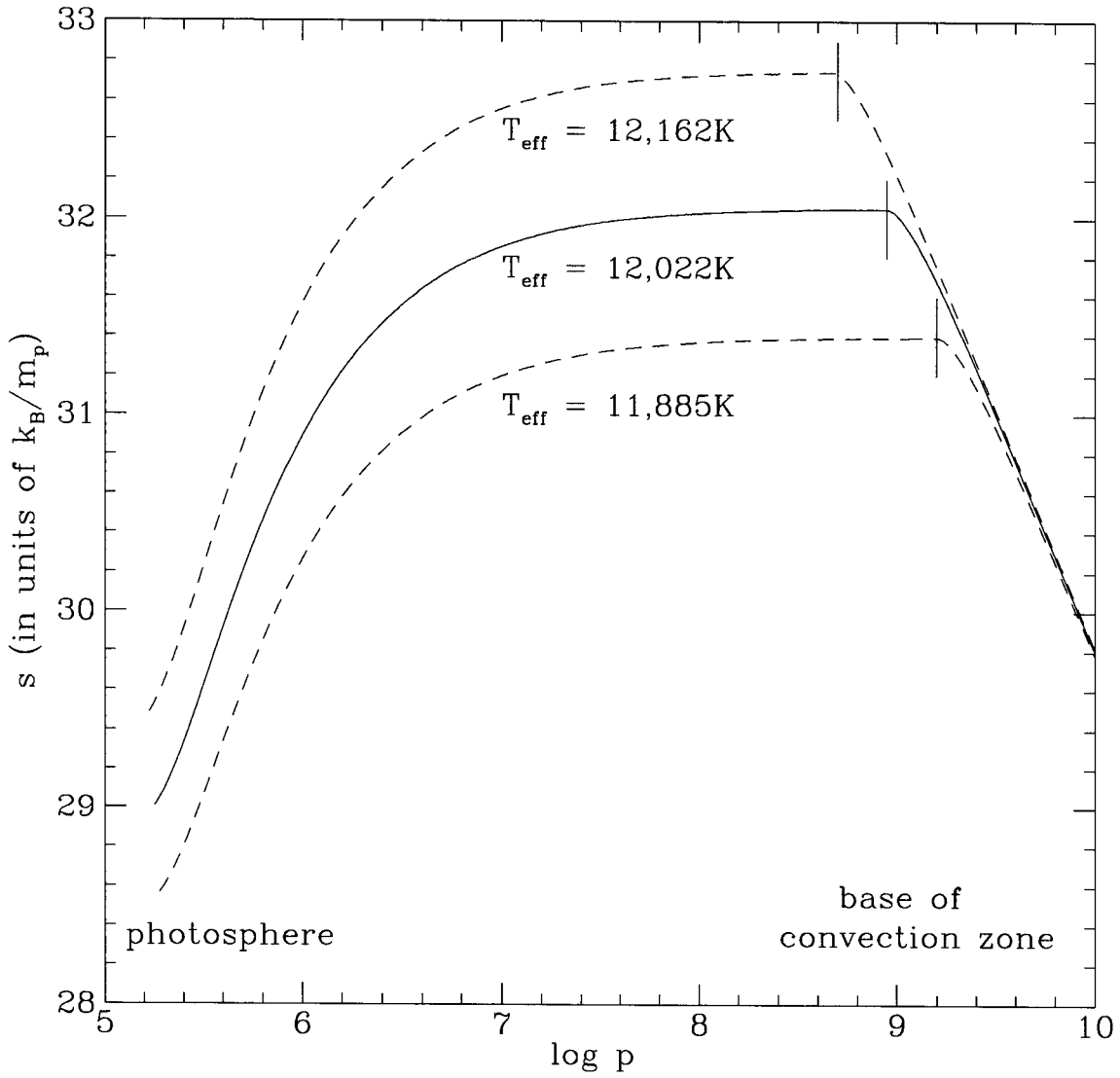

Figure 8.2: Entropy profiles in the upper atmosphere for three adjacent stellar models. The bottom of the convection zone (marked with short vertical bars) moves down by a scale-height when the surface flux varies by $\sim 4\%$. And there is a fast convergence towards the radiative interior. The construction of these models is detailed in Appendix B.

thermal and dynamical equilibria at any moment during pulsation. In Figure 8.2, the three static atmosphere models are therefore equivalent to pulsation at maximum (the top curve), pulsation at rest (the middle one) and pulsation at minimum (the lower one). The size of the convection zone shrinks (expands) as the uniform entropy level in the convection zone (s_b) rises (drops).

At any instant t during the pulsation, with the depth of the convection zone being $z_b(t)$ and thermal time $\tau_b(t)$, the extra heat stored in the convection zone is

$$\begin{aligned} dQ &= F\tau_{b0}ds_b + \int_{z_{b0}}^{z_b} \rho T \frac{k_B}{m_p}(s_b - s_0)\, dz \\ &= F\tau_{b0}ds_b + \int_{z_{b0}}^{z_b} \rho T \frac{k_B}{m_p}\left[ds_b - \left(\frac{ds}{d\ln p}\right)_0 d\ln p\right] dz. \end{aligned} \tag{8.1}$$

Here, all equilibrium quantities are denoted with subscript $_0$, and $(ds/d\ln p)_0$ is the equilibrium entropy gradient. The first term in the right-hand side is the heat absorbed by the whole convection zone (with its static size) when its entropy is raised by ds_b, $ds_b = s_b - s_0$; the second term represents the extra heat required by the expansion of the convection zone. The entropy in this newly expanded region is assumed to be s_b as well, and z_b is determined as the depth where $s_b = s_0$.

At any instant, the first law of thermo-dynamics requires

$$\begin{aligned} \left(\frac{\delta F}{F}\right)_{\rm ph} &= \left(\frac{\delta F}{F}\right)_{\rm b} - \frac{1}{F}\frac{dQ}{dt} \\ &= \left(\frac{\delta F}{F}\right)_{\rm b} - \tau_{b0}\frac{ds_b}{dt} - (\tau_b - \tau_{b0})\frac{ds_b}{dt} - \frac{dz_b}{dt}\left\{\rho T\frac{k_B}{m_p}\left[ds_b - \left(\frac{ds}{d\ln p}\right)_0 d\ln p\right]\right\}_{z_b} \\ &= \left(\frac{\delta F}{F}\right)_{\rm b} - \tau_b\frac{ds_b}{dt}. \end{aligned} \tag{8.2}$$

We differentiate equation (8.1) to obtain the above result. Equation (8.2) is similar to the key equations in Chapter 3, only τ_b in this case is a time dependent function.

As in Chapter 3, the entropy change in the convection zone is intimately related to the flux variation at the surface,

$$\delta s_b = (B + C)\left(\frac{\delta F}{F}\right)_{\rm ph}. \tag{8.3}$$

Here, the photospheric property is represented by $(B + C) = (B + C)(t)$.

Expand $(B + C)(t)$ and $\tau_b(t)$ in terms of $(\delta F/F)_{\rm ph}$ to the first order,

$$\begin{aligned} (B + C) &\simeq (B + C)_0\left[1 + \beta\left(\frac{\delta F}{F}\right)_{\rm ph}\right], \\ \tau_b &\simeq \tau_{b0}\left[1 + \gamma\left(\frac{\delta F}{F}\right)_{\rm ph}\right]. \end{aligned} \tag{8.4}$$

Using the stellar models as those shown in Figure 8.2, in the temperature range of ZZ Ceti variables,

$$\begin{aligned} \beta &= \frac{\partial \ln(B+C)}{\partial \ln F} \sim \frac{1}{4}\frac{\partial \ln(B+C)}{\partial \ln T_{\rm eff}} \sim \text{a few}, \\ \gamma &= \frac{\partial \ln \tau_b}{\partial \ln F} \sim \frac{1}{4}\frac{\partial \ln \tau_b}{\partial \ln T_{\rm eff}} \sim 15. \end{aligned} \tag{8.5}$$

The exact values of β and γ can in principle be measured using the combination frequencies and be used to infer stellar structure. Moreover, the width of the theoretical instability strip is a function of $(\beta+\gamma)$ (see Chap. 3).

Let X be the observed flux variation,

$$X = \left(\frac{\delta F}{F}\right)_{\rm ph}. \tag{8.6}$$

Combining equations 8.2, 8.3 and 8.4, we obtain

$$f(t)\frac{dX}{dt} + X = \left(\frac{\delta F}{F}\right)_{\rm b}, \tag{8.7}$$

where $\tau_{c0} = (B+C)_0\tau_{b0}$, and $f(t) = \tau_{c0}[1 + (2\beta+\gamma)X + 2\beta\gamma X^2] = \tau_{c0}[1 + f_1 X + f_2 X^2]$. Note that f_2 would have other terms coming from the second order expansion of $(B+C)$ and τ_b. We ignore them for our order of magnitude analysis here. Equation (8.7) describes the production of combination frequencies given linear input $(\delta F/F)_b$. It also describes the motion of a pendulum with time varying mass driven by a periodic external force in a viscous medium.

8.2.2 Solutions

In this section, we consider only normalized mode amplitudes. We delay the discussion on angular dependences to §8.2.3. We solve for the amplitudes of the combination frequencies.

1) *Solutions for a Single Mode*

When the input is a single sinusoidal signal,

$$\left(\frac{\delta F}{F}\right)_{\rm b} = A\cos(\omega_a t). \tag{8.8}$$

The solution for $(\delta F/F)_{\rm ph}$ can be written in the form

$$X = a_1\cos(\omega_a t + \phi_1) + a_2\cos(2\omega_a t + \phi_2) + a_3\cos(3\omega_a t + \phi_3). \tag{8.9}$$

Expanding equation (8.7) and neglecting terms of high order, we arrive at

$$a_1 \left[\cos\left(\omega_a t + \phi_1\right) - \omega_a \tau_{c0} \sin\left(\omega_a t + \phi_1\right)\right] = A \cos\left(\omega_a t\right); \tag{8.10}$$

$$a_2 \left[\cos\left(2\omega_a t + \phi_2\right) - 2\omega_a \tau_{c0} \sin\left(2\omega_a t + \phi_2\right)\right] = \frac{f_1 \omega_a \tau_{c0}}{2} a_1^2 \sin\left(2\omega_a t + 2\phi_1\right); \tag{8.11}$$

$$\begin{aligned} a_3 \left[\cos\left(3\omega_a t + \phi_3\right) - 3\omega_a \tau_{c0} \sin\left(3\omega_a t + \phi_3\right)\right] &= \frac{f_2 \omega_a \tau_{c0}}{4} a_1^4 \sin\left(3\omega_a t + 3\phi_1\right) \\ &+ \frac{3 f_1 \omega_a \tau_{c0}}{2} a_1 a_2 \sin\left(3\omega_a t + \phi_1 + \phi_2\right). \end{aligned} \tag{8.12}$$

Solving the above equations sequentially for a_i, we obtain

$$\begin{aligned} a_1 &= \frac{A}{\sqrt{1 + (\omega_a \tau_{c0})^2}}. \\ a_2 &= \frac{a_1^2}{2} \frac{f_1 \omega_a \tau_{c0}}{\sqrt{1 + (2\omega_a \tau_{c0})^2}}, \\ a_3 &= \frac{a_1^3}{4} \frac{\omega_a \tau_{c0} \sqrt{f_2^2 + (\omega_a \tau_{c0})^2 (2 f_2 - 3 f_1^2)^2}}{\sqrt{(1 + (3\omega_a \tau_{c0})^2 (1 + (2\omega_a \tau_{c0})^2)}}. \end{aligned} \tag{8.13}$$

The expression for a_1 is identical to equation (3.44) in Chapter 3; it reflects the reduction in the surface flux perturbation due to the thermal content of the convection zone. Typically, a_1 is only of order 10^{-3} to 10^{-2}. The harmonics can be visible mostly thanks to the largeness of f_1 (of order 20).[5] The convection zone can divert sufficient energy from the principal modes to the combination frequencies because its thermal content is boosted up by both the superadiabatic layer and the ionizing photosphere. The flux perturbations with the combination frequencies are not associated with physical displacements and velocities.

The phases, ϕ_1 and ϕ_2, are,

$$\begin{aligned} \phi_1 &= -\arctan(\omega \tau_{c0}), \\ \phi_2 &= 2\phi_1 - \frac{\pi}{2} - \arctan(2\omega \tau_{c0}). \end{aligned} \tag{8.14}$$

The phase of the surface flux lags behind that of $(\delta F/F)_b$ by ϕ_1, as described in Chapter 3.

2) *Solutions: Two Modes*

When there are two linear input signals with frequencies ω_a and ω_b, the following form of the solution is adopted:

$$\begin{aligned} X &= a_1 \cos\left(\omega_a t + \phi_1\right) + a_2 \cos\left(2\omega_a t + \phi_2\right) + a_3 \cos\left(3\omega_a t + \phi_3\right) + \\ &\quad b_1 \cos\left(\omega_b t + \theta_1\right) + b_2 \cos\left(2\omega_b t + \theta_2\right) + b_3 \cos\left(3\omega_b t + \theta_3\right) + \end{aligned}$$

[5] Such a large f_1 also helps to make the a_3 term visible.

$$c_2 \cos\left((\omega_a - \omega_b)t + \psi_1\right) + c_{3a} \cos\left((2\omega_a - \omega_b)t + \psi_2\right) + c_{3b} \cos\left((\omega_a - 2\omega_b)t + \psi_3\right) +$$
$$d_2 \cos\left((\omega_a + \omega_b)t + \delta_1\right) + d_{3a} \cos\left((2\omega_a + \omega_b)t + \delta_2\right) + d_{3b} \cos\left((\omega_a + 2\omega_b)t + \delta_3\right). \quad (8.15)$$

The subscripts for the different coefficients are chosen to represent their orders. The amplitudes and phases of the harmonic terms are given in equations (8.13) and (8.14). The solutions for the cross terms are presented here.

$$\begin{aligned} c_2 &= \frac{a_1 b_1}{2} \frac{f_1(\omega_a - \omega_b)\tau_{c0}}{\sqrt{1 + ((\omega_a - \omega_b)\tau_{c0})^2}}, \\ d_2 &= \frac{a_1 b_1}{2} \frac{f_1(\omega_a + \omega_b)\tau_{c0}}{\sqrt{1 + ((\omega_a + \omega_b)\tau_{c0})^2}}; \end{aligned} \quad (8.16)$$

$$\begin{aligned} \psi_1 &= (\phi_1 - \theta_1) - \frac{\pi}{2} - \arctan((\omega_a - \omega_b)\tau_{c0}) \\ \delta_2 &= (\phi_1 + \theta_1) - \frac{\pi}{2} - \arctan((\omega_a + \omega_b)\tau_{c0}). \end{aligned} \quad (8.17)$$

Expressions for c_{3a}, c_{3b}, d_{3a} and d_{3b} are not listed here. They are similar to a_3 in order of magnitude.

The amplitude ratio c_2/d_2 yields the value of τ_{c0}, independent of the inclination angle.

Since the photosphere would not have enough thermal power to affect these combinations frequencies, we expect the above amplitude and phase relations holds for all wavelengths at all times.

8.2.3 Angular Dependences

The angular dependence of the pulsation affects the magnitude of flux perturbations integrated over the visible disc.

In this section, we assume all principal modes have spherical degrees $\ell = 1$ in Y_1^m, where $m \in [-1, 1]$. We also assume that rotation breaks the frequency degeneracy between different m's, and that the observers can resolve them.

The combination frequencies have different angular dependencies from those of their principal modes. In fact, the a_1^2 dependence of the a_2 term tells us that the component at frequency $2\omega_a$ has an angular function that is the product of two Y_1^m's, while that at $3\omega_a$ is the product of three Y_ℓ^m's. Similarly for the other combinations.

The linear decomposition of the product of any two $\ell = 1$ spherical harmonics goes as

$$\begin{pmatrix} Y_1^{-1} \\ Y_1^0 \\ Y_1^1 \end{pmatrix} \begin{pmatrix} Y_1^{-1} & Y_1^0 & Y_1^1 \end{pmatrix} = \begin{pmatrix} \sqrt{\frac{3}{10\pi}} & 0 & 0 & 0 & 0 & 0 \\ 0 & \sqrt{\frac{3}{20\pi}} & 0 & 0 & 0 & 0 \\ 0 & 0 & \sqrt{\frac{1}{20\pi}} & 0 & 0 & -\sqrt{\frac{1}{4\pi}} \\ 0 & \sqrt{\frac{3}{20\pi}} & 0 & 0 & 0 & 0 \\ 0 & 0 & \sqrt{\frac{1}{5\pi}} & 0 & 0 & \sqrt{\frac{1}{4\pi}} \\ 0 & 0 & 0 & \sqrt{\frac{3}{20\pi}} & 0 & 0 \\ 0 & 0 & \sqrt{\frac{1}{20\pi}} & 0 & 0 & -\sqrt{\frac{1}{4\pi}} \\ 0 & 0 & 0 & \sqrt{\frac{3}{20\pi}} & 0 & 0 \\ 0 & 0 & 0 & 0 & \sqrt{\frac{1}{10\pi}} & 0 \end{pmatrix} \begin{pmatrix} Y_2^{-2} \\ Y_2^{-1} \\ Y_2^0 \\ Y_2^1 \\ Y_2^2 \\ Y_0^0 \end{pmatrix}. \tag{8.18}$$

Similar decomposition can be taken for the product of three Y_ℓ^m's to determine the non-zero components in the combinations.

Next we consider the effect of the inclination angle. There are two coordinate systems in Figure 8.3, defined by the spin axis and the observer respectively. The transformation between the two coordinate systems, $(\Theta, \Phi) \leftrightarrow (\theta, \phi)$ can be derived using two Cartesian coordinates associated with the the two spherical coordinates respectively. These are

$$\begin{pmatrix} X \\ Y \\ Z \end{pmatrix} = \begin{pmatrix} \sin\Theta\cos\Phi \\ \sin\Theta\sin\Phi \\ \cos\Theta \end{pmatrix}, \tag{8.19}$$

and

$$\begin{pmatrix} x \\ y \\ z \end{pmatrix} = \begin{pmatrix} \sin\theta\cos\phi \\ \sin\theta\sin\phi \\ \cos\theta \end{pmatrix}. \tag{8.20}$$

The two Cartesian coordinates are related to each other through a unitary rotational transformation matrix,

$$\begin{pmatrix} X \\ Y \\ Z \end{pmatrix} = \begin{pmatrix} \cos\Theta_0 & 0 & -\sin\Theta_0 \\ 0 & 1 & 0 \\ \sin\Theta_0 & 0 & \cos\Theta_0 \end{pmatrix} \begin{pmatrix} x \\ y \\ z \end{pmatrix}, \tag{8.21}$$

where Θ_0 is defined in Figure 8.3. Therefore,

$$\cos\Theta = \sin\Theta_0 \sin\theta\cos\phi - \cos\Theta_0\cos\theta. \tag{8.22}$$

Given a flux variation of angular depedence, $aY_\ell^m(\Theta, \Phi)$, the total flux perturbation integrated

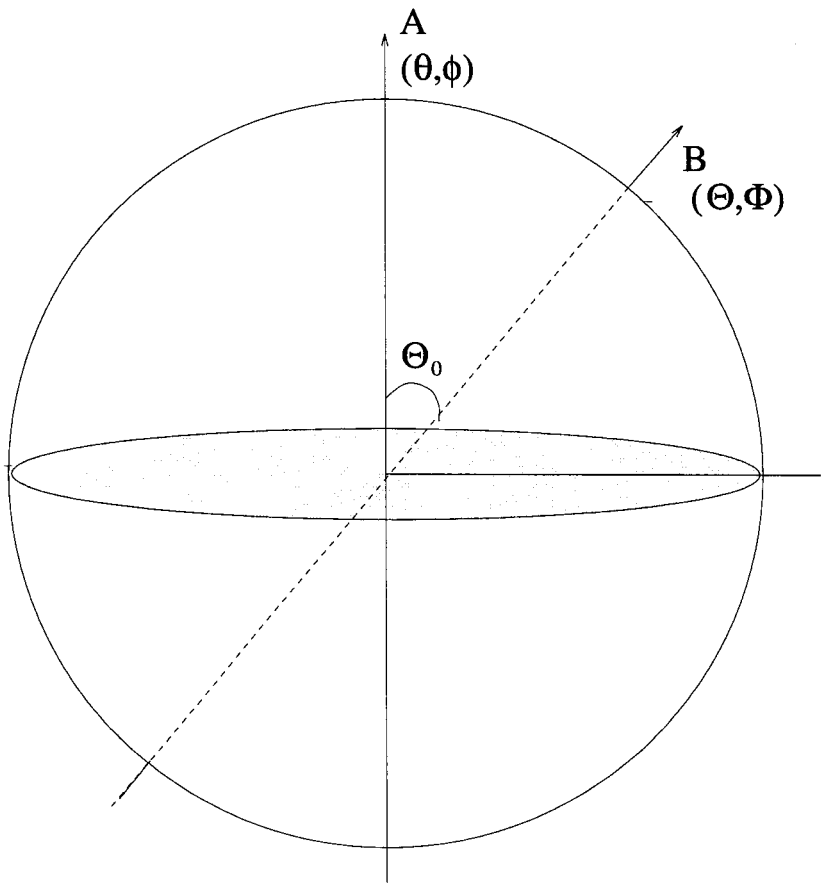

Figure 8.3: Two spherical coordinate systems of relevance in a pulsating white dwarf. The spin axis B defines the stellar coordinate, expressed in (Θ, Φ); while the line-of-sight of the observer (A) defines another coordinate system, (θ, ϕ). B is Θ_0 away from A. We take $\Phi_0 = 0$, where Φ_0 is the projection angle of B axis on A's equatorial plane (the shaded plane). This angle is arbitrary since we cannot resolve the disk spatially and different Φ_0 are degenerate. In this plot, only the upper hemisphere is observable. The transformation between the two, $(\Theta, \Phi) \leftrightarrow (\theta, \phi)$, is done in equation (8.21).

over the visible hemisphere is

$$\delta F = a \int_0^{2\pi} \int_0^1 Y_\ell^m(\Theta, \Phi) h(\mu) \mu d\mu d\phi = a g_\ell^m. \tag{8.23}$$

Here, $\mu = \cos\theta$. $h(\mu)$ is the prescribed limb-darkening law; it is in general a function of frequency and is normalized by $\int_0^1 h(\mu)\mu d\mu = 1$. One power of μ is needed inside the integrand to reflect the projection of the area along the line of sight. We call g_ℓ^m the 'angular function'. It relates the physical variation with the observable one. In general, there is not a simple, analytical functional form for g_ℓ^m.

We adopt Eddington's limb-darkening law, i.e., $h(\mu) = 1 + 3/2\mu$. For some simple $Y_\ell^m(\Theta, \Phi)$, the values of their g_ℓ^m are

$$\begin{aligned}
g_0^0 &= 1.256, \\
g_1^{-1} &= -1.538 \sin\Theta_0, \\
g_1^0 &= 2.175 \cos\Theta_0, \\
g_1^1 &= 1.538 \sin\Theta_0, \\
g_2^{-2} &= 0.789 \sin^2\Theta_0, \\
g_2^{-1} &= 1.881 \sin(2\Theta_0), \\
g_2^0 &= -0.161 + 0.483\cos^2\Theta_0, \\
g_2^1 &= -1.881 \sin(2\Theta_0), \\
g_2^2 &= 0.789 \sin^2\Theta_0.
\end{aligned} \tag{8.24}$$

In particular, when the viewing angle $\Theta_0 = 0$ (viewed pole on), $g_0^0 = 1.256$, $g_1^0 = 2.175$, $g_2^0 = 0.322$, and all the others vanish – if the star rotates pole on, we cannot observe any rotational splittings. Or, when $\Theta_0 = \pi/2$ (the rotation axis lies on the plane of the sky), $g_1^0 = 0$, $g_1^{-1} = g_1^1 = 1.53$, $g_2^{-2} = g_2^2 = 0.788$, $g_2^{-1} = g_2^1 = 0$, $g_2^0 = 0.161$. The physical amplitudes of the higher order combinations are smaller, but their angular functions (g_ℓ^m) may be larger for a favorable viewing angle (Θ_0).

8.3 Applications to Pulsating White Dwarfs

When applying results from §8.2.1 to the pulsating white warfs, we encounter complications: when the observations last long enough to resolve rotationally split frequencies (as in §8.3.1), chances are that many principal modes have varied their amplitudes during this time. On the other hand, when short span data are used (as in §8.3.2), there is no information on the m values for the frequencies.

8.3.1 GD358

This is a DB variable. Structual similarity between DBVs and DAVs leads us to assume that the results from §8.2.1 apply here as well.

1) *Fine Structure in the Combination Frequencies*

For this star, the WET run (Winget et al. 1994) has yielded a high resolution power spectrum. The star is rotating, and not only the different components in the real modes are well resolved, the combination frequencies are also shown to have multiple splittings with numbers larger than the principal modes (see Fig. 8 in that paper, or Table 8.1 in this section). The analysis of Winget et al. (1994) shows that the complicated fine structure is a natural result of the superposition of multiplets in the principal modes. If the two principal modes are both $\ell = 1$ modes, and they have different frequency splittings, their combinations may have up to nine non-degenerate components.

Consider the cross-term of two $\ell = 1$ modes, with $m_a = -1$ and $m_b = -1$. It has an angular dependence of Y_2^{-2}. If mode 1 and 2 have integrated light variations $(\delta F/F)_a^{(-1)} = A_a^{(-1)} g_1^{(-1)}$ and $(\delta F/F)_b^{(-1)} = A_b^{(-1)} g_1^{(-1)}$, where the superscript denotes the m value, the observed flux variations associated with this cross term (with $m = -2$) will be

$$\begin{aligned}\left(\frac{\delta F}{F}\right)_{(-1,-1)} &= \frac{A_a^{(-1)} A_b^{(-1)}}{2} \frac{f_1(\omega_a+\omega_b)\tau_{c0}}{\sqrt{1+(\omega_a+\omega_b)^2\tau_{c0}^2}} g_2^{-2} \\ &= \frac{1}{2}\left(\frac{\delta F}{F}\right)_a^{(-1)} \left(\frac{\delta F}{F}\right)_b^{(-1)} \frac{f_1(\omega_a+\omega_b)\tau_{c0}}{\sqrt{1+(\omega_a+\omega_b)^2\tau_{c0}^2}} \frac{g_2^{-2}}{g_1^{-1} g_1^{-1}},\end{aligned} \tag{8.25}$$

with the subscript $(-1,-1)$ on $(\delta F/F)$ telling the m values of the two principal modes. The dependence on Θ_0 cancels out exactly and the final result is

$$\left(\frac{\delta F}{F}\right)_{(-1,-1)} = 0.167 \left(\frac{\delta F}{F}\right)_a^{(-1)} \left(\frac{\delta F}{F}\right)_b^{(-1)} \frac{f_1(\omega_a+\omega_b)\tau_{c0}}{\sqrt{1+(\omega_a+\omega_b)^2\tau_{c0}^2}}. \tag{8.26}$$

The independence on Θ_0 is true for a few other combinations:

$$\begin{aligned}\left(\frac{\delta F}{F}\right)_{(-1,0)} &= -0.562 \left(\frac{\delta F}{F}\right)_a^{(-1)} \left(\frac{\delta F}{F}\right)_b^{(0)} \frac{f_1(\omega_a+\omega_b)\tau_{c0}}{\sqrt{1+(\omega_a+\omega_b)^2\tau_{c0}^2}}; \\ \left(\frac{\delta F}{F}\right)_{(+1,0)} &= -0.562 \left(\frac{\delta F}{F}\right)_a^{(+1)} \left(\frac{\delta F}{F}\right)_b^{(0)} \frac{f_1(\omega_a+\omega_b)\tau_{c0}}{\sqrt{1+(\omega_a+\omega_b)^2\tau_{c0}^2}}; \\ \left(\frac{\delta F}{F}\right)_{(+1,+1)} &= 0.167 \left(\frac{\delta F}{F}\right)_a^{(+1)} \left(\frac{\delta F}{F}\right)_b^{(+1)} \frac{f_1(\omega_a+\omega_b)\tau_{c0}}{\sqrt{1+(\omega_a+\omega_b)^2\tau_{c0}^2}}.\end{aligned} \tag{8.27}$$

The combinations, $(0,-1)$ and $(0,+1)$, can be derived from symmetry. These relations can be used to infer the values of f_1 and τ_{c0}. When τ_{c0} is very long, the flux amplitudes of these combinations

give f_1 directly.

The combinations where the final m value is 0 are a bit more complicated, since their ℓ values can either be 2 or 0 (see eq. [8.18]). Since the angular function of Y_2^0 (g_2^0) is consistently smaller than Y_{00} by at least a factor of 3, we neglect the Y_2^0 part here. The observed flux for the $m = 0$ components in the combination frequencies is therefore related to the principal modes as

$$\begin{aligned}\left(\frac{\delta F}{F}\right)_{(-1,+1)} &= \frac{0.265}{\sin^2\Theta_0}\left(\frac{\delta F}{F}\right)_a^{(-1)}\left(\frac{\delta F}{F}\right)_b^{(+1)}\frac{f_1(\omega_a+\omega_b)\tau_{c0}}{\sqrt{1+(\omega_a+\omega_b)^2\tau_{c0}^2}},\\ \left(\frac{\delta F}{F}\right)_{(0,0)} &= \frac{0.133}{\cos^2\Theta_0}\left(\frac{\delta F}{F}\right)_a^{0}\left(\frac{\delta F}{F}\right)_b^{0}\frac{f_1(\omega_a+\omega_b)\tau_{c0}}{\sqrt{1+(\omega_a+\omega_b)^2\tau_{c0}^2}},\end{aligned} \tag{8.28}$$

and symmetry gives $(\delta F/F)_{(+1,-1)}$. When f_1, τ_{c0} and all the amplitudes are known, the amplitude ratio between the $m = 0$ component of the combination frequencies and the main mode can be used to deduce Θ_0, the inclination angle of the rotation axis relative to the line of sight.

For a preliminary study, we choose $f_1 = 20$ (although the theoretical value of f_1 can fall anywhere between 10 and 30, depending on the star[6]), and $(\omega_a + \omega_b)\tau_{c0} = 10.0$.[7] This choice is based on the knowledge that $\omega_a\tau_{c0}$ and $\omega_b\tau_{c0}$ both have to be larger than unity for the two principal modes to be overstable (see Chap. 3). With these values, we have $f_1(\omega_a + \omega_b)\tau_{c0}/\sqrt{1 + (\omega_a + \omega_b)^2\tau_{c0}^2} = 19.9$. This quantity being much larger than unity is the main reason why we can see the combination frequencies, even though their principal modes are weak. The prediction for different components is listed in Table 8.1 for the combination of $(k = 15) + (k = 13)$. Both the absolute amplitudes and the relative sizes for different components agree with our predictions. Orientation of the rotation axis cannot be constrained well. Our solution for Θ_0 ranges from 20 deg to 70 deg. Either the time-varying nature of the mode amplitudes, or the inconsistencies in the theory, prevents us from obtaining a perfect fitting (accurate down the observational errors).

2) *Combination Frequencies at Large*

With other principal modes also contributing to the combination frequencies, we have extra handles on the problem. We list in Table 8.2 the observed flux variations of the identified eigenmodes and their combinations in GD358.

First, we infer the values of τ_{c0} for this star arguing that the longest overstable mode in the star is likely to satisfy $\omega\tau_{c0} \sim 1$. This gives rise to $\tau_{c0} \sim 130$ s.

Second, we try to infer τ_{c0} using equation (8.16), which estimates the amplitude ratio for the pair of combination frequencies that are the sums and differences of the same pair of principal modes respectively. When assuming that only the two ($m = 0$) components from the principal modes

[6]Here, we assume the DB white dwarf is qualitatively similar to a DA in the upper atmoshphere.

[7]The prediction for the amplitudes only changes by a factor of 1.4 when this number changes from 1 to 1000. This also means that the amplitudes of the combination frequencies are not sensitive measures for the depth of the convection zone.

observed freq. ν (μHz)	Parent Modes $k = 13$ & $k = 15$				amplitude (mma)	predicted amplitude (mma)
	m_a	(mma)	m_b	(mma)		
3033.07	-1	6.28	-1	9.33	< 0.1	0.19
3038.65	0	5.78	-1	9.33	< 1.0	0.60
3039.0	-1	6.28	0	19.03	1.55	1.34
3044.5	0	5.78	0	19.03	2.14	$0.29/\cos^2\Theta_0$
3044.76	+1	5.46	-1	9.33	< 1.5	$0.13/\sin^2\Theta_0$
3046.0	-1	6.28	+1	9.27	1.79	$0.15/\sin^2\Theta_0$
3050.5	+1	5.46	0	19.03	1.12	1.16
3051.5	0	5.78	+1	9.27	0.84	0.60
3057.5	+1	5.46	+1	9.27	0.92	0.17

Table 8.1: Pulsation amplitudes for different components in the $(k = 13) + (k = 15)$ combination. The observed values are adapted from Figure 8 of Winget et al. (1994), some of them are upper-limit estimates based on that figure. The frequency (ν) here is measured in cycle-per-sec, while the frequency in the text (ω) is in radian-per-second, $\nu = \omega/2\pi$. This is true for all later figures and tables. The amplitudes are in unit of mma.

contribute, the angular dependence disappears and we have

$$\frac{c_2}{d_2} = \frac{(\omega_a - \omega_b)}{(\omega_a + \omega_b)} \frac{\sqrt{1 + (\omega_a + \omega_b)^2 \tau_{c0}^2}}{\sqrt{1 + (\omega_a - \omega_b)^2 \tau_{c0}^2}}. \tag{8.29}$$

Using the pair of $(15 - 17)$ and $(15 + 17)$, we obtain $\tau_{c0} = 1300\,\mathrm{s}$; while from the pair of $(9 - 15)$ and $(15 + 9)$, there is no physical solution for τ_{c0}. There are three possible reasons for the incompetence of this method. The signal-to-noise ratio is low in the low frequency range, and the observation suffers strongly from systematic and random errors caused by perturbations in the earth's atmosphere.[8] Also, in reality, various components from the principal modes contribute to the combination frequencies. Moreover, the amplitudes of the principal modes are observed to vary during the whole run.

Third, we attempt to fit the amplitude spectrum of all combination frequencies with only two free parameters, $f_1/\cos^2\Theta_0$ and τ_{c0}. We have limited information about the m values of the combination frequencies. Judging from their frequencies, most of them are likely combinations $(m = 0) + (m = 0)$ or $(m = -1) + (m = +1)$. Here, we adopt $(m = 0) + (m = 0)$ and use the second equation in (8.28). The best solution found is plotted in Figure 8.4.[9]

Our conclusion from the three exercises in this section is that τ_{c0} for GD358 falls between 400 s to 1000 s. $\Theta_0 \sim 70\,\mathrm{deg}$ when a value of $f_1 = 20$ is used. We provide reasonable fits to the observed

[8] This is unfortunate, since the amplitudes in the low frequency range are most sensitive to τ_{c0}.

[9] We do not attempt to estimate the amplitudes for the three mode combinations (e.g., $(17 + 17 + 17)$). But as we mentioned before, a rough order of magnitude estimate yields similar magnitudes for these frequencies and those involving only two.

frequency (μHz)	tentative identification k	m	amplitude (mma)	frequency (μHz)	tentative identification k	m	amplitude (mma)
130.19	15 - 17	?(-2,0,+2)	3.18	2150.57	9	-1	1.45
726.82	9 - 15	?(0)	1.73	2154.10	9	0	4.53
846.21	8 - 14	?(-2)	2.05	2157.67	9	1	2.72
937.87	8 - 15	?(-2)	1.71				
1233.5	18	0(?)	$\sim$ 3.0	2358.85	8	-1	4.86
1291.00	17	-1	4.95	2362.56	8	0	4.98
1297.58	17	0	14.5	2366.46	8	1	3.51
1304.12	17	1	5.84				
				2531.02	18 + 17	?(0)	1.54
1355.58	16	-1	1.55	2595.23	17 + 17	?(0)	1.98
1361.85	16	0	3.46	2660.84	18 + 15	?(0)	2.31
1368.50	16	1	2.66	2724.96	17 + 15	?(0)	4.34
				2816.62	17 + 14	?(0)	1.74
1421.27	15	-1	9.33	2848.28	15 + 15	?(-1)	1.9
1427.27	15	0	19.03	2913.94	17 + 13	?(0)	1.57
1434.04	15	1	9.27	2946.65	15 + 14	?(0)	4.46
				3044.66	15 + 13	?(0)	2.17
1512.72	14	-1	3.55	3124.38	17 + 11	?	0.66
1518.95	14	0	8.35	3296.02	17 + 10	?(+1)	0.67
1525.62	14	1	4.29	3451.95	17 + 9	?(0)	1.46
				3581.47	15 + 9	?(0)	1.11
1611.80	13	-1	6.28	3660.00	17 + 8	?(0)	1.11
1617.38	13	0	5.78	3789.86	15 + 8	?(0)	2.03
1623.49	13	1	5.46	3892.41	17 + 17 + 17	?	0.85
				3958.23	17 + 17 + 16	?	1.10
1733.88	12	0	1.34	4022.65	17 + 17 + 15	?	1.33
				4114.34	17 + 17 + 14	?	0.57
1840.46	11	-1	1.61	4152.33	17 + 15 + 15	?	0.79
1845.88	11	0	1.34	4211.58	17 + 17 + 13	?	0.84
1852.12	11	1	1.26	4244.25	17 + 15 + 14	?	1.55
				4342.55	17 + 15 + 13	?	0.75
1989.26	10	-1	0.55	4725.19	8 + 8	?(0)	0.94
1993.68	10	0	1.09	4879.23	17 + 15 + 9	?	0.69
1998.83	10	1	1.22				

Table 8.2: Frequencies at which power is seen in GD358, with their possible identifications. Compiled using Table 2 and Table 3 of Winget et al. 1994. The m values for the combination frequencies are guessed based on their exact frequencies.

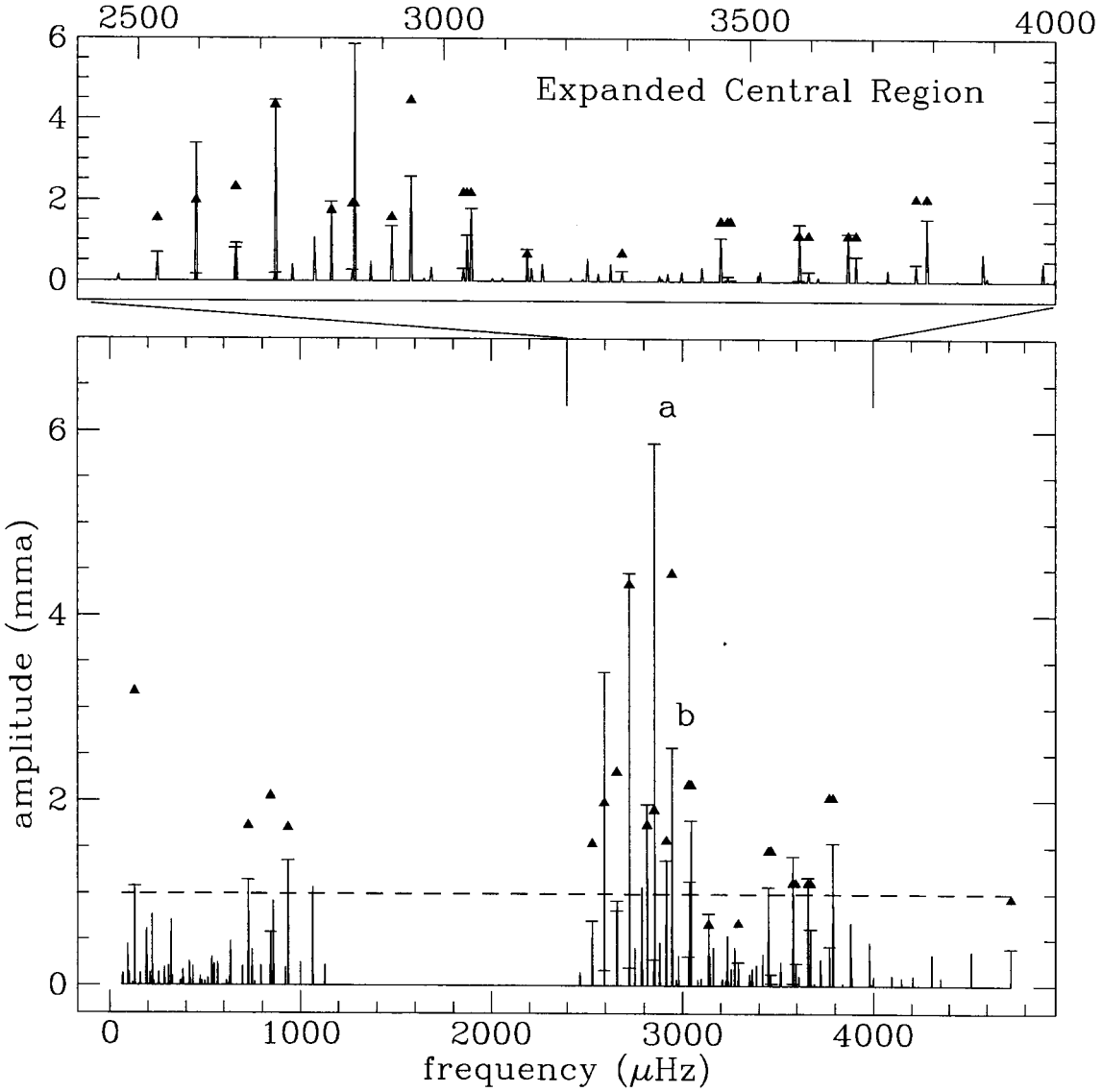

Figure 8.4: The observed and theoretical amplitudes of combination frequencies in GD 358. The observed values are marked with solid triangles. And the theoretical best fit solution ($f_1/\cos^2\Theta_0 = 133$, $\tau_{c0} = 400\,\mathrm{s}$) brings about combination frequencies with amplitudes marked by the solid vertical lines. The horizontal bars are plotted on top of those that are believed to have observed counterparts. The dashed line at 1 mma is the approximate detection limit in this WET observation. The top panel is the expansion of the central region in the lower panel. Two obvious misfits at 2848.28νHz (marked 'a' in the lower panel) and 2946.65νHz (marked 'b') can both be due to the inappropriate adoption of m components for the principle modes in the theory. a is likely to have $m = -1$, although it is mysterious why the $m = 0$ component, presumably the strongest combination component, does not appear in the power spectrum. b is likely to be the composite result of three pairs of principle modes with different m values. All combinations that are predicted to be observable are seen.

number	identification	amplitude (mma)	phase (deg)	freq. ν (μ Hz)	period (s)
1	F1-F3	7.0(0.7)	-0.2(6.3)	98.15	10188.93
2	F1-F4	4.0(0.7)	-46.6(10.9)	341.72	2926.34
3	F1-F2	6.4(0.7)	27.1(6.4)	403.67	2477.26
4	F6-F1	2.7(0.7)	25.7(15.5)	699.42	1429.75
5	F7	5.5(0.7)	-169.3(8.5)	900.44(4.43)	1110.57(5.46)
6	F2	27.0(0.7)	-71.3(2.0)	1224.66(0.76)	816.55(0.50)
7	F4	9.1(0.7)	-44.5(5.8)	1286.61(2.82)	777.24(1.70)
8	F3	14.6(0.7)	41.9(3.2)	1530.19(1.46)	653.52(0.62)
9	F1	31.8(0.7)	134.7(1.5)	1628.33(0.7)	614.13(0.26)
10	F5-F1	3.6(0.7)	-13.4(12.6)	1897.83	526.92
11	F6	6.3(0.7)	-16.4(7.1)	2327.76(3.28)	429.60(0.61)
12	F2+F2	9.8(0.7)	34.4(5.2)	2449.32	408.28
13	F3+F2	5.2(0.7)	24.2(8.2)	2754.85	363.00
14	F2+F1	8.3(0.7)	-3.4(5.1)	2852.99	350.51
15	F4+F1	4.7(0.7)	23.9(9.3)	2914.94	343.06
16	F3+F1	5.3(0.7)	-9.8(7.8)	3158.52	316.60
17	F1+F1	4.5(0.7)	13.0(9.1)	3256.66	307.06
18	F5	5.8(0.7)	-63.1(7.3)	3526.17(3.05)	283.59(0.25)
19	F6+F1	2.8(0.7)	-49.0(14.9)	3956.09	252.78
20	F5+F1	3.5(0.7)	12.8(12.6)	5154.50	194.01

Table 8.3: The power spectrum of ZZ Psc (a tabular form of Figure 8.1, van Kerkwijk et al. 1998). The errors for the amplitudes, phases, and periods of the principal frequencies are included in the parentheses behind the fitting result. The fitting routine is such that the combination frequencies are fixed once their parent modes' frequencies are found. The phases of the combination frequencies are defined as the difference between their real phase and those of their parent modes, i.e., $\phi - (\phi_a \pm \phi_b)$, + sign is taken when $\omega = \omega_a + \omega_b$, and vice versa.

amplitudes based on simple assumptions. This gives confidence that with a better data set (taking away the effect of time-varying ampltiudes), we will be able to determine the stellar parameters quite well.

8.3.2 ZZ Psc

ZZ Psc (variable name G29-38) is a relatively cool DA variable with large amplitudes. It has been observed many times (see, Kleinman 1995). Everytime, it seems, the power spectrum is different. Observers say this star has many 'states'.

The data presented in Table 8.3 were taken with the Keck II telescope in November 1996. The total time duration is about five hours. We choose to use this short data set instead of many other much longer ones in favour of its high signal-to-noise ratio and the absence of complications due to mode varying. The disadvantage is the possibility of mode beating, especially among multiplets split by rotation. Kleinman (1995) suggests a rotation period of order ten days for this star; this may

imply little beating during the observation. We ignore it here. And as before, we assume all principal modes are $\ell = 1$, and only their $m = 0$ components contribute to the combination frequencies.

Analogous to what we do in §8.3.1, we search for the best solution of $f_1 / \cos^2 \Theta_0$ and τ_{c0} to match the observed power spectrum of combination frequencies. This is shown in Figure 8.5. Compared to results in Figure 8.4, the fit for ZZ Psc is far more successful. Our best solution gives $\tau_c \sim 200\,\mathrm{s}$, which implies $\omega\tau_c \sim 1.1$ for the longest period overstable mode, consistent with our driving theory in Chap. 3.

There are a few oddities in the general good fitting of Figure 8.5. We have not been able to fit 'a' with any success. The amplitude at this very low frequency may be subject to contamination from other sources that have similar time span, e.g., telescope noise and quasi-periodic fluctuations in the earth atmosphere. Mode F1 (at 614.26 s) is the largest mode during the Keck observation. It is a mystery to us why the second harmonic of F1 ('d') should be so weak, as it is expected to show the largest amplitude among all combination frequencies.[10] Spectroscopic evidence suggests that F_4 mode is $\ell = 2$ (van Kerkwijk et al. 1998); this might explain the underestimated amplitude in 'b' ($F_4 - F_1$). We have no answer for the inconsistency seen at frequency 'c' ($F_2 + F_1$).

The phases of combination frequencies are good indicators of τ_{c0} without the interference of inclination angle and f_1. But we have not been able to obtain useful information from the phase angles in Table 8.3. This is a good test of our theory and should be worked out in the future.

With a $\tau_c \sim 200\,\mathrm{s}$, ZZ Psc is situated relatively close to the red edge of the DA instability strip. At the blue end, one would expect $\tau_c \sim 20\,\mathrm{s}$.

Bibliography

Bergeron, P., Fontaine, G., Brassard, P., et al. 1993, AJ, 106, 1987

Brassard, P., Fontaine, G., & Wesemael, F. 1995, ApJS, 96,545

Brickhill, A. J. 1992, MNRAS, 259, 519

Clemens, J. C., 1993, Baltic Astronomy, 2, 407

Dziembowski, W. 1983, Acta Astron., 32, 147

Fontaine, G., Bergeron, P., Vauclair, G., Brassard, P., Wesemael, F., Kawaler, S. D., Grauer, A. D., & Winget, D. E. 1991, ApJ, 378, L49

Kepler, S. O., Robinson, E. L., Nather, R. E., & McGraw, J. T. 1982, ApJ, 254, 676

[10] Similar phenomenum is seen in Figure 8.4 (the 'a' point). There it might be because of the incorrect m value used in the theoretical estimate. Is it true here as well? What happens to the $m = 0$ combination? Could there be any physical mechanism in the star that preferrentially suppresses combinations of dominant modes relative to other combinations?

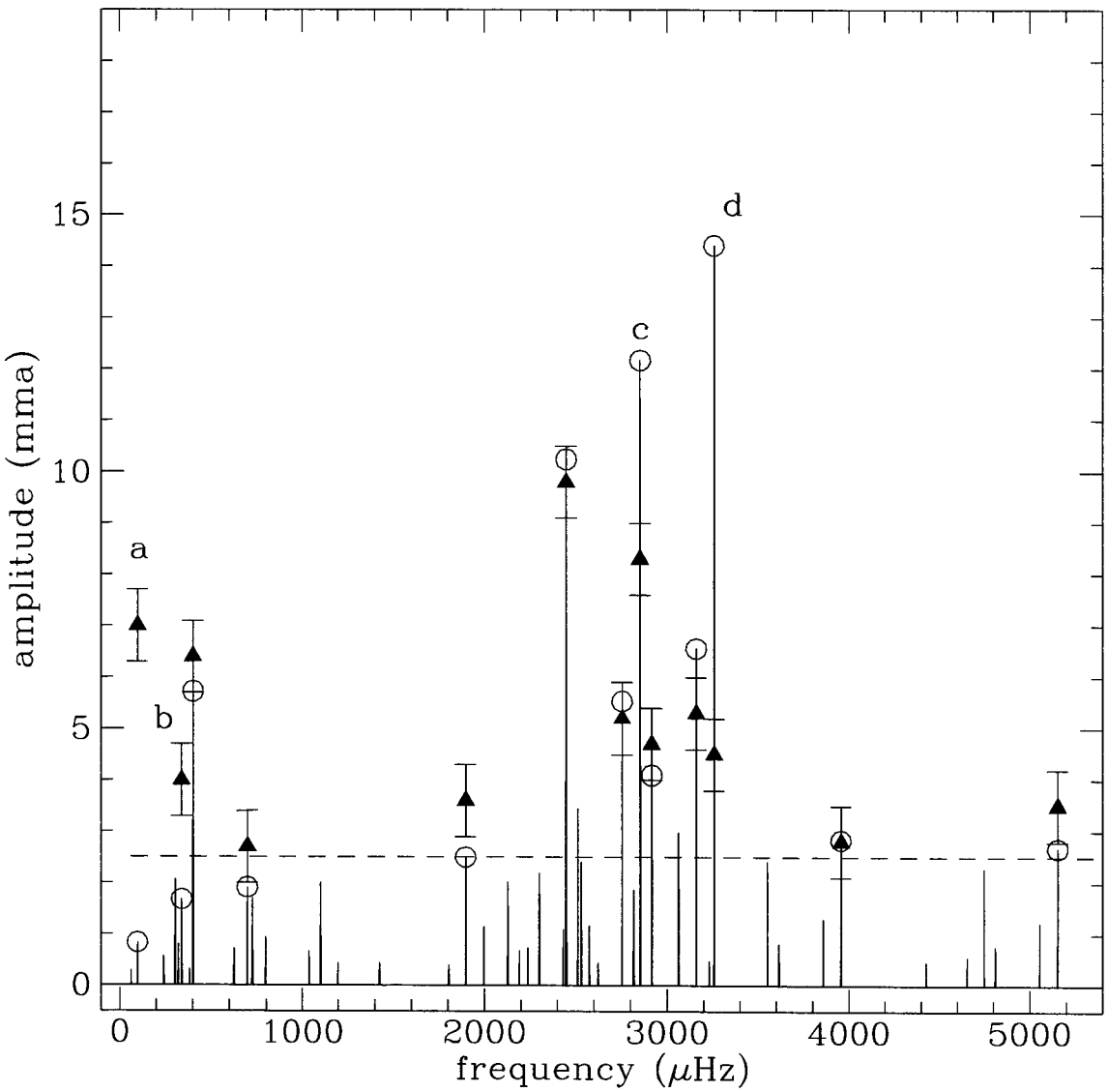

Figure 8.5: A comparison between theory and observation in the case of ZZ Psc. This figure is similar to Figure 8.4, but with horizontal bars substituted with open circles. Realistic error estimates are in dashed lines. The best solution shown here has $f_1/\cos^2\Theta_0 = 120$, $\tau_c = 200\,\mathrm{s}$. We could not obtain any reasonable solution that fits the amplitude for the lowest frequency (labeled 'a'). There are also some other inconsistencies between our best fit and the data, labeled 'b', 'c' and 'd' respectively. Most signifcantly, the predictions of 'd' by any reasonable solution always much exceed the observed value.

Kleinman, S. J., Nather, R. E., Winget, D. E., et al. 1994, ApJ, 436, 875

Kleinman, S. J., 1995, Ph.D. thesis, University of Texas at Austin

McGraw, J. T. 1976, ApJ, 210, L35

McGraw, J. T. 1978, in Current Problems in Stellar Pulsations and Instabilities, ed. Fischecl D., Lesh J. R., & Sparks, W. M., (NASA technical memorandum)

O'Donoghue, D., Warner, B., & Cropper M. 1992, MNRAS, 258, 415

Robinson, E. L., Stover, R. J., Nather, R. E., & McGraw, J. T. 1978, ApJ, 220, 614

Winget, D. E., Nather, R. E., Clemens, J. C., et al. 1990, ApJ, 357, 630

Winget, D. E., Nather, R. E., Clemens, J. C., et al. 1994, ApJ, 430, 839

van Kerkwijk, M. H., et al. 1998, in preparation

Appendix A Index of Variables

White Dwarf

z, z_b	$z = R - r$, R is the stellar radius, z_b, the depth of the convection zone
H_p	pressure scale-height, $H_p \equiv \frac{p}{g\rho}$
c_s	local sound speed, $c_s^2 \equiv (\frac{\partial p}{\partial \rho})_s \equiv \Gamma_1 \frac{p}{\rho}$
N^2	Brunt-Väisälä Frequency squared
L_ℓ	Lamb frequency for spherical degree ℓ, $L_\ell^2 \equiv \ell(\ell+1)(\frac{c_s}{r})^2$
κ	radiative opacity
s	dimensionless specific entropy (measured in units of k_B/m_p)
$\tau_{\rm th}$	local thermal time scale, $\tau_{\rm th} \equiv \frac{1}{F}\int_0^z dz\, \rho c_p T \frac{k_B}{m_p}$
τ_b	similar to $\tau_{\rm th}(z = z_b)$, $\tau_b \equiv \frac{1}{F}\int_0^z dz\, \rho T \frac{k_B}{m_p}$
A, B, C	dimensionless numbers defined in §3.2.4
τ_c	thermal adjustment time scale for the convection zone, $\tau_c = (B + C)\tau_b$
∇, $\nabla_{\rm ad}$	$\nabla \equiv (\frac{d\ln T}{d\ln p})$, $\nabla_{\rm ad} \equiv (\frac{d\ln T}{d\ln p})_s$
p_ρ, p_T	$p_\rho \equiv \left(\frac{\partial \ln p}{\partial \ln \rho}\right)_T \equiv \chi_\rho$, $p_T \equiv \left(\frac{\partial \ln p}{\partial \ln T}\right)_\rho \equiv \chi_T$
$p_{\rho T}$, $p_{\rho\rho}$, p_{TT}	$p_{\rho T} \equiv \left(\frac{\partial p_\rho}{\partial \ln T}\right)_\rho$, $p_{\rho\rho} \equiv \left(\frac{\partial p_\rho}{\partial \ln \rho}\right)_T$, $p_{TT} \equiv \left(\frac{\partial p_T}{\partial \ln T}\right)_\rho$
s_ρ, s_T	$s_\rho \equiv \left(\frac{\partial s}{\partial \ln \rho}\right)_T$, $s_T \equiv (\frac{\partial s}{\partial \ln T})_\rho \equiv c_v$
$s_{\rho T}$, $s_{\rho\rho}$, s_{TT}	$s_{\rho T} \equiv \left(\frac{\partial s_\rho}{\partial \ln T}\right)_\rho$, $s_{\rho\rho} \equiv \left(\frac{\partial s_\rho}{\partial \ln \rho}\right)_T$, $s_{TT} \equiv (\frac{\partial s_T}{\partial \ln T})_\rho$
ρ_s, T_s	$\rho_s \equiv \left(\frac{\partial \ln \rho}{\partial s}\right)_p$, $T_s \equiv (\frac{\partial \ln T}{\partial s})_p \equiv 1/c_p$
$t_{\rm cv}$	dynamical time in the convection zone, or eddy turn-over time, $t_{\rm cv} \sim \frac{H_p}{v_{\rm cv}}$
$v_{\rm cv}$	convective velocity for the largest eddies
ν	kinematic viscosity coefficient, $\nu \sim v_{\rm cv} H_p$

Gravity Mode

n, ℓ, m	radial, angular, azimuthal eigennumbers of the eigenmodes
ω, ν	eigenfrequencies, $\omega = \frac{2\pi}{\text{period}}$, $\nu = \frac{1}{\text{period}}$
ξ_h, ξ_z	horizontal and vertical displacements of the eigenfunction (or their radial dependences only, depending on the context)
k_z, k_h	vertical and horizontal wave-vectors, $k_z \sim \frac{d}{dz}$, $k_h \sim \frac{d}{dx} \sim \frac{\sqrt{\ell(\ell+1)}}{R}$
v_{gz}	group velocity for the wave in the z direction, $v_{gz} \equiv \frac{\partial \omega}{\partial k_z}$
$\mathcal{F}$	energy flux in the wave, $\mathcal{F} \equiv \rho v_{gz} \omega^2 (\xi_h^2 + \xi_z^2)$
$\frac{\delta p}{p}, \frac{\delta \rho}{\rho}, \frac{\delta T}{T}$	fractional Lagrangian pressure, density and temperature perturbations
p'	Eulerian pressure perturbation
δF_r,$\delta F_{\rm cv}$, δs	Lagrangian radiative flux, convective flux, entropy perturbations
$\delta s_{\rm ph}$, δs_b	entropy perturbations at the photosphere and at z_b respectively
$\delta F_{\rm ph}$, δF_b	flux perturbations at the photosphere and at z_b
δQ	heat absorbed/released by the convection zone during pulsation
z_1 (z_u)	the upper lid of the g-mode's propagating cavity, approximately the first node of $\frac{\delta p}{p}$, z_1 is pushed down when the convection zone reaches deeper
z_ω	$z_\omega \equiv \frac{3}{2}\frac{\omega^2}{g k_h^2}$, $z_1 \sim z_\omega$ when the convection zone is negligible
z_ℓ	the lower boundary of g-mode propagating cavity, here $\omega^2 \sim N^2$
τ_1, τ_ω	the thermal time at the depth of z_1 and z_ω
$\langle W \rangle$	work done to the mode after one cycle of pulsation
$\langle W_{\rm cvz} \rangle$, $\langle W_{\rm rad} \rangle$	work from the convective and the radiative regions
γ	growth/damping rate for the mode energy
$\gamma_{\rm cvz}$, $\gamma_{\rm rad}$	energy growth/damping rates from the convective and the radiative regions
$\gamma_{\rm vis}$	energy damping rate from kinematic viscosity
ω_i	the imaginary part of the eigenfrequency, it is also the amplitude growth/damping rate, $\omega_i \sim \frac{\gamma}{2}$
C_D	drag coefficient relating shear stress to velocity gradient

Appendix B Atmospheric Models for Hydrogen White Dwarfs

B.1 Introduction

The depth of the convection zone for white dwarfs residing inside the DA instability strip depends extremely sensitively on the effective temperature. The sensitivity originates from the photosphere where hydrogen is partially ionized. The ionization fraction depends sensitively on temperature, which gives rise to the sensitive dependence on temperature of both the photospheric entropy and the superadiabatic gradient below the photosphere. The depth of the convection zone is determined by these two quantities, as the radiative interior converges quickly for different temperatures (see Fig. B.1).

For our study, we need white dwarf models with fine grids in the upper atmosphere (especially in the superadiabatic region) so that the above mentioned sensitive dependence is correctly captured; we also need models closely neighbouring each other across the whole range of the instability strip. Both these considerations require us to make new white dwarf models, in addition to the ones kindly provided to us by P. Bradley (for reference, see Bradley et al. (1993). These series of closely neighboured models can be used not only to study the linear instability of gravity-modes inside the instability strip, but also to study the effect of finite amplitude pulsations, since at any phase during the pulsation, the upper atmosphere is in both dynamical and thermal equilibrium.

DA white dwarfs with effective temperatures around $12,000\,\mathrm{K}$ have long finished their gravitational settling of the elements. In the outer layer of the star, the composition is effectively pure hydrogen. Stars cooler than the DA instability strip may have chemical mixing when the convection zone reaches down towards the helium layer.

When the stellar surface gravity ($\log g$), stellar mass, and the effective temperature (T_{eff}) are specified, the photosphere can be located (in terms of pressure), and inward integration can be carried out to construct the upper atmosphere of the star. This procedure is accurate as long as the depth of the region we are working on is much smaller than the stellar radius. We only work with pure hydrogen; this eliminates the uncertainty in specifying helium-hydrogen interface.

We will compare our models with those from Bradley, and try to explain the differences. Later, we will use these new models to calculate various gravity-modes.

B.2 Model Making

B.2.1 Hydrogen Models

We use the Lawrance Livermore equation of state and opacity table (Rogers et al. 1996, Iglesias & Rogers 1996). The tables and the interpolation programs are from the ftp://dplasma.llnl.gov/.

The stellar photosphere is defined as the place where optical depth reaches 2/3 (Rybicki & Lightman 1979, Mihalas 1978). For given opacity and equation of state, $T_{\rm eff}$ determines the photospheric pressure and the opacity. For a radiative photosphere in hydrostatic equilibrium, $F_{\rm rad} = F$, and gas pressure is given by

$$p = \frac{2}{3}\frac{g}{\kappa}. \tag{B.1}$$

The condition of being radiative should be tested using the following criterion,

$$\frac{ds}{d\ln p} = \left.\frac{\partial s}{\partial \ln T}\right|_p \frac{F}{8\sigma T_{\rm eff}^4} + \left.\frac{\partial s}{\partial \ln p}\right|_T \leq 0. \tag{B.2}$$

Here, equation (B.1) is used, as well as the flux equation of radiative transfer.

When equation (B.2) is not true, i.e., the photosphere is partially convective, $F_{\rm rad} + F_{\rm cv} = F = \sigma T_{\rm eff}^4$, the partition of fluxes is determined by the following conditions:

$$\begin{aligned}
\left(\frac{ds}{d\ln p}\right)_{\rm rad} &= \left.\frac{\partial s}{\partial \ln T}\right|_p \frac{F_{\rm rad}}{8\sigma T_{\rm ph}^4} + \left.\frac{\partial s}{\partial \ln p}\right|_T, \\
\left(\frac{ds}{d\ln p}\right)_{\rm cv} &= f\left(-\left.\frac{\partial s}{\partial \ln \rho}\right|_p\right)^{\frac{1}{3}} \left(\frac{1}{\rho p}\right)^{\frac{1}{3}} \left(\frac{m_p}{k_B}\frac{F_{\rm cv}}{T_{\rm ph}}\right)^{\frac{2}{3}}, \\
\left(\frac{ds}{d\ln p}\right)_{\rm rad} &= \left(\frac{ds}{d\ln p}\right)_{\rm cv}.
\end{aligned} \tag{B.3}$$

The second equation in equation (B.3) is derived in §3.2.2 (eq. [3.12] to [3.15]). The dimensionless number f is defined to be the convective inefficiency in this appendix. The smaller value f takes, the more efficient the convection is. In the literature, convective efficiency is parametrized in terms of α, the ratio of the mixing-length to the pressure scale-height. The precise value of α not only lacks clear physical meaning but also depends upon the detailed implementation of the mixing-length ansatz. Two notations are related by $f \propto \alpha^{-4/3}$; the exact relation can be obtained by comparing stellar models of similar convection zones but different parametrization.

For a partially convective photosphere, photospheric temperature (where $p = \frac{2}{3}g/\kappa$) is different from the effective temperature, and is approximated by

$$\sigma T_{\rm ph}^4 = F_{\rm rad} + \frac{1}{2}F_{\rm cv}, \tag{B.4}$$

while the purely radiative case have $T_{\rm ph} = T_{\rm eff}$. The factor of $\frac{1}{2}$ in front of $F_{\rm cv}$ originates from the fact that in an optically thin region, the turbulent eddies carry heat flux in the form of kinetic energy and deposit it into the thermal energy of the local gas, which thereupon radiates half of that heat back into the star (isotropic radiation).

When the location of the photosphere is determined as a function of $T_{\rm eff}$ (or equivalently, the stellar flux F), we can integrate downward the following equations simultaneously,

$$\begin{aligned}
\frac{dp}{dz} &= \rho g, \\
\frac{d\ln T}{d\ln p} &= \left.\frac{\partial \ln T}{\partial \ln p}\right|_s + \left.\frac{\partial \ln T}{\partial s}\right|_p \frac{ds}{d\ln p}, \\
\frac{ds}{d\ln p} &= \left(\frac{ds}{d\ln p}\right)_{\rm rad} = \left(\frac{ds}{d\ln p}\right)_{\rm cv}, \\
\left(\frac{ds}{d\ln p}\right)_{\rm rad} &= \left.\frac{\partial s}{\partial \ln T}\right|_p \frac{3\kappa p F_{\rm rad}}{16\sigma T^4 g} + \left.\frac{\partial s}{\partial \ln p}\right|_T, \\
\left(\frac{ds}{d\ln p}\right)_{\rm cv} &= f\left(-\left.\frac{\partial s}{\partial \ln \rho}\right|_p\right)^{\frac{1}{3}} \left(\frac{1}{\rho p}\right)^{\frac{1}{3}} \left(\frac{m_p}{k_B}\frac{F_{\rm cv}}{T}\right)^{\frac{2}{3}}, \\
F_{\rm rad} + F_{\rm cv} &= F.
\end{aligned} \tag{B.5}$$

In the temperature range we are interested in, the photosphere (sometimes) and the region below it are convectively unstable. At reaching the bottom of the convection zone, $\frac{ds}{d\ln p} \leq 0$, the integration can be continued as long as we set $F_{\rm cv} = 0$, and ignore $\left(\frac{ds}{d\ln p}\right)_{\rm cv}$.

We integrate the model down to $\log p = 16.0$, which corresponds to a mass of $10^{-6} M_\odot$. For comparison, the mass of the convection zone at the very red end of the instability strip is of order $10^{-12} M_\odot$, while the generic hydrogen layer mass for DA white dwarfs is of order $10^{-4} M_\odot$. Furthermore, the depth corresponding to this pressure is of order 10^7cm, about a factor of 100 smaller than the total stellar radius, the thin-layer approximation is valid, and we can ignore curvature as well as changes in gravity.

B.2.2 Model Characteristics

Our white dwarf models consist of two layers, a convective envelope whose depth depends on the effective temperature sensitively, and a radiative region below it. Even at the bottom of the model, the effect of degeneracy is not important.

First, we look at the radiative regions in our models. We try to explain the convergence of entropy profile (and temperature, density, etc.) in the radiative interior (Fig. B.1), which is also witnessed by Brickhill (1991).

The radiative interior is governed by the equations of hydrostatic equilibrium and radiative diffusion, supplemented by the equation of state and the opacity law. With an opacity law specified

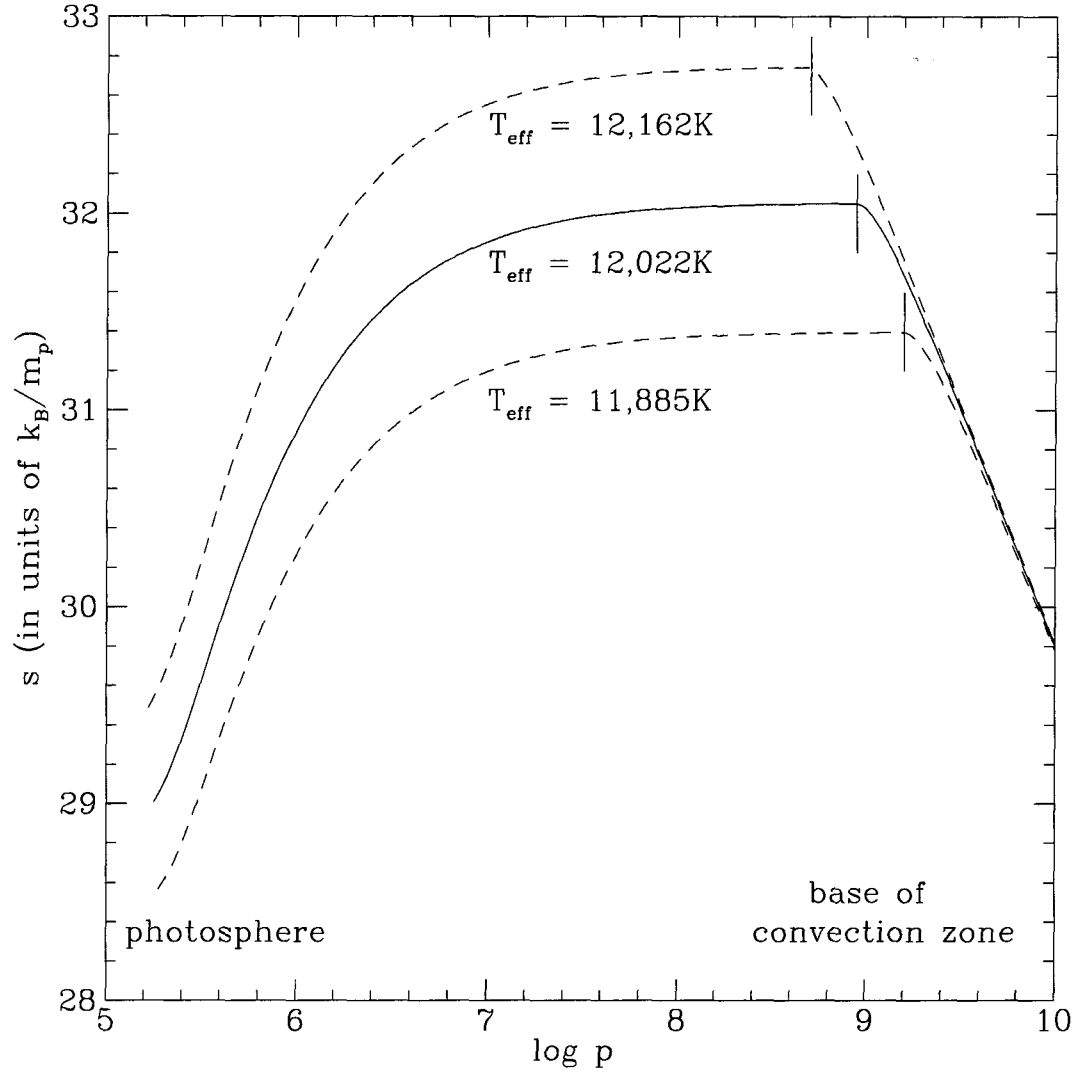

Figure B.1: Entropy profile for three adjacent white dwarf models. The superadiabatic region is emphasized by using $\log p$ as the horizontal axis. The bottom of the convection zone deepens extremely steeply with lower temperature. Notice the convergence onto an almost unique entropy profile in the radiative interior. A few quantities can be extracted from this graph and be compared with analytical estimates: the entropy jump in the superadiabatic zone, Δs; entropy at the photosphere and the base, $s_{\rm ph}$, s_b; the depth of the convection zone (in terms of τ_b) as a function of $T_{\rm eff}$. In this group of models, convective efficiency $f = 0.32$, and we will consistently stick to this f value in the whole thesis except as otherwise noted.

by two constant exponents, κ_ρ and κ_T, where

$$\kappa \propto \rho^{\kappa_\rho} T^{\kappa_T}. \tag{B.6}$$

It is easily verified that the envelope is a polytrope with $T \propto z$, $\rho \propto z^m$, and $p \propto z^{m+1}$, where z is the depth measured from the photosphere. More precisely, m is related to the opacity law as

$$m = \frac{-\kappa_T + 3}{\kappa_\rho + 1}, \tag{B.7}$$

and

$$T = \left[\frac{3(\kappa_\rho - \kappa_T + 4)}{4(\kappa_\rho + 1)} \left(\frac{\mu}{k_B}\right)^c \frac{EF}{acg}\right]^{1/(\kappa_\rho - \kappa_T + 4)} p^{(\kappa_\rho + 1)/(\kappa_\rho - \kappa_T + 4)}. \tag{B.8}$$

Using the numerical values $\kappa_\rho = 0.8$ and $\kappa_T = -5$, as are typical of fully ionized hydrogen gas, we obtain $m \approx 4$ and

$$T \propto F^{1/10} p^{1/5}. \tag{B.9}$$

The weak dependence of the temperature profile on the stellar flux, F, accounts for the convergence of the convective envelopes onto nearly the same $T - p$ relation in the radiative interior. For fully ionized ideal gas, $\Gamma_1 = 5/3$, and entropy is

$$s \propto \ln \frac{T^{5/2}}{p}. \tag{B.10}$$

This connects entropy with temperature and pressure, and it further leads to

$$s \propto -\frac{1}{2} \ln p, \tag{B.11}$$

i.e., s decreases with depth – the radiative zone is stably stratified as it must be.

Now we turn to the convection zone. Here, we focus on entropy. The newly made models can be used to measure the parameter B and C, as defined in equations (3.30) and (3.32). These two numbers reflect the changes of entropy levels when the stellar fluxes are changed. We estimate them from Figure B.1,

$$\begin{aligned} B &\sim 13.0, \\ C &\sim 4.4. \end{aligned} \tag{B.12}$$

For comparison, the analytical expressions for B and C (eqs. [3.31] and [3.33]) give

$$B \sim 10.6,$$

$$C \sim 5.4, \tag{B.13}$$

when we use equation of state and opacity of pure hydrogen. The two groups of numbers are in reasonable agreements. This is one piece of evidence that our pure hydrogen models reasonably, accurately describe the upper convection zones.

As stated in §B.1, we are mostly interested in the depth of the convection zone as a function of $T_{\rm eff}$. We can observe this from Figure B.2, for a variety of mixing-lengths. Shown in the figure is the thermal adjustment time at the base of the convection zone, $\tau_c = (B + C)\tau_b$, as well as the values of $(B + C)$. These quantities are defined in §3.2.4.

After the convection first appears at around $15,000\,\mathrm{K}$, the convection zone deepens with decreasing temperature. A smaller f indicates a more efficient convection, which needs a smaller entropy gradient in the superadiabatic layer, and therefore deepens the convection zone (recall that entropy increases outward in the radiative zone). But when temperature has become so low that superadiabatic region becomes less and less important as compared to the whole convection zone, there is a convergence in the depth of the zone for different values of f.

The deepening of the convection zone as a function of $T_{\rm eff}$ can be approximated by a scaling law,

$$\tau_c \propto T_{\rm eff}^{55}, \tag{B.14}$$

at the temperature range of $13,000\,\mathrm{K} \geq \mathrm{T_{eff}} \geq 12,000\,\mathrm{K}$ (for $f = 0.25$). This number is rather independent of the mixing-lengths as long as we measure it in the right region (i.e., τ_c between $100\,\mathrm{s}$ to $1000\,\mathrm{s}$). This dependence is much less steep than the one implied by Bradley's DA models, for which we find a power index more like 90. Our value widens the instability strip by a factor of 2 in $T_{\rm eff}$. We can also derive this dependence analytically, as is done in §B.5. This leads to a similar but less strong scaling relation, as the change in $(B + C)$ is not taken into account.

B.2.3 Model Comparisons

Our simple models can also be compared with Bradley's models in detail. Given our difference (as is discussed at the end of §B.2.2), sensible comparison are possible only when using models with the same depth of the convection zone. We accomplish this by adjusting the value of f such that at the same $T_{\rm eff}$, our convection zone extends to the same depth as Bradley's model. It is not consistent in the sense that neighbouring models would need different f. Two examples are shown, in Figure B.3 for a hotter model ($T_{\rm eff} = 12,420\,\mathrm{K}$), and Figure B.4, for a cooler one ($T_{\rm eff} = 11,720\,\mathrm{K}$). The individual comparisons are very good. Both the Brunt-Väisälä and the temperature, density profiles are similar. But the hotter one is with $f = 0.32$, while the cooler one needs a more efficient convection, $f = 0.20$. This may be understood as that models from Bradley

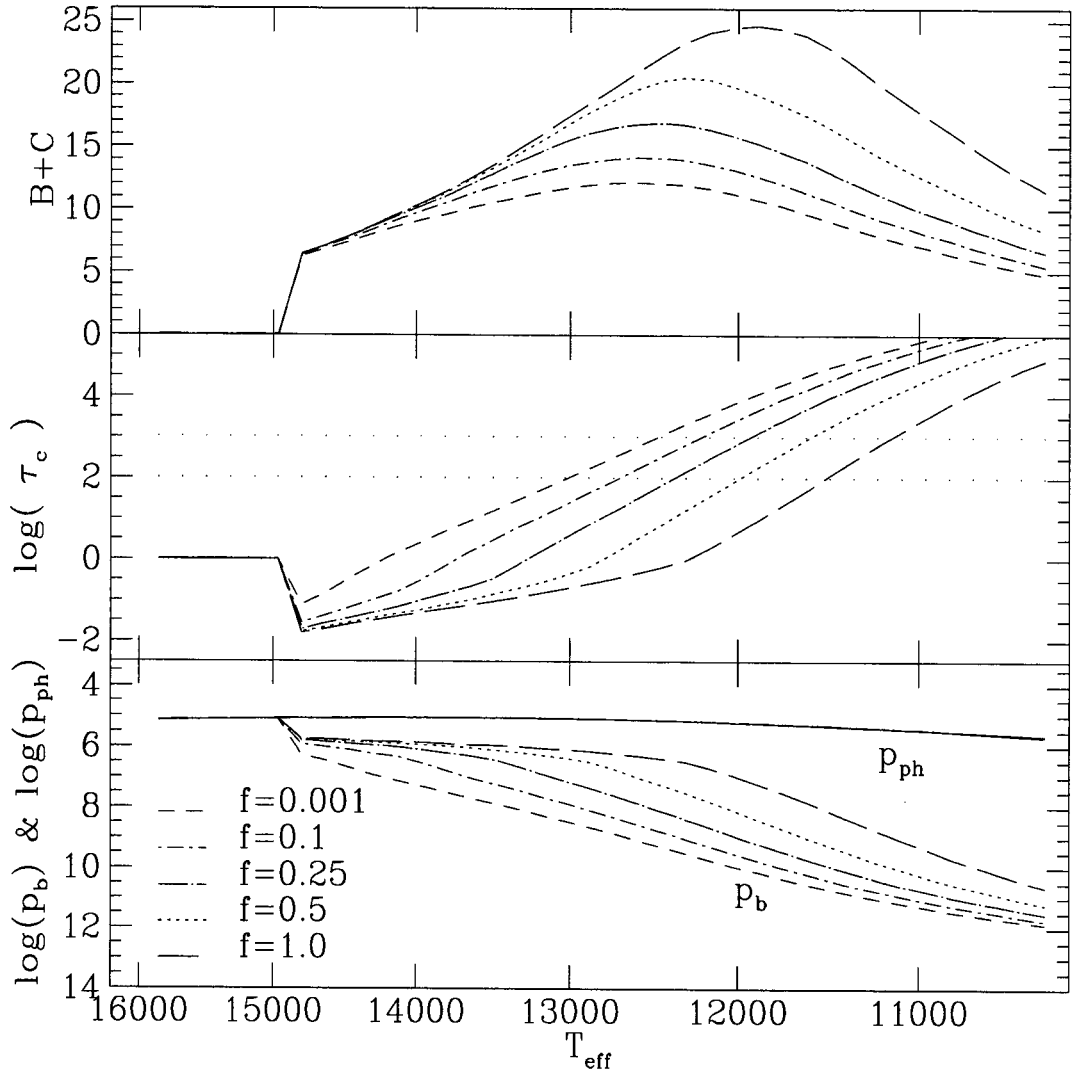

Figure B.2: The depth of the convection zone as a function of $T_{\rm eff}$ and the convective efficiency f. $f = 0.001$ corresponds to a model that has very small superadiabatic gradient in the whole convection zone, while $f = 1.0$ is for a model with very inefficient convection. Recall that $f \propto \alpha^{-\frac{4}{3}}$, where α is the mixing-length ratio. Independent of f, atmospheric convection sets in at around 15,000 K. The photosphere starts becoming convective at a temperature $T_{\rm eff} \sim 14,800$ K; this causes a kink in the depth of the convection zone, due to our approximate treatment of the photospheric temperature (eq. [B.4]). The photosphere returns to radiative at $T_{\rm eff} \sim 11,000$ K. The dotted horizontal lines in the center plot represents $\tau_c = 100$ s and 1000 s, corresponding to the shortest and the longest mode periods observed. The fiducial location of the ZZ Ceti instability strip as a function of the mixing-length ratio reads directly from this plot.

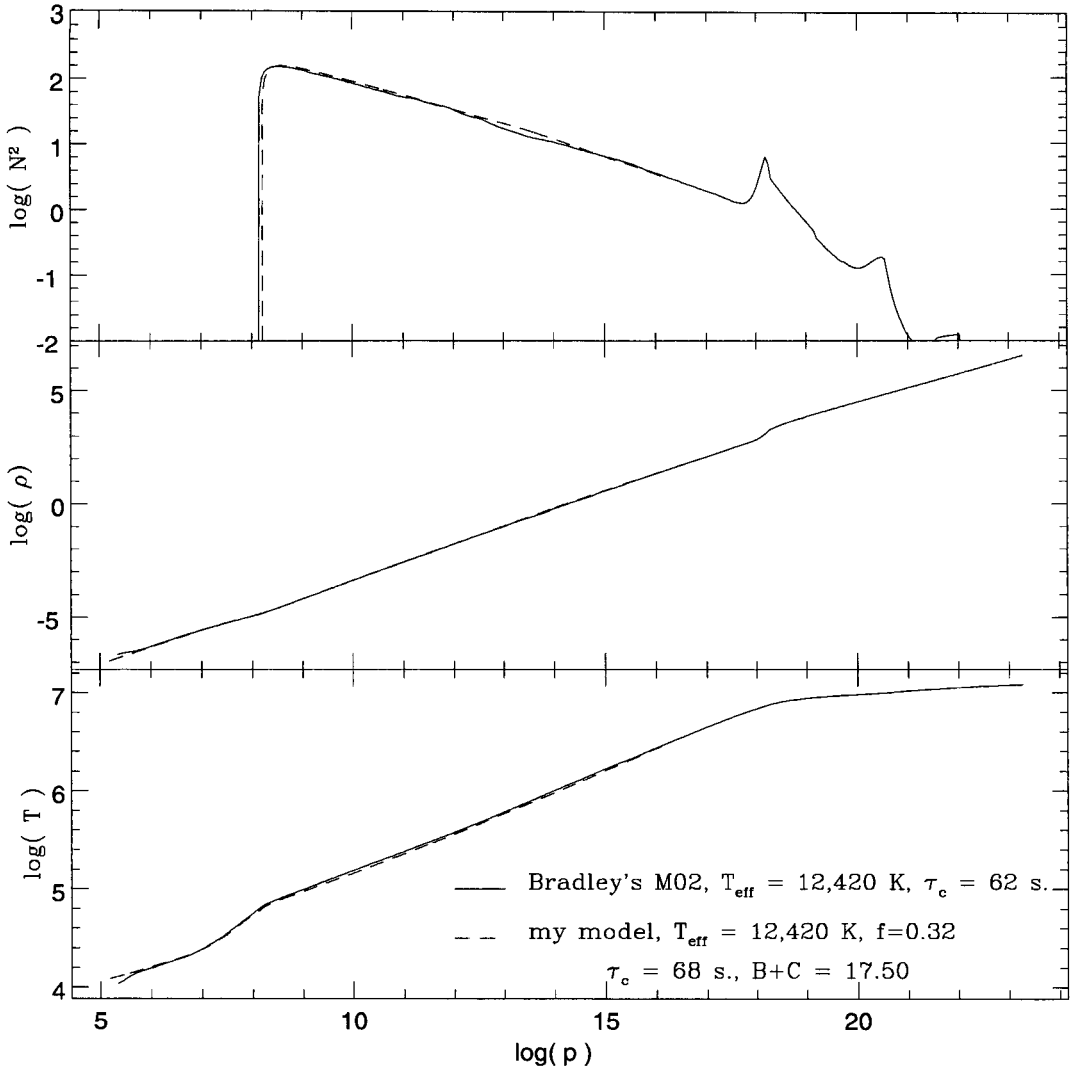

Figure B.3: Comparison between Bradley's model (solid lines that extend to the stellar center) and our simple model (dashed lines that go down to $\log p = 16$). At $T_{\rm eff} = 12,420\,{\rm K}$, we need $f = 0.32$ to reproduce the thickness of the convection zone as seen in Bradley's model.

have too deep a convection zone at the cooler temperatures, or the entropy jumps at his cooler models are smaller than our estimate. We suggest that insufficient grids in the upper atmosphere (especially the superadiabatic region) may be the reason for this behaviour. We would get a very narrow width for the DA instability strip if we use Bradley's models.

B.3 G-Modes

B.3.1 Mode Making

Since our white dwarf models do not go down all the way to the stellar center, we cannot obtain stellar eigenfrequencies. We could, however, use the eigenfrequencies from Bradley's models, and

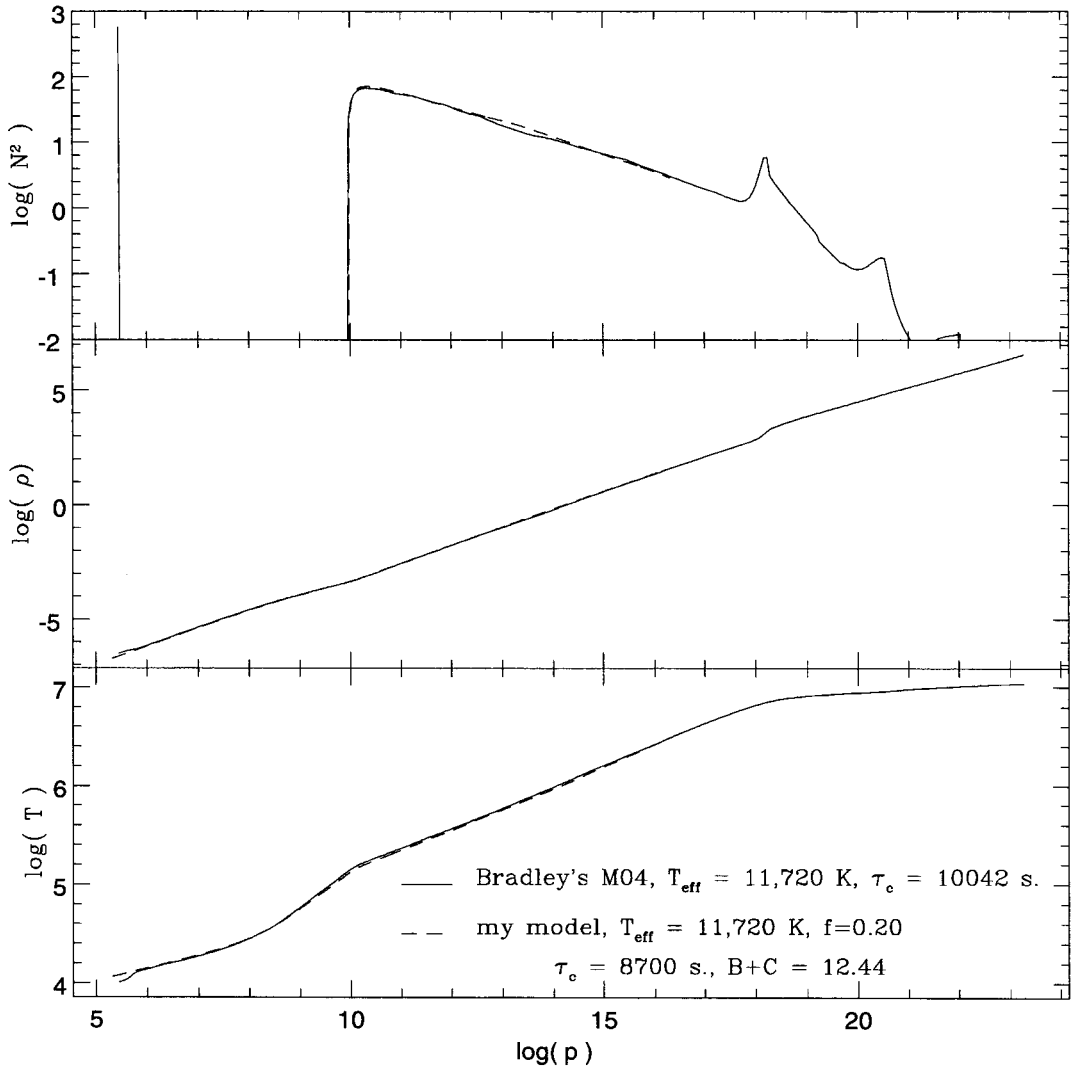

Figure B.4: Similar to Figure B.3, but for a cooler model, $T_{\rm eff} = 11,720\,{\rm K}$, M04 in Bradley's series of models. Here a much smaller f value is needed to fit his model, which implies that his cooler models are likely to have too deep a convection zone. The instability strip width obtained using his models would likely be narrower than that using our models (using the same value of f throughout).

calculate the corresponding eigenfunctions using our models. Since the eigenfrequencies do not depend sensitively on the temperature of the stars, or the depth of the convection zone (except for very high order modes), this treatment is not unreasonable. In this section, we take eigenfrequencies from Bradley's 12,820 K model.

Adopting $\delta p/p$ as the representative eigenfunction variable (instead of ξ_h, ξ_z or $\delta\rho/\rho$, $\delta T/T$), the equation for eigenfunction goes as (eq. [2.14]),

$$\frac{d^2}{d\ln p^2}\left(\frac{\delta p}{p}\right)+\frac{d}{d\ln p}\left(\frac{\delta p}{p}\right)+\left(\frac{p}{\rho g}\right)^2\left[k_h^2\left(\frac{N^2}{\omega^2}-1\right)+\left(\frac{\omega}{c_s}\right)^2\right]\left(\frac{\delta p}{p}\right)=0. \tag{B.15}$$

To integrate the above equation inward, the following two initial conditions are used, i.e., at $z=0$,

$$\begin{aligned}\frac{\delta p}{p} &= 0.01,\\ \frac{d}{d\ln p}\left(\frac{\delta p}{p}\right) &= \left[k_h^2\left(\frac{N^2}{\omega^2}-1\right)+\left(\frac{\omega}{c_s}\right)^2\right]\left(\frac{p}{\rho g}\right)^2\frac{1}{2-\frac{d\ln p}{d\ln\rho}}\frac{\delta p}{p}.\end{aligned} \tag{B.16}$$

The value 0.01 is an arbitrary number, taken such that the numerical accuracy is easily preserved throughout the integration. The second condition is derived by realizing that in the outer evanescent region, the boundary condition is basically free-slip, or, $\delta p/p$ is flat when approaching $z=0$. We assume that in equation (2.14), the second order derivative is much smaller in magnitude than the first order one.

Normalization as the kind illustrated in §2.7 is used.

B.3.2 Mode Comparisons

Integration of equation (B.15) gives rise to a 'partial' mode structure, which can be compared with the corresponding eigenmode in the 'full body' models made by Bradley, at least in the region where both exist. We compare modes in models that have the same $T_{\rm eff}$ and τ_c, as is shown in Figure B.5 for three different modes.

The conclusion in this section is, for the same stellar models and the same mode frequencies, the mode structure in our simple models are similar to those in the full-body models made by Bradley. These partial 'modes' will be used in Chapter 5 for nonadiabatic calculations.

B.4 Chemical Abundances

We can also construct upper atmosphere white dwarf models that have helium, or heavy metals (carbon, oxygen, etc.). This is to study the effect of chemical abundances on the depth of the convection zone. We find that chemical mixing would not significantly alter the depth of the convection

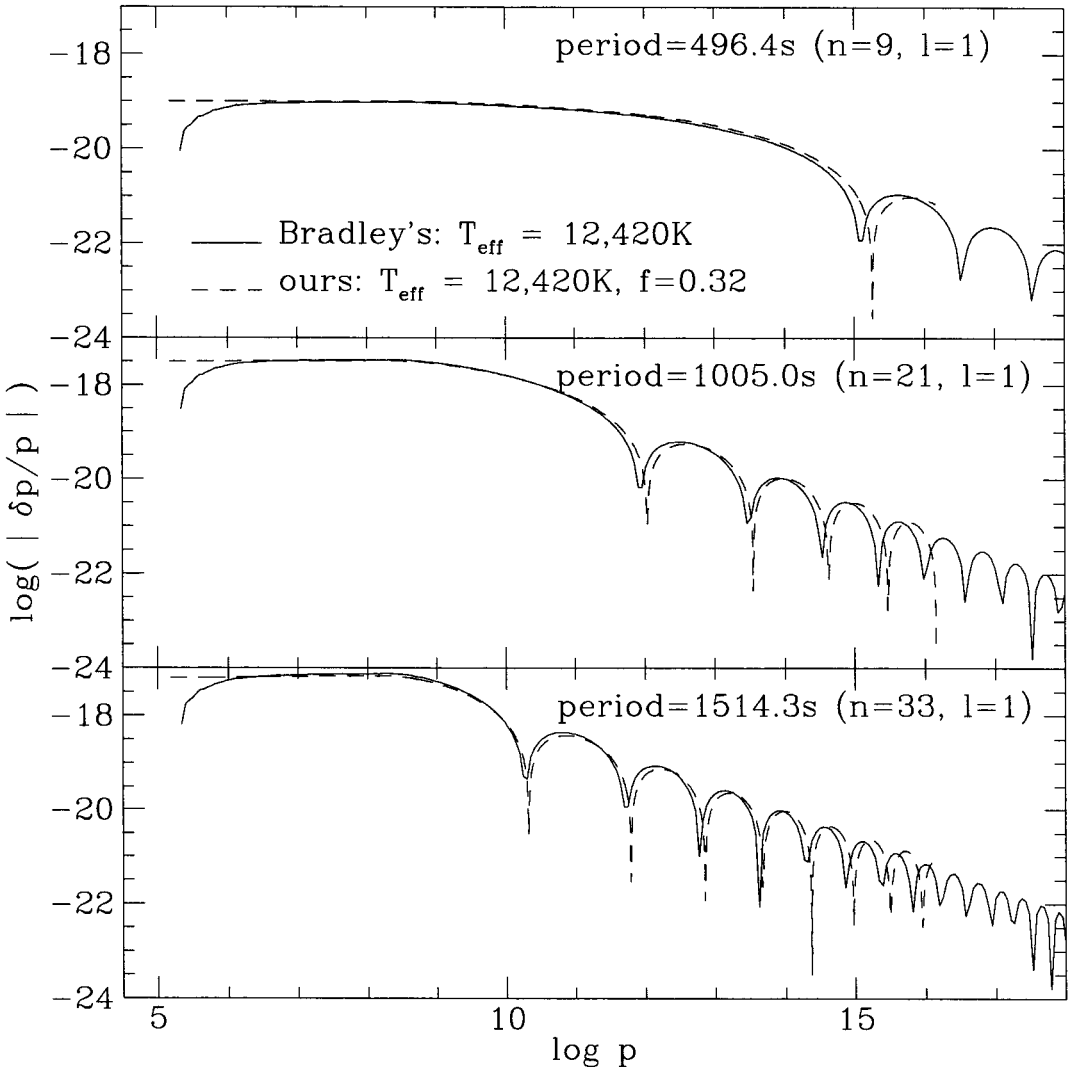

Figure B.5: Eigenmode structures calculated using one of Bradley's models (solid lines, $T_{\rm eff} = 12,420\,{\rm K}$, $\tau_c = 62\,{\rm s}$, normalized) and from one of our atmosphere models that have the same τ_b (dashed curves, $T_{\rm eff} = 12,420\,{\rm K}$, $f = 0.32$ and $\tau_c = 68\,{\rm s}$). Eigenfrequencies are taken from Bradley's model. The dashed curves are required to have the same magnitude at the surface as the solid ones.

zone, as long as the abundances are within ranges allowed by observations.

B.5 Instability Strip

Using hydrogen models made in this Appendix, we are able to estimate roughly the width of the ZZ Ceti instability strip.

The boundaries of the instability strip are determined by the dependence of τ_c on T_e. This dependence is complicated by our inability to calculate the superadiabatic gradient in the convection zone accurately based on First Principles. Common practice is to parameterize convective efficiency in terms of α, the ratio of the mixing-length to the pressure scale-height. Here, we use f, where $f \propto \alpha^{-4/3}$, to crudely estimate the entropy jump $s_b - s_{\rm ph}$ (as given by equation (3.14)).

Several steps are needed to determine the dependence of τ_c on T_e and α. Some require equation of state and/or opacity tables; we use those provided by LLNL. Given T_e, we find $\rho_{\rm ph}$ and $s_{\rm ph}$ by solving equation (3.18). Then for each choice of α (f), we obtain s_b from equation (3.14). Equating the radiative and adiabatic temperature gradients yields a second relation which together with the value of s_b enables us to solve for ρ_b, T_b, and p_b. We calculate τ_b from equation (3.35) after changing integration variable from z to p. Multiplying τ_b by $B+C$, obtained from equations (3.31) and (3.33), we arrive at τ_c. We describe a different numerical method to construct the convection zone in this Appendix. When given $T_{\rm e}$ and photospheric equation of state and opacity laws, other physical parameters of the photosphere is completely determined, taking into account the ratio of energy flux transported radiatively and convectively. Inward integration of the model is carried out with a certain mixing-length prescription of the entropy profile (quantified by the number f). The bottom of the convection zone is reached when the entropy gradient becomes negative inward. We construct a series of white dwarf models for a variety of mixing-length prescriptions.

We examine the dependence of τ_c on T_e and α in two ways. The first consists of analytical evaluation of the partial derivatives $\partial \ln \tau_c / \partial \ln T_e$ and $\partial \ln \tau_c / \partial \ln \alpha$. This approach has the benefit of directly exhibiting the most important terms. The second method involves the numerical solution of the equations enumerated in the previous paragraph.

Several of the relations needed here were derived earlier and are summarized in §3.2.4. Since we are dealing with static models, where necessary we set $\omega = 0$. Two simplifying approximations apply in the bottom part of the convective envelope, namely, hydrogen is fully ionized and the entropy gradient is vanishingly small.

The dependence of Δs_b on $\Delta T_e/T_e$ and $\Delta\alpha/\alpha$ follows from equations (3.14), (3.41), and (3.45),

$$\Delta s_b = 4(B+C)\frac{\Delta T_e}{T_e} - \frac{4}{3}(s_b - s_{\rm ph})\frac{\Delta\alpha}{\alpha}. \tag{B.17}$$

Expressing Δs_b in terms of $\Delta\rho_b/\rho_b$ and $\Delta T_b/T_b$, we arrive at

$$-2\Delta\rho_b/\rho_b + 3\Delta T_b/T_b = 4(B+C)\frac{\Delta T_e}{T_e} - \frac{4}{3}(s_b - s_{\rm ph})\frac{\Delta\alpha}{\alpha}. \tag{B.18}$$

Equating the radiative and adiabatic temperature gradients and taking differentials provides a second relation between $\Delta\rho_b/\rho_b$, $\Delta T_b/T_b$, and $\Delta F/F$,

$$-(1+\kappa_\rho)\frac{\Delta\rho_b}{\rho_b} + (3-\kappa_T)\frac{\Delta T_b}{T_b} = 4\frac{\Delta T_e}{T_e}. \tag{B.19}$$

Solving equations (B.18) and (B.19) for $\Delta\rho_b/\rho_b$ and $\Delta T_b/T_b$ gives

$$\frac{\Delta\rho_b}{\rho_b} = \frac{4}{5A}\left\{[3-(B+C)(3-\kappa_T)]\frac{\Delta T_e}{T_e} + \frac{1}{3}(3-\kappa_T)(s_b - s_{\rm ph})\frac{\Delta\alpha}{\alpha}\right\}, \tag{B.20}$$

and

$$\frac{\Delta T_b}{T_b} = \frac{4}{5A}\left\{[2-(B+C)(1+\kappa_\rho)]\frac{\Delta T_e}{T_e} + \frac{1}{3}(1+\kappa_\rho)(s_b - s_{\rm ph})\frac{\Delta\alpha}{\alpha}\right\}, \tag{B.21}$$

where A is defined in equations (3.28) and (3.29).

These last two relations imply

$$\frac{\Delta p_b}{p_b} = \frac{4}{5A}\left\{[5-(B+C)(4+\kappa_\rho-\kappa_T)]\frac{\Delta T_e}{T_e} + \frac{1}{3}(4+\kappa_\rho-\kappa_T)(s_b - s_{\rm ph})\frac{\Delta\alpha}{\alpha}\right\}. \tag{B.22}$$

Appeal to equations (3.39) and (3.40) yields

$$\tau_c = \frac{5(B+C)p_b^2}{gF\rho_b}. \tag{B.23}$$

Taking differentials,

$$\begin{aligned}\frac{\Delta\tau_c}{\tau_c} &= \frac{4}{5A}\left\{[7-(B+C)(5+2\kappa_\rho-\kappa_T)]\frac{\Delta T_e}{T_e} + \frac{1}{3}(5+2\kappa_\rho-\kappa_T)(s_b - s_{\rm ph})\frac{\Delta\alpha}{\alpha}\right\} \\ &\quad + \frac{\Delta(B+C)}{(B+C)} - 4\frac{\Delta T_e}{T_e}.\end{aligned} \tag{B.24}$$

The variation on the value of $(B+C)$ is not very large (see Fig. B.2). At fixed α (the mixing-length ratio),

$$\frac{\Delta\tau_c}{\tau_c} \approx \left[-(5+2\kappa_\rho-\kappa_T)\frac{4(B+C)}{5A} + (\frac{28}{5A} - 4)\right]\frac{\Delta T_e}{T_e}, \tag{B.25}$$

while at fixed τ_c,

$$\frac{\Delta T_e}{T_e} \approx \frac{1}{3}\frac{(s_b - s_{\rm ph})}{(B+C)-7}\frac{\Delta\alpha}{\alpha}. \tag{B.26}$$

Equation (B.25) describes the deepening of convection zone as the effective temperature of the white dwarf decreases. When taking reasonable values, $\kappa_T = -5$, $\kappa_\rho = 0.8$, $A = 5$, $(B+C) \sim 15$,

and get

$$\frac{\Delta\tau_c}{\tau_c} \approx -31\frac{\Delta T_e}{T_e}. \tag{B.27}$$

Observationally, the longest periods for overstable modes inside the observed ZZ Ceti instability strip extend from 100 s to 1200 s as we go to cooler and cooler pulsators. If the thermal adjustment time (τ_c) has similar range (the fractional variation in τ_c is equivalent to $\Delta \ln \tau_c$, the changes in $\ln \tau_c$), equation (B.27) results in a corresponding $\Delta T_e \sim 900\,\mathrm{K}$, at $T_e \sim 12,000\,\mathrm{K}$. Here, we relied on information about observed period range to derive this width.

A straightforward reading from Figure B.2 produces a number close to 500 K for the same range of τ_c (100 to 1200 s). The discrepancy comes from our neglecting the change in $(B+C)$ (photospheric properties) in the above estimate. But even with the realistic scaling (equation (B.14)), the true width of the instability strip may still be more like 1000 K, as τ_c at the red edge is likely to be much longer than $1200/2\pi$ s.[1] Estimate based on white dwarf number statistics also leads to a width of $\sim 1000\,\mathrm{K}$.

In Chapters 5 and 4, we derive the instability width without consulting the observed period range, when taking into account of complications such as heat leakage and viscous stress. Models made in the §B.2 are used in these calculations.

Bibliography

Bradley, P. A., Winget, D. E., & Wood, M. A. 1993, ApJ, 406, 661

Brickhill, A. J. 1991, MNRAS, 251, 673

Iglesias, C. A., & Rogers, F. J. 1996, ApJ, 464, 943

Mihalas, D. 1978, Stellar Atmosphere, (Freeman)

Rogers, F. J., Swenson, F. J., & Iglesias, C. A. 1996, ApJ, 456, 902

Rybicki, G. B., & Lightman, A. P. 1979, Radiative Processes in Astrophysics, (John Wiley and Sons), 12

[1] At the red edge, the longest overstable mode is already quite invisible; this requires $\omega\tau_c \gg 1$ for 1200 s.

Appendix C The Symplectic Integrator

In this appendix, we describe the principle of symplectic integrator and its application in numerically evolving the amplitude equations.

There are two main advantages of using a symplectic integrator, as compared to conventional integrators. The first one is its efficiency. In a problem with two very different time scales, as the one we are interested in,[1] to accurately simulate the long term dynamics, we need to use an integrator so that our time steps can be as long as the mode periods. This is possible in the case of the symplectic integrator as it fully utilizes one characteristic of the Hamiltonian system, as we will explain later.

The other major advantage of symplectic integrators over other integrators of the same order[2] is its accuracy. Except from numerical round-off errors, there is no secular drift in the total energy of the system when using a symplectic integrator. This is remarkable given that long time integration using other integrators (e.g., explicit Runge-Kutta), however high their orders are, will always bring about fictitious numerical energy growth or loss. It is therefore easy to see why the symplectic integrators have been so much in vogue after their invention. There will, however, be deviations in the positions – or for coupled oscillators, the phases of the modes – from those of an exact solution. But even with this, it is superior to other kinds of integrators in that the deviations grow linearly with time, while for others they grow quadratically.

Here, we first develop the symplectic integrator for a conservative Hamiltonian system, we then add the complication of dissipation. Our adoption of this integrator has allowed us to carry out simulations that were previously prohibitively time-consuming.

C.1 Hamiltonian System

A Hamiltonian system is one whose flow preserves volume in the $2N$ dimensional phase space, $(\vec{p}, \vec{q})$, i.e., the area of any closed loop projected onto a plane $p_i q_j$ is preserved as the system evolves. Here, $\vec{p}$ is the general momentum, and $\vec{q}$ the general position. This symplectic nature of a Hamiltonian flow is a constraint on the dynamics, and special integrators can be designed to carry out numerical evolution of the system. The following discussion is mostly taken from Yoshida (1990), Saha & Tremaine (1992) and Malhotra (1994).

[1] There is the fast time scale of mode oscillation, and the slow time scale of macroscopic dynamics. Most interesting things happen on the slow scale.

[2] The order of the integrator reflects the dependence of error on the time step.

We consider Hamiltonians of the form,

$$H = H_T + H_V, \tag{C.1}$$

where H_T and H_V are both integrable, when taken separately (Malhotra 1994). H_T usually stands for linear, periodic kinetic motions, e.g., Keplerian motion of a planet, linear oscillation of an eigenmode, circling of plasma in an accelerator, etc. H_V usually represents the interactions among components in the system, it is considered as a perturbation to the regular motion of the system, and an integrable H_V generally requires that H_V depends on position ($\vec{q}$) only, but not on velocity.

With the notation $\vec{z} = (\vec{q}, \vec{p})$, the Hamiltonian equations can be written as

$$\frac{d}{dt}\vec{z} = D_H \vec{z}, \tag{C.2}$$

where D_H is the Hamiltonian operator, and is defined as $D_G F \equiv \{F, G\}$. Here braces stand for Poisson bracket, with $\{F, G\} \equiv F_{\vec{q}} G_{\vec{p}} - F_{\vec{p}} G_{\vec{q}}$, where $F_{\vec{q}} = \frac{\partial F}{\partial \vec{q}}$ and so on. If we let $A \equiv D_{H_T}$ and $B \equiv D_{HV}$, the evolution of $\vec{z}$ is a formal solution to equation (C.2),

$$\vec{z}(\tau) = \exp(\tau D_H)\vec{z}(0) = \exp\left[\tau(A + B)\right]\vec{z}(0). \tag{C.3}$$

Normally, A and B are not commutable, so $\exp(A + B)$ is not equal to $\exp(A)\ \exp(B)$. In fact, a Baker-Campbell-Hausdorff (BCH) identity leads to

$$\exp(A)\ \exp(B) = \exp(C), \tag{C.4}$$

and

$$C = A + B + \frac{1}{2}[A, B] + \frac{1}{12}([A, A, B] + [B, A, A]) + (\text{higher order terms}). \tag{C.5}$$

Here the commutator $[X, Y] \equiv XY - YX$, and the higher order commutator is algebraically defined to be $[X, X, Y] \equiv [X, [X, Y]]$.

Obviously, the original evolution is equivalent to the following evolution, subjecting to operators A and B at different times,

$$\exp(\frac{1}{2}\tau A)\exp(\tau B)\exp(\frac{1}{2}\tau A) = \exp\left[\tau(A + B) + < \text{error} >\right]. \tag{C.6}$$

This is a second-order symplectic integrator, as we will explain below. In practical applications, one first advances the system under the operator A for a time of $1/2\tau$, then evolves the system under the operator B for a full τ, and last, under A again for $1/2\tau$. After these three steps of evolution, the system formally flows from $\vec{z}(0)$ to $\vec{z}(\tau)$. In our system of coupled oscillators, we can carry

out the above steps with the amplitude equations, i.e., the first step is to 'drift' the phases of the normal modes for half the time step, as described by rotation of the phases; then give a 'kick' to the amplitudes and phases as due to interactions alone; and last, 'drift' the modes again for another half a time step. In practice, the third step of the $n-1$ time can be merged with the first step for time n, and this may look like a two-step integrator, and may be mistaken for a first-order integrator. But as we will explain below, it is really a second-order one. This 'drift-kick-drift' scheme is similar to what is used in the solar system dynamics, when gravity of planets is taken into account as perturbations (Wisdom & Holman 1991).

We can estimate the truncation error. This error exists as we cut off the BCH identity only at the second order (eq. [C.5]), and there is a difference between the second-order integrator and the actual evolution. By manipulating the BCH identity (Saha & Tremaine 1992), we get

$$\begin{aligned}\exp(\frac{1}{2}A)\exp(B)\exp(\frac{1}{2}A) &= \exp\Big(A+B-\frac{1}{48}[A,A,B] \\ &\quad +\frac{1}{24}[A,B,A]+\frac{1}{12}[B,B,A]+<\text{higher order}>\Big), \quad \text{(C.7)}\end{aligned}$$

using the property that $[A,A]=0$. This leads to the following error estimate,

$$H_{\rm err}=\frac{\tau^3}{12}\left\{[H_V,H_V,H_T]+\frac{1}{2}[H_T,H_V,H_T]-\frac{1}{4}[H_T,H_T,H_V]\right\}+O(\tau^5). \quad \text{(C.8)}$$

This is different from equation (14) of Saha & Tremaine (1992). But we are not concerned with the exact form of the error; we are interested in the power index in the dependence of $H_{\rm err}$ on τ. We argue that the integrator in equation (C.6) is a second-order one, not a first-order one as is claimed in Saha & Tremaine. More universally, Yoshida (1990) argues that an operator of time reversibility (or non-dissipative) can only be expanded into terms that involve τ^n, where n is an odd number. In this sense, we could only find symplectic integrators that are of even orders, since formally orders of the integrators are one power lower than its error's dependence on τ. Yoshida (1990) gave two methods to derive symplectic integrators to arbitrary even orders.

The system evolving using the second-order integrator is also a Hamiltonian system, only with its Hamiltonian changed to $H'=H_T+H_V+H_{\rm err}$. Since this integrator exactly describes the evolution of H', it is a **symplectic** one. The truncation error is its difference from a system with H_T+H_V. We can be assured of its symplecticity to the limit of round-off errors introduced by the whimsy computers which we use to trace the system numerically.

The accuracy and efficiency of symplectic integrators have been extensively demonstrated by Sanz-serna & Calvo (1993), Broucke (1993), Okunbor (1992), and Malhotra (1994). When comparing symplectic integrators with other integrators, all authors draw similar conclusions: when using the same time step, the symplectic ones are more accurate; when allowing the same error, the symplectic

ones can do with larger time steps. For both cases, the differences are at least a factor of 10. This is also confirmed by our numerical experiments in conservative systems, where we compare second-order symplectic integrator with a fourth-order Runge-Kutta and with an adjustable step-size Runge-Kutta.

C.2 Extension to Weakly Dissipative System

The discussion in §C.1 is oriented towards conservative Hamiltonian systems. In the coupled oscillator systems we are interested in, oscillations are usually driven or damped, on time scales much longer than the mode periods. Malhotra (1994) shows that for gravitational systems, when one takes into account of the dissipation only during the 'drifts', the error is of order $O(\tau^3)$. Hence the above symplectic integrator can be revised to deal with non-conservative systems.

Translated into algorithms for coupled oscillator systems with driving and damping, which have amplitude equations of the form,

$$\frac{dA_i}{dt} = i\omega_i A_i + \gamma_i A_i + < \text{interaction terms} >, \tag{C.9}$$

the revised integrator would be:

drift 1: evolve the complex amplitudes for half a time step, $A_i = \exp(\gamma_i + i\omega_i)A_i(0)$;

kick: add the interaction term to the amplitudes, $A_i = A_i + <$ interaction terms $> *dt$, where the interaction terms are evaluated after drift 1;

drift 2: similar to drift 1, evolve the amplitudes for another half time step.

In practice, drift 2 and drift 1 can be merged into a single drift over a whole time step.

Our simulations as documented in Appendix E are made possible by the adoption of the above symplectic method.

Bibliography

Broucke, R. A. 1993, Annals of New York Academy of Sciences, 206, 126

Malhotra, R. 1994, Celestial Mechanics Dynamics, 60, 373

Okunbor, D. 1992, Physica D. 60, 314

Saha, P., & Tremaine, S. 1992, AJ, 104, 1633

Sanz-Serna, J. M., & Calvo, M. P. 1993, International Journal of Modern Physics C., 4, 385

Wisdom, J., & Holman, M. 1991, AJ, 102, 1528

Yoshida, H. 1990, Phys. Let. A, 150, 262

Appendix D Amplitude Instability in the Amplitude Equations

D.1 Introduction

For a globally interacting multi-mode system (every mode interacts with every other mode equally strongly), the amplitude equations are

$$\frac{dA_i}{dt} = i\omega_a A_i + i\frac{3\kappa}{\sqrt{8}}\omega_i A^2, \tag{D.1}$$

where $A \equiv \sum_i (A_i + A_i^*)$.[1] We find an intrinsic instability for systems evolving according to the above amplitude equation; we call this the amplitude instability.

Total energy in the system can be separated into two parts, the kinetic energy (H_2) and the interaction energy (H_3),

$$H_{\rm tot} = H_2 + H_3 = \sum_i A_i A_i^* + \frac{1}{\sqrt{8}}\kappa A^3. \tag{D.2}$$

In the absence of driving and damping, the conservation of $H_{\rm tot}$ gives rise to the amplitude equation (D.1), which then describes in detail how mode-mode interactions cause energy to flow between H_2 and H_3. Behaviour of a conservative system is usually time-reversible.

The values of $H_{\rm tot}$ determine behaviour of the system. When the total energy involved in the system is higher than some critical value, an exponential growth of the mode amplitude will occur. Here, the kinetic energy goes to positive infinity, while the interactive energy goes to negative infinity, keeping $H_{\rm tot}$ constant (Fig. D.1). This is the amplitude instability we encounter in numerical simulations. As will be demonstrated below, the threshold energy associated with this instability is not very large, and it scales down with increasing number of modes. In reality, we know that white dwarfs pulsate at finite energy with many modes simultaneously observable. In this appendix, we would try to explain the condition for and the origin of the amplitude instability. In the final part of this appendix, we argue that this instability does not happen in real pulsating stars.

[1] Obviously, as long as κA is constant, κ can be taken as any value without changing the system dynamics.

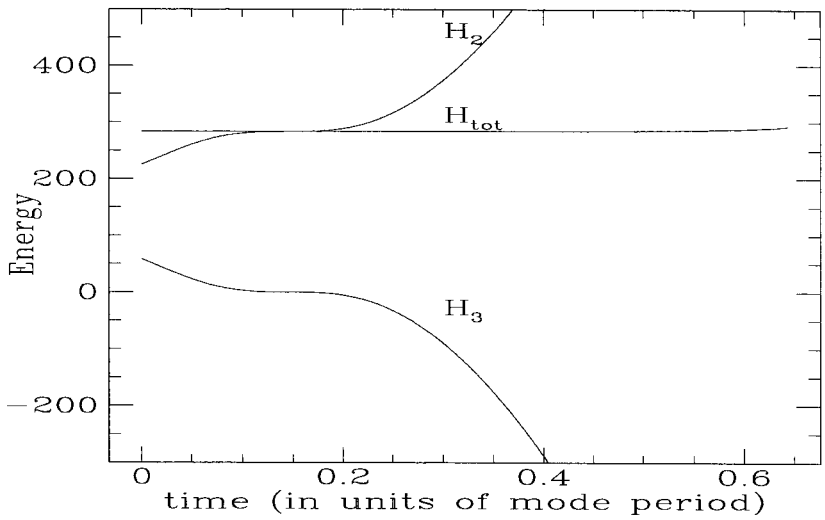

Figure D.1: The instability in action. The total energy $H_{\rm tot} = 250.0$ (we take $\kappa = 10^{-2}$ in this appendix) is kept constant while both H_2 and H_3 grow unconstrainedly.

D.2 One-Mode System

To simplify the situation further, let us consider a one-mode system. The amplitude equation becomes

$$\frac{dA}{dt} = i\omega A + i\frac{3\kappa}{\sqrt{8}}\omega A^2, \tag{D.3}$$

with $A = 2(A)_{real} = 2|A|\cos\phi$. The amplitude instability in such a one-mode system may develop within a few periods whenever $H_{\rm tot}$ surpasses a critical value. We derive this critical value below.

D.2.1 Instability Condition, Derivation I

The first way to derive the critical energy for amplitude instability to happen in the amplitude equation (D.3) is to consider the geometrical boundary (allowable range of the amplitudes) set by $|\cos\phi| \leq 1$. This gives

$$|A|^2 - \sqrt{8}\kappa|A|^3 \leq H_{\rm tot} \leq |A|^2 + \sqrt{8}\kappa|A|^3. \tag{D.4}$$

The mode is only allowed to travel within the above region at given $H_{\rm tot}$. These accessible regions for A are plotted in Figure D.2 for various $H_{\rm tot}$. If the trajectory of the amplitude is bound between $|A|_1$ and $|A|_3$, the system is stable. But when $H_{\rm tot} \geq H_{\rm crit} = \frac{1}{54\kappa^2}$, the amplitude is free to go to infinity. This is a necessary condition for instability, but not sufficient for immediate instability, since we also observe systems that are stable for a very long time even if their $H_{\rm tot} > H_{\rm crit}$. But if we wait for sufficiently long time, every system satisfying this condition will go unstable. The origin of the 'waiting time' is explained later.

The above conclusion does not change whether the mode is overstable or damped, presumably

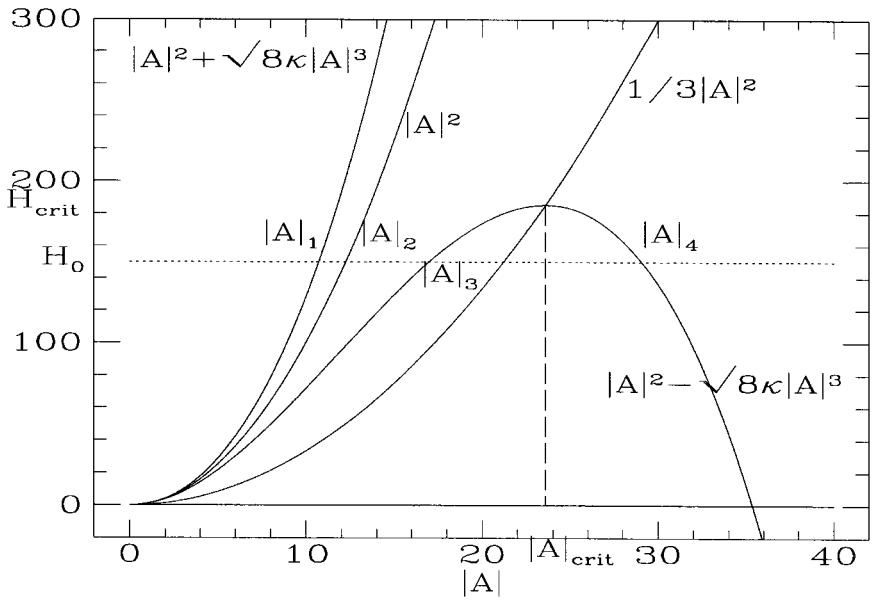

Figure D.2: A plot that shows the accessible regions for the amplitude $|A|$ when given $H_{\rm tot}$: when $H_{\rm tot} < H_{\rm crit}$, $|A| \in [|A|_1, |A|_3] \cap [|A|_4, \infty)$. $H_{\rm crit}$ is at the point where the curve $|A|^2 - \sqrt{8\kappa}|A|^3$ reaches maximum level. And for $H_{\rm tot} > H_{\rm crit}$, $|A|$ can wander to infinity even if starting from zero.

because the instability happens in a much shorter time scale, of order the mode periods. The only difference is that a system with driving may start from low $H_{\rm tot}$ and grow into unstable regime.

D.2.2 Instability Condition, Derivation II

Another way to derive the condition for instability is presented here. We separate the real and imaginary parts of the mode amplitude in equation (D.3),

$$\begin{aligned} \frac{dA_r}{dt} &= -\omega A_i, \\ \frac{dA_i}{dt} &= \omega A_r + \frac{6\kappa\omega}{\sqrt{2}} A_r^2, \end{aligned} \tag{D.5}$$

and get

$$\frac{d}{dt}(A_i^2 + A_r^2) = \frac{12\omega\kappa}{\sqrt{2}} A_i A_r^2. \tag{D.6}$$

Observing these three equations, we find that, whenever the following two conditions occur simultaneously,

$$\begin{aligned} A_r &< -\frac{\sqrt{2}}{6\kappa}, \\ A_i &< 0. \end{aligned} \tag{D.7}$$

A_r grows to negative infinity, while A_i will increase to positive infinity, with $|A|^2$ growing to positive

infinity. So equation (D.7) is the sufficient condition for the instability (but not a necessary one).

What's the relation between this sufficient condition and the necessary condition found in §D.2.1? $A_r < -\frac{\sqrt{2}}{6\kappa}$ necessarily leads to $H_2 > H_{\text{crit}}$.

D.2.3 Analogy to Something Simple

For better insight, we design a physical analogy for the one-mode amplitude equation. From the above equation for real and imaginary parts of the amplitude, we write down a second order ODE for A_r,

$$\frac{d^2A_r}{dt^2} = -\omega^2(A_r + \frac{6\kappa}{\sqrt{2}}A_r^2). \tag{D.8}$$

Let $\theta = \frac{6\kappa}{\sqrt{2}}A_r$, we have

$$\frac{d^2\theta}{dt^2} = -\omega^2(\theta + \theta^2). \tag{D.9}$$

This equation describes a conservative motion with a potential Ψ,

$$\begin{aligned} \frac{d\theta}{dt} &= v, \\ \frac{dv}{dt} &= -\frac{d\Psi}{d\theta}, \end{aligned} \tag{D.10}$$

where

$$\Psi = \omega^2(\frac{\theta^2}{2} + \frac{\theta^3}{3}). \tag{D.11}$$

The dynamics are depicted in Figure D.3, where a small ball is set to motion on a hard surface with shape Ψ. When $|\theta| \ll 1$, the motion is similar to a simple linear oscillator and is confined within the valley; but when the motion is large in amplitude, the ball can fall off from the negative side. This is the instability we see in the numerical simulations for one-mode couplings. When there are more than one-mode involved, the analogy is still valid, but the surface is no longer one-dimensional. The valley persists, but becomes shallower and shallower as the number of modes increases.

D.2.4 When Including Four-mode Couplings

When four-mode coupling is included, the critical energy is significantly increased, or in other words, instability is temporarily stopped.

For simplicity, we make the 4-mode coupling coefficient $\Theta = \kappa^2$, equation (D.10) is valid with the shape of the potential being

$$\Phi = \omega^2(\frac{\theta^2}{2} + \frac{\theta^3}{3} + \frac{\sqrt{2}}{9}\theta^4). \tag{D.12}$$

This potential does not drop off at $\theta \sim 1$, and the system is stable at a previously dangerous energy,

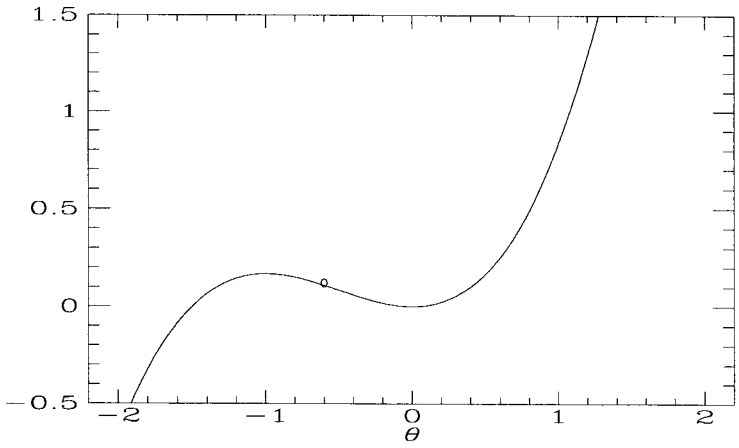

Figure D.3: The motion of a small ball on a frictionless surface, the shape of which is described by $\Psi = \theta^2/2 + \theta^3/3$. Whenever the small ball has sufficient energy to climb over the hill on the left-hand side, it can escape to $\theta = -\infty$, as is the case for the instability in the amplitude equations.

as is verified by numerical experiments.

D.3 Multi-mode System

D.3.1 N = 2

The instability involving many modes is very interesting to examine in detail. Firstly, we look at a system with two modes. Here, we can still work analytically.

For a Hamiltonian system,

$$H_{\text{tot}} = |A_1|^2 + |A_2|^2 + \sqrt{8}\kappa[|A_1|cos\theta_1 + |A_2|cos\theta_2]^3, \tag{D.13}$$

where $|A_i|, \theta_i$ are the amplitude and phase of mode i. H_{tot} being an integral of motion, the system has only three degrees of freedom; its trajectory (path of time evolution) can be visualized in a three-dimensional space. When we further project the trajectory onto the two-dimensional $(|A_1|, |A_2|)$ plane, the trajectory will be confined to some area (finite or infinite) as is shown in Figure D.4. The two groups of curves confining the area are determined from $|\cos\theta_i| \leq 1$, for $i = 1$ and 2. There exists a critical energy level H_{crit} above which no initial condition is stable after long enough evolution; this H_{crit} can be derived by considering the local maximum of H_{tot} when $\cos\theta_i = -1$. And we get

$$H_{\text{crit}} = \frac{1}{54\kappa^2 N^3}, \tag{D.14}$$

where $N = 2$. Again, this is a necessary condition for instability. Figure D.4 shows the geometry in phase space when H_{tot} is given.

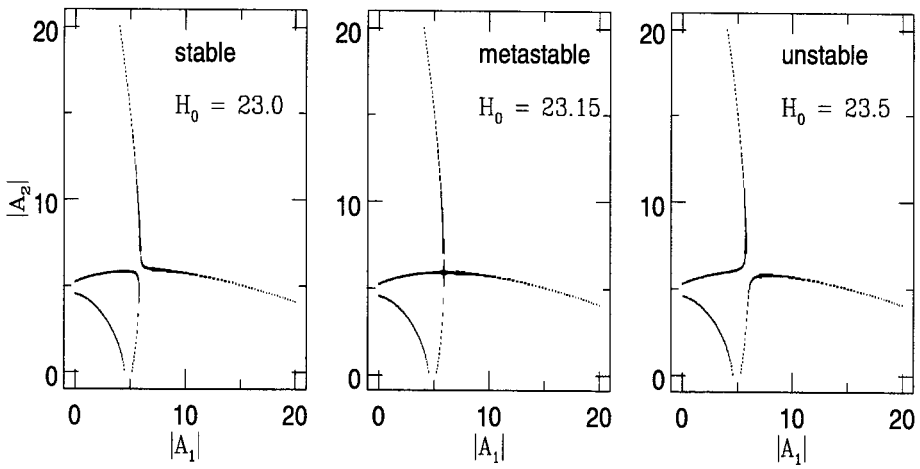

Figure D.4: The accessible phase space for various $H_{\rm tot}$ projected onto the amplitude plane. At given $H_{\rm tot}$, regions are separated by the dotted curves into the lower-left triangular space and the upper-right open space. Under the force of interaction, mode amplitudes move inside regions that they start from. When this region connects to infinity, as is the case when $H_{\rm tot} > H_{\rm crit} = 23.15 = 1/(54\kappa^2 2^3)$, the system may undergo amplitude instability. The escape angle $\theta_{\rm esc}$ for an unstable system is defined here as the opening angle viewed from the zero point.

When $H_{\rm tot}$ is only slightly higher than $H_{\rm crit}$, an immediate escape requires a phase condition of $\cos\theta_i \sim -1$ for both $i = 1$ and 2. In this case H_3 is the coherent sum of all couplings. This is met in the system from time to time by chance, when phases are sufficiently randomized through interactions, i.e., phases are not locked to each other as is the case for very strong interactions. When $H_{\rm tot} \gg H_{\rm crit}$, less strict phase condition applies and the system suffers higher probability for instability.

D.3.2 $N > 2$

Easily proven, the above necessary condition for instability can be extended to the multimode case, with $H_{\rm crit}$ written as

$$H_{\rm crit} = \frac{1}{54\kappa^2 N^3}. \tag{D.15}$$

Here, N is the number of modes inside the system that have appreciable energies. In a conservative system, this is the total number of modes; while in a driven/damped system, it is usually the number of excited modes. We carry out a whole spectrum of simulations with driven/damped multi-mode systems. If the system finally gets to a stable equilibrium state, we find out that the energy of the system always falls below $H_{\rm crit}$ (Fig. D.5).

As stated in §D.3.1, the system becomes unstable at the instant when some or all of the modes take phases $\cos\theta_i \sim -1$. When $H_{\rm tot} \sim H_{\rm crit}$, all the modes are required to participate in this conspiracy; but when the system is very much super-critical, i.e., $f \equiv H_{\rm tot}/H_{\rm crit} \gg 1$, only a small fraction of the modes are required. This explains why the system takes shorter and shorter time to

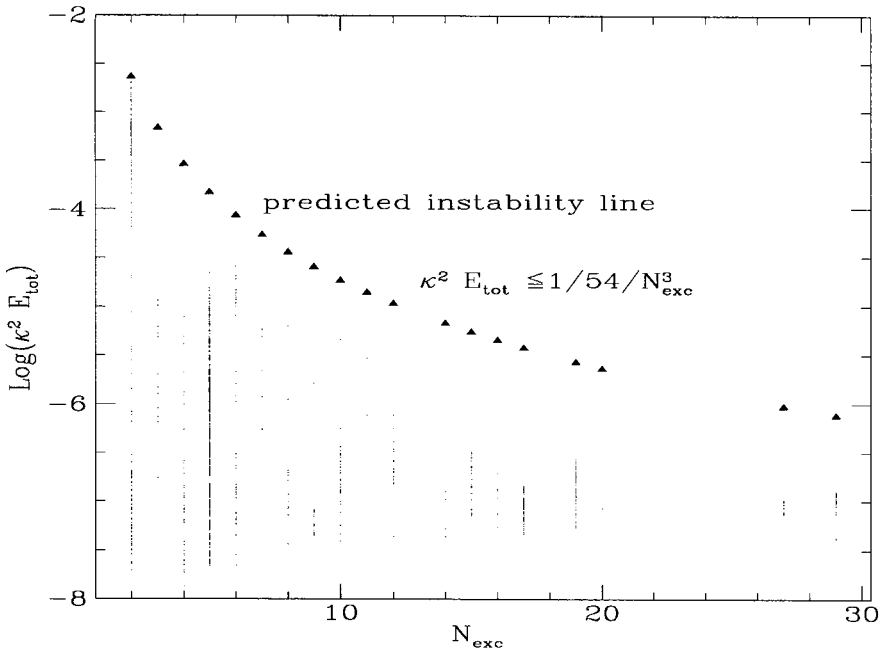

Figure D.5: Comparison between energy of the systems that can maintain equilibrium (small dots) and the critical energy beyond which the amplitude instability happens (the solid triangles). The systems simulated here have driven/damping modes, with $N_{\rm exc}$ of excited modes and an ensemble of driving/damping rates. All modes are globally coupling with a strength of κ. $H_{\rm crit}$ is a very robust upper limit to the equilibrium energy of these system, when only the number of excited modes are used in the instability criterion.

go unstable as its energy increases, as is shown in Figure D.6.

D.4 Physical Considerations: Caution

In a physically meaningful nonlinear system (for example, a pulsating white dwarf), the amplitude instability as exposed above does not exist.

First, the criterion for instability (eq. [D.15]) have to be modified. In a pulsating white dwarf, for example, κ is nonzero only for three-mode couplings that satisfy the wave vector closure.[2] The number of effective coupling in this case is of order N^2 instead of N^3, where N is the total number of modes. And the $H_{\rm crit}$ is of order

$$H_{\rm crit} \sim \frac{1}{C\kappa^2 N}, \tag{D.16}$$

where C is a constant of order unity or bigger. When $H_{\rm tot} \sim H_{\rm crit}$, this gives

$$\kappa A N \sim 1, \tag{D.17}$$

[2]For simplicity, here we assume all valid couplings in a white dwarf have the same coupling strength. Using the realistic coupling strength does not alter our conclusion below.

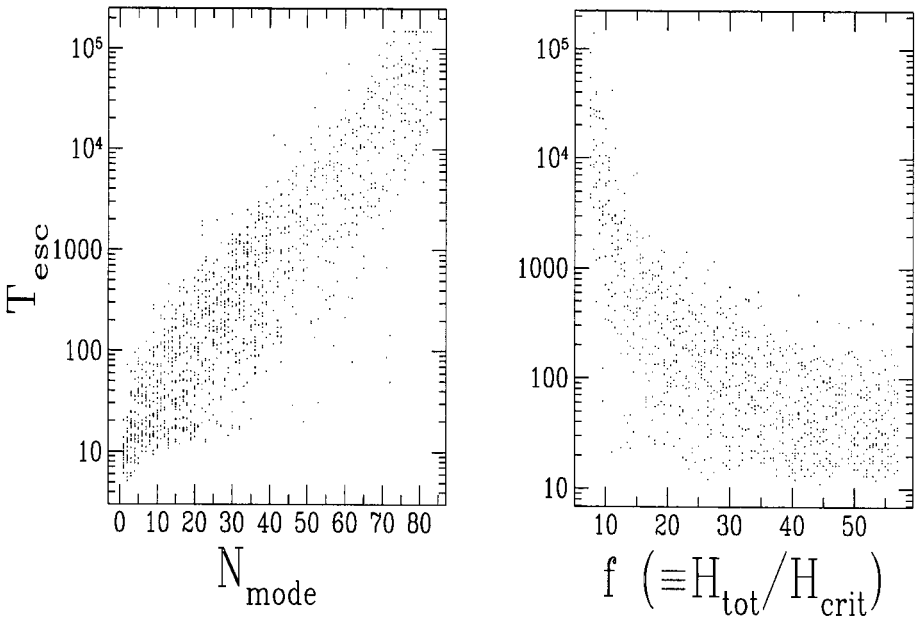

Figure D.6: The escape time $T_{\rm esc}$ as functions of the number of modes (left panel) and $f = H_{\rm tot}/H_{\rm crit}$ (right panel). Here, the escape time is defined as the time for the system to discover amplitude instability, when starting from random initial condition. In both cases, more modes and smaller f brings about quicker instability. In the left panel, $f = 10.0$, and $T_{\rm esc}$ scales exponentially with $N_{\rm mode}$. When $N_{\rm mode}$ is fixed, $T_{\rm esc}$ scales in power law with f.

assuming $H_2 \gg H_3$.

Second, when equation (D.17) is satisfied, the perturbed quantity (in the white dwarf, this is the total Lagrangian density perturbation at the surface, $(\frac{\delta\rho}{\rho})_{\rm tot}$) would have approached unity when the instability happens. When all phases of the modes are such that their amplitudes constructively sum to the total amplitude,

$$\left(\frac{\delta\rho}{\rho}\right)_{\rm tot} \sim N\left(\frac{\delta\rho}{\rho}\right)_{\rm mode} \sim NA \times Norm, \tag{D.18}$$

where $Norm$ is the energy-normalized surface amplitude for a single mode. Density perturbation in every mode is related to the amplitude A as $\delta\rho/\rho \sim \kappa A$ as both terms are the nonlinear parameters. Equation (D.17) thus gives rise to

$$\left(\frac{\delta\rho}{\rho}\right)_{\rm tot} \sim \kappa AN \sim 1. \tag{D.19}$$

Or, whenever the total density at one point of the star is of order unity, $H_2 \sim H_3 \sim H_4...$, and the assumption of weak nonlinearity breaks down. Higher order interactions have to be simultaneously taken into account. In fact, the system behaves more like a shock wave at this point.

In a pulsating white dwarf, we suggest that equation (D.17) is never satisfied. As we show in Chapter 7, each overstable mode in the star is limited to some small amplitude by parametric resonances. The amplitude instability discussed here is unlikely to happen.

Appendix E Dynamics of Globally Coupled Multi-mode Systems

E.1 Introduction

This appendix is devoted to understanding the intricate dynamics in multi-mode systems ($N > 3$). We have discussed the amplitude equations and the energy equations in Chapter 6. We then introduce the efficient 'symplectic integrator' in Appendix C for the numerical study of the amplitude equations. Having investigated dynamics of a system with only three modes (§6.3), we turn now to the far more difficult problem of understanding a system with a large number of modes.

Here, we first deal with 'globally coupled' systems (§E). Inside such an idealized system, any three modes can form a triplet and the coupling coefficient is equally strong in any triplet. Interactions in a realistic system are different: energy and angular momentum conservation constrains the possibility of forming triplets, and the coupling strength depends strongly on the structure of the three eigenmodes. But since the amplitude equations for a globally coupled system are significantly simplified, it is more accessible for both numerical and analytical studies. Many of the properties for globally coupled systems hold for realistic systems as well, such as the amplitude instability (see Appendix D) and the concept of weak turbulence.

We analyze the dynamics for both conservative systems (no driving and damping for the modes) and systems with weak dissipation (with driving and damping).

One prominent aspect of a conservative system, globally coupled or not, is energy equipartition among the pulsation modes and the process leading towards it. Energy is diffused across the phase space on time scales that depend on mode densities and pulsation amplitudes. This diffusion gives rise to a thermal equilibrium, in which every normal mode (or every degree of freedom) of the system oscillates with comparable energy. The stochastic fluctuations of energy in each mode satisfy the Boltzman distribution, as long as the total energy of the system is sufficiently large, i.e., the system is at 'weak turbulence'.[1]

For systems with weak dissipation, the equilibrium state is not energy equipartition. Statistically, the energy flux flowing into the excited modes (by some external forcing or extracted from the luminosity of the star) equals the flux lost to the damped modes. The energy equations are used to estimate the total energy of the system at equilibrium; the results compare favorably with results from numerical integrating the amplitude equations.

[1] 'Weak turbulence' mentioned here is equivalent to 'resonance overlap' in the literature of nonlinear dynamics.

What comes as a surprise is that at equilibrium, many modes (both excited and damped ones) are 'slaved' to oscillate at frequencies other than their original ones. Only a few modes dominate the system energy and dynamics. This behaviour is shown most clearly in Figure E.9, in which mode energies are observed to be organized into beautiful, rhythmic patterns in frequency space. We believe that 'slaving' is unique to these globally coupled, dissipative, multi-mode systems when the condition of 'weak turbulence' is not satisfied. In pulsating stars, 'slaving' never happens. Our arguments are based on the differences between globally coupled systems and realistic systems. As a result of the 'amplitude instability' (see Appendix D), globally coupled systems cannot have energy high enough to realize 'weak turbulence'. Weak turbulence brings about phase randomization and relieves 'slaving'. Amplitude instability does not happen in a real star, because the couplings there are not global, but rather 'patchy'. The condition for amplitude instability in this case coincides with the condition for strong nonlinearity. In real stars, there can exist true weak turbulence which prevents slaving.

To gain insights into dynamics of pulsating white dwarfs, we simulate systems that have 'patchy' couplings, where modes are allowed to couple to each other only when they satisfy frequency and angular momentum closure ('resonance') simultaneously. We have carried out rather preliminary explorations of such systems. They exhibit dynamics that are qualitatively similar to those in globally coupled systems, but the same behaviour may appear at much higher total energy. To fully understand mode selections, mode switchings and all other intricate dynamics in a pulsating white dwarfs, it seems that simulations as complicated as a real white dwarf will be necessary.

E.2 Conservative Systems – Energy Equipartition

E.2.1 Energy Equipartition in the Literature

Interesting dynamics in a conservative system involve the process of going towards energy equipartition, in which every degree of freedom in the system acquires similar energy after sufficient interactions. The memories about the initial conditions are forgotten during the interactions, and the final state, i.e., energy equipartition, is universal. Understanding the process towards equipartition is a vast field in itself, and here we give an extremely elementary review for the purpose of further discussions.

In classical statistical mechanics, at sufficiently high energy (so that the classical concept of density of states is applicable), every degree of freedom in the system possesses an energy of $1/2k_B$, where k_B is the Boltzman constant. This is the theoretical basis for deriving the specific heat of ideal gases, molecular or atomic (Callen 1985). Suppose, initially, only a small fraction of the gas particles has energy, while others are cooled to zero temperature. The re-distribution of energy among normal modes of the system (every degree of freedom in the system corresponds to one normal mode)

is accomplished through close-range scatterings between gas particles.[2] Associated with energy equipartition is the concept of ergodicity, i.e., any point in phase space will be visited by the system, sooner or later. Though we could easily believe that energy equipartition is the equilibrium for an ergodic system, ergodicity is not a necessary condition (e.g., conservative Hamiltonian systems are confined to the equi-energy surface yet still achieve equipartition).

It has become an implicit assumption in thermodynamics that a system at equilibrium satisfies energy equipartition. In the process of investigating the validity of this assumption, Fermi, Pasta and Ulam (1965) posed the famous FPU problem in 1954. As a simplification to the interacting gas, they considered a chain of nonlinearly coupled oscillators. They observed numerically that these oscillators may not always relax to equipartition state, but instead, for some particular initial conditions, the oscillators recurringly visit their initial states with a 'super-period' (Tuck & Menzel 1972). Questions are therefore raised: is there a threshold below which there is no energy equipartition? And what is the threshold? If the system is above this threshold, then how long will it take to reach equipartition?

Later studies have more or less answered these questions, and revealed interesting dynamics occurring at different energies. One important concept has been developed on the way, the so-called 'Arnold Diffusion', which reveals the existence of a universal instability in a nonlinear system with degree of freedom greater or equal to 3 (Chirikov 1979). Briefly, we consider a nonlinear oscillator with an amplitude-dependent frequency,

$$\omega(A) = \omega_0 + \delta\omega(A). \tag{E.1}$$

When a (small) periodic force with frequency ω_f (ω_f is close to ω_0 for analytical convenience) acts upon it, there will be resonant energy absorption when the frequency of the oscillator and that of the force are in resonance,

$$m\omega(A) + n\omega_f = 0, \tag{E.2}$$

with m, n being integers. The order of the resonance is the sum $|m| + |n|$. The above equation yields the amplitude of the oscillator when it is in resonance. Resonance can happen even when the above equation is only approximately satisfied – since the force has small but finite value, it does not take forever (a true δ-function in frequency) to transfer energy into the oscillator. The width of the resonance is roughly the inverse of the time it takes for the external force to impart a significant amount of energy to the oscillator, and is proportional to $\sqrt{f_0}$, where f_0 is the strength of the external force. The region of resonance is bounded by a separatrix, outside which free oscillation with frequency ω_0 dominates, and inside which the oscillator is slaved under frequency of the external force.

[2] Although the ideal gas approximation neglects collisions, these scatterings are essential for diffusing energy and producing systems that look like ideal gas.

There should be at least three frequencies in a system for Arnold Diffusion to happen. An example is if two external forces with frequencies ω_{f1} and ω_{f2} simultaneously act on the oscillator with frequency ω_0. At sufficiently small strength, the oscillator stays in either one of the resonance regions, as determined by its initial condition. In the phase space of the oscillator, between the separatrixes, interaction between two resonances produces 'narrow chaotic layers'; therefore, diffusion may occur along (not across) the resonance layers, due to the existence of two incommensurate driving resonances. This happens even when f_1 and f_2 approach zero, though the volume of phase space occupied by chaotic motion shrinks (exponentially?), and the diffusion has to go through narrower and narrower tunnels; it appears that the diffusion time extends exponentially. This is the 'slow Arnold Diffusion'. Most of the trajectories are still locked within the domain of one or the other resonance.

Chirikov (1979) found that, when the amplitudes of the driving forces are sufficiently large, or the frequencies ω_{f1} and ω_{f2} are sufficiently close, there could be 'resonance overlaps'. Trajectories can wander from the domain of one resonance to the other, and the relative measure for chaotic trajectories (with positive Lyapunov exponent) approaches unity.[3] If we measure the rate of change of energy in the oscillator, and define this as the diffusion rate, numerical experiments and analysis show that the diffusion rates depend on the strength of the resonances as a power law (e.g., see De Luca et al. 1995).

When there are many oscillators interacting with each other in a system, they are to each other the external forces discussed above. When there are more than three oscillators in the system, there is weak chaos, but the energy diffusion rate only becomes practically fast when the total energy in the system rises above some threshold that depends on the number of oscillators and the coupling strengths. Below this value, the energy equipartition is exponentially difficult to reach (De Luca et al. 1995; Galgani et al. 1992).

There is perhaps an academic point we can make about chaotic orbits. In a phase space that is accessible for one chaotic orbit, it is possible to define an 'invariant spectrum' (Contopoulos et al. 1995). This spectrum can be obtained either by integrating the orbit for a long time, or by measuring it for random points in this phase space at the same time. The 'invariant spectrum' can also yield the value of the maximum Lyapunov exponent. It is rather amazing that a seemingly random motion can be simplified into regular quantities; I consider this as 'chaos tamed'.

E.2.2 Energy Diffusion for Globally Coupled Oscillators

We study here the process of energy diffusion in systems with globally coupled oscillators, to illustrate the understandings discussed in §E.2.1.

[3]But this is not equivalent to ergodicity; though any point in the phase space will be infinitely close to a chaotic trajectory, there is nonzero measure of stable oscillations even at rather high nonlinearity. This shows that ergodicity is a sufficient but not necessary condition for energy equipartition.

We adopt the amplitude equations in (6.15), and take κ to be constant for different couplings. The non-resonant interactions will be automatically averaged out when we integrate these equations, and only the resonant ones contribute significantly to the overall dynamics. With N modes in the system, the amplitude equation is

$$\frac{dA_i}{dt} = i\omega_i A_i + i\frac{3\kappa}{\sqrt{8}}A^2, \tag{E.3}$$

where $A = \sum_j (A_j + A_j^*)$. The systems are set up with frequencies of the modes spread randomly but evenly across a range of $\Delta\omega \sim \omega_i$ (i.e., the frequency of the modes is comparable to the range of the frequencies).

An important parameter in gauging the rate of energy diffusion is the closeness of a mode to resonant interactions. For every mode, on average, the closest combination of interactions is away from exact resonance by a frequency of $(\delta\omega)_{\min} \sim \Delta\omega/(2N^2)$: every mode will attend N^2 combinations, so on average, the best one will be $1/N^2$ closer than the worst ones (see Fig. E.1). And, if we look at the whole system, and ask what is the best resonance the system can host, systematically, we find a minimum of $(\delta\omega)_{\min}$ being $\Delta\omega/N^3$, given that the total number of combinations is of order N^3. These two scaling laws are confirmed by simulations shown in Figure E.1.

When investigating the process of energy equipartition, a usual practice is to give some initial energy to part of the system (the 'privileged'), and none to the remainder. We can plot the energy growth in the latter to study the secular changes that lead to equipartition. Rapid variations in energy, resulting from near resonances, do not lead to equipartition; only the secular trend in these variations do. Also, the frequency detuning estimates for the system as a whole may not be very useful, since only three-mode couplings that involve at least one of the 'privileged' modes are significant. If the 'privileged' modes lie either at the low or high frequency end of the system, we could estimate $(\delta\omega)_{\min}$ as in Figure E.2. Apparently, when counting only interactions that involve one or two such modes, the $(\delta\omega)_{\min}$ is much larger than in Figure E.1.

It follows from discussions in §E.2.1 that when there is resonance overlap for every mode, there will be stochastic instability and fast Arnold Diffusion across the resonances, and we expect the system to undergo equipartition rapidly. In §E.2.1, the resonance width is determined by the strength of the external forces. Here, these external frequencies are provided instead by mode couplings. The width of the resonance is determined by the amplitudes of the modes in resonance. As we mentioned above, this width is also the inverse of the interaction time scale over which significant energy can be exchanged. We estimate this nonlinear time scale using the energy equation (6.17). Assuming every mode has comparable energy, we get

$$\frac{dE}{dt} \sim \frac{\omega^2\kappa^2(\delta\omega)}{(\delta\omega)^2}E^2, \tag{E.4}$$

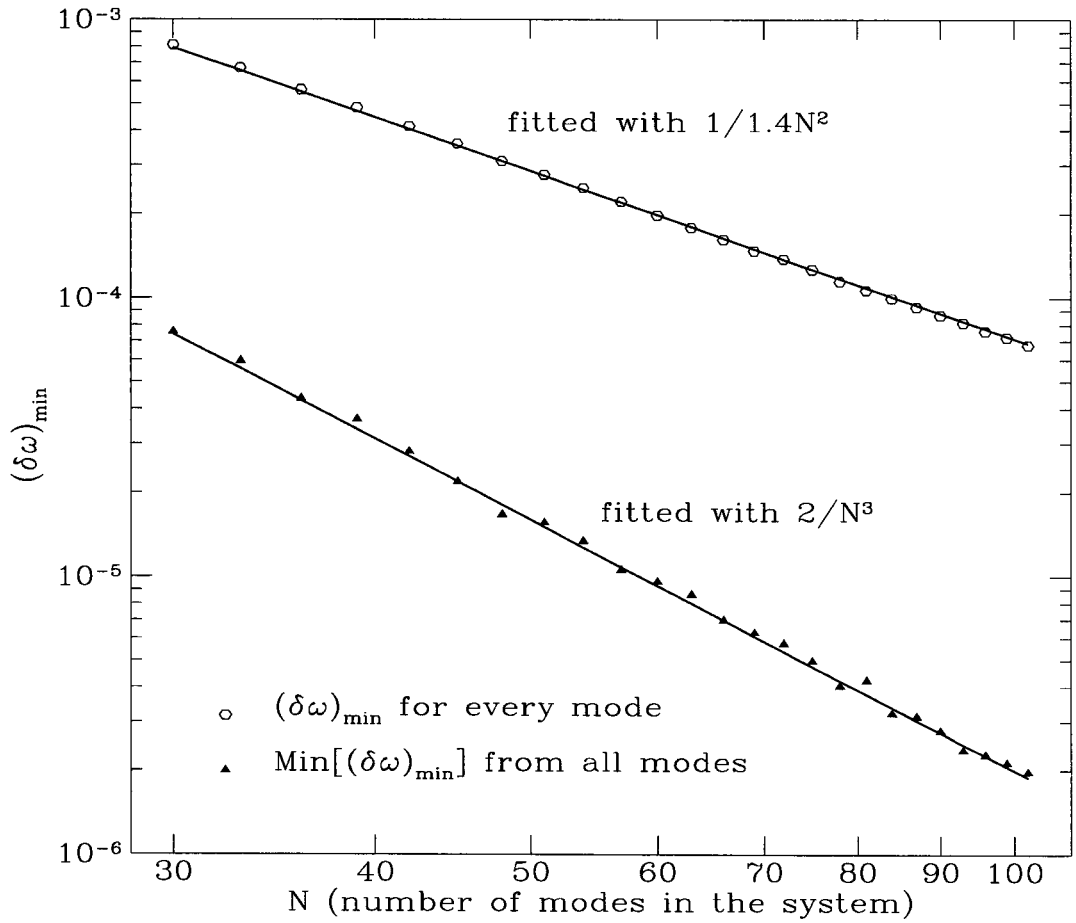

Figure E.1: Given a group of N modes with frequencies randomly but evenly distributed between 0.0 and 1.0, the best frequency detuning for every mode when all interactions ($\delta\omega = \omega_i \pm \omega_j \pm \omega_k$, with i, j, k taken from the pool of N modes) are considered is $(\delta\omega)_{\min}$ (averaged over all modes), and the smallest such detuning among all modes is Min$[(\delta\omega)_{\min}]$. We take averages of 1000 such random systems. When N increases, the detuning improves as estimated, with the average detuning scaled as $1/N^2$, and the best detuning scaled as $1/N^3$.

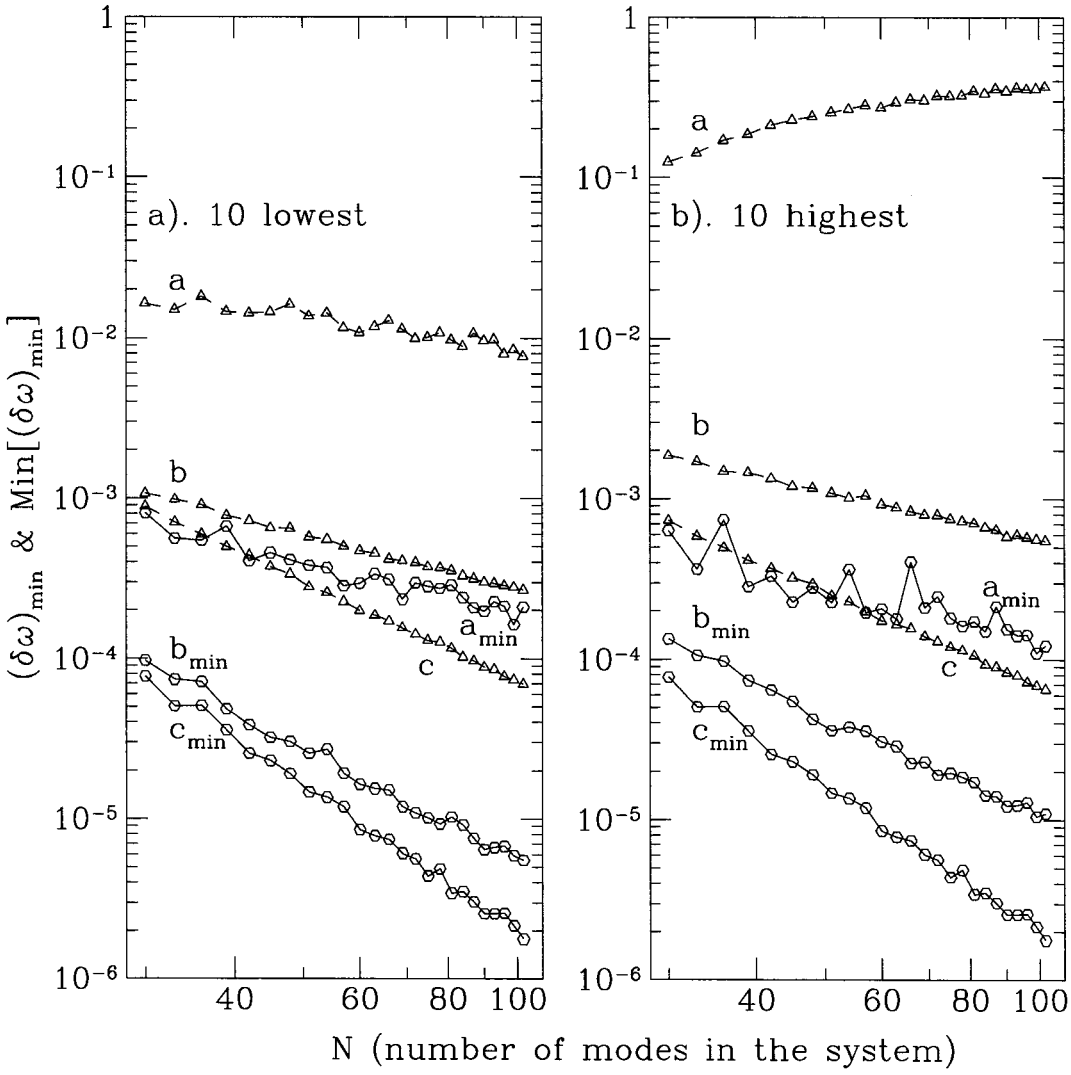

Figure E.2: Frequency detuning as a function of number of modes. Similar to Figure E.1, but not all triplets are allowed as is the case there. In the left panel, a stands for $(\delta\omega)_{\min}$ when at least two out of the three modes are taken from the subpopulation of ten lowest frequency modes; $a_{\min}$ is for the minimum detuning of all such couplings. b is the mean detuning for couplings that have at least one such low frequency mode, and c is the mean for all possible couplings, with $b_{\min}$ and $c_{\min}$ being their respective minimum values. The right hand panel is similar except the subpopulation is now the ten highest frequency modes. If the ten highest energy modes are also those that have the highest energy (as in a pulsating white dwarf), the increase in a with N in the right hand panel implies a longer diffusion time for systems with larger N, when the total energy is fixed. For large N systems, low frequency modes will be able to diffuse energy out more efficiently than the high frequency ones at the same total energy.

where we have assumed that the frequency detuning is larger than the nonlinear line-width and there is no dissipation (driving or damping). If we define the diffusion time as the time it takes to change the energy in every mode significantly, or $dE \sim E$, while the nonlinear line-width is the inverse of this time, we get

$$\tau_{\text{diff}} \sim \frac{(\delta\omega)}{\omega^2\kappa^2 A^2}, \tag{E.5}$$

where A is the amplitude and $E = A^2$. The resonance overlap condition,

$$(\delta\omega)\,\tau_{\text{diff}} \leq 1, \tag{E.6}$$

can be translated to a condition on the amplitudes. The minimum amplitudes for resonance overlap can be derived using the expression for $(\delta\omega)_{\text{min}}$. Here, $(\delta\omega)_{\text{min}}$ is the frequency detuning for average modes in an N-mode system. According to Figure E.1, $(\delta\omega)_{\text{min}} \sim \omega/N^2$, and we find the condition for fast Arnold Diffusion in a globally coupled system,

$$\kappa A \geq \frac{1}{N^2}. \tag{E.7}$$

Or, equivalently, the total energy of the system has to be larger than $1/(\kappa^2 N^3)$ (the amplitudes add up in-coherently). Since different modes have different chances for resonance, some may satisfy the overlap condition at a much smaller amplitude (smaller by a factor of N^2 if it has the smallest $(\delta\omega)_{\text{min}}$ in the system). In systems where only some of the modes have large amplitudes, the useful combinations are restricted, so $(\delta\omega)_{\text{min}}$ is larger, and the overlap condition is satisfied only at correspondingly higher amplitudes. In fact, as is briefly mentioned in the caption for Figure E.2, if the 'privileged' sub-system is composed of modes with the lowest frequencies, the typical resonances are better than when it is comprised of modes with the highest frequencies. This characteristic is also observed by Pettini & Cerrutisolar (1991). The second type of systems have a higher threshold for fast energy equipartition, or equivalently, at similar energy, they show much longer diffusion time than the low frequency type.

When a system has more energy than required by equation (E.7), the diffusion time shortens correspondingly. Consider an average mode in the system. If it has n overlapping resonances, where $n \sim 1/(\tau_{\text{diff}}(\delta\omega)_{\text{min}})$, with τ_{diff} estimated in equation (E.5), its diffusion time shortens as

$$\tau_{\text{short}} \sim \tau_{\text{diff}}/\sqrt{n} \sim \frac{1}{\omega\kappa^3 A^3 N^4}; \tag{E.8}$$

the factor of $1/\sqrt{n}$ follows from the fact that the n resonances incoherently act to remove/infuse energy from/into this mode. The diffusion time for individual modes depends inversely on A to the third power, and on N to the fourth power. Above the threshold, a system with larger N can be

more quickly equipartitioned, and the threshold (in terms of total energy in the system) gets lowered with larger N. Most numerical simulations to date deal with systems with 10^3 or fewer modes, while a real physical system, e.g., a cubic centimeter box of gas at room temperature, has N of order 10^{24}. The assumption of energy equipartition for gas at equilibrium is therefore well feasible, as a result of the fast Arnold diffusion.

We would have liked to test the predictions for the diffusion rates in equation (E.5) and (E.8), but as is shown in Appendix D, whenever κA is larger than $1/(\sqrt{54}N^{3/2})$, a globally coupled system with only cubic nonlinearity will suffer from an intrinsic instability, called (by us) the 'amplitude instability'. Condition (E.7) is obviously above this limit. Hence, one is forced to include quartic nonlinearity in the amplitude equations to stabilize the systems. This may partly explain why in many studies to date, quartic nonlinearity has been favoured, even though it is an order weaker than the cubic one. We use the following form of amplitude equations,

$$\frac{dA_i}{dt} = i\omega_i A_i + i\frac{3\kappa}{\sqrt{8}}A^2 + i6\Theta A^3, \tag{E.9}$$

where $A = \sum_i (A_i + A_i^*)$, and the four-mode coupling coefficient Θ is taken to be $\Theta = \kappa^2$. This form is chosen such that the fourth order Hamiltonian becomes

$$H_4 = \frac{3}{2}\kappa^2 A^4. \tag{E.10}$$

For comparison, $H_3 = \frac{\kappa}{\sqrt{8}}A^3$. We can show that including the quartic nonlinearity does not significantly change the overlap condition.

Energy equipartition can be seen in systems with nonlinearities of the above form, and this is shown in Figure E.3.

When the energy of the system is above the resonance overlap threshold, we find that there is usually a swift growth of energy in the initially zero-amplitude modes for a short period of time. Afterwards, energy diffusion proceeds slower. This could be due to an inhomogeneous density of resonances in the phase space of the modes. Initial interactions always tend to pull the modes into a strong resonance which cause some energy to be exchanged between the modes. But later, when many modes are slaved to oscillate with the first resonance, they are artificially removed from the influence of other resonances. Slow diffusion is required to emancipate the slaved modes from the influence of these strong resonances. Only then fast diffusion can proceed. This slow diffusion process is observed as a 'plateau' in the time dependence of the energy.

For an easily thermalized system (quick energy equipartition), mode energy follow a Boltzman distribution, i.e., every mode spends most of its time near zero energy state, and wanders in the energy space with its mean energy being the temperature of the system (average energy). In such a state, the system visits all points in phase space with a probability depending exponentially on the

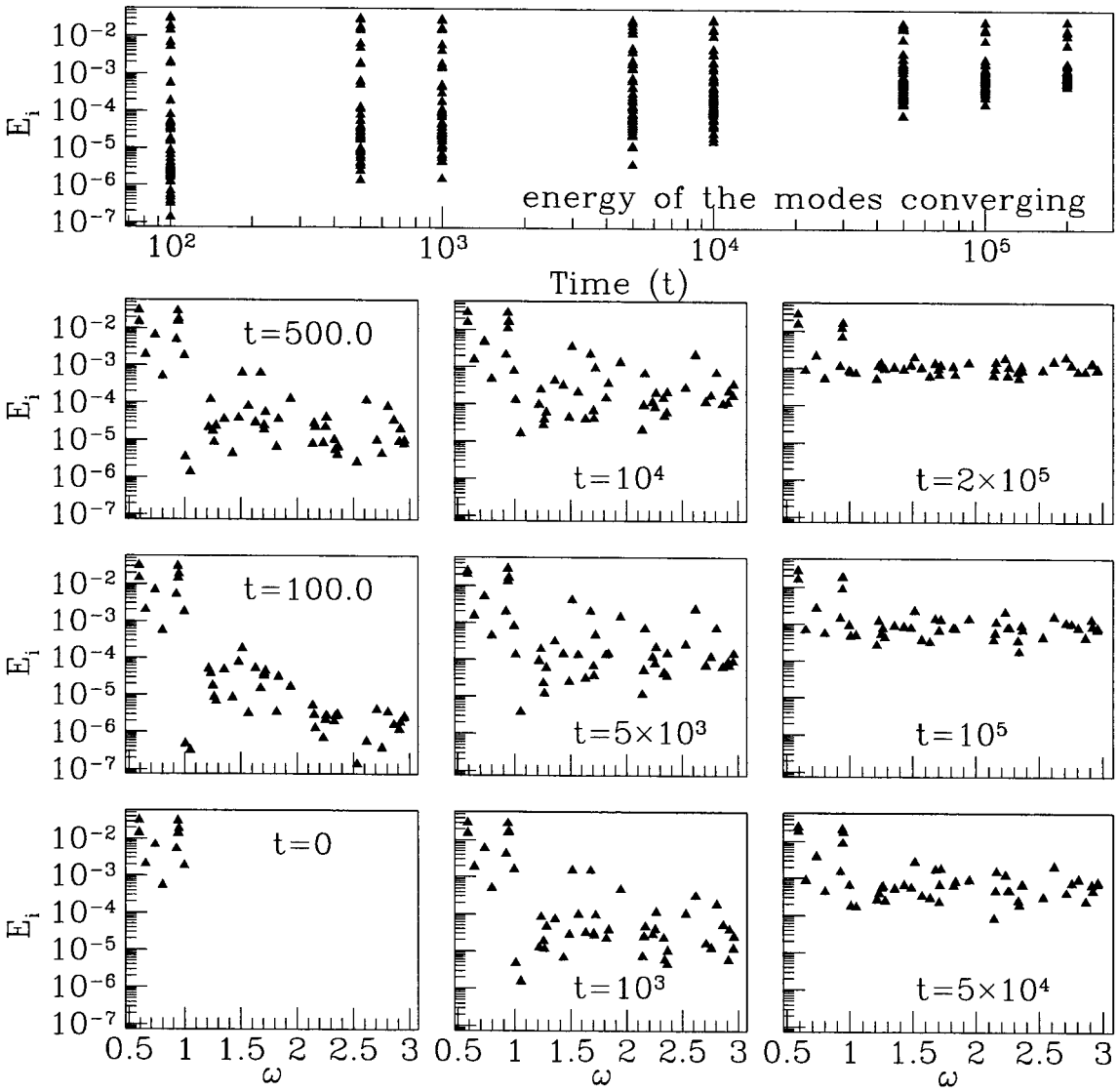

Figure E.3: Energy equipartition in a system with both cubic and quartic nonlinearities. Here, $N = 50$, and the frequencies are chosen randomly between 0.0 and 3.0. We take $\kappa = 1/N$, $\Theta = \kappa^2$. Initially only the ten lowest frequency modes are given energy, while the others have none. As time goes by, energy distribution among the modes become more and more homogeneous (the upper long panel). The energy distribution as a function of mode frequency is shown in the lower nine panels for different times. We see that the process of energy equipartition occurs in a reasonably short time scale; in this case the diffusion time is of order 10^4.

energy; the summation of the trajectories therefore yields the Boltzman distribution. In this limit, the system becomes a good heat bath and every mode is well thermalized inside it. We show in Figure E.4 a few examples of this Boltzman distribution for cases in which the energy of the system is sufficiently large (there is also an example for the case when modes could not be thermalized).

We could quantify the behaviour during fast diffusion using the concept of 'auto-correlation time'. This time scale should be of order the interaction time scale, i.e., the diffusion time scale.

E.3 Dissipative Systems – Dynamical Equilibrium

For dissipative systems, the main feature in the dynamics is the energy flowing out of the excited modes and into the damped modes. We consider how fast damped modes can absorb energy and how this determines the system energy at equilibrium. Then we discuss the equilibrium characteristics, including the problem of mode slaving and energy fluctuations.

E.3.1 Energy Flow into Damped Modes

For fast energy diffusion to occur, the line-width has to be wide enough that the best combination becomes resonant. This line-width can arise from nonlinear interactions, as is discussed in §E.2.2. It can also be due to dissipation. Finite growth/damping rates effectively broaden the line-width for a mode by disturbing the sinusoidal variations. Whenever $\gamma > (\delta\omega)_{\min}$, diffusion across resonances can be realized independent of the mode energy.

We look at a simple three-mode system in order to understand the rate of energy flow in the presence of dissipation. We take $\omega_1 = 0.5929165$, $\omega_2 = 0.6885052$, $\omega_3 = 1.27642$, and $(\delta\omega)_{\min} = \omega_2 + \omega_1 - \omega_3 = 0.005$; we will write it as $\delta\omega$, as it is the only detuning we are interested in. We start with $E_1 = E_2$, and $E_3 = 0$, assuming damping through mode 3 with γ_3 ($\gamma_3 > 0$). We want to understand how fast energy is flowing into mode 3 in such a system. For this purpose, we trace the total energy of the system, and we define $\gamma_{\rm tot}$ as the rate of energy disappearing into mode 3, $\gamma_{\rm tot}$ is the absolute value of the total damping rate. The relation between $\gamma_{\rm tot}$ and γ_3 reflects how fast mode 3 is absorbing energy from its two high-browed partners, since $\gamma_{\rm tot}E_{\rm tot} = \gamma_3 E_3$ ($E_{\rm tot} = E_1 + E_2 + E_3$).

We estimate E_3 at equilibrium,[4] as a function of γ_3. There are two limits which we have to consider. Firstly, the limit when $\gamma_3 \ll \delta\omega$. The energy equation for mode 3 yields

$$2\gamma_3 E_3 \sim \frac{\omega^2 \gamma_3 \kappa^2 E_1^2}{\gamma_3^2 + (\delta\omega)^2}. \tag{E.11}$$

[4]It is not an equilibrium in the true sense, since energy is constantly flowing out of the system. But in the limit that the interaction time is much shorter than the damping time, we could think of the system as being approximate at equilibrium.

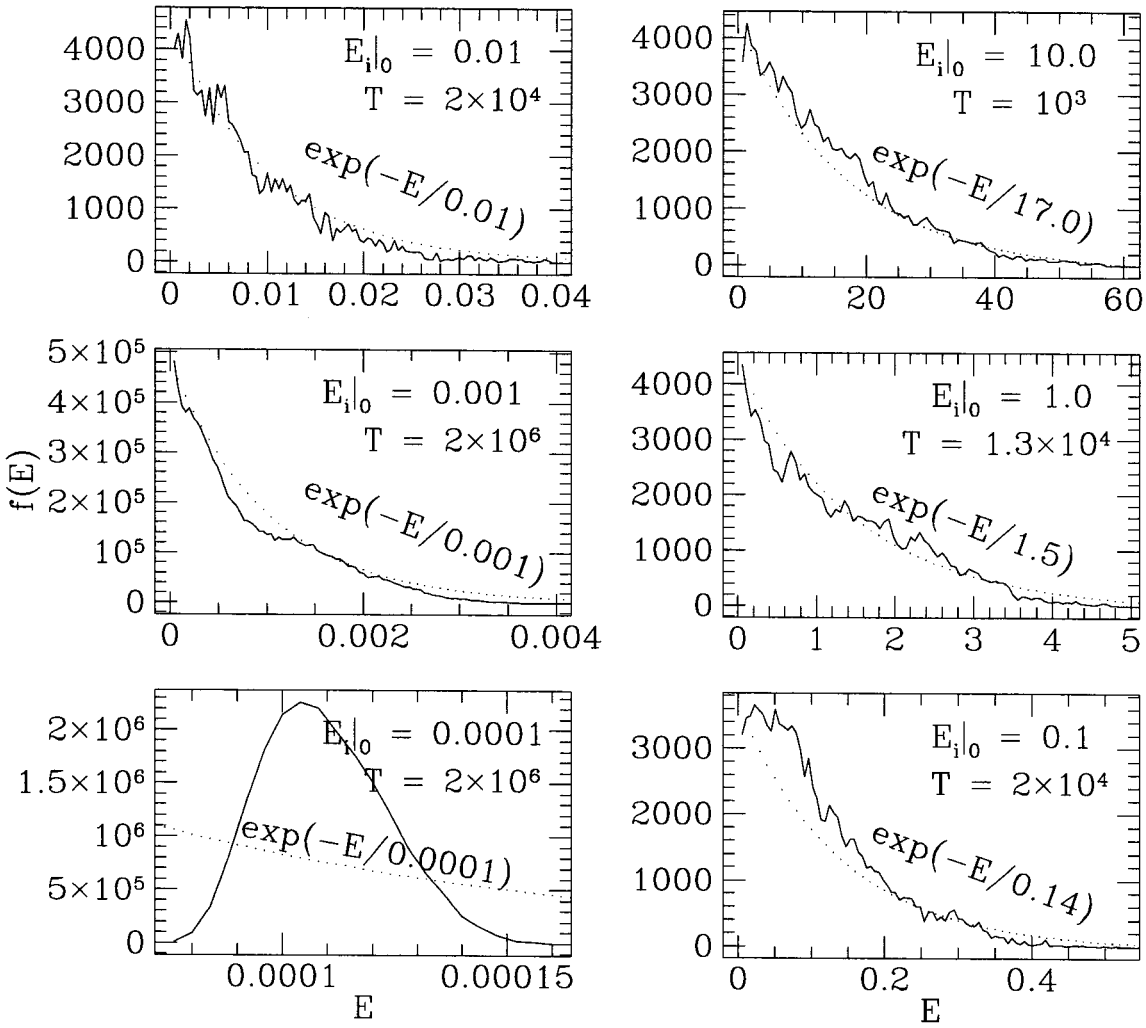

Figure E.4: Energy fluctuation for an average mode in a globally coupled system with $N = 25$. We test for the hypothesis that mode energy displays Boltzman distribution when there is true energy diffusion, which also leads to energy equipartition. The distribution of energy ($f(E)$) represents the amount of time the mode spends with a particular energy. The shape of the distribution depends on the initial energy in the mode, which increases from bottom to top, and from left to right. The distribution does approach that of a Boltzman one (the dotted lines) when initial energy is large, in which the mode spends most of the time with small energy. At the coolest end (the lower left panel), there is no true thermal relaxation (energy equipartition) in the system and there is only a spread of energy around the initial value. Here, the mean frequency of the system is 0.5, and T is the integration time (also approximately the equipartition time) to accumulate the plotted distributions. $\kappa = 1.0$, and quartic nonlinearity is included.

Here, we have assumed that E_3 is insignificant compared to energy in the other two modes. γ_3^2 in the determinator can be removed as well. This leads to a relation between $\gamma_{\rm tot}$, γ_3 and E_1,

$$\gamma_{\rm tot} \sim \frac{\gamma_3 E_3}{2E_1} \sim \left(\frac{\omega\kappa}{(\delta\omega)}\right)^2 \frac{\gamma_3 E_1}{2}. \tag{E.12}$$

In the limit of $\gamma_3 \geq (\delta\omega)$,

$$\gamma_{\rm tot} \sim \left(\frac{\omega\kappa}{\gamma_3}\right)^2 \frac{\gamma_3 E_1}{2}. \tag{E.13}$$

As said, we have assumed $E_3 \ll E_1 \sim E_2$. If this condition is not satisfied, $\gamma_{\rm tot}$ becomes of order γ_3. In Figure E.5, we compare these estimates with numerical results. The agreement is good and confirms our understanding of the energy flow in such a simple system.

We proceed with systems a step more complicated, i.e., a 20 mode system with the first ten modes having large initial amplitudes and the last 10 modes being damped with a rate γ. In this case, in the limit of $\gamma \geq (\delta\omega)$, the number of important resonances for every mode is of order $\gamma/(\delta\omega)$. We use the subscript j for the last ten modes, and i for the first ten. For every damped mode in this limit, its energy will be

$$2\gamma E_j \sim \frac{\omega^2\gamma\kappa^2 E_i^2}{\gamma^2 + (\delta\omega)^2}\left(\frac{\gamma}{(\delta\omega)}\right). \tag{E.14}$$

Hence, the total damping rate,

$$\gamma_{\rm tot} \sim \frac{10\gamma E_j}{10E_i} \sim \omega^2\kappa^2\frac{E_i}{(\delta\omega)}, \tag{E.15}$$

is independent of γ, different from the system that has only three modes. This difference is confirmed by experiments (see Figure E.6). In 20 mode systems, $\delta\omega$, the minimum detuning for triplets that involve one damped mode and two large amplitude modes is of order $1/2/(N-10)^2 \sim 1/200$.

The above results on equilibrium energy indirectly confirm the estimates given by equation (6.17), which gives us confidence in using it on more complicated systems.

E.3.2 Equilibrium Energy

We study multi-mode systems with N_e modes driven at a rate of γ_e and N_d modes damped at a rate of γ_d (Wu 1995).

To estimate the equilibrium energy, we assume that there is no phase correlation among modes (i.e., complete phase randomization), which is a good approximation when the number of modes is large. We can then average over phases in the amplitude equations and write down simplified energy equation as we did in deriving equation (6.17). Here, we assign negligible energy to damped modes, as well as comparable energy (E) to every driven mode. This leads to the following energy equation for any driven mode,

$$\frac{dE}{dt} \simeq 2\gamma_e E - \sum \beta E^2. \tag{E.16}$$

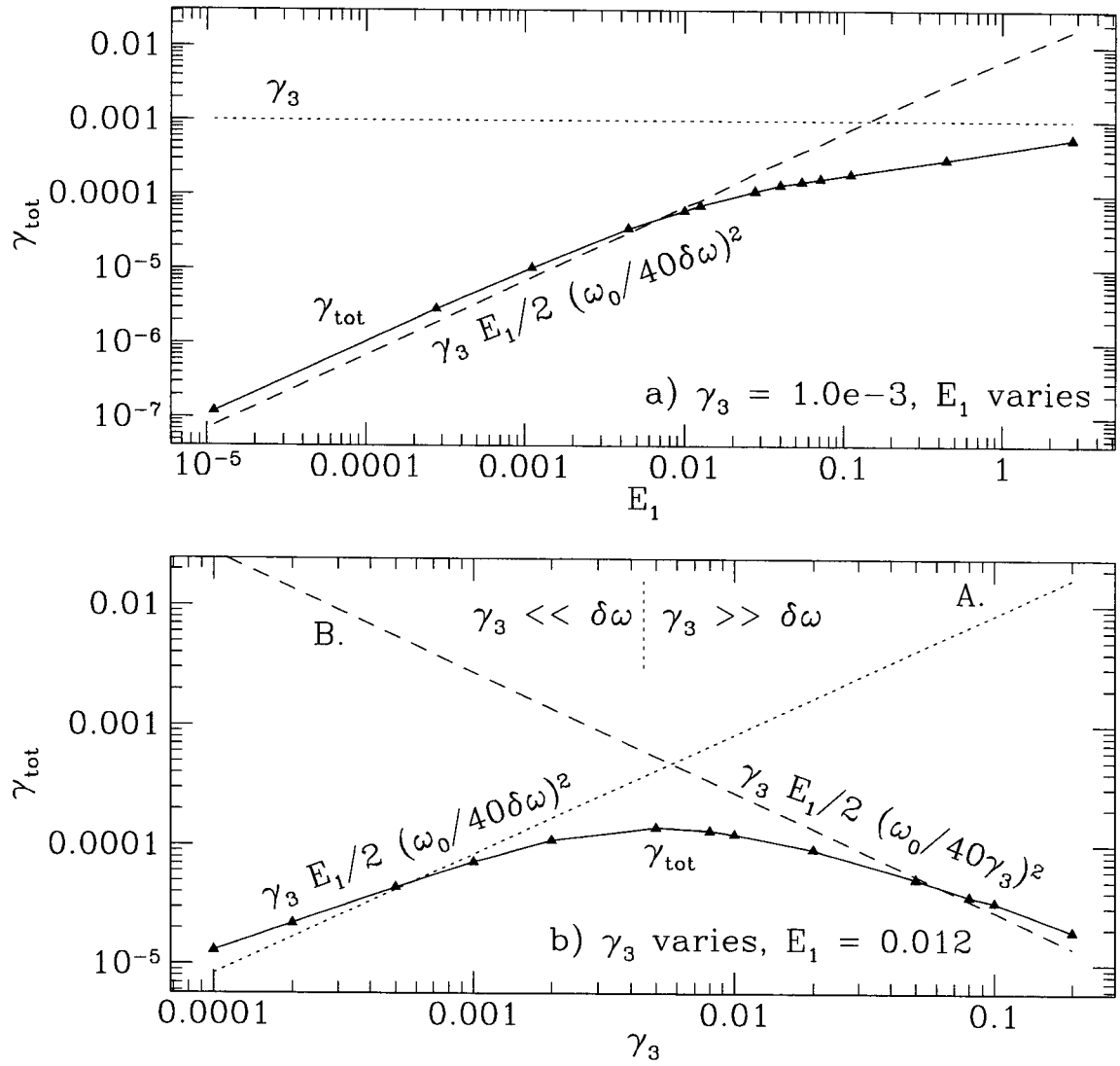

Figure E.5: The total dissipation rate ($\gamma_{\rm tot}$) in a three mode system as a function of mode energy (upper) and mode damping rates (lower). Here modes 1 and 2 have large initial energy (E_1), $\omega_1 + \omega_2 \approx \omega_3$, and mode 3 is damped with a rate of γ_3 ($\gamma_3 > 0$). Energy is transported out of mode 1 and 2 and is dissipated in mode 3. The total dissipation rate is defined as $\gamma_{\rm tot} \equiv \gamma_3 E_3/(E_{\rm tot})$. In the upper panel, $\gamma_3 = 0.001 \leq \delta\omega \sim 0.005$. The triangles are numerical data, and the dashed/dotted lines are theoretical estimates for $E_3 \ll E_1$ and $E_3 \approx E_1$. Initial energy in the system is fixed in the lower panel, and $\gamma_{\rm tot}$ approaches the two theoretical limits made in equation (E.12) for $\gamma_3 \ll \delta\omega$ and in equation (E.13) for $\gamma_3 \gg \delta\omega$ respectively. Here, $\kappa = 1/20$; quartic nonlinearity of the form (E.9) is added to prevent amplitude instability.

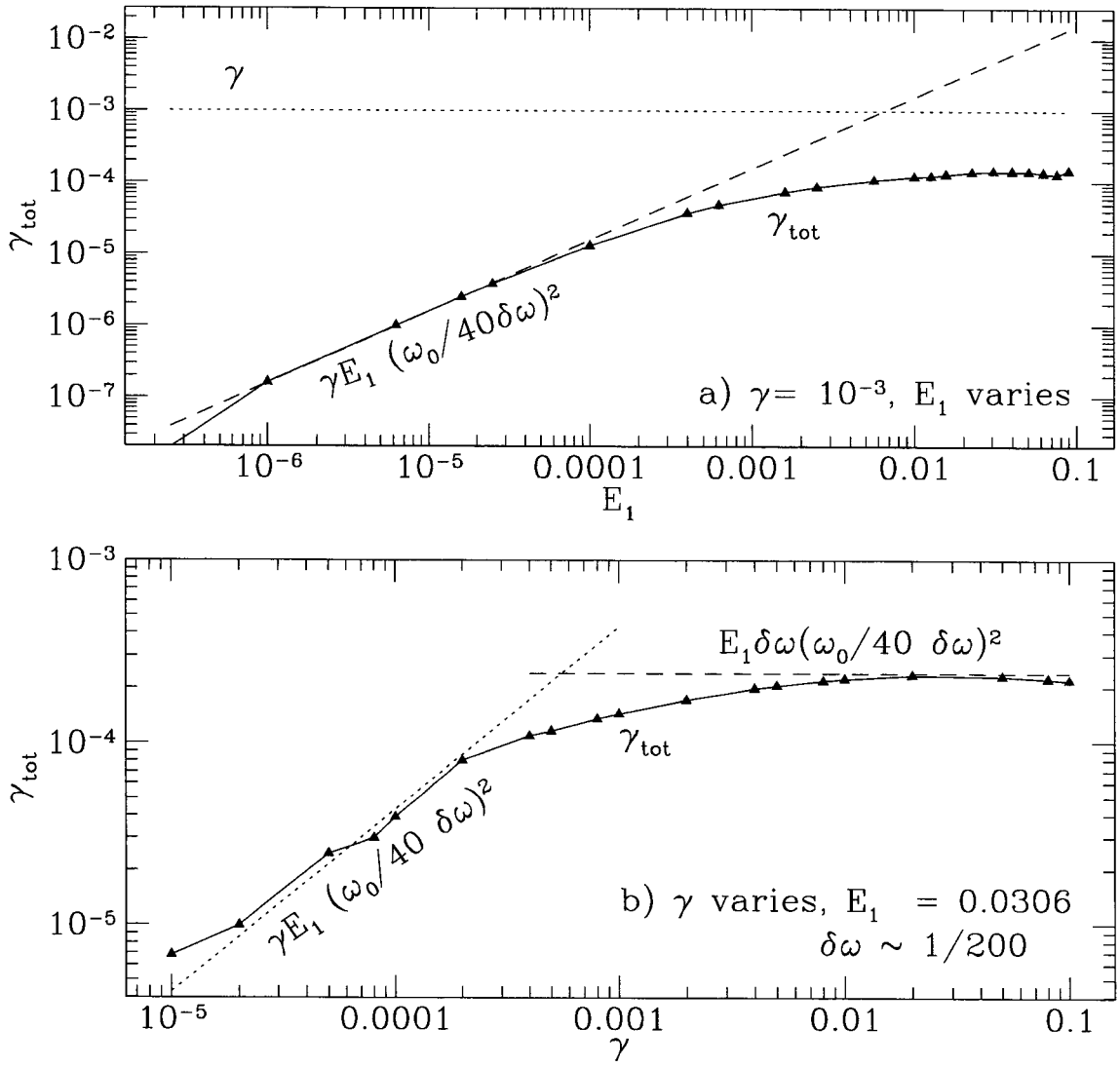

Figure E.6: Similar to Figure E.5, but for a 20-mode system with the first 10 modes excited initially and the last 10 damped with a rate of γ. Here, $\delta\omega$ is the minimum detuning for every damped mode and it is of order 5×10^{-2}. Notice the difference from the three mode case in the bottom panel $\gamma \geq (\delta\omega)$: even when the last 10 modes are infinitely damped, the system still suffers finite dissipation, as predicted by equation (E.15). Here $\kappa = 1/20$; quartic nonlinearity is also added.

The summation is carried out over all triplets that consist of two driven modes and one damped one, taking the minimum frequency detuning within each triplet. These triplets are the ones that work most efficiently to transport energy from the source to the sink, thus constricting the overstable modes to finite amplitudes. The coupling strength β for such a triplet is given by

$$\beta \simeq 9\kappa^2\omega^2 \left[\frac{\gamma}{\gamma^2 + (\triangle\omega)^2}\right], \tag{E.17}$$

where $\gamma = |\gamma_1| + |\gamma_2| + |\gamma_3|$, with modes 1 and 2 driven, and mode 3 damped. In general, damping is much stronger in magnitude than driving, i.e., $\gamma \simeq |\gamma_3| \simeq \gamma_d$. $\triangle\omega$ is the amount of detuning from frequency resonance for the triplet. The part in parenthesis in equation (E.17) is a Lorentzian profile, which accounts for this detuning. When $|\triangle\omega| = 0$, the coupling is called *exact resonance*; when $|\triangle\omega| \leq \gamma$, it is *near-resonance*; otherwise, it is *non-resonance.*

In equilibrium, the energy of every driven mode is approximately given by

$$E \simeq \frac{2\gamma_e}{\sum\beta}, \tag{E.18}$$

and the total energy in the system by

$$E_{\rm tot} \simeq N_e E \simeq N_e \frac{2\gamma_e}{\sum\beta} \tag{E.19}$$

As we discussed in §E.3.1, there are two different limits for such a dissipative system. First, when none of the combinations is close to resonance, i.e., when all $|\triangle\omega| \gg \gamma$, the dynamics is dominated by the one that comes closest, and fast Arnold Diffusion is not possible (since we are using only three-mode coupling in this section, our amplitudes cannot reach the criterion set in eq. [E.7], since they have to satisfy eq. [D.14] to avoid the amplitude instability). For this case,

$$E_{\rm tot} \simeq \frac{2}{9}\frac{N_e(\triangle\omega)^2_{\rm min}\gamma_e}{\kappa^2\omega^2\gamma_d}. \tag{E.20}$$

When chances for resonance and near-resonance are fairly good, i.e., many $|\triangle\omega|_{\rm min} \ll \gamma$, the summation is necessary and can be substituted by multiplying β with an estimate of the number of such (near-)resonances, $\gamma/\omega_{\rm min}$. Fast Arnold Diffusion is guaranteed.

A simple one-dimensional system is designed to test the above conclusions, as well as to familiarize ourselves with the kinds of nonlinear behavior that is present in a real star. The system consists of N_e driven modes, and N_d damped ones, whose frequencies are chosen randomly over a range of $\triangle\omega_e$ and $\triangle\omega_d$, respectively. We let $\triangle\omega_e$ fall within $\triangle\omega_d$. The driving rates for the N_e driven modes are chosen randomly between zero and some positive number, with central value γ_e; similarly for the

N_d damped modes, except with a negative central value of γ_d. Under these conditions,

$$|\triangle\omega|_{\min} \sim \frac{\triangle\omega_e}{N_e N_d}. \tag{E.21}$$

We define

$$C \equiv \frac{|\triangle\omega|}{\gamma}, \tag{E.22}$$

and

$$C_{\min} \equiv \frac{|\triangle\omega|_{\min}}{\gamma}. \tag{E.23}$$

$C_{\min} \gg 1$ represents the first situation discussed above. We have

$$E_{\text{tot}} \sim \frac{2}{9}\frac{N_e\gamma_e\gamma_d}{\kappa^2\omega^2}C_{\min}^2, \tag{E.24}$$

when $C_{\min} \ll 1$, the number of near-resonances (with $C \leq 1$) is large and can be approximated by $\frac{1}{C_{\min}}$, which leads to

$$E_{\text{tot}} \sim \frac{2}{9}\frac{N_e\gamma_e\gamma_d}{\kappa^2\omega^2}C_{\min}. \tag{E.25}$$

Notice the different dependences for the above two results on N_e and N_d. With the help of equation (E.21), energy in equation (E.24) scales as

$$E_{\text{tot}} \propto \frac{1}{N_e N_d^2}, \tag{E.26}$$

while in equation (E.25)

$$E_{\text{tot}} \propto \frac{1}{N_d}. \tag{E.27}$$

The independence of E_{tot} on N_e after $C_{\min}$ passes unity from above is due to saturation of the number of possible combinations between any two driven modes; before this happens, the bigger the number of driven modes, the smaller the total energy. Our numerical experiments yield results that agree with the above estimates satisfactorily, as can be seen in Figure E.7.

E.3.3 When at Equilibrium

We emphasize two aspects of the system dynamics when at dynamical equilibrium. First, the dominance of a couple of overstable modes and their slaving of other modes; second, the fluctuations associated with the dynamical equilibrium.

For simplicity, we again study a system with only three modes. Assume mode 1 and 2 are overstable with rates $\gamma_1 = \gamma_2 = \gamma$, and $\omega_3 \sim \omega_1 + \omega_2$ is damped with a rate of γ_3. We use a detuning $\delta\omega = \omega_1 + \omega_2 - \omega_3 = 0.005$, while typically $\gamma_1 = 10^{-4}$, and $\gamma_3 = -10^{-2}$. The results here should be representative for any combination. We show that at equilibrium, slaving of the third mode to

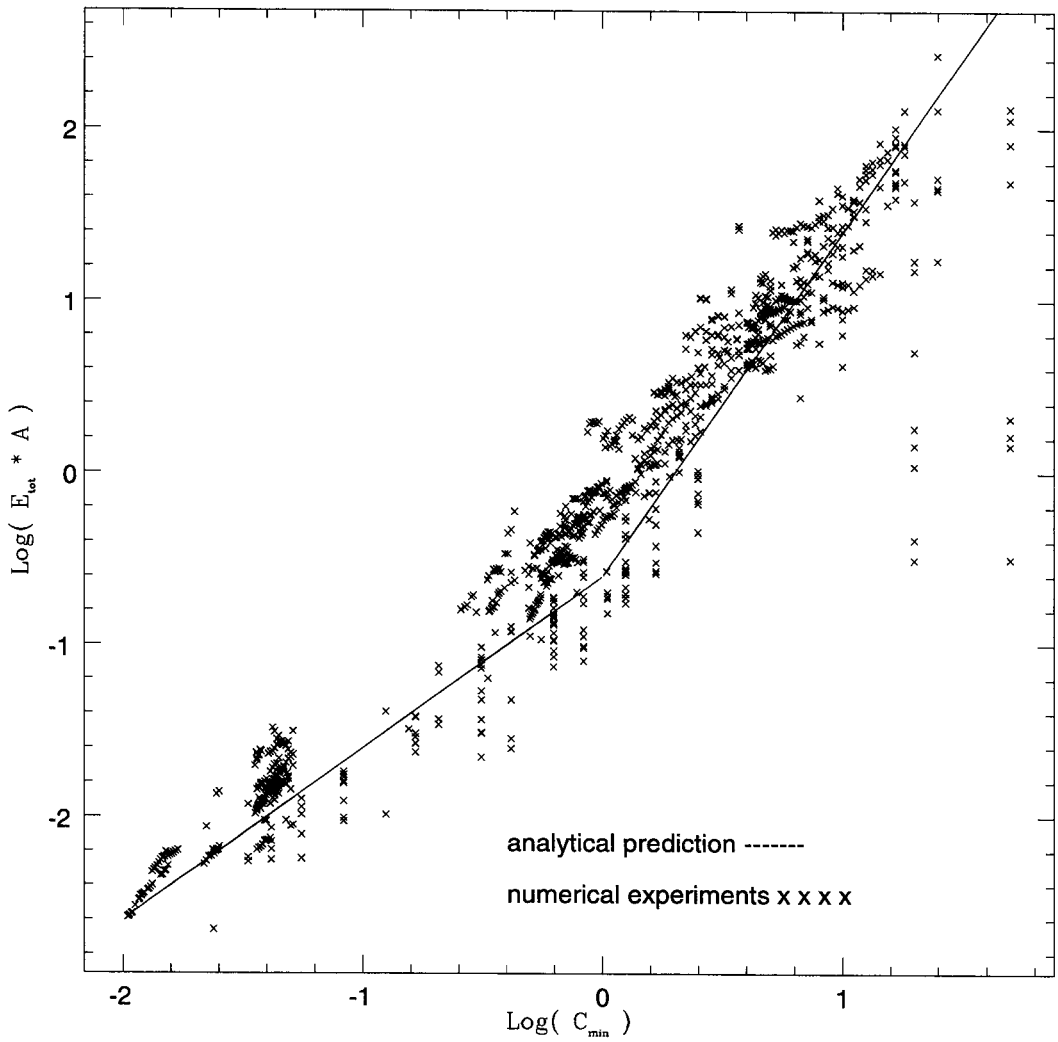

Figure E.7: Total energy in a driven/damped system as a function of $C_{\min}$, the ratio between detuning and damping (eq. [E.23]). Simple estimates are compared with results from numerical simulations. The solid line represents equations (E.24) & (E.25), with a somewhat arbitrary break at the point of $C_{min} = 1$. Here, the energy scaling factor $\frac{1}{A} = \frac{2}{9}\frac{N_e\gamma_e\gamma_d}{\kappa^2\omega^2}$. The large scatter at $C_{min} \gg 1$ is associated with the small values of N_e there (mostly $N_e = 1$); since the analytical results only describe the simulations statistically, a bigger N_e (or N_d) provides a better fit, as is clear elsewhere in the plot. The only nonlinearity in these experiments is those due to three-mode couplings.

the frequency determined by the two excited modes is prominent. This affects the dynamics of the system. We use an amplitude equation of the form (with $\kappa = \sqrt{2}/36$),

$$\frac{dA_i}{dt} = \gamma_i A_i + i\omega_i A_i + \frac{i\omega_i}{24} A^2 + \frac{i\omega_i}{48} A^3, \tag{E.28}$$

where A is a summation over real parts of the amplitudes, $A = \sum_{j=1}^{3}(A_j + A_j^*)$. The addition of the fourth order interactions helps to keep the system free from the amplitude instabilities (see Appendix D). It does not change the dynamics too much since the terms are usually small compared to the three-mode coupling terms. The system is started with random initial amplitudes and phases, and integrated forward using a second-order symplectic integrator. The final equilibrium state is reached when there are no more secular changes in mode energy. At equilibrium, apart from random variations over short time scale, we should have $\gamma_1 E_1 + \gamma_1 E_2 + \gamma_3 E_3 \simeq 0$.

First, we show that in this system, the naive equilibrium state of $E_1 \sim E_2 \gg E_3$, with mode 1 and 2 contributing energy simultaneously to mode 3 is not a stable configuration.

As is clear from the energy equation (6.17), mode 1 and 2 lose energy in a ratio of ω_1/ω_2. If we define the quasi-particle number as $N_i = E_i/\omega_i$, three-mode coupling takes one quasi-particle out of each driven mode, and put one into the damped mode. But mode 1 and 2 are gaining energy with the same rate, $2\gamma_1 E_1 \sim 2\gamma_2 E_2$. Hence, there is an energy budget unbalance for at least one of the two driven modes when they have similar energy.

So, how about a solution $E_1 \sim \omega_1/\omega_2 E_2 \gg E_3$? This solution is not stable against small perturbations. Let $E_1 = E_1(0) + \epsilon$, $E_2 = E_2(0) + \delta$, $E_1(0)$ $E_2(0)$ are solutions that make $dE_i/dt = 0$. When neglecting the smaller nonlinear terms, the perturbed forms of equation (6.17) look like,

$$\frac{d\epsilon}{dt} = -\frac{\gamma_1 \omega_1}{\omega_2}\delta; \tag{E.29}$$

$$\frac{d\delta}{dt} = -\frac{\gamma_1 \omega_2}{\omega_1}\epsilon. \tag{E.30}$$

Convert these to second-order differential equations, and it is clear that both ϵ and δ are going to grow exponentially with a rate of γ_1, i.e., the solution is not stable.

According to the above reasoning, a stable equilibrium state will not depend on the reaction of $\omega_1 + \omega_2 \rightarrow \omega_3$ alone. In fact, other channels of energy transfer have to become dominant, even though the frequency detuning, $\delta\omega$, associated with them are much larger. For these interactions, we find that one mode becomes the dominant one and starts forcing some of the other modes into slaved oscillations. Which mode achieves this status depends on the initial conditions and the frequency ratios.

The fact that the most obvious interaction channel ($\omega_1 + \omega_2 \rightarrow \omega_3$) is not necessarily the most important one appears in many three-mode systems we investigated. A variety of results are shown

in Figure E.8. Notice the different degrees of slaving, as well as the interesting fact that one of the excited modes has to stay at very low energy. There is strong phase locking in these simple dynamical systems, and even excited modes can be slaved. Here, the natural frequencies of the three modes are not necessarily in resonance.

In contrast to the systems with two excited modes, a parametrically excited system ($\omega_1 \rightarrow \omega_2+\omega_3$, with mode 1 excited and the other two damped) can lose energy stably through the best resonance.

Also, in systems that have more than two excited modes, effective combinations are many. Phase randomization is realized, and the obvious channels can be the best ones. But even in these systems, slaving may be important. In fact, as is strongly suggested by Figure E.9, mode slaving is rather universal among globally coupled dissipative systems, whose dynamics are not ideally turbulent. One may have to wonder whether a slaved mode in the pulsating white dwarf can still be called an eigenmode, though.

We find that globally coupled systems, even for large N, will gradually evolve towards an energy distribution pattern in which a small population of overstable modes dominate the dynamics. These excited modes, together with the damped modes related to them through resonances, become the main reservoir of energy. This is shown in Figure E.9, where energy of the modes is seen to depend smoothly on frequency, we call these the 'beautiful patterns'. The presence of these patterns implies the presence of mode slaving, and therefore the failure of the random phase approximation. The system is in a chaotic yet not turbulent state. The effective line-widths of the modes are narrower than either the linear driving/damping rates or the nonlinear line-width one would estimate from the mode amplitudes. The whole system is organized into many limit cycle oscillations.

In deriving equations (E.24) & (E.25), we assume that every excited mode have similar energy, and we estimate the total energy in the system from this. But in reality, each dynamical system that contributes to one data point in Figure E.7 has an un-even distribution of energy among even excited modes. Fortunately, the results tested in that figure depend only weakly on this assumption.

When there is no more secular change in mode energy, we say that the system has reached equilibrium. And when a system allows fast diffusion across resonances and satisfies phase randomization (as opposed to the phase locking seen in most of the examples discussed above), we say the system is in weak turbulence. For an equilibrium system exhibiting weak turbulence, every mode is still jigglings in energy space, exchanging heat constantly and satisfying $dE_i/dt = 0$ only statistically. Moreover, the size of the fluctuations in this state can be of order the amplitudes themselves. This is similar to the conservative case, in which the energy is distributed as a Boltzman function (Fig. E.4).

We consider the time scale for these energy fluctuations. A hand-waving argument goes as follows: at statistical equilibrium, an excited mode gains energy from the stellar background, and loses it through nonlinear interaction. For statistical equilibrium to hold any time, these two processes

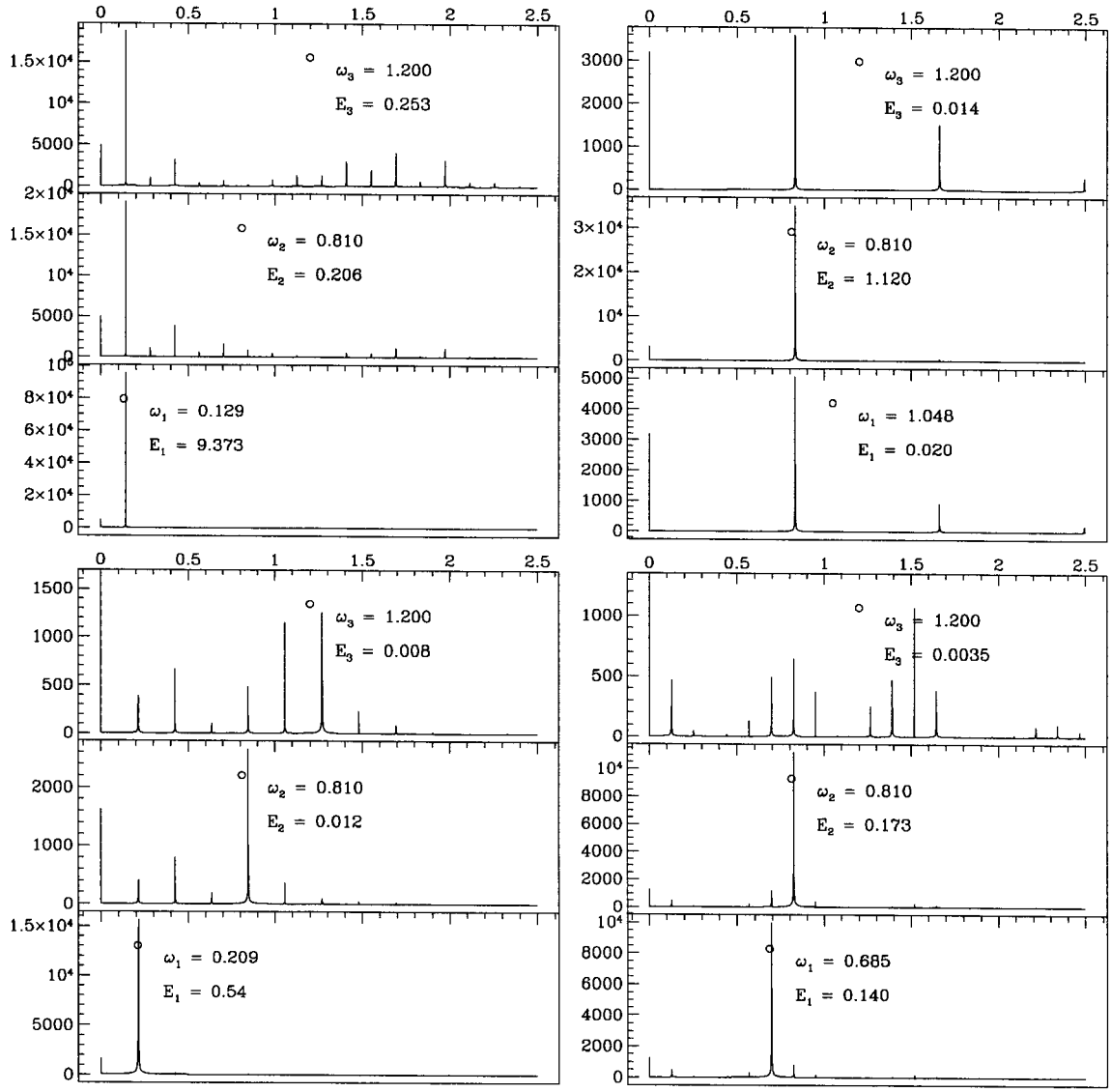

Figure E.8: We study the slaving of modes in a small dynamical system where two modes are driven with $\gamma = 10^{-4}$, and the third mode is damped $\gamma_3 = -10^{-2}$. The horizontal axis is frequency, the vertical one is the amplitude of Fourier transform for the real part of the mode amplitudes. Shown here are four systems, each occupying three panels, corresponding to the three modes in each system. Listed are the natural frequencies and equilibrium energy for every mode. The small open circle sits at the natural frequency of the mode. Notice the different degrees and forms of slaving. Lower left: mode 2 is slaved to $4\omega_1$. Upper left: mode 2 is slaved to ω_1. Lower right: both driven modes oscillate at their natural frequencies. Upper right: mode 1 is slaved to ω_2. In none of these cases, mode 3 is oscillating at its natural frequency. We include four-mode coupling in these simulations, but it is not the main channel of energy transport, judging from the types of slaving behaviour here. We are baffled, in any case, by the presence of seemingly very high order resonances. For example, in the lower left case, there seems to be five-mode coupling, though this is not allowed by the amplitude equations.

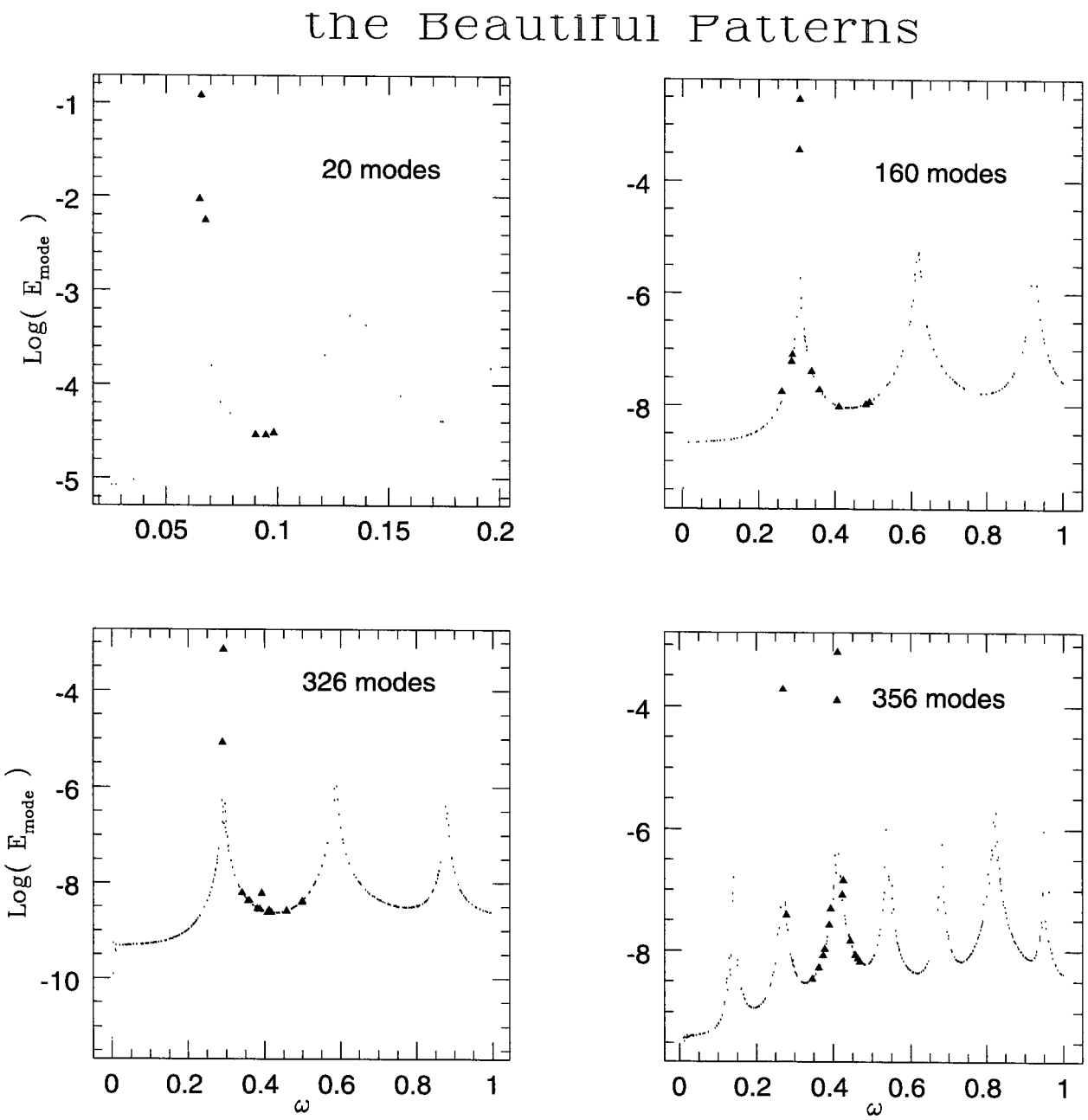

Figure E.9: Another example of the slaving behaviour. Here, four globally coupled large dynamical systems are observed at their equilibrium. They differ in their total number of modes. The triangles represent overstable modes, while the dots represent damped modes. Apparently, stable equilibrium in this kind of systems requires specific pattern of energy distribution, in which a few overstable modes dominate the scene. The pattern becomes more and more organized as N increases, and the damped modes (and some excited modes) are obviously in forced oscillation. Here, only cubic nonlinearity is used in the amplitude equations.

should have similar time scales. So, in the limit of weak turbulence, pulsation modes have amplitude changes of order the amplitudes themselves, and the time scale of the amplitude changes should be of order their respective driving or damping times.

We stress that the above results are for systems in truly turbulent state. We have considered mainly globally coupled system in this chapter. In these systems, modes are closely chained to each other in both phases and amplitudes, and show a strong coherence that is not generic of real pulsating stars. A pulsating white dwarf presumably possesses many relatively inter-dependent sub-populations.

We must mention again that we started investigating globally coupled systems with only cubic nonlinearity both for its simplicity and computational convenience. But the amplitude instability intrinsic to cubic nonlinearity (Appendix D) reduces the importance of these studies. Normal modes in a physical system do not experience such an instability. The results we obtain for the globally coupled systems are, at best, only illustrative to the dynamics in a real system, which has non-constant coupling coefficients for different resonances, and has strict angular selection rules that exclude global coupling. For a pulsating white dwarf, the amplitude instability only becomes possible when $(\delta\rho/\rho)_{\rm tot}$ caused by pulsation approaches unity. But at this point, the perturbative approach breaks down and we need not worry about this instability. Also, the behaviour of mode slaving (in which a subordinate mode oscillates at alien frequency) is unique to the truncation of mode couplings in the amplitude equations. In a pulsating star, when the condition for mode slaving is present, the higher order couplings have become as important as the lowest order ones, and the assumption leading to the amplitude equations breaks down.

E.4 Realistic Multi-mode System – First View

Here, we investigate the dynamics of a more realistic system. This system is a small sub-population among the normal mode hierarchy in a pulsating white dwarf. We can choose this sub-population arbitrarily, and take into account all couplings among its members.

Here, we select a few low-order (radial order n), low degree (spherical degree ℓ as in $Y_{\ell m}$) modes, with $n = 1, 2...7$, $\ell = 1, 2, ...5$ (we set all $m = 0$). There are 35 modes in this group and a total of 749 combinations that are allowed by angular selection rules ($\ell_3 = |\ell_1 - \ell_2|, |\ell_1 - \ell_2| + 2, ..., |\ell_1 + \ell_2| - 2, |\ell_1 + \ell_2|$). The modes we choose for the experiments are modes that are likely to be important in a pulsating white dwarf; some of them will be visible in the observed power spectrum. We investigate the dynamics of such a conservative system ($\gamma = 0.0$).

First, we demonstrate that a realistic system can reach energy equipartition without encountering the amplitude instability, unlike a globally coupled system. The initial conditions are such that only the $\ell = 1$ modes have large energy. The $\ell = 1$ branch also has relatively low frequency. We show by

numerical experiments that energy equipartition happens after finite time when the total energy in the system is sufficiently large. The 749 combinations form a diffusive web for any mode to travel across the resonances and to get infinitely close to any location in the phase space, i.e., we observe fast Arnold diffusion and strong stochastic behaviour. The energy equipartition process is shown in Figure E.10, in which the amplitudes (the squared root of energy) of individual modes approaches a uniform distribution after a time of 10^8 s, when the mode periods are of order 100 s. The amplitudes we use in this experiment are comparable to the observed amplitudes of the pulsations, i.e., the density compression $(\delta\rho/\rho)$ for overstable mode is of order a few percent.

The diffusion time ($\sim 10^6$ mode periods) can be further shortened when the system we choose better resembles a white dwarf in terms of number of modes and combinations.

At equilibrium, every mode acquires equal amount of energy, independent of their mode masses. This is shown as the constancy of energy, but non-constancy of $(\delta\rho/\rho)$ in Figure E.10.

On the other hand, if we give initial energy to the $\ell = 5$, $n = 1, ...7$ modes (which have on average higher frequencies), the energy equipartition process is much slower, as is seen in Figure E.11. But the main explanation for this behaviour is not the resonance property of the modes (as is invoked in the discussion around Figure E.2), but rather the average magnitudes of κ, which decreases as a function of ℓ when n is kept constant. This characteristic of κ is demonstrated in §G.3.

Bibliography

Callen, H. B. 1985, Thermodynamics & Introduction to Thermostatistics, (New York:Wiley)

Chirikov, B. V. 1979, Phys. Rep., 52, 263

Contopoulos, G., Voglis, N., Efthymiopoulos, C., & Grousouzakou, E. 1995, in Waves in Astrophysics, ed. Hunter, J. H., & Wilson, R. E., Annals of New York Academy of Sciences, 773,145

De Luca, J., Lichtenberg, A. J., & Lieberman, M. A. 1995, Chaos, 5,283

Fermi, E., Pasta, J., & Ulam, S. 1954, E. Fermi: Collected Papers, ed. by Segre, E., (University of Chicago), 1965

Galgani, L., Giorgilli, A., Martinoli, A., & Vanzini, S. 1992, Phsica D, 59,334

Pettini, M., & Cerrutisolar, M., 1991, Phys. Rev. A., 44, 975

Tuck, J., & Menzel, M. 1972, Adv. Math. 9, 399

Wu, Y. 1995, in Waves in Astrophysics, ed. Hunter, J. H., & Wilson, R. E., Annals of New York Academy of Sciences, 773,296

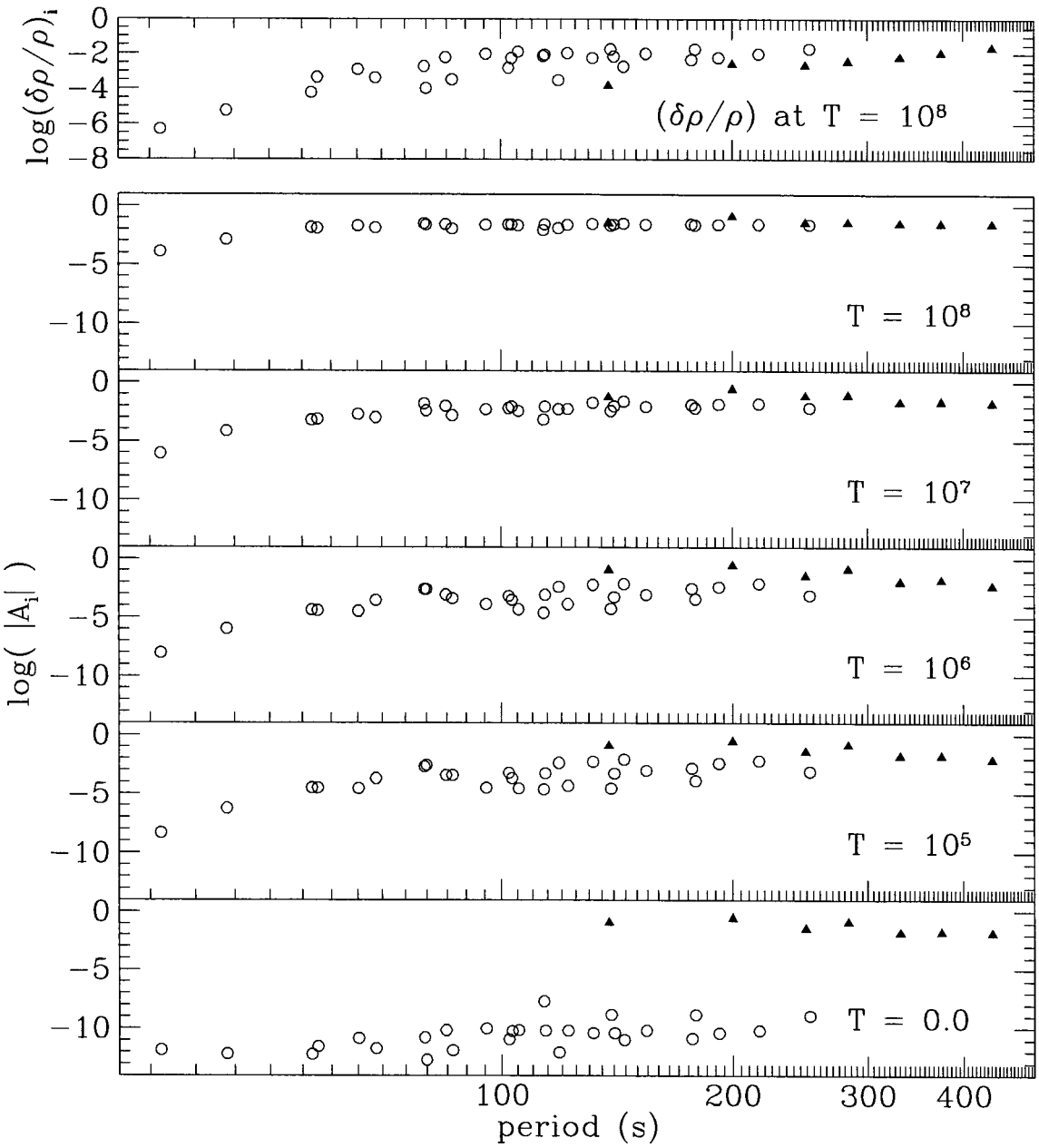

Figure E.10: The process towards energy equipartition in a numerical experiment where 35 modes and 749 couplings among these modes are included (see the text for the choice of the modes). We are *not* dealing with a globally coupled system. The system is conservative, and 7 modes are given initially large amplitudes, similar to the observed magnitudes of $(\delta\rho/\rho)$ in a pulsating white dwarf. The rest are given much smaller initial energy. Evolution of the time-averaged A_i due to nonlinear interaction is plotted in the subsequent panels. At a time as early as $T = 10^5$, a fast process has given rise to approximate equipartition for the majority of the modes. A much longer time ($T = 10^8$) is necessary for the completion of this process, possibly due to the existence of strong resonances and inhomogeneous phase space attractors (see §E.2.2). The physical amplitudes $(\delta\rho/\rho)_i$ (plotted in the upper-most panel for $T = 10^8$) is related to A_i by its normalization value and a constant 10^{19} such that, $(\delta\rho/\rho)_i = 10^{19}(\delta\tilde{\rho}/\rho)A_i$, and $(\delta\tilde{\rho}/\rho)$ is the normalized value of $(\delta\rho/\rho)$ at z_ω, the top of the propagating cavity of the mode (see Chap. 2).

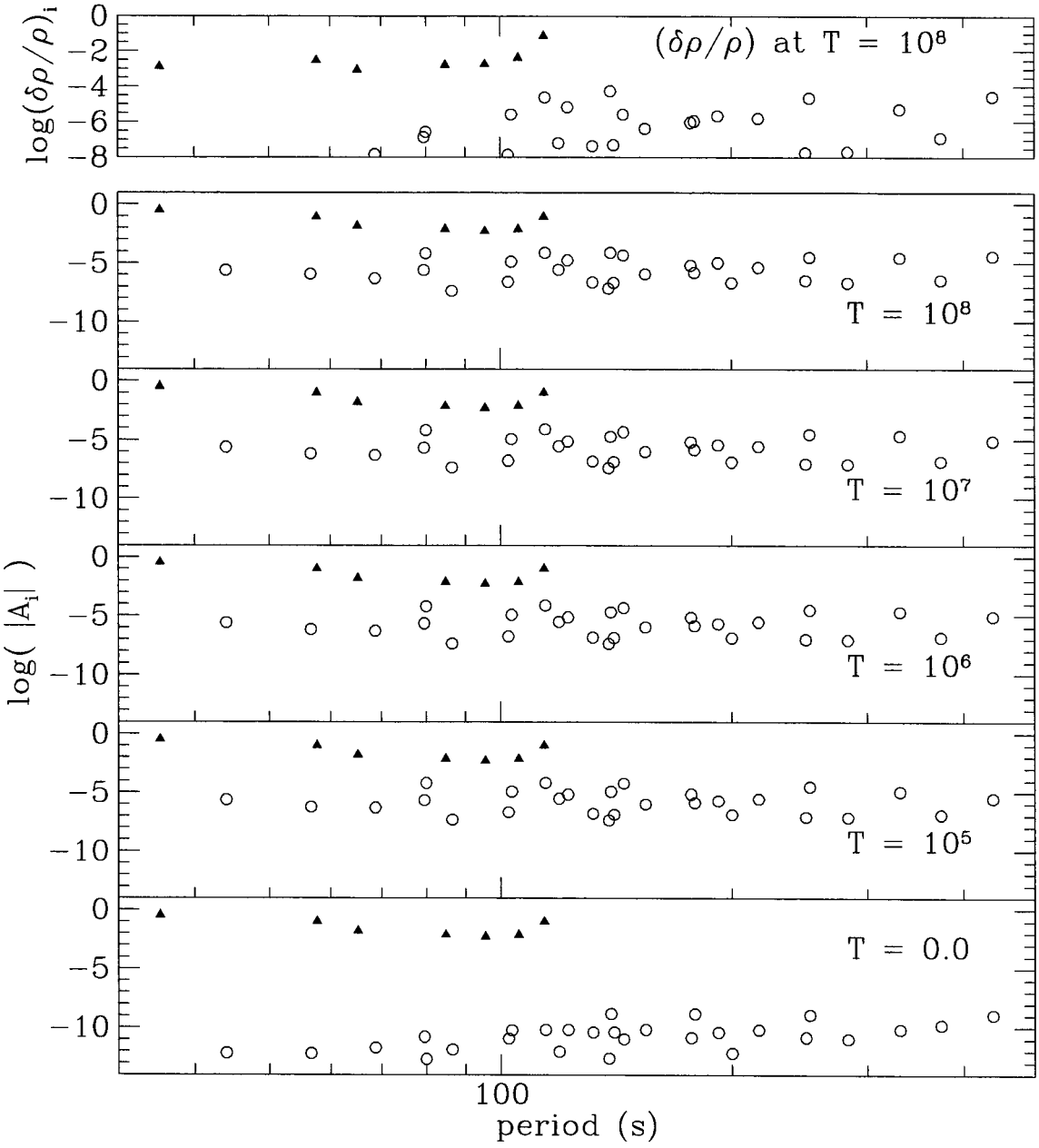

Figure E.11: Similar to Figure E.10, but with the seven relatively high frequency modes initially excited. The total energy in the system is similar to that in Figure E.10. Energy equipartition is achieved much later, as a result of the difficulty in finding good, efficient resonances for these high frequency modes.

Appendix F Deriving the Energy Equations from the Amplitude Equations

F.1 Introduction

In this appendix, we detail our effort in deriving the secular forms of the amplitude equations. Called energy equations, these forms are useful in understanding the evolution and equilibrium of coupled dynamical systems. As all fast oscillating terms are removed using the random phase approximation, only slowly varying dynamics is preserved in the equations, and the confusion is minimized. We should caution that at many times, dynamics described by the amplitude equations does not produce sufficient phase mixing and satisfy the random phase approximation. At such times, the energy equation may not describe the most important dynamics in the system.

We consider a system with at most three modes and one single coupling. The energy equation derived for it can be easily generalized to other systems. We derive expressions for energy equations in a conservative system, as well as a dissipative system. Expressions for the latter case is not seen anywhere in literature.

Equation (6.15) describes the evolution of mode i's amplitude under both the phase rotation and the three-mode coupling with mode j and k. Here, we decompose that complex equation into two real equations: equation for amplitude modulus evolution,

$$\frac{dA_i}{dt} = \gamma_i A_i + \omega_i S_i |K_{ijk}| A_j A_k \sin(\Phi_{ijk} + \delta); \tag{F.1}$$

and equation for phase evolution,

$$\frac{d\phi_i}{dt} = \omega_i + \omega_i |K_{ijk}| \frac{A_j A_k}{A_i} \cos(\Phi_{ijk} + \delta). \tag{F.2}$$

Here, A_i are the modulus of the amplitude for mode i, the complex amplitude $\tilde{A}_i = A_i \exp(-i\phi_i) = A_i \exp(-i\omega_i t - i\psi_s(t))$. Mode energy $E_i = J_i\omega_i = \tilde{A}_i \tilde{A}_i^* = A_i^2$. The phase combination $\Phi_{ijk} = S_i * \phi_i + S_j * \phi_j + S_k * \phi_k$, where $s_{i,j,k}$ takes $+1$ or -1. The coupling strength between modes (i, j, k) is $K_{ijk} = |K_{ijk}| \exp(-i\delta)$. γ_i is the driving or damping rate for mode i.

In later derivations, we rely heavily on the concept of quasiparticle numbers, M_i. It is related to A_i as

$$M_i = \frac{A_i}{\sqrt{\omega_i}}; \tag{F.3}$$

therefore, $M_i^2 = E_i/\omega_i$.

In terms of quasiparticle numbers,

$$\frac{dM_i}{dt} = \gamma_i M_i + S_i f_{ijk} \sin(\delta\omega\, t + \Phi_{ijk} + \delta) M_j M_k, \tag{F.4}$$

and the phase equation changes into one for ψ_i, the part of the total phase ϕ_i that does not rotate fast,

$$\frac{d\psi_i}{dt} = f_{ijk} \cos(\delta\omega\, t + \Phi_{ijk} + \delta) \frac{M_j M_k}{M_i}, \tag{F.5}$$

with a new coupling strength

$$f_{ijk} = |K_{ijk}| * \sqrt{\omega_i \omega_j \omega_k}. \tag{F.6}$$

F.2 Energy Equations for Conservative Systems

Kumar & Goldreich (1989) derive the energy equation for the above amplitude equations in the case of $\gamma_i = 0$. They get

$$\frac{dE_{i2}}{dt} = S_i \omega_i K_{ijk}^2 (S_i \omega_i E_{j0} E_{k0} + S_j \omega_j E_{i0} E_{k0} + S_k \omega_k E_{i0} E_{j0}) (\frac{\sin(\delta\omega\, t)}{\delta\omega}), \tag{F.7}$$

or, equivalently, in terms of quasiparticle numbers,

$$\frac{dE_{i2}}{dt} = S_i \omega_i f_{ijk}^2 (S_i M_{j0}^2 M_{k0}^2 + S_j M_{i0}^2 M_{k0}^2 + S_k M_{i0}^2 M_{j0}^2) \frac{\sin(\delta\omega\, t)}{\delta\omega}. \tag{F.8}$$

Here, E_{i2} is the second order perturbation on E_i with the following expansion,

$$E_i(t) = E_{i0} + E_{i1}(t) + E_{i2}(t) + \ldots. \tag{F.9}$$

They find that E_{i1} does not have secular changes due to three-mode couplings.

Here, we provide a new (but similar) way of deriving the energy equation and show later that using the perturbations of energy (E_i, as is done in Kumar & Goldreich 1989) and using the perturbations of quasiparticle numbers (M_i) give essentially the same results.

We perturbatively expand M_i as

$$M_i(t) = M_{i0} + M_{i1}(t) + M_{i2}(t) + \ldots. \tag{F.10}$$

The relations between expansion terms for E_i and M_i are

$$E_i = \omega_i M_i M_i \simeq \omega_i (M_{i0} + M_{i1}(t) + M_{i2}(t)) * (M_{i0} + M_{i1}(t) + M_{i2}(t))$$

$$\simeq \omega_i(M_{i0}^2 + 2M_{i0}M_{i1} + M_{i1}^2 + 2M_{i0}M_{i2} + ...), \tag{F.11}$$

or, more explicitly,

$$\begin{aligned} E_{i0} &= \omega_i M_{i0}^2, \\ E_{i1} &= \omega_i 2M_{i0}M_{i1}, \\ E_{i2} &= \omega_i(M_{i1}^2 + 2M_{i0}M_{i2}). \end{aligned} \tag{F.12}$$

We further expand phase ψ_i as

$$\psi_i(t) = \psi_{i0} + \psi_{i1}(t) + \psi_{i2}(t) + ... \tag{F.13}$$

With the γ's set to zero, equations (F.4) and (F.5) become

$$\begin{aligned} \frac{dM_i}{dt} &= S_i f_{ijk} \sin(\delta\omega\, t + \Phi_{ijk} + \delta) M_j M_k, \\ \frac{d\psi_i}{dt} &= f_{ijk} \cos(\delta\omega\, t + \Phi_{ijk} + \delta) \frac{M_j M_k}{M_i}. \end{aligned} \tag{F.14}$$

Assuming all perturbations are zero at time $t = 0$, the zeroth order quantities can be substituted into the right-hand side of equation (F.14). Integrating it over time yields expressions for the first order quantities,

$$\begin{aligned} M_{i1}(t) &= S_i f_{ijk} M_{j0} M_{k0} \frac{\cos({\Phi_{ijk}}^0 + \delta) - \cos(\delta\omega\, t + {\Phi_{ijk}}^0 + \delta)}{\delta\omega}, \\ \psi_{i1}(t) &= f_{ijk} \frac{M_{j0}M_{k0}}{M_{i0}} \frac{\sin(\delta\omega\, t + {\Phi_{ijk}}^0 + \delta) - \sin({\Phi_{ijk}}^0 + \delta)}{\delta\omega}, \end{aligned} \tag{F.15}$$

where ${\Phi_{ijk}}^0 = S_i\psi_{i0} + S_j\psi_{j0} + S_k\psi_{k0}$.

Now, to derive the second order quantities, we need to substitute the above first order ones back into the right-hand side of equation (F.14) again. Noting that

$$\begin{aligned} \frac{M_j M_k}{M_i} &\simeq (M_{j0} + M_{j1})(M_{k0} + M_{k1})(\frac{1}{M_{i0}} - \frac{M_{i1}}{{M_{i0}}^2}) \\ &\simeq \frac{M_{j0}M_{k0}}{M_{i0}} + \frac{M_{j0}}{M_{i0}}M_{k1} + \frac{M_{k0}}{M_{i0}}M_{j1} - \frac{M_{j0}M_{k0}}{M_{i0}^2}M_{j1}, \end{aligned} \tag{F.16}$$

as well as,

$$\begin{aligned} M_j M_k &\simeq M_{j0}M_{k0} + M_{j0}M_{k1} + M_{k0}M_{j1}, \\ \sin(\delta\omega\, t + \Phi_{ijk} + \delta) &= \sin(\delta\omega\, t + {\Phi_{ijk}}^0 + \delta) + \cos(\delta\omega\, t + {\Phi_{ijk}}^0 + \delta){\Phi_{ijk}}^1, \\ \cos(\delta\omega\, t + \Phi_{ijk} + \delta) &= \cos(\delta\omega\, t + {\Phi_{ijk}}^0 + \delta) - \sin(\delta\omega\, t + {\Phi_{ijk}}^0 + \delta){\Phi_{ijk}}^1, \end{aligned} \tag{F.17}$$

where ${\Phi_{ijk}}^1 \equiv S_i\psi_{i1} + S_j\psi_{j1} + S_k\psi_{k1}$, we obtain the following relations, adopting the assumption of random phases,

$$\begin{aligned}
\frac{dM_{i2}}{dt} &= S_i f_{ijk}(M_{j0}M_{k1} + M_{k0}M_{j1})\sin(\delta\omega\, t + {\Phi_{ijk}}^0 + \delta) \\
&\quad + S_j f_{ijk} M_{j0}M_{k0}\cos(\delta\omega\, t + {\Phi_{ijk}}^0 + \delta)(S_i\psi_{i1} + S_j\psi_{j1} + S_k\psi_{k1}) \\
&= S_i f_{ijk}^2(2S_j M_{k0}^2 M_{i0} + 2S_k M_{j0}^2 M_{i0} + S_i\frac{M_{j0}^2 M_{k0}^2}{M_{i0}}) * \\
&\quad \sin(\delta\omega\, t + {\Phi_{ijk}}^0 + \delta)\frac{\cos({\Phi_{ijk}}^0 + \delta) - \cos(\delta\omega\, t + {\Phi_{ijk}}^0 + \delta)}{\delta\omega}. \qquad \text{(F.18)}
\end{aligned}$$

The random phase approximation adopted above leads to expressions for the secular changes in phases and amplitudes. As an essential part of this derivation, the random phase approximation stresses that the phases of various components in a coupled system are not causally connected, as their natural frequencies are different. It is necessary that the small part of the phase, ψ_i, remains small in comparison to the rotating part of the phase (ωt); in other words, the mode is assumed to rotate close to its natural frequency. As is shown in Chapter 6, this assumption is not always satisfied in systems with small number of modes and strong interactions, and in these cases, the random phase approximation breaks down.

We come back to our derivations. For simplicity, we split the angles inside *sin* and *cos* functions in equation (F.18) into

$$\begin{aligned}
\alpha &= \frac{\delta\omega\, t + 2{\Phi_{ijk}}^0 + 2\delta}{2}, \\
\beta &= \frac{\delta\omega\, t}{2}. \qquad \text{(F.19)}
\end{aligned}$$

Simple trigonometry transforms equation (F.18) into

$$\frac{dM_{i2}}{dt} = S_i f_{ijk}^2(2S_j M_{k0}^2 M_{i0} + 2S_k M_{j0}^2 M_{i0} + S_i\frac{M_{j0}^2 M_{k0}^2}{M_{i0}})\frac{\sin^2\alpha\sin 2\beta + \sin 2\alpha\sin^2\beta}{\delta\omega}. \qquad \text{(F.20)}$$

The random phase approximation leads to the following expressions,

$$\begin{aligned}
< \sin 2\alpha > &= 0, \\
< \sin^2\alpha > &= \frac{1}{2}. \qquad \text{(F.21)}
\end{aligned}$$

And we have

$$\frac{dM_{i2}}{dt} = S_i f_{ijk}^2(S_j M_{k0}^2 M_{i0} + S_k M_{j0}^2 M_{i0} + \frac{1}{2}S_i\frac{M_{j0}^2 M_{k0}^2}{M_{i0}})(\frac{\sin(\delta\omega\, t)}{\delta\omega}); \qquad \text{(F.22)}$$

this is the final result for M_{i2}.

Derivation for ψ_{i2} is analogous to what we just did above and leads to

$$\frac{d\psi_{i2}}{dt} = f_{ijk}^2(S_k M_{j0}^2 + S_j M_{k0}^2)(\frac{1-\cos(\delta\omega\, t)}{\delta\omega}). \tag{F.23}$$

When there are more than three modes, the right-hand sides of equations (F.22) and (F.23) should sum over all possible combinations.

For $t \ll \frac{1}{\delta\omega}$, we have

$$\begin{aligned} \frac{\sin(\delta\omega\, t)}{\delta\omega} &\sim t, \\ \frac{1-\cos(\delta\omega\, t)}{\delta\omega} &\sim 2\delta\omega\, t^2. \end{aligned} \tag{F.24}$$

This brings equation (F.22) and (F.23) to their final form

$$\frac{dM_{i2}}{dt} = S_i f_{ijk}^2(S_j M_{k0}^2 M_{i0} + S_k M_{j0}^2 M_{i0} + \frac{1}{2} S_i \frac{M_{j0}^2 M_{k0}^2}{M_{i0}})t, \tag{F.25}$$

$$\frac{d\psi_{i2}}{dt} = 2 f_{ijk}^2(S_k M_{j0}^2 + S_j M_{k0}^2)\delta\omega\, t^2. \tag{F.26}$$

Equation (F.25) can also be derived differently. Take a second order derivative of M_i with respect to time, applying random phase approximation to it, we get

$$\frac{d^2 M_i}{dt^2} = S_i f_{ijk}^2(S_j M_{k0}^2 M_{i0} + S_k M_{j0}^2 M_{i0} + \frac{1}{2} S_i \frac{M_{j0}^2 M_{k0}^2}{M_{i0}}). \tag{F.27}$$

Using the following Taylor expansion,

$$M_i(t) = M_i(0) + \frac{dM_i}{dt}|_{t=0}\, t + \frac{1}{2}\frac{d^2 M_i}{dt^2}|_{t=0}\, t^2 + \ldots, \tag{F.28}$$

we obtain the secular changes for M_i as

$$< M_i(t) - M_i(0) >= \frac{1}{2} S_i f_{ijk}^2(S_j M_{k0}^2 M_{i0} + S_k M_{j0}^2 M_{i0} + \frac{1}{2} S_i \frac{M_{j0}^2 M_{k0}^2}{M_{i0}})t^2. \tag{F.29}$$

In a differential form, this is

$$< \frac{dM_i}{dt} >= S_i f_{ijk}^2(S_j M_{k0}^2 M_{i0} + S_k M_{j0}^2 M_{i0} + \frac{1}{2} S_i \frac{M_{j0}^2 M_{k0}^2}{M_{i0}})t. \tag{F.30}$$

Identical to equation (F.25).

At first look, it's not obvious that equation (F.25) is equivalent to equation (F.8). We prove here

that they are indeed equivalent. We have, from equation (F.12),

$$\frac{dE_{i2}}{dt} = \omega_i(\frac{dM_{i1}^2}{dt} + 2M_{i0}\frac{dM_{i2}}{dt}). \tag{F.31}$$

Knowing $M_{i1}(t)$ and $\frac{dM_{i2}}{dt}$, we can derive a new expression for $\frac{dE_{i2}}{dt}$, and compare it with equation (F.8). This is carried out here.

Using equation (F.15), we have

$$M_{i1}^2 = S_i^2 f_{ijk}^2 M_{j0}^2 M_{k0}^2 \frac{4\sin^2\alpha\sin^2\beta}{\delta\omega^2}. \tag{F.32}$$

Applying again the random phase approximation, we obtain

$$M_{i1}^2 = S_i^2 f_{ijk}^2 M_{j0}^2 M_{k0}^2 \frac{2\sin^2\beta}{\delta\omega^2}, \tag{F.33}$$

which further gives

$$\frac{dM_{i1}^2}{dt} = S_i^2 f_{ijk}^2 M_{j0}^2 M_{k0}^2 \frac{\sin 2\beta}{\delta\omega}. \tag{F.34}$$

Combining this result with equation (F.22), we get

$$\begin{aligned}\frac{dE_{i2}}{dt} &= \omega_i(\frac{dM_{i1}^2}{dt} + 2M_{i0}\frac{dM_{i2}}{dt}) \\ &= 2S_i\omega_i f_{ijk}^2(S_i M_{j0}^2 M_{k0}^2 + S_j M_{i0}^2 M_{k0}^2 + S_k M_{i0}^2 M_{j0}^2)\frac{\sin(\delta\omega\, t)}{\delta\omega},\end{aligned} \tag{F.35}$$

a factor of 2 off from equation (F.8).

We suspect that the difference of a factor of 2 comes from different mode counting method employed here and that in Kumar & Goldreich (1989).

F.3 Generalization to Dissipative Systems

It is straightforward to generalize the results in equation (F.8) to the cases when $\gamma_i \neq 0$. We regard γ_i as the imaginary part of the complex frequency, $\tilde{\omega}_i = \omega_i + i\gamma_i$. We let $B_i = A_i e^{-i\tilde{\omega}_i}$, where $E_i = |B_i|^2$.

Assuming $|\gamma_i| \ll \omega_i$, we can revise equation (F.8) into

$$\frac{dE_{i2}}{dt} = S_i\omega_i K_{ijk}^2(S_i\omega_i E_{j0}E_{k0} + S_j\omega_j E_{i0}E_{k0} + S_k\omega_k E_{i0}E_{j0})(\frac{\sin(\delta\tilde{\omega}\, t)}{\delta\tilde{\omega}}), \tag{F.36}$$

where $\delta\tilde{\omega} = s_i\tilde{\omega}_i + s_j\tilde{\omega}_j + s_k\tilde{\omega}_k = \delta\omega + i(s_i\gamma_i + s_j\gamma_j + s_k\gamma_k) = \delta\omega + i\Gamma$.

Using the fact that

$$\sin\theta = \frac{e^{i\theta} - e^{-i\theta}}{2i}, \tag{F.37}$$

the real part of equation (F.36) becomes,

$$\frac{dE_{i2}}{dt} = S_i\omega_i K_{ijk}^2 (S_i\omega_i E_{j0}E_{k0} + S_j\omega_j E_{i0}E_{k0} + S_k\omega_k E_{i0}E_{j0}) \frac{\Gamma}{(\Gamma)^2 + (\delta\omega)^2}. \qquad \text{(F.38)}$$

This is the energy equation for a dissipative system.

Bibliography

Kumar, P., & Goldreich, P. 1989, ApJ, 342, 558

Appendix G 3-Mode Coupling Coefficients

In this appendix, we detail our numerical calculations of the 3-mode coupling coefficient, the value of which is pivotal in determining the amplitudes of gravity-modes in pulsating white dwarfs. Here, we ignore the nonadibaticity in the pulsations, and work with the adiabatic eigenfunctions.

The expression of the coupling coefficient is equation (6.11). It involves products of the various covariant derivatives on the three eigenfunctions. We list the properties and expressions of the covariant derivatives for scalars, vectors and tensors in §G.1.

Most of our analytical derivations in this appendix are aimed at reducing the complexity in the expression for the coupling coefficient. Numerically, we go through three separate methods to pin down the final answer for κ (§G.2).

In §G.2.1, we describe briefly the first numerical method to calculate κ. Also in this section, we employ the properties of the eigenfunctions (as derived in Chap. 2) to estimate the magnitudes of different terms in the coupling coefficient. We find that the largest terms originate from the curvature of the spherical coordinate systems that we adopt, and they can be several orders of magnitude bigger than the physical terms. But as is shown later in that section, these curvature terms cancel each other. The first numerical method suffers from the inaccuracy in calculating this cancellation. The second numerical method presented in §G.2.2 takes this cancellation into proper account. The results obtained there are more reliable than from the first method.

The third numerical method is described in §G.2.3. This one is first developed by Kumar & Goodman (1996), and it employs the technique of integration by parts. We show that this method is again superior to the other two, though the results from all three methods agree to the order of magnitude. The radial integrand of κ from this method does not reflect the strength of local physical coupling. To study the local coupling strength, as is useful in the case of travelling waves and nonadiabatic eigenfunctions, we resort to the second numerical method.

Finally, in §G.3, we derive a simple expression for κ in the incompressible limit. This expression is used to confirm many of the scaling relations obtained numerically.

G.1 Preparation - Covariant Derivatives

The full expression of the coupling strength for coupling between any three mode, copied from equation (6.11), is

$$\begin{aligned}\kappa_{\alpha\beta\gamma} \equiv & -\int d^3x \frac{p_0}{6}\Big\{(\Gamma_1-1)\Big[(\nabla\cdot\vec{\xi})_\alpha(\xi^i_{;j})_\beta(\xi^j_{;i})_\gamma+(\nabla\cdot\vec{\xi})_\beta(\xi^i_{;j})_\gamma(\xi^j_{;i})_\alpha+(\nabla\cdot\vec{\xi})_\gamma(\xi^i_{;j})_\alpha(\xi^j_{;i})_\beta\Big] \\ & +\Big[(\xi^i_{;j})_\alpha(\xi^j_{;k})_\beta(\xi^k_{;i})_\gamma+(\xi^i_{;j})_\alpha(\xi^j_{;k})_\gamma(\xi^k_{;i})_\beta\Big]+\Big[(\Gamma_1-1)^2(\nabla\cdot\vec{\xi})_\alpha(\nabla\cdot\vec{\xi})_\beta(\nabla\cdot\vec{\xi})_\gamma\Big]\Big\} \\ = & \int d^3x(d\kappa_1+d\kappa_2+d\kappa_3), \end{aligned} \tag{G.1}$$

where the symbol ';' denotes covariant derivatives, e.g., $\xi^i_{;j}$ stands for j direction covariant derivative on i component of the vector $\vec{\xi}$. $d\kappa_1$, $d\kappa_2$ and $d\kappa_3$ represent the three radial integrals that build up κ.

Unlike in Chapter 2, where plane-parallel approximation is adopted, here we treat the eigenfunctions in spherical coordinates. The spherical coordinates are the natural and convenient coordinates for a spherical star, and in the case of no strong rotation or magnetic field, the angular dependences of the eigenfunctions can be expressed in terms of a family of complete, ortho-normal functions, $Y_{\ell m}$. There are a set of angular selection rules defining what modes can be coupled together, the rules themselves results from the conservation of angular momentum.[1] We consider modes in spherical coordinates, not only to take these selection rules into account naturally, but also to comply to the 'industrial standard', as the real pulsations are observed in these coordinates. However, this choice of coordinate system also brings us some unwanted complications, such as large curvature terms that cancel each other in the end but obscure the physical terms on the way.

G.1.1 Coordinate Basis

In spherical coordinates with basis vectors that are dimensionless (they can also be regarded as having unit lengths), we decompose $\vec{\xi}$ into

$$\vec{\xi}=\xi^r\vec{e}_r+\xi^\theta\vec{e}_\theta+\xi^\phi\vec{e}_\phi=\left[\xi_r(r),\xi_h(r)\frac{\partial}{\partial\theta},\xi_h(r)\frac{1}{\sin\theta}\frac{\partial}{\partial\phi}\right]Y_{\ell m}(\theta,\phi). \tag{G.2}$$

The ξ_h used in Chapter 3 is equivalent to our $\xi_h\partial Y_{\ell m}/\partial\theta$ here (a matter of notation); $\xi_r(r)$ and $\xi_h(r)$ have dimensions of length.

When we calculate a scalar defined by covariant derivatives (e.g., $X=(\nabla\cdot\vec{\xi})\xi^i_{;j}\xi^j_{;i}$), the final result should be independent of the coordinate systems we use to calculate it. This allows us to use the covariant basis since many of its properties (like metric tensor, and Christoffel symbols, as we would go into later) are already derived in textbooks for tensor analysis (for example, see Arfken

[1] In a plane-parallel geometry, this is equivalent to the conservation of horizontal wave vectors.

1985). We go through the definitions and formulations briefly below.

We prefer to use the covariant basis with dimensional vectors $\vec{\varepsilon}_i$, which are related to $\vec{e}_i$ by the scale factors h_i: $\vec{\varepsilon}_i = h_i\vec{e}_i$, with $h_r = 1$, $h_\theta = r$ and $h_\phi = r\sin\theta$. $\vec{\varepsilon}_i$ have the dimensions of h_i. In such a coordinate system, the displacement vector is decomposed into

$$\vec{\xi} = (\xi^r)'\vec{\varepsilon}_r + (\xi^\theta)'\vec{\varepsilon}_\theta + (\xi^\phi)'\vec{\varepsilon}_\phi = \left[\xi_r(r), \frac{1}{r}\xi_h(r)\frac{\partial}{\partial\theta}, \xi_h(r)\frac{1}{r\sin^2\theta}\frac{\partial}{\partial\phi}\right] Y_{\ell m}(\theta,\phi), \tag{G.3}$$

where $\xi_r(r)$ and $\xi_h(r)$ are the same as the ones in equation (G.2).

The covariant basis vectors are related to each other by

$$\vec{\varepsilon}_i \cdot \vec{\varepsilon}_j = g_{ij}, \tag{G.4}$$

and g_{ij}, the covariant metric tensor for spherical coordinates, is

$$g_{ij} = \begin{pmatrix} 1 & 0 & 0 \\ 0 & r^2 & 0 \\ 0 & 0 & r^2\sin^2\theta \end{pmatrix}. \tag{G.5}$$

The corresponding contravariant metric tensor g^{ij} is

$$g^{ij} = \begin{pmatrix} 1 & 0 & 0 \\ 0 & \frac{1}{r^2} & 0 \\ 0 & 0 & \frac{1}{r^2\sin^2\theta} \end{pmatrix}. \tag{G.6}$$

The Christoffel Symbols are defined by the following operation,

$$\frac{\partial\vec{\varepsilon}_i}{\partial q^j} = \Gamma^k_{ij}\vec{\varepsilon}_k, \tag{G.7}$$

where $q^r = r$, $q^\theta = \theta$ and $q^\phi = \phi$. The covariant derivatives are expressed using this tensor as

$$V^i_{;j} \equiv \frac{\partial V^i}{\partial q^j} + V^k\Gamma^i_{kj}, \tag{G.8}$$

where the rule of Einstein summation applies. The Christoffel symbols can be computed from g_{ij} by the formula,

$$\Gamma^k_{ij} = \frac{1}{2}g^{sk}\left(\frac{\partial g_{is}}{\partial q^j} + \frac{\partial g_{js}}{\partial q^i} - \frac{\partial g_{ij}}{\partial q^s}\right). \tag{G.9}$$

For the metric in equation (G.5), the only nonvanishing parts of Γ are (Lightman et al. 1975)

$$\Gamma^r_{\theta\theta} = -r,$$

$$\begin{aligned}
\Gamma^r_{\phi\phi} &= -r\sin^2\theta, \\
\Gamma^\theta_{r\theta} &= \Gamma^\theta_{\theta r} = \frac{1}{r}, \\
\Gamma^\theta_{\phi\phi} &= -\sin\theta\cos\theta, \\
\Gamma^\phi_{\phi r} &= \Gamma^\phi_{r\phi} = \frac{1}{r}, \\
\Gamma^\phi_{\phi\theta} &= \Gamma^\phi_{\theta\phi} = \frac{\cos\theta}{\sin\theta}.
\end{aligned} \tag{G.10}$$

G.1.2 Covariant Derivatives for Vectors

These lead to the following covariant derivatives for an arbitrary vector $\vec{V}$. With a decomposition of $V^r\vec{\varepsilon}_r + V^\theta\vec{\varepsilon}_\theta + V^\phi\vec{\varepsilon}_\phi$, we have

$$\begin{aligned}
V^r_{;r} &= V^r_{,r} = \frac{\partial V^r}{\partial r}, \\
V^r_{;\theta} &= V^r_{,\theta} - rV^\theta, \\
V^r_{;\phi} &= V^r_{,\phi} - V^\phi r\sin^2\theta, \\
V^\theta_{;r} &= V^\theta_{,r} + \frac{1}{r}V^\theta, \\
V^\theta_{;\theta} &= V^\theta_{,\theta} + \frac{1}{r}V^r, \\
V^\theta_{;\phi} &= V^\theta_{,\phi} - \sin\theta\cos\theta V^\phi, \\
V^\phi_{;r} &= V^\phi_{,r} + \frac{1}{r}V^\phi, \\
V^\phi_{;\theta} &= V^\phi_{,\theta} + \frac{\cos\theta}{\sin\theta}V^\phi, \\
V^\phi_{;\phi} &= V^\phi_{,\phi} + \frac{1}{r}V^r + \frac{\cos\theta}{\sin\theta}V^\theta,
\end{aligned} \tag{G.11}$$

where the subscript ',' stands for partial derivatives (as compared to covariant). The divergence of $\vec{V}$ is

$$\nabla\cdot\vec{V} = \frac{\partial V^r}{\partial r} + \frac{\partial V^\theta}{\partial\theta} + \frac{\partial V^\phi}{\partial\phi} + \frac{2}{r}V^r + \frac{\cos\theta}{\sin\theta}V^\theta. \tag{G.12}$$

For the displacement vector in equation (G.3), this divergence becomes

$$\nabla\cdot\vec{\xi} = \left[\frac{1}{r^2}\frac{\partial}{\partial r}\left(r^2\xi_r(r)\right) - \frac{\xi_h(r)}{r}\ell(\ell+1)\right]Y_{\ell m}(\theta,\phi), \tag{G.13}$$

noting that $\nabla^2 Y_{\ell m} = -\ell(\ell+1)Y_{\ell m}$.[2] This expression is identical to the one that would be derived if using the dimensionless basis $\vec{e}_i$. This reflects the invariance of scalars during coordinate transforms.

For convenience, we write down explicitly the covariant derivatives in terms of $\xi_h(r)$ and $\xi_r(r)$.

[2]The Laplace on the sphere, ∇^2, is formmally $\equiv g^{\alpha\beta}\nabla_\alpha\nabla_\phi$, where α, β only go through θ and ϕ.

By definition,

$$\begin{aligned}
\xi^r &= \xi_r(r)Y_{\ell m}(\theta,\phi), \\
\xi^\theta &= \frac{1}{r}\xi_h(r)\frac{\partial}{\partial\theta}Y_{\ell m}, \\
\xi^\phi &= \frac{1}{r\sin^2\theta}\xi_h(r)\frac{\partial}{\partial\phi}Y_{\ell m}.
\end{aligned} \tag{G.14}$$

And we have

$$\begin{aligned}
\xi^r_{;r} &= \frac{\partial}{\partial r}\xi_r(r)Y_{\ell m}, \\
\xi^r_{;\theta} &= \xi_r(r)\frac{\partial}{\partial\theta}Y_{\ell m} - \xi_h(r)\frac{\partial}{\partial\theta}Y_{\ell m}, \\
\xi^r_{;\phi} &= \xi_r(r)\frac{\partial}{\partial\phi}Y_{\ell m} - \xi_h(r)\frac{\partial}{\partial\phi}Y_{\ell m}, \\
\xi^\theta_{;r} &= \frac{1}{r}\frac{\partial}{\partial r}\xi_h(r)\frac{\partial}{\partial\theta}Y_{\ell m}, \\
\xi^\theta_{;\theta} &= \frac{1}{r}\xi_h(r)\frac{\partial^2}{\partial\theta^2}Y_{\ell m} + \frac{1}{r}\xi_r(r)Y_{\ell m}, \\
\xi^\theta_{;\phi} &= \frac{1}{r}\xi_h(r)\frac{\partial^2}{\partial\theta\partial\phi}Y_{\ell m} - \frac{1}{r}\frac{\cos\theta}{\sin\theta}\xi_h(r)\frac{\partial}{\partial\phi}Y_{\ell m}, \\
\xi^\phi_{;r} &= \frac{1}{r}\frac{\partial}{\partial r}\xi_h(r)\frac{1}{\sin^2\theta}\frac{\partial}{\partial\phi}Y_{\ell m}, \\
\xi^\phi_{;\theta} &= \frac{1}{r}\xi_h(r)\left[-\frac{1}{\sin^2\theta}\frac{\partial}{\partial\phi}Y_{\ell m} + \frac{1}{\sin^2\theta}\frac{\partial^2}{\partial\theta\partial\phi}Y_{\ell m}\right], \\
\xi^\phi_{;\phi} &= \frac{1}{r\sin^2\theta}\xi_h(r)\frac{\partial^2}{\partial\phi^2}Y_{\ell m} + \frac{1}{r}\xi_r(r)Y_{\ell m} + \frac{1}{r}\xi_h(r)\frac{\cos\theta}{\sin\theta}\frac{\partial}{\partial\theta}Y_{\ell m}.
\end{aligned} \tag{G.15}$$

G.1.3 Covariant Derivatives for Scalars and Tensors

As will be needed in §G.2.3, we list here the relations leading to covariant derivatives of scalars.

Consider a scalar of the form, $p = \hat{p}(r)f(\theta,\phi)$, where $\hat{p}$ is the radial dependence, and $f(\theta,\phi)$ the angular one. The first order covariant differentiation transforms it into a vector,

$$\begin{aligned}
p_{;r} &= \frac{\partial}{\partial r}\hat{p}f(\theta,\phi) \\
p_{;\theta} &= \hat{p}\frac{\partial}{\partial\theta}f(\theta,\phi) \\
p_{;\phi} &= \hat{p}\frac{\partial}{\partial\phi}f(\theta,\phi)
\end{aligned} \tag{G.16}$$

and

$$\begin{aligned}
p^{;r} &= g^{rr}p_{;r} = \frac{\partial}{\partial r}\hat{p}f(\theta,\phi), \\
p^{;\theta} &= g^{\theta\theta}p_{;\theta} = \frac{1}{r^2}\hat{p}\frac{\partial}{\partial\theta}f(\theta,\phi),
\end{aligned}$$

$$p^{;\phi} = g^{\phi\phi}p_{;\phi} = \frac{1}{r^2\sin^2\theta}\hat{p}\frac{\partial}{\partial\phi}f(\theta,\phi). \tag{G.17}$$

The second covariant derivatives of p (making it $p^{i}_{;j}$) follow the same rules as in equation (G.15). In particular, for a scalar that has $f(\theta,\phi) =$ constant, the only nontrivial second covariant derivatives are

$$\begin{aligned} p^{;r}_{;r} &= \frac{d^2p}{dr^2}, \\ p^{;\theta}_{;\theta} &= \frac{1}{r}\frac{dp}{dr}, \\ p^{;\phi}_{;\phi} &= \frac{1}{r}\frac{dp}{dr}. \end{aligned} \tag{G.18}$$

To calculate the third order covariant derivatives of a scalar, we use the following formula taken from Lightman et al. (1975),

$$\left(p^{i}_{;j}\right)_{;k} = \left(p^{i}_{;j}\right)_{,k} + \Gamma^{i}_{nk}p^{n}_{;j} - \Gamma^{n}_{jk}p^{i}_{;n}. \tag{G.19}$$

Applying it to a scalar that does not depend on θ and ϕ, the only nonzero components are

$$\begin{aligned} p^{;r}_{;rr} &= \frac{d^3p}{dr^3}, \\ p^{;r}_{;\theta\theta} &= r^2\frac{d}{dr}\left(\frac{1}{r}\frac{dp}{dr}\right), \\ p^{;r}_{;\phi\phi} &= r^2\sin^2\theta\frac{d}{dr}\left(\frac{1}{r}\frac{dp}{dr}\right), \\ p^{;\theta}_{;r\theta} &= \frac{d}{dr}\left(\frac{1}{r}\frac{dp}{dr}\right), \\ p^{;\theta}_{;\theta r} &= \frac{d}{dr}\left(\frac{1}{r}\frac{dp}{dr}\right), \\ p^{;\phi}_{;r\phi} &= \frac{d}{dr}\left(\frac{1}{r}\frac{dp}{dr}\right), \\ p^{;\phi}_{;\phi r} &= \frac{d}{dr}\left(\frac{1}{r}\frac{dp}{dr}\right). \end{aligned} \tag{G.20}$$

G.2 Three Numerical Methods

In this section, we describe three different methods that are implemented into a computer to calculate the coupling coefficients. The work can be divided into two steps, one is to integrate the angular dependences of the coupling coefficients over the sphere, the second is to integrate over the radius. The first part can usually be done analytically, as is shown here, while the second part is done numerically.

G.2.1 The Direct Method

1). *Methodology*

In this method, both the angular and the radial integration are accomplished numerically.

For the angular part, we programme the information on covariant derivatives of vectors (eq. [G.11]) into the software package Mathematica (Wolfram 1991) and integrate the angular products numerically, using the package's internal definition for spherical harmonics, and keeping the radial dependences of the displacements symbolic ($\xi_r(r)$, $\xi_h(r)$).

For example, we consider one of the terms in the expression for κ, namely, $(\nabla \cdot \vec{\xi})_\alpha (\xi^i_{;j})_\beta (\xi^j_{;i})_\gamma$. When the ℓ and m for α, β and γ are specified, we can use Mathematica to derive symbolically the covariant derivatives, the output expressed in terms of $\xi_r(r)$, $\xi_h(r)$ and their radial derivatives, as well as $Y_{\ell m}$ and their derivatives with respect to θ and ϕ for all three modes. There are nine linearly independent terms (different radial functions) generated from such a procedure, one of such terms is $1/r^2(\delta\rho/\rho)_\alpha(\xi_h)_\beta(\xi_h)_\gamma$, where $(\delta\rho/\rho)_\alpha = -[1/r^2 d/dr(r^2\xi_r) - \ell(\ell+1)\xi_h/r]_\alpha$. We then extract the angular dependences for these nine terms, integrate the angular dependences over the 4π ster-radian, and store the integration results. Later we read these results into a fortran program, which also calculates the radial eigenstructures for any mode with a frequency ω and a spherical degree of ℓ. This program combines the information on the angular integrations with the radial integrations, and submit to us the final results on κ, for any three-mode combinations.

From the results of angular integrations (by Mathematica), we establish the angular selection rules: κ vanishes for combinations of three modes that do not satisfy simultaneously the following two angular selection rules, i.e., $\ell_\gamma = |\ell_\alpha - \ell_\beta|, |\ell_\alpha - \ell_\beta| + 2, ..., |\ell_\alpha + \ell_\beta| - 2, |\ell_\alpha + \ell_\beta|$, and $m_\alpha = m_\beta + m_\gamma$, in a triplet combination with frequency match $\omega_\alpha \sim \omega_\beta + \omega_\gamma$. These selection rules are the central feature of a realistically coupled system; global couplings as the kind adopted for discussions in Chapter 6 can only serve as an illustration of the dynamics. This 'patchy coupling' also relieves us from calculating a large number of combinations: for N modes, the number of valid combinations drops from N^3 as in global coupling to of order N^2 in a real star.

2). *Analysis of a Special Case*

When we consider only modes that have $m = 0$, we can estimate the size of different terms in the expression for κ. Our results here hold also for the cases with $m \neq 0$.

When $m = 0$, $\xi_\phi = 0$, and all gradients involving ϕ vanishes except for $\xi^\phi_{;\phi}$, which has a leading term of order $\xi_h(r)/r$ due to curvature. This was quite a surprise to us till we saw that this curvature term does not matter in the end, as physical intuition would have it.

We consider a triplet involving a low-order, low degree parent mode (α) and two daughter modes (β, γ) of roughly half its frequency (parametric resonance). The daughter modes start to propagate

below $z_{\omega\beta} \sim z_{\omega\gamma} \ll z_{\omega\alpha}$, where $z_\omega = \omega^2/gk_h^2$ is approximately the first radial node of the wave-functions. As we will show, most of the contribution to the coupling strength comes from a depth $z < z_{\omega\alpha}$. There are many terms in the expression (6.11), and there are terms that are formally much larger than the others.

From §2.4.2, we know that $\nabla \cdot \xi = -\delta\rho/\rho$ in the propagating region of the mode is much smaller than either $k_z\xi_z$ or $k_h\xi_h$, which are comparable to each other, and all three terms are comparable in the upper evanescent region. Therefore, the terms that do not include $\nabla \cdot \xi_\beta$ or $\nabla \cdot \xi_\gamma$ are the largest. We look at one such term in the region $z_b < z_{\omega\beta} < z < z_{\omega\alpha}$, where z_b is the bottom of the convection zone. The largest integrand in κ due to $(\nabla \cdot \vec{\xi})_\alpha(\xi^i_{;j})_\beta(\xi^j_{;i})_\gamma$ is $(\nabla \cdot \vec{\xi})_\alpha(\xi^\theta_{;r})_\beta(\xi^r_{;\theta})_\gamma$, which formally[3] has a largest term of the order,

$$\begin{aligned} d\kappa_a &= -\frac{p_0}{6}(\Gamma_1 - 1)(\nabla \cdot \vec{\xi})_\alpha(\xi^\theta_{;r})_\beta(\xi^r_{;\theta})_\gamma \\ &\sim \frac{p_0}{6}(\nabla \cdot \vec{\xi})_\alpha \frac{1}{r}\sqrt{\ell_\beta(\ell_\beta+1)}\sqrt{\ell_\gamma(\ell_\gamma+1)}\frac{d}{dr}(\xi_h)_\beta(\xi_h)_\gamma \\ &\sim \frac{p_0}{r}(\nabla \cdot \vec{\xi})_\alpha \ell_\beta(\ell_\beta+1)\frac{d}{dr}(\xi_h^2)_\beta. \end{aligned} \tag{G.21}$$

Here, we approximate $\partial Y_{\ell m}/\partial\theta$ as $\sqrt{\ell(\ell+1)}Y_{\ell m}$. And the integrations over θ and ϕ have been carried out and yield a factor of order unity; this factor is ignored from now on. In estimating $\xi^r_{;\theta}$, we take the curvature term, since for g-modes, $\xi_h \gg \xi_r$.

Integration of the above integrand over radius can be done using the technique of integration by parts and yields

$$\begin{aligned} \int_0^R r^2 dr d\kappa_a &= \int_0^R r^2 dr \frac{d}{dr}\left[\frac{p_0}{r}(\nabla \cdot \vec{\xi})_\alpha \ell_\beta(\ell_\beta+1)(\xi_h^2)_\beta\right] - \\ &\qquad \int_0^R r^2 dr \frac{d}{dr}\left[\frac{p_0}{r}(\nabla \cdot \vec{\xi})_\alpha\right]\ell_\beta(\ell_\beta+1)(\xi_h^2)_\beta \\ &\sim \int_0^R dr \frac{d}{dr}\left[r p_0(\nabla \cdot \vec{\xi})_\alpha \ell_\beta(\ell_\beta+1)(\xi_h^2)_\beta\right] - \\ &\qquad \int_0^R r^2 dr \frac{d}{dr}\left[\frac{p_0}{r}(\nabla \cdot \vec{\xi})_\alpha\right]\ell_\beta(\ell_\beta+1)(\xi_h^2)_\beta \\ &\sim -\int_0^R r dz \rho_0 g(\nabla \cdot \vec{\xi})_\alpha \ell_\beta(\ell_\beta+1)(\xi_h^2)_\beta. \end{aligned} \tag{G.22}$$

The radial integral of the complete differential vanishes: at the surface, $p_0 \to 0$; close to the center, $r \to 0$, while everything else is regular.

The above integral can be further simplified by invoking the concept of mode mass, which is

[3]But as we will show later, this formally large term cancels with another part of κ, and therefore is not very interesting. We will discuss this more carefully later.

associated with the normalization of the displacement,

$$\omega^2 R^2 \ell(\ell+1) \int_0^R dz \rho_0 \xi_h^2 = 1. \tag{G.23}$$

The displacement is considered normalized if the total kinetic energy in the wave is unity. The integral of $\int_{z_{n1}}^{z_{n2}} dz \rho_0 \xi_h^2$ is constant between any two neighbouring node points z_{n1} and z_{n2}. Or, contributions to the mode mass of β (or γ) come equally from between any two of its radial nodes. At the same time, the value of $(\nabla \cdot \vec{\xi})_\alpha$ is relatively constant for $z < z_{\omega\alpha}$, and drops off after that with a scale length of $1/k_z \ll H_p$. Therefore, in expression (G.22), only contribution from $z < z_{\omega\alpha}$ is most important. We can truncate the integration and integrate only between the surface and $z_{\omega\alpha} \ll R$. Inside the evanescent zone, $(\nabla \cdot \vec{\xi})_\alpha$ is evaluated using the normalization formula,

$$(\nabla \cdot \vec{\xi})_\alpha \sim -(\delta\rho/\rho)_{z_\omega} \sim \frac{1}{\sqrt{n_\alpha L \tau_{\omega\alpha}}}. \tag{G.24}$$

The truncated integration $\int_0^{z_{\omega\alpha}} dr r^2 \rho_0 \ell_\beta(\ell_\beta+1)(\xi_h^2)_\beta$ is $(1/\omega_\beta^2)n'/n_\beta$ fraction of the total energy in mode β (which is unity), where n' is the number of nodes for mode β within $z_{\omega\alpha}$, and it is determined as

$$\frac{n'}{n_\beta} \sim \frac{\int_0^{z_{\omega\alpha}} k_z dz}{\int_0^R k_z dz}. \tag{G.25}$$

Inside the propagating region for mode β, $k_z \sim 1/\sqrt{z z_{\omega\beta}}$. Assuming $z_{\omega\alpha} \gg z_{\omega\beta}$, we have

$$\frac{n'}{n_\beta} \sim \frac{2}{n_\beta}\sqrt{\frac{z_{\omega\alpha}}{z_{\omega\alpha}}} \sim \frac{4}{n_\beta}\frac{\ell_\beta}{\ell_\alpha} \sim 4\frac{\ell_\beta}{n_\beta \ell_\alpha} \sim \frac{1}{n_\alpha}, \tag{G.26}$$

using the definition of z_ω and assuming that $\omega_\beta \sim \omega_\alpha/2$, as well as $\ell_\alpha = 1$. The dispersion relation is $\omega^2 \propto l/n$ or $\omega \propto l/n$, depending on the value of n (see Fig. 2.2). These discussions further lead to the following estimate,

$$\int_0^R r^2 dr d\kappa_a \sim \frac{g}{R\omega^2}\frac{1}{\sqrt{n_\alpha^3 L \tau_{\omega\alpha}}}. \tag{G.27}$$

Notice that this expression does not depend on ℓ_β, and it increases with n_α steeply, as $\tau_{\omega\alpha}$ decreases with n_α.

For comparison, a small term $(\nabla \cdot \vec{\xi})_\alpha (\nabla \cdot \vec{\xi})_\beta (\nabla \cdot \vec{\xi})_\gamma$ in the expression for κ is of order

$$\begin{aligned} d\kappa_3 &= -\frac{p_0}{6}(\Gamma_1 - 1)^2 (\nabla \cdot \vec{\xi})_\alpha (\nabla \cdot \vec{\xi})_\beta (\nabla \cdot \vec{\xi})_\gamma \\ &\sim p_0 (\nabla \cdot \vec{\xi})_\alpha \left(\frac{\delta\rho}{\rho}\right)_\beta^2 \\ &\sim p_0 (\nabla \cdot \vec{\xi})_\alpha \frac{1}{n_\beta L \tau_{\omega\beta}} \left(\frac{z_{\omega\beta}}{z}\right)^{\frac{3}{2}} \frac{\rho_{\omega\beta}}{\rho(z)} \end{aligned}$$

$$\sim \quad (\nabla \cdot \vec{\xi})_\alpha \frac{1}{n_\beta L \tau_{\omega\beta}} \frac{g z_{\omega\beta}^{\frac{3}{2}} \rho_{\omega\beta}}{\sqrt{z}}, \tag{G.28}$$

where we have used the scaling with z of $(\delta\rho/\rho)_\beta$ in the propagating region (see §2.4.2), as well as the normalized amplitudes for modes at z_ω (see also that section). We approximate $p_0 \sim \rho_0 g z$. The depth dependence of $d\kappa_2$ implies the largest contribution coming from a scale-height around $z_{\omega\beta}$, first node of the daughter mode. Inside the evanescent region of mode β, $d\kappa_2$ increases with depth.

Radially integrating the above expression and substituting in values of $(\nabla \cdot \vec{\xi})_\alpha$ at $z_{\omega\alpha}$, we get

$$\begin{aligned} \int_0^R r^2 dr d\kappa_2 &\sim R^2 \int_0^{z_{\omega\alpha}} dz \frac{1}{\sqrt{n_\alpha L \tau_{\omega\alpha}}} \frac{1}{n_\beta} \left(\frac{z_{\omega\alpha}}{z_{\omega\beta}}\right)^{\frac{1}{2}} \\ &\sim \frac{1}{\sqrt{n_\alpha^3 L \tau_{\omega\alpha}}}. \end{aligned} \tag{G.29}$$

In deriving this, we make use of the definition of z_ω, and $\tau(z) \sim pz/F \sim 4\pi R^2 \rho g z^2/L$. A relation between n_β and n_α of $n_\beta \sim 2 n_\alpha \ell_\beta$ is also used, taking $\ell_\alpha = 1$. This term is smaller than equation (G.27) by a factor of $g/(R\omega_\alpha^2)$, which is much larger than unity for g-modes. This term is important, however, given the cancellations among the large terms.

The comparison between numerical results and estimates in equations (G.27) and (G.29) is plotted in Figure G.1. The agreement is good over a broad range of n_α, except where $z_{\omega\alpha} < z_b$.

3). *Complications*

Here, we show that the curvature term in equation (G.21), considered to be among the largest terms in κ, cancels with another curvature term coming from $d\kappa_2$ in equation (G.1). Therefore, all the unphysical terms disappear.

This second curvature term comes from $\xi^i_{;j}\xi^j_{;k}\xi^k_{;i}$, in the expression for κ (eq. [G.1]) In the case of $m = 0$, this term can be dissected into the following combinations,

$$\begin{aligned} &(\xi^i_{;j})_\alpha (\xi^j_{;k})_\beta (\xi^k_{;i})_\gamma + (\xi^i_{;j})_\alpha (\xi^j_{;k})_\gamma (\xi^k_{;i})_\beta = \\ &\Big\{ (\nabla \cdot \vec{\xi_\alpha}) \left[(\xi_\beta)^r_{;\theta} (\xi_\gamma)^\theta_{;r} + (\xi_\gamma)^r_{;\theta} (\xi_\beta)^\theta_{;r} \right] + (\nabla \cdot \vec{\xi_\beta}) \left[(\xi_\alpha)^r_{;\theta} (\xi_\gamma)^\theta_{;r} + (\xi_\gamma)^r_{;\theta} (\xi_\alpha)^\theta_{;r} \right] + \\ &\quad (\nabla \cdot \vec{\xi_\gamma}) \left[(\xi_\beta)^r_{;\theta} (\xi_\alpha)^\theta_{;r} + (\xi_\alpha)^r_{;\theta} (\xi_\beta)^\theta_{;r} \right] \Big\} \\ &- \Big\{ (\xi^\phi_{;\phi})_\alpha \left[(\xi_\beta)^r_{;\theta} (\xi_\gamma)^\theta_{;r} + (\xi_\gamma)^r_{;\theta} (\xi_\beta)^\theta_{;r} \right] + (\xi^\phi_{;\phi})_\beta \left[(\xi_\alpha)^r_{;\theta} (\xi_\gamma)^\theta_{;r} + (\xi_\gamma)^r_{;\theta} (\xi_\alpha)^\theta_{;r} \right] + \\ &\quad (\xi^\phi_{;\phi})_\gamma \left[(\xi_\beta)^r_{;\theta} (\xi_\alpha)^\theta_{;r} + (\xi_\alpha)^r_{;\theta} (\xi_\beta)^\theta_{;r} \right] \Big\} \\ &+ \Big\{ 2(\xi^r_{;r})_\alpha (\xi^r_{;r})_\beta (\xi^r_{;r})_\gamma + 2(\xi^\theta_{;\theta})_\alpha (\xi^\theta_{;\theta})_\beta (\xi^\theta_{;\theta})_\gamma + 2(\xi^\phi_{;\phi})_\alpha (\xi^\phi_{;\phi})_\beta (\xi^\phi_{;\phi})_\gamma \Big\}, \end{aligned} \tag{G.30}$$

given that $(\nabla \cdot \vec{\xi}) = \xi^r_{;r} + \xi^\theta_{;\theta} + \xi^\phi_{;\phi}$. The first group of terms in the right-hand side is similar to term $d\kappa_a$ in equation (G.21) and combines with that term to change the factor $\Gamma_1 - 1$ to Γ_1.

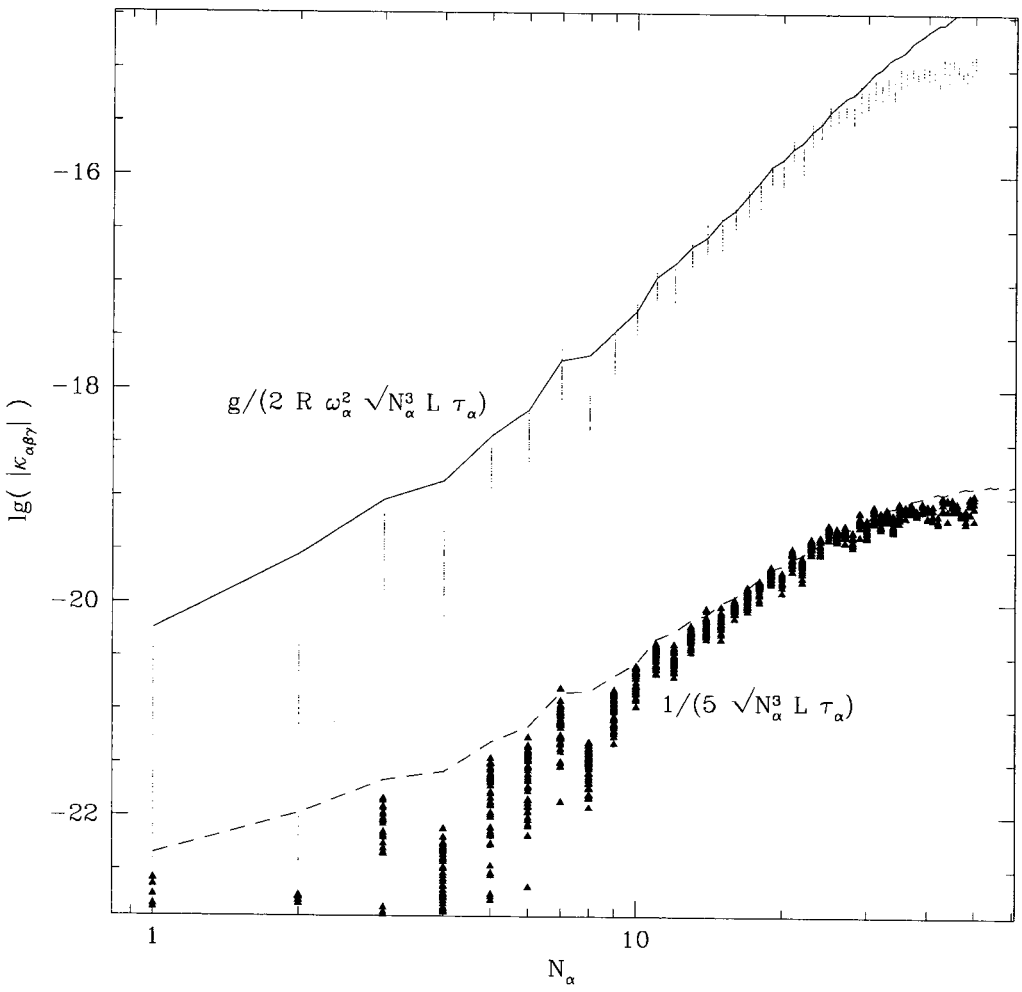

Figure G.1: The magnitudes of the largest ($d\kappa_1$) and the smallest terms ($d\kappa_2$) in the expression for the coupling coefficient, numerically integrated (dots) and estimated using equations (G.27) (solid curve) and (G.29) (dashed curve). The model we used for this calculation has $T_{\rm eff} = 12,800\,{\rm K}$, and the convection zone is too thin to interfere with our estimates. The numerical results deviate from the estimates at larger n_α, possibly due to the fact that the upper cavity of mode α is approaching the bottom of the convection zone. This deviation becomes more significant as we use cooler and cooler stars.

First, we show that equation (2.10) can be manipulated into

$$\begin{aligned}
\omega^2 \rho r \xi_r &= pr\frac{d}{dr}\left(\frac{\delta p}{p}\right) - g\rho r\left(\frac{\delta p}{p} - \frac{\delta\rho}{\rho} - \frac{d\xi_r}{dr}\right) \\
&= pr\frac{d}{dr}\left(\frac{\delta p}{p}\right) - g\rho r\left(\frac{\delta p}{p} + 2\xi_r\rho g - \frac{\ell(\ell+1)}{r}\xi_h\right) \\
&= r\frac{d}{dr}(\delta p) + \rho g\ell(\ell+1)\xi_h - 2\xi_r\rho g, \qquad \text{(G.31)}
\end{aligned}$$

so

$$(\omega^2\rho r + 2\rho g)\xi_r = r\frac{d}{dr}(\delta p) + \rho g\ell(\ell+1)\xi_h, \qquad \text{(G.32)}$$

where equation of continuity has been used. The two terms on the right-hand side are larger than the left-hand side by at least a factor of (ξ_h/ξ_r).

When ignoring terms of order (ξ_r/ξ_h) or smaller, integration by parts yields

$$\begin{aligned}
&\int d^3xp\Gamma_1(\nabla\cdot\vec{\xi}_\alpha)\left[(\xi_\beta)^r_{;\theta}(\xi_\gamma)^\theta_{;r} + (\xi_\gamma)^r_{;\theta}(\xi_\beta)^\theta_{;r}\right] \\
\sim\ & -\frac{\Lambda_\beta^2 + \Lambda_\gamma^2 - \Lambda_\alpha^2}{2} < \Lambda_\alpha\Lambda_\beta\Lambda_\gamma > \int r^2 dr \frac{1}{r}(\delta p)_\alpha \frac{d}{dr}\xi_{h\beta}\xi_{h\gamma} \\
\sim\ & \frac{\Lambda_\beta^2 + \Lambda_\gamma^2 - \Lambda_\alpha^2}{2} < \Lambda_\alpha\Lambda_\beta\Lambda_\gamma > \int dr r \frac{d}{dr}(\delta p)_\alpha (\xi_{h\beta}\xi_{h\gamma}), \qquad \text{(G.33)}
\end{aligned}$$

where $\nabla^2 Y_{\ell m} = -\Lambda^2 Y_{\ell m}$, and $\Lambda^2 = \ell(\ell+1)$. The symbol $< \quad >$ represents the integration of the product of three spherical harmonics over the sphere. Analytical integration of the angular dependences is made possible by the following formula from Appendix A of Kumar & Goodman (1996),

$$\begin{aligned}
< Y_\alpha g^{ij}\hat{\nabla}_i Y_\beta \hat{\nabla}_j Y_\gamma > &= \frac{\Lambda_\beta^2 + \Lambda_\gamma^2 - \Lambda_\alpha^2}{2} < \Lambda_\alpha\Lambda_\beta\Lambda_\gamma > \\
&\equiv F^\alpha_{\beta\gamma} T_{\alpha\beta\gamma}; \\
< g^{im}g^{jn}(\hat{\nabla}_i\hat{\nabla}_j Y_\alpha)(\hat{\nabla}_m Y_\beta)(\hat{\nabla}_n Y_\gamma) > &= \frac{(\Lambda_\alpha^2)^2 - (\Lambda_\beta^2 - \Lambda_\gamma^2)^2}{4} < \Lambda_\alpha\Lambda_\beta\Lambda_\gamma > \\
&\equiv G^\alpha_{\beta\gamma} T_{\alpha\beta\gamma}. \qquad \text{(G.34)}
\end{aligned}$$

Here $\hat{\nabla}_i$ is defined to be the covariant derivative on the surface of the sphere (see their appendix), and $T_{\alpha\beta\gamma} \equiv < \Lambda_\alpha\Lambda_\beta\Lambda_\gamma >$.

Relations similar to equation (G.33) exist for the terms involving $(\nabla\cdot\xi)_\beta$ and $(\nabla\cdot\xi)_\gamma$.

The second parenthesesed term in equation (G.30) transforms into

$$\begin{aligned}
\int d^3xp \Big\{ &(\xi^\phi_{;\phi})_\alpha\left[(\xi^r_{;\theta})_\beta(\xi^\theta_{;r})_\gamma + (\xi^r_{;\theta})_\gamma(\xi^\theta_{;r})_\beta\right] + (\xi^\phi_{;\phi})_\beta\left[(\xi^r_{;\theta})_\alpha(\xi^\theta_{;r})_\gamma + (\xi^r_{;\theta})_\gamma(\xi^\theta_{;r})_\alpha\right] + \\
&(\xi^\phi_{;\phi})_\gamma\left[(\xi^r_{;\theta})_\beta(\xi^\theta_{;r})_\alpha + (\xi^r_{;\theta})_\alpha(\xi^\theta_{;r})_\beta\right]\Big\}
\end{aligned}$$

$$
\begin{aligned}
\sim\ & \left[\Lambda_\alpha^4-(\Lambda_\beta^2-\Lambda_\gamma^2)^2+\Lambda_\beta^4-(\Lambda_\gamma^2-\Lambda_\alpha^2)^2+\Lambda_\gamma^4-(\Lambda_\alpha^2-\Lambda_\beta^2)^2\right]\frac{<\Lambda_\alpha\Lambda_\beta\Lambda_\gamma>}{4}\\
& \int drp\left[\xi_{h\alpha}\frac{d}{dr}\left(\xi_{h\beta}\xi_{h\gamma}\right)+\xi_{h\beta}\frac{d}{dr}\left(\xi_{h\alpha}\xi_{h\gamma}\right)+\xi_{h\gamma}\frac{d}{dr}\left(\xi_{h\beta}\xi_{h\alpha}\right)\right]\\
\sim\ & \left[\Lambda_\alpha^2\left(\frac{\Lambda_\beta^2+\Lambda_\gamma^2-\Lambda_\alpha^2}{2}\right)+\Lambda_\beta^2\left(\frac{\Lambda_\alpha^2+\Lambda_\gamma^2-\Lambda_\beta^2}{2}\right)+\Lambda_\gamma^2\left(\frac{\Lambda_\beta^2+\Lambda_\alpha^2-\Lambda_\gamma^2}{2}\right)\right]\\
& <\Lambda_\alpha\Lambda_\beta\Lambda_\gamma>\int drp\frac{d}{dr}\left(\xi_{h\alpha}\xi_{h\beta}\xi_{h\gamma}\right)\\
=\ & \left[\Lambda_\alpha^2\left(\frac{\Lambda_\beta^2+\Lambda_\gamma^2-\Lambda_\alpha^2}{2}\right)+\Lambda_\beta^2\left(\frac{\Lambda_\alpha^2+\Lambda_\gamma^2-\Lambda_\beta^2}{2}\right)+\Lambda_\gamma^2\left(\frac{\Lambda_\beta^2+\Lambda_\alpha^2-\Lambda_\gamma^2}{2}\right)\right]\\
& <\Lambda_\alpha\Lambda_\beta\Lambda_\gamma>\int dr\rho g\left(\xi_{h\alpha}\xi_{h\beta}\xi_{h\gamma}\right), \qquad \text{(G.35)}
\end{aligned}
$$

ignoring again terms of order ξ_r/ξ_h smaller than the ones kept here.

According to equation (G.32), the expression in equation (G.35) cancels with the combination of equation (G.33) and two other terms similar to it, down to the order of $(\xi_r/\xi_h) \ll 1$. So the large terms (terms estimated in eq. [G.27]) due to curvature of the coordinate system cancel out as expected – the scale-height in the upper atmosphere is much smaller than the radius of the star, and plane-parallel symmetry should apply nearly perfectly. But this cancellation also adds complications to our numerical computation. The true signal is embedded alongside these large terms, which can be several orders of magnitude above the true signal. Only using stellar models with fine grids and accurate integration could we discern the true signal. This is indeed the weakness of this direct method. We discuss alternatives in the following sections.

G.2.2 Improvements to the Direct Method

The direct method presented in §G.2.1 can be improved upon by pushing the limit of analytical calculations and removing the curvature terms analytically. We deal with triplets with $m = 0$ only.

The angular integrations are mostly analytical in this section, and completely analytical in §G.2.3.

The steps leading to a new expression of κ are scattered around §G.2.1. Here, we present only the final expression. Let

$$\kappa = -\frac{1}{6}T_{\alpha\beta\gamma}\int_0^R drr^2 d\kappa, \qquad \text{(G.36)}$$

we have

$$
\begin{aligned}
d\kappa\ =\ & (\Gamma_1-1)^2 p(\nabla\cdot\xi)_\alpha(\nabla\cdot\xi)_\beta(\nabla\cdot\xi)_\gamma+\frac{2p}{r^3}\xi_{h\alpha}\xi_{h\beta}\xi_{h\gamma}Q_{\alpha\beta\gamma}\\
& +2p\frac{d\xi_{r\alpha}}{dr}\frac{d\xi_{r\beta}}{dr}\frac{d\xi_{r\gamma}}{dr}+4\frac{p}{r^3}\xi_{r\alpha}\xi_{r\beta}\xi_{r\gamma}\\
& +\frac{p}{r}\left\{F^\alpha_{\beta\gamma}\left[\Gamma_1(\nabla\cdot\xi)_\alpha-\frac{1}{r}\xi_{r\alpha}\right]\left[\xi_{r\beta}\frac{d\xi_{h\gamma}}{dr}+\xi_{r\gamma}\frac{d\xi_{h\beta}}{dr}-\frac{d}{dr}\left(\xi_{h\beta}\xi_{h\gamma}\right)\right]+F^\beta_{\alpha\gamma}[...]+F^\gamma_{\alpha\beta}[...]\right\}
\end{aligned}
$$

$$
\begin{aligned}
&+\frac{p}{r^2}\left\{S_{\alpha\beta\gamma}\xi_{h\alpha}\left[\xi_{r\beta}\frac{d\xi_{h\gamma}}{dr}+\xi_{r\gamma}\frac{d\xi_{h\beta}}{dr}-\frac{d}{dr}\left(\xi_{h\beta}\xi_{h\gamma}\right)\right]+S_{\beta\gamma\alpha}\xi_{h\beta}[...]+S_{\gamma\alpha\beta}\xi_{h\gamma}[...]\right\}\\
&+(\Gamma_1-1)\frac{p}{r^2}\left\{(\nabla\cdot\xi)_\alpha\left[r^2\frac{d\xi_{r\beta}}{dr}\frac{d\xi_{r\gamma}}{dr}+2\xi_{r\beta}\xi_{r\gamma}-\xi_{r\beta}\xi_{h\gamma}\Lambda_\gamma^2-\xi_{r\gamma}\xi_{h\beta}\Lambda_\beta^2+\xi_{h\beta}\xi_{h\gamma}H^\alpha_{\beta\gamma}\right]\right.\\
&\quad\left.+(\nabla\cdot\xi)_\beta[...]+(\nabla\cdot\xi)_\gamma[...]\right\}\\
&+\left\{2\frac{p}{r^3}\left[H^\alpha_{\beta\gamma}\xi_{r\alpha}\xi_{h\beta}\xi_{h\gamma}+H^\beta_{\gamma\alpha}\xi_{r\beta}\xi_{h\alpha}\xi_{h\gamma}+H^\gamma_{\alpha\beta}\xi_{r\gamma}\xi_{h\beta}\xi_{h\alpha}\right.\right.\\
&\quad\left.\left.-\Lambda_\alpha^2\xi_{h\alpha}\xi_{r\beta}\xi_{r\gamma}-\Lambda_\beta^2\xi_{h\beta}\xi_{r\alpha}\xi_{r\gamma}-\Lambda_\gamma^2\xi_{h\gamma}\xi_{r\beta}\xi_{r\alpha}\right]\right\}. \qquad \text{(G.37)}
\end{aligned}
$$

We shorten the expression with '...', the meaning of which should be clear from the context. Here, the angular integration results are defined with

$$
\begin{aligned}
T_{\alpha\beta\gamma} &\equiv \int d\theta d\phi \sin\theta Y_\alpha Y_\beta Y_\gamma \equiv <\Lambda_\alpha\Lambda_\beta\Lambda_\gamma>,\\
F^\alpha_{\beta\gamma} &\equiv \frac{1}{T_{\alpha\beta\gamma}}<Y_\alpha\frac{\partial Y_\beta}{\partial\theta}\frac{\partial Y_\gamma}{\partial\theta}>=\frac{1}{2}\left(\Lambda_\beta^2+\Lambda_\gamma^2-\Lambda_\alpha^2\right),\\
G^\alpha_{\beta\gamma} &\equiv \frac{1}{T_{\alpha\beta\gamma}}<\frac{\partial Y_\alpha}{\partial\theta}\frac{\partial Y_\beta}{\partial\theta}\frac{\partial Y_\gamma}{\partial\theta}>=\frac{1}{4}\left[\Lambda_\alpha^4-\left(\Lambda_\beta^2-\Lambda_\gamma^2\right)^2\right],\\
S_{\alpha\beta\gamma} &\equiv \frac{1}{T_{\alpha\beta\gamma}}<\frac{\cos\theta}{\sin\theta}\frac{\partial Y_\alpha}{\partial\theta}\frac{\partial Y_\beta}{\partial\theta}\frac{\partial Y_\gamma}{\partial\theta}>=\left(G^\alpha_{\beta\gamma}+G^\beta_{\alpha\gamma}+G^\gamma_{\alpha\beta}\right),\\
H^\alpha_{\beta\gamma} &\equiv \frac{1}{T_{\alpha\beta\gamma}}<Y_\alpha\frac{\partial^2 Y_\beta}{\partial\theta^2}\frac{\partial^2 Y_\gamma}{\partial\theta^2}+\frac{\cos^2\theta}{\sin^2\theta}Y_\alpha\frac{\partial Y_\beta}{\partial\theta}\frac{\partial Y_\gamma}{\partial\theta}>=\Lambda_\beta^2\Lambda_\gamma^2-S_{\alpha\beta\gamma}-F^\alpha_{\beta\gamma},\\
Q_{\alpha\beta\gamma} &\equiv \frac{1}{T_{\alpha\beta\gamma}}<\frac{\cos^3\theta}{\sin^3\theta}\frac{\partial Y_\alpha}{\partial\theta}\frac{\partial Y_\beta}{\partial\theta}\frac{\partial Y_\gamma}{\partial\theta}+\frac{\partial^2 Y_\alpha}{\partial\theta^2}\frac{\partial^2 Y_\beta}{\partial\theta^2}\frac{\partial^2 Y_\gamma}{\partial\theta^2}>. \qquad \text{(G.38)}
\end{aligned}
$$

These are expressions for $m=0$ triplets only. The two quantities, $Q_{\alpha\beta\gamma}$ and $T_{\alpha\beta\gamma}$, have to be calculated numerically.

Expression (G.37) still suffers from the large cancellation between curvature terms. We manually remove the curvature terms, i.e., the terms of the forms $(\nabla\cdot\xi)\xi_h d\xi_h/dr$ and $\xi_h d(\xi_h\xi_h)/dr$, and taking the differences between these large terms into a slightly simplified expression for $d\kappa$, which is

$$
\begin{aligned}
d\kappa &= (\Gamma_1-1)^2 p(\nabla\cdot\xi)_\alpha(\nabla\cdot\xi)_\beta(\nabla\cdot\xi)_\gamma+\frac{2p}{r^3}\xi_{h\alpha}\xi_{h\beta}\xi_{h\gamma}Q_{\alpha\beta\gamma}\\
&\quad+2p\frac{d\xi_{r\alpha}}{dr}\frac{d\xi_{r\beta}}{dr}\frac{d\xi_{r\gamma}}{dr}+4\frac{p}{r^3}\xi_{r\alpha}\xi_{r\beta}\xi_{r\gamma}\\
&\quad+\frac{p}{r}\left\{\left[F^\alpha_{\beta\gamma}\Gamma_1(\nabla\cdot\xi)_\alpha-F^\alpha_{\beta\gamma}\frac{1}{r}\xi_{r\alpha}+S_{\alpha\beta\gamma}\frac{1}{r}\xi_{h\alpha}\right]\left(\xi_{r\beta}\frac{d\xi_{h\gamma}}{dr}+\xi_{r\gamma}\frac{d\xi_{h\beta}}{dr}\right)\right.\\
&\quad\left.+\left[F^\beta_{\gamma\alpha}...\right](...)+\left[F^\gamma_{\alpha\beta}...\right](...)\right\}\\
&\quad+\frac{p}{r^2}\left\{F^\alpha_{\beta\gamma}\xi_{r\alpha}\frac{d}{dr}\left(\xi_{h\beta}\xi_{h\gamma}\right)+F^\beta_{\alpha\gamma}\xi_{r\beta}\frac{d}{dr}\left(\xi_{h\alpha}\xi_{h\gamma}\right)+F^\gamma_{\alpha\beta}\xi_{r\gamma}\frac{d}{dr}\left(\xi_{h\alpha}\xi_{h\beta}\right)\right\}\\
&\quad+(\Gamma_1-1)\frac{p}{r^2}\left\{(\nabla\cdot\xi)_\alpha\left(r^2\frac{d\xi_{r\beta}}{dr}\frac{d\xi_{r\gamma}}{dr}+2\xi_{r\beta}\xi_{r\gamma}-\xi_{r\beta}\xi_{h\gamma}\Lambda_\gamma^2-\xi_{r\gamma}\xi_{h\beta}\Lambda_\beta^2+\xi_{h\beta}\xi_{h\gamma}H^\alpha_{\beta\gamma}\right)\right.\\
&\quad\left.+(\nabla\cdot\xi)_\beta(...)+(\nabla\cdot\xi)_\gamma(...)\right\}\\
&\quad+2\frac{p}{r^3}\left\{\left(H^\alpha_{\beta\gamma}\xi_{r\alpha}\xi_{h\beta}\xi_{h\gamma}+H^\beta_{\gamma\alpha}\xi_{r\beta}\xi_{h\alpha}\xi_{h\gamma}+H^\gamma_{\alpha\beta}\xi_{r\gamma}\xi_{h\beta}\xi_{h\alpha}\right.\right.
\end{aligned}
$$

$$-\Lambda_\alpha^2\xi_{h\alpha}\xi_{r\beta}\xi_{r\gamma}-\Lambda_\beta^2\xi_{h\beta}\xi_{r\alpha}\xi_{r\gamma}-\Lambda_\gamma^2\xi_{h\gamma}\xi_{r\beta}\xi_{r\alpha})\}$$
$$-\frac{1}{r^2}\left\{F^\alpha_{\beta\gamma}\xi_{h\beta}\xi_{h\gamma}\left(\rho r\omega^2\xi_r+2\xi_r\rho g+\delta p\right)_\alpha+F^\beta_{\alpha\gamma}\xi_{h\alpha}\xi_{h\gamma}(...)+F^\gamma_{\alpha\beta}\xi_{h\beta}\xi_{h\alpha}(...)\right\}. \qquad \text{(G.39)}$$

The terms in the last parentheses are the differences between the two large curvature terms; they appear to be comparable to the other terms.

The improved method described here significantly improves the calculations of κ. The influence of the curvature terms is removed analytically, and the results on κ is more accurate.

G.2.3 The Method of Integration-by-parts

Following Kumar & Goodman (1996), we can rewrite the expression for κ employing the technique of integration by parts. The angular dependences can be analytically integrated using formula from their paper.

We first pretend that we work in Cartesian coordinates. This means that the covariant derivatives are equivalent to partial derivatives, and makes it easier to integrate by parts. For example,

$$\begin{aligned}
&\int d^3x p(\nabla\cdot\xi)\xi^i_{;j}\xi^j_{;i}\\
=&\int d^3x\left\{\left[p(\nabla\cdot\xi)\xi^i\xi^j_{;i}\right]_{;j}-\left[p(\nabla\cdot\xi)\right]_{;j}\xi^i\xi^j_{;i}-\left[p(\nabla\cdot\xi)\right]\xi^i(\nabla\cdot\xi)_{;i}\right\}\\
=&\int d^3x\left\{\left[p(\nabla\cdot\xi)\right]_{;ji}\xi^i\xi^j+p_{;i}\xi^i(\nabla\cdot\xi)^2\right\}, \qquad \text{(G.40)}
\end{aligned}$$

where vanishing surface integrals are assumed, as well as the implicit rule of Einstein summation.

For another term in κ,

$$\begin{aligned}
&\int d^3x p\xi^i_{;j}\xi^j_{;k}\xi^k_{;i}\\
=&-\int d^3x\left[p_{;j}\xi^i\xi^j_{;k}\xi^k_{;i}+p\xi^i(\nabla\cdot\xi)_{;k}\xi^k_{;i}+p\xi^i\xi^j_{;k}\xi^k_{;ij}\right]\\
=&\int d^3x\left[-\frac{1}{2}p_{;ijk}\xi^i\xi^j\xi^k+\frac{3}{2}\left(p\nabla\cdot\xi\right)_{;ji}\xi^i\xi^j+\frac{3}{2}\left(\xi\cdot\nabla p\right)_{;ij}\xi^i\xi^j\right.\\
&-\left(p\nabla\cdot\xi\right)_{;i}\xi^i(\nabla\cdot\xi)+3\left(\xi\cdot\nabla p\right)_{;i}\xi^i(\nabla\cdot\xi)-p(\nabla\cdot\xi)^3\\
&\left.+2\left(\xi\cdot\nabla p\right)(\nabla\cdot\xi)^2-\frac{3}{2}p_{;ij}\xi^i\xi^j(\nabla\cdot\xi)\right]. \qquad \text{(G.41)}
\end{aligned}$$

We introduce the Eulerian pressure perturbation p', satisfying

$$p'=\delta p-\xi_r\frac{dp}{dr}=-\Gamma_1 p(\nabla\cdot\xi)-\left(\xi\cdot\nabla p\right), \qquad \text{(G.42)}$$

where δp is the Lagrangian pressure perturbation. Adiabaticity of the perturbation is assumed.

The final expression for κ is

$$\kappa = \int d^3x \left\{ -\frac{1}{6}p_{;ijk}\xi^i\xi^j\xi^k - \frac{1}{2}p_{;ij}\xi^i\xi^j(\nabla\cdot\xi) - \frac{1}{2}p'_{;ij}\xi^i\xi^j \right. \\ \left. -p'_{;i}\xi^i(\nabla\cdot\xi) + \frac{\Gamma_1(\Gamma_1+1)}{6}p(\nabla\cdot\xi)^3 \right\}. \tag{G.43}$$

The derivatives on the displacement ξ are transferred to pressure through this exercise. As we will show later, this further improves the accuracy in calculating κ.

With just a simple transformation, the above equation agrees with those in Appendix A of Kumar & Goodman (1996).

Permutation among modes yields

$$\begin{aligned}\kappa = & -\frac{1}{6}\int d^3x \left\{ p_{;ijk}(\xi^i)_\alpha(\xi^j)_\beta(\xi^k)_\gamma \right. \\ & + \left[p_{;ij}(\xi^i)_\alpha(\xi^k)_\beta(\nabla\cdot\xi)_\gamma + p_{;ij}(\xi^i)_\beta(\xi^k)_\gamma(\nabla\cdot\xi)_\alpha + p_{;ij}(\xi^i)_\gamma(\xi^k)_\alpha(\nabla\cdot\xi)_\beta \right] \\ & + \left[(p'_{;ij})_\alpha(\xi^i)_\beta(\xi^j)_\gamma + (p'_{;ij})_\beta(\xi^i)_\alpha(\xi^j)_\gamma + (p'_{;ij})_\gamma(\xi^i)_\beta(\xi^j)_\alpha \right] \\ & + \left\{ (p'_{;i})_\alpha \left[(\xi^i)_\beta(\nabla\cdot\xi)_\gamma + (\xi^i)_\gamma(\nabla\cdot\xi)_\beta \right] + (p'_{;i})_\beta \left[(\xi^i)_\alpha(\nabla\cdot\xi)_\gamma + (\xi^i)_\gamma(\nabla\cdot\xi)_\alpha \right] \right. \\ & \left. \left. + (p'_{;i})_\gamma \left[(\xi^i)_\beta(\nabla\cdot\xi)_\alpha + (\xi^i)_\alpha(\nabla\cdot\xi)_\beta \right] \right\} - \Gamma_1(\Gamma_1+1)p(\nabla\cdot\xi)^3 \right\}. \end{aligned} \tag{G.44}$$

Now for practical operation, we switch back to spherical coordinates. The expression for covariant derivatives on scalars can be found in §G.1.3. The Eulerian pressure perturbation has an angular dependence of $p' = \hat{p}'Y_{\ell m}$, and all angular dependences in the new integral for κ can be integrated using equation (G.34). We get

$$\begin{aligned} d\kappa = & + \left[\frac{d^3p}{dr^3}\xi_{r\alpha}\xi_{r\beta}\xi_{r\gamma} - \Gamma_1(\Gamma_1+1)p(\nabla\cdot\xi)_\alpha(\nabla\cdot\xi)_\beta(\nabla\cdot\xi)_\gamma \right] \\ & + F^\alpha_{\beta\gamma} \left\{ \xi_{h\beta}\xi_{h\gamma} \left[\frac{d}{dr}\left(\frac{1}{r}\frac{dp}{dr}\right)\xi_{r\alpha} + \frac{1}{r}\frac{dp'_\alpha}{dr} + \frac{1}{r}\frac{dp}{dr}(\nabla\cdot\xi)_\alpha \right] + (\nabla\cdot\xi)_\alpha \left[\frac{1}{r}p'_\beta\xi_{h\gamma} + \frac{1}{r}p'_\gamma\xi_{h\beta} \right] \right. \\ & \left. + \xi_{r\alpha} \left[\frac{d}{dr}\left(\frac{1}{r}p'_\gamma\right)\xi_{h\beta} + \frac{d}{dr}\left(\frac{1}{r}p'_\beta\right)\xi_{h\gamma} \right] \right\} + F^\beta_{\alpha\gamma}\{...\} + F^\gamma_{\alpha\beta}\{...\} \\ & + \left\{ \xi_{r\beta}\xi_{r\gamma} \left[\frac{d^2}{dr^2}p'_\alpha + \frac{d^2p}{dr^2}(\nabla\cdot\xi)_\alpha \right] + \xi_{r\alpha}\xi_{r\gamma}[...] + \xi_{r\beta}\xi_{r\alpha}[...] \right\} \\ & + \left\{ (\nabla\cdot\xi)_\alpha \left[\frac{d}{dr}p'_\beta\xi_{r\gamma} + \frac{d}{dr}p'_\gamma\xi_{r\beta} \right] + (\nabla\cdot\xi)_\beta[...] + (\nabla\cdot\xi)_\gamma[...] \right\} \\ & + \left\{ G^\alpha_{\beta\gamma}\frac{1}{r^2}p'_\alpha\xi_{h\beta}\xi_{h\gamma} + G^\beta_{\alpha\gamma}\frac{1}{r^2}p'_\beta\xi_{h\alpha}\xi_{h\gamma} + G^\gamma_{\beta\alpha}\frac{1}{r^2}p'_\gamma\xi_{h\beta}\xi_{h\alpha} \right\}, \end{aligned} \tag{G.45}$$

where $d\kappa$ is defined in equation (G.36), and p' is the shorthand of $\hat{p}'$.

Numerical realization of this expression is made more accurate with the following two expressions,

$$\frac{dp'}{dr} = \rho(\omega^2 - N^2)\xi_r - \frac{g}{c^2}p';$$

$$\frac{d}{dr}\left(\frac{1}{r}\frac{dp}{dr}\right)\xi_r + \frac{1}{r}\frac{dp'}{dr} + \frac{1}{r}\frac{dp}{dr}(\nabla\cdot\xi) = \frac{1}{r^2}\xi_r\left[\rho g + \rho\omega^2 r - \rho r\frac{dg}{dr}\right]. \quad \text{(G.46)}$$

The first expression is used to reduce the order of radial derivatives on p', which would otherwise cause numerical noise; the second is to capture the cancellation between terms. These two equations help to produce a smoother $d\kappa$, and lead to answers for κ that are more credible.

Note that, after integration by parts, the radial dependence ($d\kappa$) of expression (G.44) is not the same as that in equation (G.1). Here, it does not tell where in the star the strongest coupling should come from and is therefore less physically revealing.

G.2.4 Conclusions

We call here the direct method (§G.2.1) the first method, the improved one (§G.2.2) the second method, and the one using integration by parts (§G.2.3) the third method.

The first method suffers strongly from the presence of the large curvature terms, and is therefore not reliable.

The second method removes this confusion. But on the other hand, it depends on the numerical gridding sensitively, as it involves numerical differentiation of many function; some of them may have sharp changes. This is demonstrated in a series of experiments, in which we calculate the coupling coefficients using white dwarf models with finer and finer grids. The results we obtain can vary by factor of unity sometimes. In general, the results approach those given by the third method, as the precision in the models and in the eigenfunctions improve.

The third method, in our opinion, is the best out of the three. It has no intrinsic problem with large cancellations, as the numerical derivatives on the eigenfunctions are minimalized. It is also stable. The results obtained using this method vary by only a few percent when the spacing between the grids changes.

All methods agree, however, to the orders of magnitudes, as is shown in Figure G.2 for a subset of couplings. The full results, involving various scaling relations, are presented in Chapter 7.

G.3 The Incompressible Limit

The dependences of κ on various mode properties can be analytically derived in the incompressible limit,

$$\begin{aligned} (\nabla\cdot\xi) &\rightarrow 0 \\ \Gamma_1(\nabla\cdot\xi) &\rightarrow \text{constant.} \end{aligned} \quad \text{(G.47)}$$

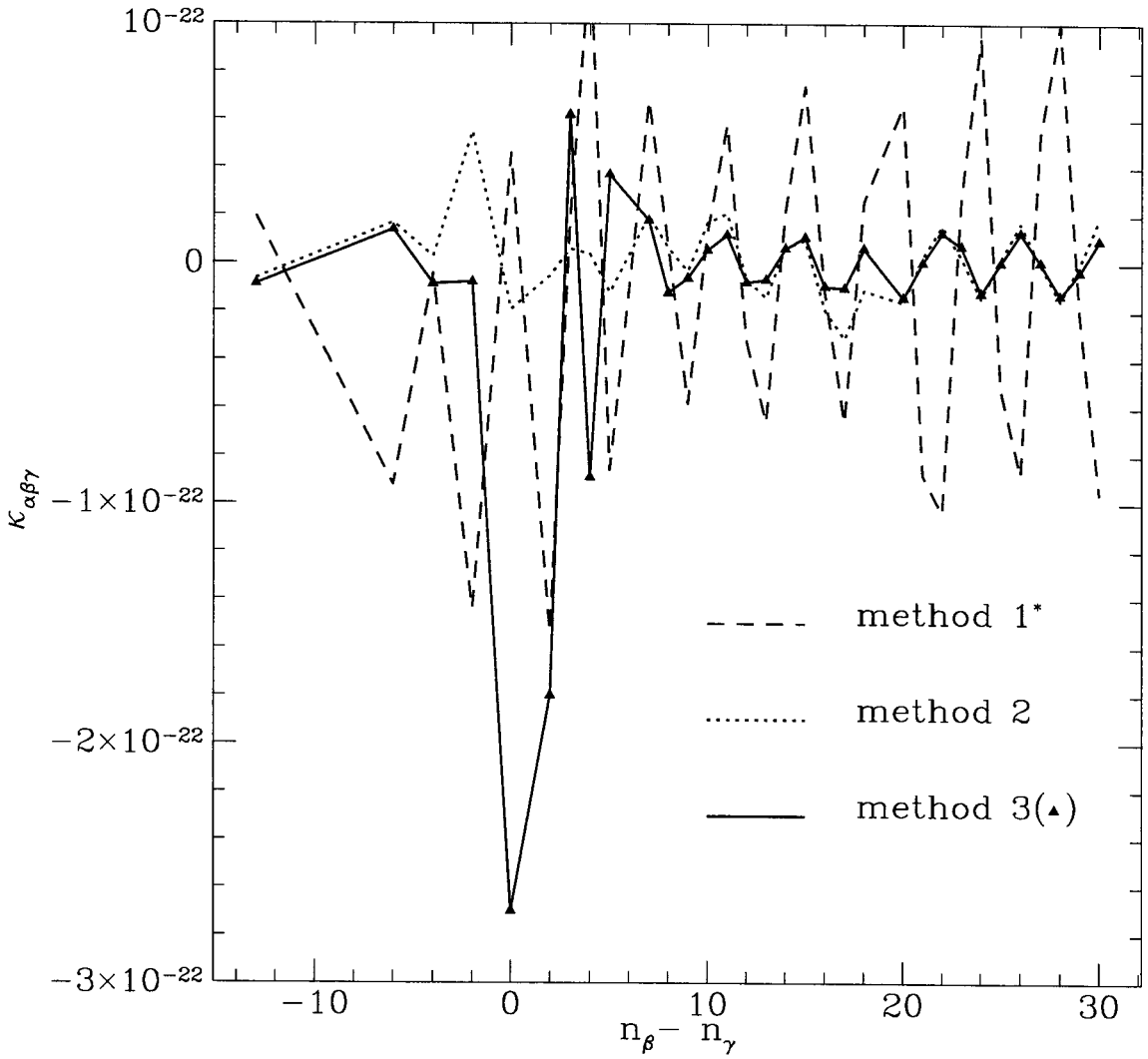

Figure G.2: The coupling coefficients calculated using three different methods for couplings that involve α mode ($(n,\ell) = (1,1)$), β and γ modes ($(n_\beta, 1)$ and $(n_\gamma, 2)$). We choose n_β and n_γ such that $\omega_\beta + \omega_\gamma \sim \omega_\alpha$ (parametric couplings). And κ is plotted against the radial difference between the last two modes, represented by $n_\beta - n_\gamma$. As expected, the coupling is the strongest when $n_\beta \sim n_\gamma$. Results from method 1 (dashed line, the direct method, §G.2.1), reduced by a factor of 5, compare poorly with results from both method 2 (dotted line, improved direct method, §G.2.2) and method 3 (solid line and solid triangles, integration-by-parts method, §G.2.3). It is adversely affected by the strong cancellations between the large curvature terms. The last two methods agree better, though method 2 fails to produce the peak around $n_\beta - n_\gamma \sim 0$. The magnitude of this peak is instead verified in the incompressible limit.

Equation (G.43) becomes

$$\kappa = \int d^3x \left\{ -\frac{1}{6} p_{;ijk} \xi^i \xi^j \xi^k - \frac{1}{2} p'_{;ij} \xi^i \xi^j \right\}. \tag{G.48}$$

The equation of motion is simplified in the incompressible limit,

$$p'_{;i} = \rho\omega^2 \xi_i - g \frac{d\rho}{dz} \xi_z \delta^i_z, \tag{G.49}$$

Stripping the angular dependence of $\nabla_h Y_{\ell m}$ off p' and ξ_h, and $Y_{\ell m}$ of ξ_z, we are left with the radial components and they are related by

$$\begin{aligned} p' &= \rho\omega^2 r \xi^h, \\ p'_{;z} &= \rho \left(\omega^2 - g \frac{d\rho}{dz} \right) \xi^z \\ \xi^z_{;z} &= \frac{\ell(\ell+1)}{R} \xi^h. \end{aligned} \tag{G.50}$$

With the following angular integration formulas,

$$\begin{aligned} A_{\alpha\beta\gamma} &= \int d\Omega \nabla_h Y^\alpha_{\ell m} \nabla_h Y^\beta_{\ell m} Y^\gamma_{\ell m} = \frac{\Lambda^2_\alpha + \Lambda^2_\beta - \Lambda^2_\gamma}{2} < \Lambda_\alpha \Lambda_\beta \Lambda_\gamma >, \\ B_{\alpha\beta\gamma} &= \int d\Omega \nabla^2_h Y^\alpha_{\ell m} \nabla_h Y^\beta_{\ell m} \nabla_h Y^\gamma_{\ell m} = -\Lambda^2_\alpha A_{\beta\gamma\alpha}, \\ C_{\alpha\beta\gamma} &= \int d\Omega Y^\alpha_{\ell m} Y^\beta_{\ell m} Y^\gamma_{\ell m} =< \Lambda_\alpha \Lambda_\beta \Lambda_\gamma >, \end{aligned} \tag{G.51}$$

and mutating terms in expression (G.48), we obtain

$$\begin{aligned} \kappa = -\frac{1}{6} \int r^2 dr \quad & \left\{ \frac{1}{r} \rho \left(\omega^2_\alpha B_{\alpha\beta\gamma} + \omega^2_\beta B_{\beta\alpha\gamma} + \omega^2_\gamma B_{\gamma\alpha\beta} \right) \xi^h_\alpha \xi^h_\beta \xi^h_\gamma \right. \\ & -2g \frac{d^2\rho}{dz^2} C_{\alpha\beta\gamma} \xi^z_\alpha \xi^z_\beta \xi^z_\gamma - g \frac{d\rho}{dz} C_{\alpha\beta\gamma} \left(\xi^z_\alpha \xi^z_\beta \xi^z_\gamma \right)_{;z} \\ & -\frac{g}{r} \frac{d\rho}{dz} \left(\xi^z_\alpha \xi^h_\beta \xi^z_\gamma A_{\alpha\beta\gamma} + \xi^z_\alpha \xi^h_\gamma \xi^z_\beta A_{\alpha\gamma\beta} + \xi^z_\beta \xi^h_\alpha \xi^z_\gamma A_{\beta\alpha\gamma} \right. \\ & \left. \left. \xi^z_\beta \xi^h_\gamma \xi^z_\alpha A_{\beta\gamma\alpha} + \xi^z_\gamma \xi^h_\alpha \xi^z_\beta A_{\gamma\alpha\beta} + \xi^z_\gamma \xi^h_\beta \xi^z_\alpha A_{\gamma\beta\alpha} \right) \right\}. \end{aligned} \tag{G.52}$$

Relating ξ^h to ξ^z through equation (G.50), integrating the functions by parts, and express $A_{\alpha\beta\gamma}$ explicitly, we finally arrive at

$$\kappa = -\frac{\left(\omega^2_\alpha B_{\alpha\beta\gamma} + \omega^2_\beta B_{\beta\alpha\gamma} + \omega^2_\gamma B_{\gamma\alpha\beta} \right)}{6} \int r dr \rho \xi^h_\alpha \xi^h_\beta \xi^h_\gamma. \tag{G.53}$$

To estimate the analytical dependence of this κ, we introduce the physical displacement $\hat{\xi}_h \sim (Rk_h)\xi^h \sim \Lambda \xi^h$, $ik_h \hat{\xi}_h \sim \Lambda^2/R \xi^h$. And we assume the daughter modes β and γ are similar in radial

structure and spherical degrees, so κ can be estimated as

$$\begin{aligned}
\kappa &\sim \int r^2 dr (ik_h\hat{\xi}_h)_\alpha \rho (k_h\hat{\xi}_h)^2_\beta \left(\omega_\alpha^2 \frac{\Lambda_\beta^2 + \Lambda_\gamma^2 - \Lambda_\alpha^2}{\Lambda_\beta^2 \Lambda_\gamma^2} + \omega_\beta^2 \frac{\Lambda_\alpha^2 + \Lambda_\gamma^2 - \Lambda_\beta^2}{\Lambda_\alpha^2 \Lambda_\gamma^2} + \omega_\gamma^2 \frac{\Lambda_\beta^2 + \Lambda_\alpha^2 - \Lambda_\gamma^2}{\Lambda_\beta^2 \Lambda_\alpha^2} \right) \\
&\sim \frac{1}{\sqrt{n_\alpha L \tau_{\omega\alpha}}} \frac{n'_\beta \Lambda_\beta^2}{n_\beta \omega_\beta^2} \left(\frac{\omega_\beta^2}{\Lambda_\beta^2} \right) \\
&\sim \frac{1}{\sqrt{n_\alpha L \tau_{\omega\alpha}}} \frac{1}{n_\alpha \ell_\alpha},
\end{aligned} \tag{G.54}$$

using similar arguments as in equations (G.24) - (G.26). This final expression has the same dependence on n_α as equation (G.29). It is of the same order as the compressibility term, equation (G.28). Moreover, it does not depend on ℓ of the daughter modes. At fixed ω_α, it grows almost linearly with ℓ_α; while at fixed n_α, it decays linearly with ℓ_α. These dependences are expected to hold also in the compressible case, and it is proven so by the integrations using method 3. Also, the incompressible results agree with results from method 3 to within a factor of 2.

Bibliography

Arfken, G. 1985, Mathematical Methods for Physicists, Third Edition, (Academic Press), 158

Kumar, P., & Goodman, J. 1996, ApJ, 466, 946

Lightman, A. P., Press, W. L., Price, R. H., & Teukolsky, S. A. 1975, Problem Books in Relativity and Gravitation, (New Jersey:Princeton University Press)

Wolfram, S. 1991, Mathematica, a system for doing mathematics by computer, (Addison-Wesley)

Appendix H Coherent Parametric Instability

In this appendix, we introduce the concept of 'coherent parametric instability'. It complements the classical 'parametric instability' and, in places where it is applicable, limits amplitudes of the parent modes to lower values than predicted using equation (6.19). We discuss one application of this concept when the parametric daughters are travelling waves in white dwarfs.

H.1 The Concept

First, we re-visit the amplitude equations (eq. [6.16]) describing a dissipative system of only three modes, $\delta\omega = \omega_1 - \omega_2 - \omega_3 \sim 0$. Retaining only resonant terms, we get

$$\begin{aligned}
\frac{dA_1}{dt} &= \gamma_1 A_1 + i\omega_1 A_1 - i\frac{3}{\sqrt{8}}\omega_1 \kappa_{123} A_2 A_3, \\
\frac{dA_2}{dt} &= \gamma_2 A_2 + i\omega_2 A_2 - i\frac{3}{\sqrt{8}}\omega_2 \kappa_{123} A_1 A_3^*, \\
\frac{dA_3}{dt} &= \gamma_3 A_3 + i\omega_3 A_3 - i\frac{3}{\sqrt{8}}\omega_3 \kappa_{123} A_1 A_2^*.
\end{aligned} \tag{H.1}$$

Here, mode 1 is excited, and modes 2, 3 are damped. Analysis in §6.3.1 shows that the energy in the daughter modes (modes 2 and 3) undergoes unstable growth whenever the energy in mode 1 rises above a threshold described by equation (6.19). 'Parametric instability' can limit the energy in overstable modes.

Consider a situation in which a fourth mode (mode 4) is also (near-)resonantly interacting with modes 1 and 2. If 4 is sufficiently similar to mode 3 such that $\kappa_{124} \sim \kappa_{123} \sim \kappa$, the daughter modes evolve according to the following amplitude equations,

$$\begin{aligned}
\frac{dA_2}{dt} &= \gamma_2 A_2 + i\omega_2 A_2 + i\frac{3}{\sqrt{8}}\omega_2 \kappa (A_1 A_3^* + A_1 A_4^*), \\
\frac{dA_3}{dt} &= \gamma_3 A_3 + i\omega_3 A_3 + i\frac{3}{\sqrt{8}}\omega_3 \kappa A_1 A_2^*, \\
\frac{dA_4}{dt} &= \gamma_4 A_4 + i\omega_4 A_4 + i\frac{3}{\sqrt{8}}\omega_4 \kappa A_1 A_2^*.
\end{aligned} \tag{H.2}$$

Mode 4 is also damped in this discussion.

We further stipulate that mode 4 be so similar to mode 3 in frequency such that $|\omega_3 - \omega_4| \leq |\gamma_3| \sim |\gamma_4|$. We call mode 4 the 'twin' of mode 3. In the case of a star, mode 3 can have a number of 'twins' depending on the mode density around it. As both are evolving in time under the same

force, A_3 and A_4 should have effectively the same phases and magnitudes. Denote the amplitude of mode 3 or 4 as A_y, and equation (H.2) can be simplified into

$$\begin{aligned} \frac{dA_2}{dt} &= \gamma_2 A_2 + i\omega_2 A_2 + i\frac{3}{\sqrt{8}}\omega_2\kappa(2A_1A_y^*), \\ \frac{dA_y}{dt} &= \gamma_y A_y + i\omega_y A_y + i\frac{3}{\sqrt{8}}\omega_y\kappa A_1 A_2^*. \end{aligned} \tag{H.3}$$

The two parametric couplings, $(\omega_1 \to \omega_2 - \omega_3)$ and $(\omega_1 \to \omega_2 - \omega_4)$, are called 'coherent'.

In general, mode 2 would be similar to mode 3 in having 'twins'. In fact, we can consider the case where both mode 2 and 3 have N_c such twin modes[1]. Equation (H.3) turns into

$$\begin{aligned} \frac{dA_x}{dt} &= \gamma_x A_x + i\omega_x A_x + i\frac{3}{\sqrt{8}}\omega_x\kappa(N_c A_1 A_y^*), \\ \frac{dA_y}{dt} &= \gamma_y A_y + i\omega_y A_y + i\frac{3}{\sqrt{8}}\omega_y\kappa(N_c A_1 A_x^*). \end{aligned} \tag{H.4}$$

Here, x denotes mode 2 or its twin modes. This equation requires that every y mode interacts with every y mode (and mode 1) with equal coupling coefficient. For each x mode, the fact that there are N_c near-identical y modes to couple with can be thought of as it interacts with one y mode N_c times more strongly. There are in total $N_c^2/2$ such coherent couplings.

And the new energy threshold due to the 'coherent parametric instability' is

$$E_1 \geq \frac{16}{9N_c^2\kappa^2}\left[\left(\frac{\delta\omega}{\omega_1}\right)^2 + \left(\frac{\Gamma}{\omega_1}\right)^2\right]. \tag{H.5}$$

Mode 1 is able to nonlinearly excite the daughter modes at this smaller value due to the effective increase in κ.

On the other hand, mode 1 witnesses an increase in κ by a factor of N_c^2 due to the coherence between the two groups of daughter modes,

$$\frac{dA_1}{dt} = \gamma_1 A_1 + i\omega_1 A_1 + i\frac{3}{\sqrt{8}}\omega_1\kappa(N_c^2 A_x A_y). \tag{H.6}$$

H.2 How to Estimate N_c?

We anchor our discussions here on the normal modes in a white dwarf. For a parent mode 1, we choose a pair of daughter modes that interact strongly with the parent mode and nearly satisfy the frequency resonance condition. We mark them as x_c and y_c, the subscript c for central. We ask, how big is the population of daughter modes, sitting around these two centroid modes respectively,

[1] The following analysis will tell that N_c is related to the property of the parent mode, and therefore is the same for modes 2 and 3.

that may be parametrically excited by mode 1 *coherently*?

Our discussions in §H.1 set two constraints on this coherent population. The first is that every daughter mode from the x group couples equally strongly with every one from the y group (and mode 1). As we argue in Appendix G, most of the coupling happens above z_1, where z_1 is the depth of the first radial node for mode 1. The coupling coefficient κ is maximized when the two daughter modes have equal numbers of radial nodes inside $z \leq z_1$. These numbers are $n' \sim n_x/n_1 \sim n_y/n_1$ (see eq. [G.26]). Two daughter modes are considered radially similar (and therefore have maximum κ) when the difference in n' is less than $1/2$. This is equivalent of $|n_x - n_y| \leq n_1/2$, while for modes x_c and y_c, $|n_x - n_y| \sim 0$. We obtain an estimate for N_c from this constraint,

$$N_{c\kappa} \sim n_1/2. \tag{H.7}$$

The second constraint concerns the coherence between mode phases during the parametric instability which lasts a time of order $1/\Gamma$. Every mode in the x (or y) group has to be close to each other in frequency,

$$\Delta\omega \leq \Gamma. \tag{H.8}$$

The number of modes falling inside this frequency width is of order

$$N_{c\omega} \sim \frac{\Delta\omega}{(\omega_x/n_x)} \sim \frac{\Gamma}{(\omega_x/n_x)}, \tag{H.9}$$

where n_x is the radial order of the x_c mode, and ω_x/n_x is the mean frequency separation among its neighbouring modes. The same relation holds for y modes.

When the daughter modes are not strongly dissipated, $|\gamma_x| \sim 1/(n_x\tau_{\omega x}) \ll \omega_x/n_x$, there is no coherent modes around the daughter pair x_c and y_c. Note that although there may be many pairs of daughter modes each having frequency detuning $\delta\omega < \Gamma$, the frequency width within each group of these daughter modes is larger than Γ. There cannot be coherent parametric instability.

When the daughter pair are strongly damped, they are travelling waves inside the star with global damping rates of order ω_x/n_x (see Chap. 5). The discussions in §7.4 suggest that these travelling waves only interact with the parent mode for $n' \sim n_x/n_1 \sim n_y/n_1$ periods. The number of coherent partners in the case of travelling waves is therefore (based on eq. [7.9]) determined by the coherence within this interaction time,

$$N_{c\omega} \sim \frac{\omega_x/n'}{\omega_x/n_x} \sim n_1. \tag{H.10}$$

This can also be obtained from equation (H.9) by using $\Gamma \sim |\gamma_x| \sim n_1\omega_x/n_x$, as only the energy loss rate for the upper n' nodes of the travelling wave is meaningful.

The number of coherent parametric couplings for mode 1 is therefore

$$N_c = \mathrm{Min}(N_{c\omega}, N_{c\kappa}) \sim \mathrm{Min}\left(\frac{\Gamma}{(\omega_x/n_x)}, \frac{n_1}{2}\right). \tag{H.11}$$

And the physical amplitude for an overstable mode can be reduced to an expression,

$$\begin{aligned} \frac{\delta\rho}{\rho} &\sim A \times \mathrm{Norm} \sim \frac{1}{\sqrt{n_1 L \tau_{\omega 1}}} \frac{1}{N_c \kappa} \left(\frac{\Gamma}{\omega_1}\right) \\ &\sim \frac{1}{\sqrt{n_1 L \tau_{\omega 1}}} \frac{\sqrt{n_1^3 L \tau_{\omega 1}}}{N_c} \left(\frac{\Gamma}{\omega_1}\right) \sim \left(\frac{n_1}{N_c}\right)\left(\frac{\Gamma}{\omega_1}\right), \end{aligned} \tag{H.12}$$

where $\Gamma \approx |\gamma_x + \gamma_y|$. For daughters that are travelling waves, $N_c \sim n_1$ and $\delta\rho/\rho \sim \Gamma/\omega_1 \sim 1/(4n_x)$.